FONDO SOCIALE EUROPEO – FSE
PROGRAMMA NAZIONALE OPERATIVO 2000/2006
"RICERCA, SVILUPPO TECNOLOGICO ED ALTA FORMAZIONE
NELLE REGIONI DELL'OBIETTIVO 1 - MISURA 1.1 (F.S.E)"

UNIVERSITY OF CALABRIA

DEPARTMENT OF CHEMICAL AND MATERIALS ENGINEERING

PHD THESIS

MODELLING OF PD-BASED MEMBRANES AND PD-BASED MEMBRANE REACTORS FOR HYDROGEN PURIFICATION AND PRODUCTION BY METHANE STEAM REFORMING

SETTORE SCIENTIFICO DISCIPLINARE (SSD):
ING-IND 26 – TEORIA DELLO SVILUPPO DEI PROCESSI CHIMICI

SUPERVISORS
PROF. FRANCESCO PAOLO DI MAIO
ING. ALBERTO DI RENZO

CANDIDATE
ING. ALESSIO CARAVELLA

PHD COURSE COORDINATOR
PROF. RAFFAELE MOLINARI

PHD COURSE CYCLE
XXI

ACADEMIC YEAR 2007-2008

A mia Madre e mio Fratello,
per l'affetto ed il sostegno che ogni giorno
mi dispensano nonostante la mia testa dura

A tutti i miei Angeli Custodi,
perché continuino a guidarmi dall'alto
tra le mille difficoltà della vità

Alla Nuova Arrivata in famiglia,
perché impari presto a camminare sulle
proprie gambe e pensare con la propria testa

A me stesso,
perché possa sempre affrontare con
passione tutto ciò che la vita avrà da offrire

It's a Long Way to the Top …

(AC/DC)

Ciò che non ci uccide, ci rende più forti.

(Friederich Nietzsche)

Puoi dimenticare ciò che hai in mente,
ma mai ciò che hai nel cuore.

(The Author)

LIST OF TABLES

CHAPTER 1

CHAPTER 2

CHAPTER 3

CHAPTER 4

CHAPTER 5

LIST OF FIGURES

CHAPTER 1

CHAPTER 2

CHAPTER 3

CHAPTER 4

CHAPTER 5

TABLE OF CONTENTS

ABSTRACT

Il presente lavoro di tesi è rivolto all'analisi, modellazione e simulazione di membrane supportate dense metalliche a base di palladio e reattori catalitici dotati di membrana della stessa tipologia. La motivazione di tale studio si inquadra nella logica della cosiddetta "*Process Intensification Strategy*" il cui fine ultimo è quello di sviluppare apparecchiature innovative in grado di fornire, a parità di condizioni, le stesse o più alte prestazioni di quelle tradizionali, ma con costi di esercizio e volumi di impianto nettamente inferiori. In questo senso – e da qui il motivo di sviluppare un lavoro di tesi sull'argomento – la tecnologia delle membrane può certamente contribuire allo scopo in modo decisivo. Entrando più specificamente nel merito dei principali argomenti di questo studio, per inquadrare meglio il suo ambito, i primi due capitoli sono incentrati sullo stato dell'arte a) dei principali processi di produzione e separazione di idrogeno e b) della tecnologia delle membrane utilizzabile per la purificazione di correnti gassose, rivolgendo particolare attenzione a quello che è uno degli argomenti principali di questo lavoro di tesi, ossia le membrane dense metalliche a base di palladio.

In seguito, l'analisi condotta nei capitoli successivi può essere idealmente divisa in due parti, nella prima delle quali (Capitoli 3 e 4) sono studiate in dettaglio le membrane dense a base di palladio. In particolare, nel Capitolo 3 è sviluppato un nuovo modello di permeazione dell'idrogeno attraverso dette membrane che permette di tener conto di diversi aspetti e problematiche non ancora affrontati esaustivamente in letteratura. Tale modello prevede che il processo di permeazione nella sua globalità sia suddiviso in stadi elementari, ciascuno dei quali caratterizzato dalle proprie equazioni cinetiche e di trasporto. Gli stadi elementari considerati sono i seguenti: 1-2) trasporto esterno dell'idrogeno dal bulk fluido alla superficie metallica e *vice-versa*, 3-4) adsorbimento a desorbimento sulla/dalla superficie metallica, 5-6) transizione dell'idrogeno atomico dalla fase di adsorbimento superficiale a quella di dissoluzione nel bulk metallico e *vice-versa*, 7) diffusione dell'idrogeno atomico attraverso il

bulk metallico e 8) trasporto esterno di massa attraverso i diversi strati porosi di un opportuno supporto multistrato. Sebbene in questo tipo di membrane si abbia solo flusso di idrogeno, per il trasporto di massa nelle fasi fluide esterne allo strato selettivo vero e proprio è stato adottato un approccio multicomponente, in modo tale da poter descrivere correttamente situazioni più vicine alla realtà di quelle solitamente considerate in letteratura (miscele di idrogeno bi-componenti). Il modello così sviluppato, validato con opportuni dati di letteratura, permette di quantificare l'influenza di ciascuno stadio di permeazione e di identificare così quelli che controllano il processo al variare delle condizioni operative.

Nel Capitolo 4, lo stesso modello di permeazione è applicato alla quantificazione di un fenomeno che, in modo più o meno significativo, riguarda tutti i processi basati sulla tecnologia delle membrane: la polarizzazione per concentrazione, che consiste nel progressivo aumento della resistenza esterna al trasporto delle specie permeanti a causa della presenza delle altre che si addensano sulla superficie dello strato selettivo. Per molto tempo, tale fenomeno, dovuto proprio alla perm-selettività della membrana, è stato considerato del tutto trascurabile per i processi in fase gassosa, ma, con lo sviluppo di membrane sempre più sottili e performanti caratterizzate da alti flussi, esso ha assunto un'importanza sempre più rilevante nel corso degli ulitmi anni. L'analisi, sviluppata in questo lavoro per membrane auto-supportate a base di palladio, permette di predire l'influenza della polarizzazione per concentrazione al variare di diverse condizioni di processo tramite un coefficiente (di polarizzazione) opportunamente definito. Le diverse situazioni così ottenute sono riassunte nelle cosiddette "mappe di polarizzazione", grafici in cui è possibile visualizzare in modo diretto l'effetto del fenomeno sulle performance della membrana e che indicano le condizioni di funzionamento migliori da adottare in un processo di purificazione di idrogeno. Alla fine del Capitolo 4, si è provveduto ad un confronto con un sistema reale di letteratura, che, oltre a dimostrare la bontà dell'analisi, indica anche che questo fenomeno, in certe condizioni operative, può essere determinante al punto tale da costituire lo stadio limitante dell'intero meccanismo di permeazione dell'idrogeno in membrane a base di palladio.

La seconda parte del presente lavoro di tesi (Capitolo 5) è invece dedicata alla modellazione, l'analisi e la simulazione di reattori catalitici a stadi dotati di membrana a base di palladio in cui è condotta la reazione di steam reforming del metano. Per questi reattori si è proceduto all'individuazione di configurazioni ottimali tramite un appropriato strumento computazionale appositamente sviluppato in Matlab®. Entrando nel merito dello studio, due tipologie di apparecchiatura costituiscono l'oggetto di indagine. La prima consiste in un reattore tubolare a membrana a stadi, composto di stadi esclusivamente reattivi (senza membrana) posti in serie alternata a stadi a membrana esclusivamente permeativi (senza catalizzatore) in cui avviene la separazione selettiva del prodotto chiave (l'idrogeno). La seconda apparecchiatura considerata è anch'essa un reattore tubolare a stadi dotato di membrana a base di palladio, ma assemblata in stadi reattivi ed inerti (entrambi costituiti di pellet), disposti anch'essi in serie alternata, in cui, diversamente dal caso precedente, la rimozione selettiva dell'idrogeno avviene in entrambe le tipologie di stadi. Dopo aver opportunamente validato il modello mediante dati di letteratura, si passa allo studio di ciascuna tipologia di reattore. In particolare, per il primo tipo si è fissato un certo numero di stadi (5 reattivi e 4 permeativi) considerando tre diverse distribuzioni di catalizzatore e di area di membrana. La prima di queste, presa come riferimento per valutare le prestazioni delle altre, è la distribuzione equi-spaziata, in cui tutti gli stadi (reattivi e permeativi) presentano la stessa lunghezza. Le altre due sono rispettivamente ricavate tramite una procedura numerica di ottimizzazione di due diverse funzioni obbiettivo, che nello specifico sono date dalla conversione di metano e dal fattore di recupero di idrogeno. Le variabili decisionali, in base alle quali ottimizzare, sono quelle che determinano la distribuzione stessa, ossia le lunghezze dei singoli stadi. Le prestazioni relative a tutte le distribuzioni considerate sono successivamente confrontate con quelle di un reattore a membrana convenzionale nelle stesse condizioni operative (stessa quantità di catalizzatore ed area di membrana), mostrando miglioramenti significativi rispetto a quest'ultimo in termini della variabile che di volta in volta è scelta come funzione obbiettivo. Un simile approccio è stato adottato per l'analisi del secondo reattore a stadi. In questo secondo caso, lo studio è suddiviso in due parti. Nella prima si sono fissate quantità di catalizzatore e numero di stadi (5 reattivi e 5 inerti), considerando tre

distribuzioni di catalizzatore, nella prima delle quali (quella di riferimento) tutto il catalizzatore è concentrato nella parte iniziale del reattore. Analogamente all'apparecchiatura precedente, la stessa procedura di ottimizzazione è stata applicata per ricavare la seconda e la terza distribuzione, massimizzando separatamente le seguenti funzioni obbiettivo: la conversione di metano e la resa in recupero di idrogeno (diversa dal fattore di recupero). Anche in questo secondo caso, i miglioramenti rispetto alla configurazione di riferimento risultano notevoli in termini delle variabili di interesse. Nella seconda parte dello studio è indagato l'effetto del numero di stadi e della quantità di catalizzatore, espressa in percentuale rispetto a quella che occupa l'intero volume del reattore a membrana convenzionale equivalente. Si trova che aumentando il numero di stadi le prestazioni del reattore crescono prima in modo significativo, per poi assestarsi ad un valore costante dipendente dalla quantità di catalizzatore considerata. Un analogo comportamento si nota facendo variare quest'ultimo parametro, poiché si osserva che, utilizzando un numero di stadi abbastanza elevato, dopo un certo punto, il reattore a stadi raggiunge in pratica le stesse prestazioni di un reattore a membrana convenzionale non mostrando significativi miglioramenti all'aggiunta di ulteriore catalizzatore. Ciò permette di quantificare l'ammontare del catalizzatore risparmiato utilizzando un reattore a stadi invece di uno interamente riempito, mostrando che tale risparmio può arrivare anche al 70-75% circa.

ABSTRACT

The present work is focussed on analysis, modelling and simulation of the supported Pd-based membranes and Pd-based membrane catalytic reactors. The motivations of this study stay in the guide-lines of the so-called "*Process Intensification Strategy*", whose principal aim is developing innovative equipments able to provide the same or higher performances than the traditional ones with lower costs and smaller plant volumes. In this sense, the reasons of developing a dissertation on membranes and membrane equipments arise from the potential ability of membrane technology to provide a significant contribution to these goals. Specifically, the analysis is developed as follows. The first two chapters are focussed on the the state of art of a) the main hydrogen production and separazion processes and b) membrane technology for gas separation, with a particular attention to the Pd-based membranes, representing one of the principal topics of the present work. Then, the analysis carried out in the successive chapters can be ideally divided into two parts, in the first one of which (Chapter 3 and 4) the Pd-based membranes are studied in details.

In particular, in Chapter 3 a new hydrogen permeation model through this type of membranes is developed, allowing to take into account several aspects and problems not yet esaustively studied in literature. According with this model, the whole hydrogen permeation process is divided into several elementary steps, each of which is modelled by its own kinetic and mass transfer equations. The steps considered are: 1-2) hydrogen external mass transfer from the fluid bulk to the metallic surface and *vice-versa*, 3-4) adsoption/desorption to/from the metallic surface, 5-6) transition of the atomic hydrogen from the state of superficial adsorption to the one of dissolution in the metallic lattice and *vice-versa*, 7) diffusion of the atomic hydrogen through the metallic bulk, and 8) hydrogen mass transport through the porous layers of a multi-layered support. In modelling the mass transfer in the fluid phases external to the Pd-based selective layer, a multicomponent approach based on the Stefan-Maxwell equations is adopted

in order to be able describe more actual situations than those usually considered in literature (hydrogen binary mixtures). Such a model, validated by means of appropriate literature data, allows to quantify the influence of each step and identify the rate-determining ones as the operating conditions change.

In Chapter 4, the same permeation model is used to quantify a phenomenon regarding more or less significantly all the membrane-based processes: the concentration polarization, consisting in the progressive increase of the resistance to external mass transfer due to the presence of the other species concentrating towards the surface of the selective layer. For a long time this phenomenon (due to the perm-selectivity of membrane) has been considered negligible for those processes involving gas separation, but, as high-performance thinner membranes have been developed, it has assumes more and more importance. This analysis, developed in this work for self-supported membranes and applicable also to supported membranes in which the support has no influence, allows to predict the effect of the concentration polarization in several operating conditions by means of an appropriately defined coefficient. Several possible different situations are summarized in the here-called "*polarization maps*", being figures where the effect of this phenomenon on membrane performance is directly viewable and also the best working conditions are indicated. At the end of the Chapter 4 a comparison with some literature data demonstrates the validity of the analysis, indicating also that, in some cases, the concentration polarization in Pd-based membranes may reach such a level to become the rate-determining step of the whole permeation mechanism.

The second part of the present dissertation (Chapter 5) concerns the modelling and simulation of Pd-based membrane catalytic staged reactors where methane steam reforming is carried out. Several optimal axial distributions of catalyst and membrane area are determined for such reactors by means of a 1-D model solved by a computational tool appropriately home-developed in Matlab®. In particular, two types of reactor are considered. The first one – here-called "*Permeative Stage Membrane Reactor*" – consists in a tube-in-tube membrane staged reactor composed of five reactive stages (without membrane) laid out in alternative series with four permeative ones, where the selective hydrogen separation occurs.

The second one – here-called "*Inert Stage Membrane Reactor*" – is also a tube-in-tube staged reactor composed of several reactive and inert stages in series (both constituted of pellets) with the membrane placed along its whole length. Hence, differently than before, the hydrogen removal occurs in both types of stages. After validating the model by means of opportune literature data, each reactor is studied. As concerns the PSMR, three different distributions are considered. The first one is characterized by equi-sized stages, whilst the remaining ones are obtained by optimizing two different objective functions, which in the specific case are methane conversion and hydrogen recovery factor. The decisional variables of optimization are the ones characterizing the distribution, i.e., the single stages' lengths. The performance related to all the obtained distributions are then compared to the ones of the equivalent conventional membrane reactor (with the same catalyst amount and membrane area).

A similar approach is adopted for the second reactor, whose analysis is divided into two parts. In the first one, stages' number and catalyst amount are set as fixed values, focussing the study on a ten stages membrane reactor (5 reactive and 5 permeative). Analogously to what done for the PSMR, three catalyst distributions are considered, in the first of which (set as reference one) the whole catalyst pack is entirely placed at the reactor inlet. The other two are achieved by optimizing methane conversion and hydrogen recovery yield by means of the same procedure as developed for the PSMR, showing higher performances than the reference distribution. In the second part of the analysis, the effect of the stages' number and catalyst amount are investigated, this last one expressed in terms of percentage with respect to the whole catalyst amount contained in the conventional membrane reactor, which is fully filled of catalytic pellets. The results of the study show that as the stages' number increases, the ISMR performances are significantly improved up to a certain point, their influence becoming negligible from this point on, whose value strictly depends on the catalyst amount.

An analogous behaviour is shown by analyzing the effect of the catalyst amount. In fact, according with the results achieved, if using a high enough stages' number (>100 ca.), the staged reactor leads up to the same performance as the conventional one with significantly lower catalyst amount. This very important result allows to quantify for the specific process the

level of catalyst saved using the staged membrane reactor instead of the conventional one, showing that this level may lead up to even 70-75%.

CHAPTER 1

HYDROGEN PRODUCTION AND PURIFICATION PROCESSES

1.1 GENERALITIES

The possible exhaustion of the fossil resources has led in the last three decades to search innovative technologies for energy production. These ones has been oriented towards energetic systems compatible as much as possible with a fully sustainable development of the human industrial activities, since the environment of the whole earth is more affected by the effects of the greenhouse gases. The principal systems of clean energy production, set up till now with good results, are the following:

- Wind-power.
- Solar power (by means of photo-voltaic cells).
- Geo-thermal power.
- Bio-mass conversion.
- Power production from hydrogen.

Among the above-mentioned energy production, a very promising process is that involving the power production directly from hydrogen streams. In fact, hydrogen is the most diffused chemical species in the universe and represents, at least virtually, a potentially inexhaustible resource. The use of this element as combustible (in a pure state) would present the great advantage of avoiding any kinds of harmful emissions, the water being the only product of its combustion. However, it has several drawbacks related to the storage and distribution, as it is possible to notice from the evaluation of some its physical properties:

- Critical temperature: -240°C.
- Boiling point: -253°C.
- Energy density (at 15°C, 100 kPa): 10.3 MJ m^{-3}.

Hence, in order to avoid the hydrogen vaporization, it is necessary to keep very low values of temperature, achievable only in super-isolated storage-boxes (for the storage) and "*thermos tanks*" (for locomotion use by cars). The hydrogen "*lightness*" implies a non-favourable energy density to be stored as gas. In fact, at 200 bar, its volume is four times larger than that of natural gas at a constant energetic content. A higher pressure is not economically convenient, since the energy compression costs would not be balanced by the hydrogen used as a

compressed combustible. Nevertheless, the company Air Liquid has already developed a gaseous hydrogen distribution net in the north of France, in Belgium and in The Netherlands. Furthermore, the BP Company built in Barcelona the first refuelling station in Europe for bus fed with hydrogen, first produced by electrolysis and then compressed for the feed. A certain amount of energy necessary for the process is obtained from solar source (5% ca.). This station represents one of the steps of the program "*Clean Urban Transport for Europe*" (*European Community*) [1.1].

At present, for hydrogen separation, the petrochemical industry exploits integrated processes, like the PSA (Pressure Swing Adsorption) or cryogenic, all techniques not adapted to be carried out in refuelling stations. A possible solution may consist in utilizing membrane-based separation modules, which are more compact, versatile and commercially already available (polymeric membranes). However, the sole polymeric membranes are not sufficient to obtain the target purity, thus it is necessary to use another kinds of membranes, like, for example, the Pd-based ones, having a virtually infinite selectivity towards hydrogen with respect to all the other gases (this type of membrane will be the main argument of the Chapter 3 and 4 of this thesis). In this sense, one of the most important challenges of the next future is to design a large-scale system where the most of the separation is carried out in polymeric modules, leaving the purification process to be operated in Pd-based modules. Obviously, in order to make this possible, the behaviour of such a kind of membranes has to be studied in the different operating conditions, which may occur in an actual hydrogen distribution system.

1.2 HYDROGEN PRODUCTION PROCESSES.

Hydrogen can be obtained from several raw materials by means of different techniques, as shown in Figure 1.1, where it is possible to notice that different hydrogen sources need different production methods. At the moment, the main hydrogen production processes can be summarized in:

- ✓ Methane Steam Reforming (MSR).
- ✓ Partial Oxidation of Methane (POM) and auto-thermal processes.

- ✓ Dry Reforming.
- ✓ Water Electrolysis.
- ✓ Separation of coking gases.
- ✓ Separation of refinery gases.
- ✓ Some innovative processes.

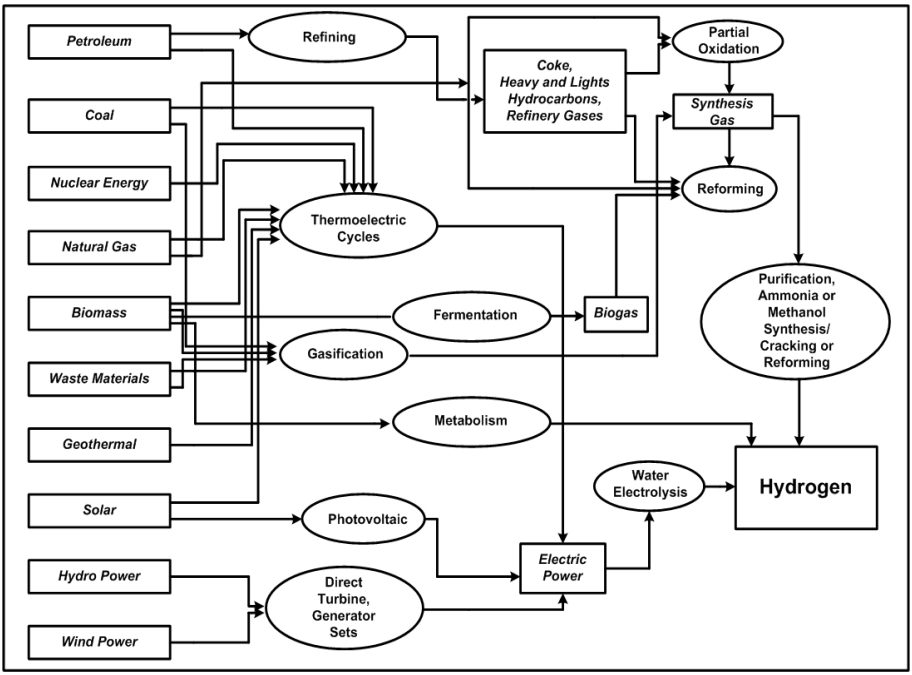

Figure 1.1 – Scheme of raw materials and the respective hydrogen production processes.

1.2.1 METHANE STEAM REFORMING

The overall reactive mechanism describing Methane Steam Reforming (MSR) involves methane and water vapour, as indicated in Eq. 1.1. This mechanism includes the following two reactions (Eq. 1.2, 1.3).

$$CH_4 + 2H_2O = CO_2 + 4H_2, \qquad \Delta\widetilde{H}_r^0 = 165\,kJ\,mol^{-1} \tag{1.1}$$

1) "*Principal Reforming*":

$$CH_4 + H_2O = CO_2 + 3H_2, \qquad \Delta\widetilde{H}_r^0 = 206\,kJ\,mol^{-1} \tag{1.2}$$

2) "*Water-Gas Shift* (*WGS*)":

$$CO + H_2O = CO_2 + H_2, \ \Delta\widetilde{H}_r^0 = -41\,kJ\,mol^{-1} \tag{1.3}$$

In Table 1.1 the operating conditions of each single step are reported. The reaction in Eq. 1.1 is highly endothermic, equilibrium limited and favoured by a high temperature and quite low pressure, implying an increase of the mole number. On the contrary, the reaction in Eq. 1.3 is moderately exothermic and, thus, favoured by a low temperature. Hence, operating at higher temperature, a larger CO production is achieved. In general, the industrial plants operate the MSR at 800-900°C, but, despite of these high values of temperature, they need appropriate catalysts. Usually, tubular reactors with a diameter of about 100 mm are used. These tubes, made of Ni-Cr alloys, are laid out in a combustion furnace [1.2]. The catalysts used are Ni-based wise supported on alumina. These types of catalysts are rapidly poisoned by sulphurated compounds, thus the impurities in the feed need to be less than 1 ppm. Another decrease of the process performance is caused by the formation of coke, which progressively covers the active catalytic sites. On an industrial point of view, this problem is solved adopting an appropriate feed ratio H_2O/CH_4. The sulphuric compounds eventually present in the natural gas are mainly H_2S, COS, CS_2, RSH and tiophene. In order to reduce their concentration up to reach acceptable values, the following separation methods can be used:

- ✓ Regenerative absorption.
- ✓ Oxidative absorption (on sulphur).
- ✓ Adsorption (on active carbon and/or molecular sieves).

- ✓ Treatment with alkali.
- ✓ Fastening technique on ZnO, NiO or Fe_2O_3.

Table 1.1 – Main steps of Methane Steam Reforming.

Stage	*Operating conditions*
Compression	Pressure: 28 - 40 bar.
De-sulphuration	Hydro-desulphuration by Mo- and Co-oxides based catalyst Adsorption on active carbon
Principal Reforming	Alumina supported Ni-based catalysts Temperature: 700-900°C Medium pressure
Secondary Reforming	Temperature: 1000 °C Appropriate catalyst
CO conversion (Ware-Gas Shift)	Two step process: Step1: Temperature of 350 - 450 °C with Fe- and Cr-oxide based catalyst Step2: Temperature of 200 - 250 °C with Zn- and Al-oxide based catalyst.
CO_2 Separation	-

The industrial plants for hydrogen production operate at such a high temperature that, in order to obtain a CO-free stream, it is necessary to cool the products of the principal reforming and use a subsequent reactor for the WGS operated at 400-450°C. The consequent yield obtained is of the order of 85-90%, but it is possible to improve it by using a post-combustion step ("*Combined Reforming*"). The main steps of the combined reforming are shown in Figure 1.2. In this case, a complete conversion is not necessary, since the remaining methane is took away by means of the combustion step, carried out in adiabatic conditions. This step, catalyzed by nickel, leads to the formation of CO_2 and water, which move the MSR reaction towards the

production of CO and H_2. For reducing the content of CO, the process can be operated at high water/CH_4 feed ratio, but in this way the volumes in the plant would be too large and a pressure higher than 40 bar (limit indicated in the plant) should be used.

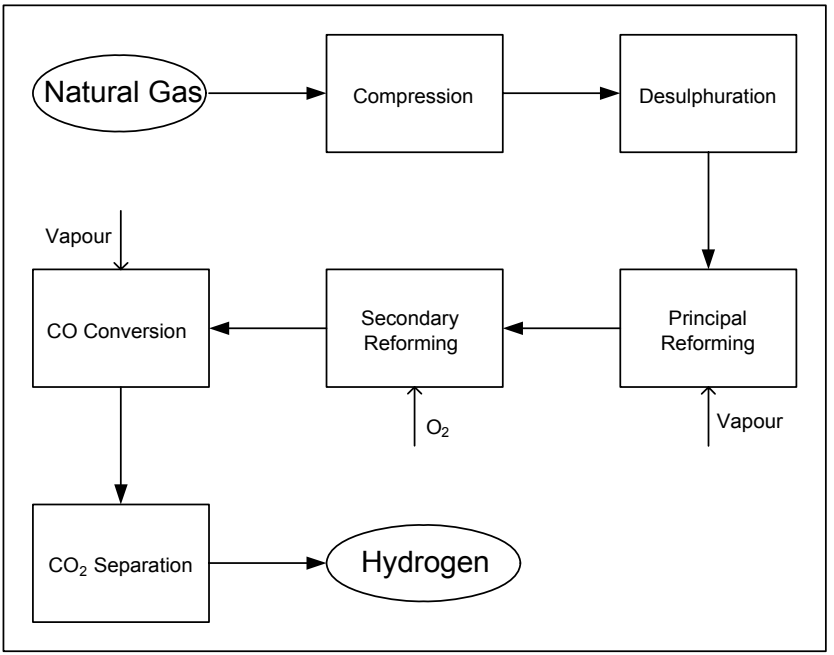

Figure 1.2 – Scheme of the main steps of the MSR process.

For all these reasons, a feed ratio of 3-4 is adopted. Another possibility to limit the CO presence is represented by the use of different feed types (like the Virgin Naphtha), but this implies the formation of gas black, which, however, is a more important inconvenient than the same CO. In the last decade, the KTI S.p.A. has introduced some technological innovations allowing a decrease of operating and initial capital costs [1.3]. The hearth of this innovative technology is a new type of reformer, the "*Heat Exchanger Reformer*" (*HER*) combined with the "*Advanced Reforming Technology*" (*ART*). As mentioned above, in the MSR it is necessary to

supply the required heat through the external surface, but, because of some design constrains, it is not possible to recover the heat exiting the outlet in such a way to cover at least a part of the energetic requirement. On the contrary, the process *HER* is based on the use of a tube-in-tube configuration, where the catalyst is laid out in the annulus. The whole reactor is located in the furnace, where the combustible gases are introduced. The external tube is protected by some sleeves, inside of which the hot fumes come up from the furnace bottom to the top.

The temperature is controlled by tuning the fuel flow rate. In 1993 a prototype of such a plant was started up in Rozemburg (The Netherlands) for producing about 100 $Nm^3\ h^{-1}$ of hydrogen. The tubes utilized have an ID of 6-8 in, but, because of this low diameter, the maximum line pressure is 19 bar. For large enough plants up to handle the flow rate coming from the refineries, the requested pressure is higher and, hence, tubes with an ID of 4 in should be used. The KTI company patented a new riser with larger heat exchange area and a small enough crossing area in such a way to allow the installation of the catalyst in standard tubes.

1.2.2 PARTIAL OXIDATION OF HYDROCARBONS AND AUTO-THERMAL PROCESSES

In the auto-thermal processes several hydrocarbons can be utilized as reactants, from the natural gas to the heavy oils. Generally speaking, the main operations for obtaining hydrogen from the hydrocarbons partial combustion processes are the following:

a. Partial oxidation reaction.
b. Removal of the eventual gas black formed during the step a).
c. Conversion of CO by means of water vapour (WGS).
d. Removal of the CO_2 formed and of residuals of CO and H_2S.

Two kinds of process exist for the partial oxidation (mainly of methane):

- ✓ Thermal process.
- ✓ Catalytic process.

In the thermal process, the temperature necessary to obtain acceptable yields is quite high, since no catalyst is used. On the contrary, in the catalytic process, the presence of the catalyst allows to operate at lower temperature and increase the selectivity of the reaction. The partial

oxidation of methane is carried out by auto-thermal way, e.g., the exothermic reaction supply the heat required by the endothermic ones. In the specific case, it is important utilizing pure oxygen instead of air, since the presence of nitrogen would increase the thermal capacity of the system and more fuel should be consumed to reach the requested temperature. In the practise, in order to reduce the oxygen and hydrocarbon consumption, it is convenient to pre-heat the reactants up to the highest allowable temperature. Generally, it is possible to reach a temperature of 500°C. Above this temperature, the oxygen becomes very reactive also towards the material of which the heat exchanger is made and methane begins to crack. Working in these conditions, a reaction temperature of about 1200°C is reached, thing that requires high costs materials of the equipments involved in the process. It is important to notice that the role of the catalyst is to accelerate the endothermic reactions in such a way that these occur at the same time as the exothermic ones (oxidations). Hence, the furnace temperature can be kept below 1200°C, allowing certain working regularity of the process and the maximum durability of the catalyst. In order to do this, the spatial catalyst distribution has to be laid out to avoid the sintering of the pellets and the formation of gas black. In the thermal process, this last occurrence (presence of gas black) is particularly important, not as much because the gas black indicates lower yields, but rather because its removal is difficult on a technological point of view. Furthermore, its presence is bad for the process successive steps, since the carbon micro-particles are involved in heterogeneous reactions with water and CO_2 which do not reach the thermodynamic equilibrium. The formation of the gas black can be explained with the following considerations. The oxygen present in the reaction mixture reacts rapidly with methane to form in a first time CO_2 and water. As a consequence, a flame develops, increasing locally the temperature. If the process is operated in defect of oxygen, in the first part of the reactor there is a mixture containing mainly CO, CO_2, water and CH_4 non-reacted. Because of the local high temperature, the methane in excess tends to decompose, causing the formation of carbon micro-particles depositing on the solid particles. Hence, in the second part of the reactor, the following chemical reactions are possible (Eq. 1.4).

$$\begin{aligned} CH_4 + CO_2 &= 2CO + 2H_2 \\ CH_4 &= C(s) + 2H_2 \\ C(s) + H_2O &= CO + H_2 \\ C(s) + CO_2 &= 2CO \end{aligned} \tag{1.4}$$

The first reaction is homogeneous and tends to reach rapidly the thermodynamic equilibrium. The same does not occur for the last three that are heterogeneous. Thus, if the residence time in the reactor is not long enough, the system does not reach the equilibrium corresponding to the operating temperature and gas black is found in the reaction products. As concerns the working pressure, the thermodynamics of the overall mechanism is favoured by low pressures. Nevertheless, at a high enough temperature, the conversion is quite high even at high pressures. Moreover, if the syngas produced has to be fed in an ammonia or methanol synthesis plant, it is more convenient to carry out the process under pressure. Generally speaking, in methane partial oxidation processes, a total conversion is usually reached. In the thermal processes, the absence of catalyst allow to use hydrocarbon feeds containing sulphuric compounds, which are found at the end of reactor as H_2S, COS, CS_2, S and tiophene, poisons for the catalyst, as said before.

After the reaction, the gases have to be subjected to quenching, which has to be as rapid as possible in order to avoid some undesirable reactions. In the industrial practise, the exiting gases are cool down by means of water, which has also a role in catching eventual traces of carbon-wise products. In thermal process, the reactor is constituted of a simple cylindrical part in which a true combustion occurs between hydrocarbon and oxygen. In order to avoid explosive phenomena, the reactants are fed separately and then mixed in a burner. Since at the exit of the burner the temperature is of the order of 3000°C, it is necessary to protect the reactor by means of refractory materials. The reactor has to be designed in such a way to allow a rapid heat transfer from the zones of the exothermic reactions to the ones where the

endothermic reactions occur. In the catalytic process, the reactor is constituted of cylindrical tubes where the Ni-based catalyst is packed. When the gases pass through the cooling zone, they bring with them water vapour, utilized successively by the WGS. A high CO conversion in this step is particularly important if hydrogen for ammonia synthesis is being produced, because CO represents a poison for the catalyst used. These kinds of reactors need quite accurate control systems, especially as concerns temperature and reactants feed ratio. In fact, even small variations of the feed ratio O_2/hydrocarbon may lead the reactor up to run-away problems, with consequent explosion risks.

1.2.3 ELECTROLYSIS OF WATER

The production of hydrogen from electrolysis of water at industrial level is quite rare, because of the high costs of electrical energy. However, the development of an appropriate sun-based technology may render it attractive in the next future. The main advantage of this process is that it is possible to reach a stream purity up to 99.8%, even though Pd-based membrane techniques may lead to a more economical processes reaching the same purity level. The reactions involved in the electrolysis are shown in Eq. 1.5.

$$\begin{aligned} &\text{Catode}: 2H_2O + 2e^- \rightarrow H_2 + 2OH^- \\ &\text{Anode}: 2OH^- \rightarrow 2e^- + 0.5O_2 + H_2O \end{aligned} \tag{1.5}$$

As a sub-product of this process, only oxygen is obtained. The electrolyte is composed of an aqueous solution of sodium or potassium carbonate for increasing the electrical conductivity of the cells, decreasing in this way the voltage drop. The choice of the hydroxides is based on the following considerations. Set the concentration, the solution of sodium carbonate has a lower cost, but is more corrosive, presents a lower conductivity and has a higher vapour tension. The water to fed in the cells has to be de-mineralized (max 8-10 mg L^{-1} of salts), in order to avoid a too much ions accumulation with consequent precipitation of low-soluble compounds. The voltage to apply between the electrodes depends on factors like: equilibrium voltage, initial

surge voltage of the metallic electrodes and surge voltage due to concentration. In fact, the voltage drop in the cell is higher than the theoretical one related to its conductivity and geometry, since the gas produced during the process causes the formation of gaseous droplet representing segregation zones with a very low conductivity. Another important factor is the system temperature, which should be as high as possible in the limits of the operating conditions, in order to make the over-voltage minimum. However, it is not possible to exceed 70-80°C to avoid a too significant evaporation which can lead to an increase of the gas humidity and corrosion intensification. Meanly, the consumption of electrical energy is about 5 kWh Nm^{-3}. A possible method to reduce the costs of the process can be represented by integrated generators of electrical energy: the energy in excess can be used for hydrogen production. The advantage for the energy producers would concern the production stabilization and transient phenomena limitation, even though at the moment companies like Enel adopt policies of costs diversification basing on time slots.

1.2.4 HYDROGEN PRODUCTION BY CHEMICAL-SOLAR PROCESS

The process in object is carried out as described in succession. The solar radiations are conveyed in the focus of a parabolic solar mirror, increasing the temperature over 2000°C. The heat so produced can be used in two ways.

- ✓ On one hand to feed a thermal machine in order to produce electric energy. For example, in USA and Spain there are pilot-plants with large mirror field conveying the solar radiations in a tower located in the focus.
- ✓ On the other hand, the high temperature in the focus can be exploited to start up chemical reactions not possible at lower temperatures. In Paul Scherrer Institut (PSI), some cyclical thermo-chemical processes are studied. In these processes water is broke down in its elements by means of several thermal reactions, like, for example, the cycle of the iron-oxide (Eq. 1.6). The reduction of Fe_3O_4 in FeO is an endothermic reaction, whilst the second step is exothermic. The calorific value of the FeO produced is higher than that of hydrogen, thus, this process develops energy. On a

thermodynamic point of view, the transformation of Fe_3O_4 in FeO requires a temperature of almost 2200°C, whereas the water decomposition occurs at about 500°C generating heat.

$$1^{st}\ \text{step}: \ Fe_3O_4 \rightarrow 3FeO + \frac{1}{2}O_2 \qquad (T \geq 2200°C)$$

$$2^{nd}\ \text{step}: 3FeO + H_2O \rightarrow Fe_3O_4 + H_2 \quad (T \cong 500°C) \tag{1.6}$$

$$\text{Overall}: \ H_2O \rightarrow H_2 + \frac{1}{2}O_2$$

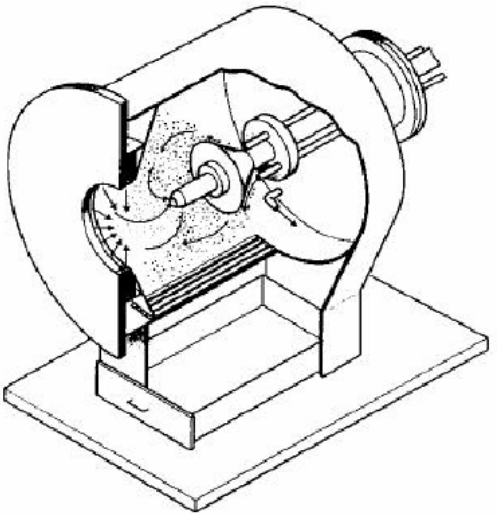

Figure 1.3 – Scheme of the Dusty Cloud Reactor for chemical-solar reactions. The concentrated solar radiations are absorbed directly by aero-sol particles suspended in an appropriate gas.

The research activity in PSI is focussed on the different aspect of this cycle, which is promising thanks to its conceptually simplicity. It has been already demonstrated that the Fe_3O_4 decomposition temperature can be reduced by adding Mn. In order to carry out this process, it is necessary the development of innovative reactors. Specifically, the one elaborated in PSI consists in the so-called "*Dusty Cloud Reactor*" (Figure 1.3). In the PSI plants it is possible to adopt for chemical-solar reactors a thermal power up to 30 kW and a temperature up to 1600°C. The Fe-oxide cycle is a very promising reaction, but implies also several risks related to the technical feasibility. The extreme temperatures, the problem of minimizing the energy losses due to the radiation and the thermo-stability of the materials constitute a hard challenge for the engineering and the chemists employed in the project. Perhaps, the solar chemistry will have success in the field of the hydrogen production only by means of hybrid fossil-solar processes, which are simpler on a technical point of view. For example, it could be possible to provide solar power to gaseous methane in the reforming reactor, since the solar heat can be produced up to 1000°C by means of the technology of the current solar stations.

The mixture H_2-CO_2 coming from the reforming would contains an amount of energy higher than that of the feed mixture (equal to the solar power supplied). The main problem to solve, even dealing with relatively simple problems, is the temporal variability of the solar input, which has to be handled appropriately.

1.2.5 INNOVATIVE PROCESSES FOR HYDROGEN PRODUCTION: MEMBRANE-BASED PROCESSES

In the last two decades, the membrane technology has been massively developed and used in reactive and separative systems. In this field, this technology can offer new opportunities of designing innovative processes and/or optimizing already existent conventional ones. In particular, an example of integrated systems is represented by the catalytic membrane reactors, in which separation and reaction occur at the same time in the membrane. The so-called "*perm-selectivity*" of a membrane (i.e. the capacity of the membrane to allow the permeation of some chemical species with different selectivities) can also be exploited to exceed the

equilibrium yield of those reactions limited by the thermodynamic equilibrium, allowing the continuous selective removal of the products from the reaction zone. Furthermore, membranes can be used also for selectively supplying one ore more reactants in order to control the reaction rate. Hence, the membrane reactors provide interesting possibilities for production, upgrading and purification of hydrogen streams. Since this argument represents the topic of this dissertation, it will be discussed exhaustively in more details in the next chapters.

1.2.6 BIO-MASS GASIFICATION

The method actually cheaper to produce hydrogen by solar processes is the thermal gasification of bio-mass (wood and other vegetable materials). Like the reforming of the natural gas, also the biomass transformation in hydrogen and CO_2 by means of vapour needs for thermal power to be supplied, usually produced by combustion of the biomass. In principle, the requested head can be generated first outside of the burner and provide it through the wall to the stream to be gasified. Alternatively, a part of the biomass can be burned with oxygen in order to produce the necessary energy. This second method, more used, is called biomass "*auto-thermal gasification*" or "*partial oxidation*". The biomass transformation with vapour generates not only hydrogen, but also several other gases and condensable organic compounds (coal tars).

A typical composition of a gaseous stream, like that produced in the experimental turbulence plant of the Paul Scherrer Institute after the water decomposition, is the following:

- ✓ 48% N_2 (from air).
- ✓ 23% CO.
- ✓ 12% H_2.
- ✓ 12% CO_2.
- ✓ 5% CH_4.

The usefulness in terms of hydrogen production is quite limited: only 22% of calorific value of the gaseous stream produced is in the form of hydrogen, whilst 33% and 45% is represented by CO and CH_4, respectively. The reason why the transformation is only partial is due to the

fact that at typical reaction temperature (about 900°C) several chemical equilibriums are established. In particular, in presence of water vapour, the Water Gas Shift occurs (Eq. 1.3). At a high temperature (850°C) the equilibrium is moved towards the reactants. Cooling the gases, the composition remains almost the same, since at a lower temperature the new equilibrium is established very slowly in absence of catalysts. The resulting hydrogen amount can be increased at the expense of the CO amount at temperature of about 300°C using an appropriate catalyst laid out in a packed bed. The optimized equipments allow to reach values from 0.7 to 0.8 Nm^3 of H_2 / kg of biomass (dry mass based), which corresponds to a hydrogen calorific value of about 50% with respect to that of the dry biomass. In principle, also the methane present in the feed stream can be converted to hydrogen by a successive reforming process. In this case, the appropriate catalyst is inserted just after the gasification step. Larson and Katofsky [1.4] compared both the production of methanol and that of hydrogen from biomass and from natural gas, respectively, highlighting that on large scale the transformation of the biomass in methanol is more expensive of 20% than the transformation in hydrogen. Nevertheless, the researchers of PSI think that the methanol synthesis represents the most convenient utilization of the gas produced by the biomass gasification, especially thinking about the use of methanol in civil transportation, since the hydrogen storage is difficult and very expensive. Furthermore, the use of methanol as liquid fuel may exploit the existent plants [1.5, 1.6], whilst for hydrogen it is necessary to develop a new distribution technology and build the corresponding infrastructures. For the applications requiring hydrogen as fuel, like the fuel cells, methanol can be also used as hydrogen carrier.

1.2.7 COAL GASIFICATION

The coal-based solids gasification represents another important source of hydrogen, especially in those countries where the petroleum reserves are quite limited. However, several are the reasons why the traditional technologies are not adapted to deal with wasted low-quality coal-based materials. In fact, the use of materials with a high content of cinders (up to 70%) is heavily limited by their resistance to oxygen diffusion, due to the presence of inert compounds

(especially Si- and Al-based compounds). Moreover, during the step of transport and storage, the wet particles tend to form agglomerates, causing a significant decrease of the surface exposed to the gasification and affecting the successive transformations. In this case, a preliminary gasification may be a good solution, on condition that an appropriate technology is available. The main reactions involved in this process are reported in Table 1.2, where the reaction enthalpies are calculated in accord with Benson [1.7].

Table 1.2 – Main reactions involved in the coal gasification.

Reaction	Enthalpy change, kJ mol^{-1}
1. $C + 0.5\ O_2 = CO$	-110.3
2. $C + CO_2 = 2\ CO$	174.3
3. $C + H_2O = CO + H_2$	131.2
4. $C + O_2 = CO_2$	-396.0
5. $CO + 0.5\ O_2 = CO_2$	-284.7
6. $CO + H_2O = CO_2 + H_2$	-43.0
7. $C + 2\ H_2 = CH_4$	-74.8
8. $CO + 3\ H_2 = CH_4 + H_2O$	-205.7
9. $CO + H_2 = 0.5\ CH_4 + 0.5\ CO_2$	-124.3

Some of these reactions are endothermic and need for much heat to reach the high process temperature. On the contrary, in the gasification made in presence of pure oxygen too high temperature are reached. Furthermore, the amount of CO_2 produced in the reaction 5 (Table 1.2) becomes too high. At the moment, the efficiency of the low-quality coal gasification is not very high, even in the best operating conditions. In fact, in the process Vellman-Galusha with rotating grid, the specific conversion varies from 400 to 500 kg m^{-2} h^{-1}, whereas the one relative to the high-pressure gasification with oxygen and vapour does not exceed 1000-1200 kg m^{-2} h^{-1} [1.8,1.9]. In the process Winkler, the gasifier design includes a cooling system (vapour generator) for reducing the temperature in the higher zone of the equipment [1.9]. In all the

cases the final product is a mixture of several gases (Table 1.2), whose the most important ones are the synthesis gases. Their separation from the others is usually carried out by means of conventional processes like adsorption, and cryogenic. However, in the last decades membrane-based separation systems have been developed at industrial level. Such systems allow high performances and a significant reduction of the operating temperature and energetic costs. It is estimated that in the world the membrane equipments for the coal gasification cover up to 50% of the whole production, whilst this value goes down to only 7% in the case of N_2-O_2 separation from air [1.10].

Table 1.3 – Effect of O_2 composition in feed air on the composition of gas produced in coal gasification.

Run	Experimental conditions*					Fuel gas composition [mol %]					
	V_g	V_c	V_H	$[O_2]$	T	H_2	O_2	N_2	CH_4	CO	CO_2
	L min^{-1}	g min^{-1}	mL min^{-1}	mol %	°C						
23	17.8	11.3	0	21.7	1000-1040	5.9	0.8	68.7	2.4	3.9	18.3
27	18.3	12.0	0	25.4	1000-1080	10.6	0.6	57.3	3.0	7.4	21.1
24	18.3	10.7	7.5	33.6	1100-1150	11.8	1.4	49.9	0.9	8.3	26.7

Coal fraction = [2 - 3] mm; ratio coal/feed gas = [1.17 - 2.97] mol_C mol_{O2}^{-1}

* V_g = gas blow rate, V_c = coal flow rate, V_H = water flow rate

In order to improve the yield in terms of synthesis gases, Belyaev *et al.* [1.11] proposed to use O_2-enriched air (OEA, 25-40% O_2). In this way it was possible to increase the composition in H_2, CO and CO_2, as shown in Table 1.3.It is believed that in the next future the use of ultra-selective membrane towards each of different gases involved in the process leads to a further decrease of the operating costs.

1.2.8 NUCLEAR STEAM REFORMING

In conventional processes, the heat necessary for the steam reforming to be carried out is provided by burning a certain amount of methane in order to reach the necessary temperature. This causes both an additional consumption of methane (principal reactant together with water) and high emissions of CO_2. To avoid these drawbacks, it is possible to exploit the heat generated by nuclear reactions in a "*High Temperature Reactor*" (*HTR*). An experimental plant that should demonstrate the feasibility of this process is the "*High Temperature engineering Test Reactor*" (*HTTR*) of the "*Japan Atomic Energy Research Institute*" (*JAERI*) [1.12]. The scheme of the plant and reformer is shown in Figure 1.4, where an operating temperature of 800°C is chosen in order to stay below the limits of the materials and obtain acceptable yields. This solution requires several security aspects to be solved before adopting this process massively. The idea consists in de-coupling the chemical plant from the nuclear one by means of an "*Intermediate Heat Exchanger*" (*IHX*).

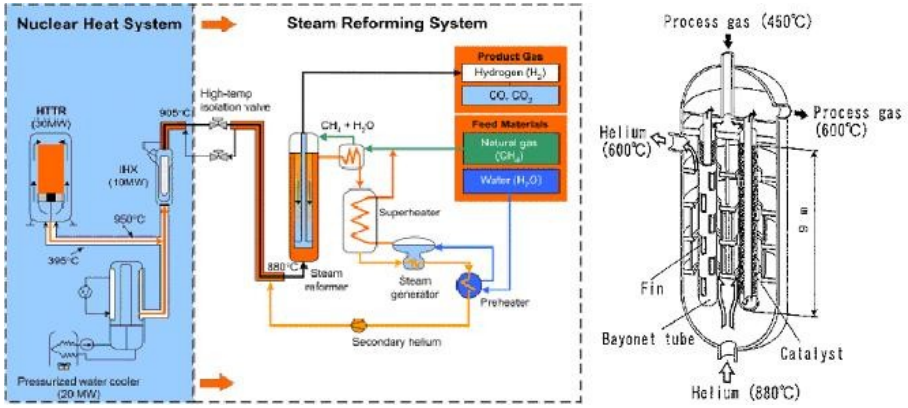

Figure 1.4 – Scheme of the JAERI plant for nuclear steam reforming and the corresponding reformer.

This separation between the two parts of the plant is necessary to avoid the following problems:

- ✓ Control of the thermal disturbs to reactor.
- ✓ Preservation of the catalytic tube structure.
- ✓ Control of the tritium permeation through the tubes.

As concerns the first point, the solution adopted by *JAERI* to limit the thermal disturbs consists in using the vapour provided by a "*Steam Generator*" (*SG*) as stabilizer of the helium inlet temperature in the *IHX*. Even in case of thermal disturbs related to malfunctions in the reforming line, the helium temperature at the outlet of *SG* can be kept constant by controlling the saturation temperature of the vapour, which can be set by tuning the pressure. The temperature fluctuations are to be limited in the range of 10°C in order to avoid the scram of the *HTTR*. The question regarding the second point is related to the pressure difference between helium and the reforming gaseous mixture and to embrittlement by hydrogen and corrosion. Hence, a most accurate as possible estimation of these phenomena is necessary to make the process secure and safe.

The third point arises from the fact that the hydrogen produced by reforming has not to be polluted by tritium. Two approaches exist to limit this problem: a) removing the tritium from the refrigerant of the primary reactor as much as possible; b) limiting the permeation through the tubes by means of a surface treatment with oxides. The most used fluid carrier in IHX is helium, but in principle CO_2, Ar, Ne, N_2 or H_2O could be utilized. This solution allows to:

- ✓ Minimize the pollution of the "chemical" part of the plant.
- ✓ Prevent vapour and/or the reforming gaseous mixture to enter the kernel in case of break of exchange tubes.
- ✓ Reduce the hydrogen permeation towards the helium of the primary circuit and tritium permeation in the opposite direction.

Unfortunately, this technology is not yet mature enough to be valid on a commercial point of view.

In particular, several problems are to be solved:

- ✓ Improving the knowledge of a) the thermodynamic behaviour of sulphuric acid at high concentrations and high temperatures and b) the thermodynamic equilibrium of iodine-based systems.
- ✓ Acquiring more accurate data in order to make the design more efficient.
- ✓ Developing materials resistant to corrosion, especially towards the boiling sulphuric acid, since such materials do not yet exist commercially.

About the last point, new steel- and ceramic- based materials are in development. JAERI demonstrated the possibility to operate in continuous cycle in laboratory scale and, thus, a larger plant is under construction. On a mechanical and structural point of view, the walls of the IHX should have a good resistance to high temperatures and creep and elastic instability phenomena. Among the commercially available alloys presenting some of the necessary properties – INCOLNEL 617 (alloy Ni-Cr-Co-Mo-based, typically used in gas turbines), HASTELLOY X (alloy Ni-Cr- Mo-based, developed for gas turbines) and INCOLOY 800H (alloy Fe-Ni-Cr-based, used in vapour generator in nuclear plants) – the most convenient one to use was demonstrated to be INCOLNEL 617 (10^5 continuous operating hours). However, because of its prohibitive cost and the high working temperatures, a development of new ceramic-based materials is in progress [1.12].

1.2.9 THERMO-CHEMICAL HYDROGEN PRODUCTION

One of the methods to decompose water consists in providing high-temperature heat (pyrolysis at about 3000°C). This would imply heavy technological complications, especially concerning the choice of the materials to use. Another possibility can be represented by the adoption of an appropriate thermo-chemical cycle in order to obtain the water decomposition, converting the provided heat in chemical energy. The studies that the Department Of Energy (DOE) of the U.S. commissioned in the '70s to General Atomics, Sandia National Laboratories and University of Kentucky identified 115 possible processes. Among these, only two were considered of interest:

- ✓ The UT3 (University of Tokyo-3), based on the cycle Ca – Br – Fe.
- ✓ The IS, based on the cycle I – S.
- ✓ The last one was preferred for the highest efficiencies achieved (up to 52%) and the nature of the reaction involved (all occurring in liquid state, contrarily to UT3). Theoretically, in such a process the sole reactant consumed is water, which is decomposed in a three steps process by heat. In this way, only H_2 and O_2 are produced, whilst the other compounds are completely re-used in the successive cycles with positive effects on the environment.

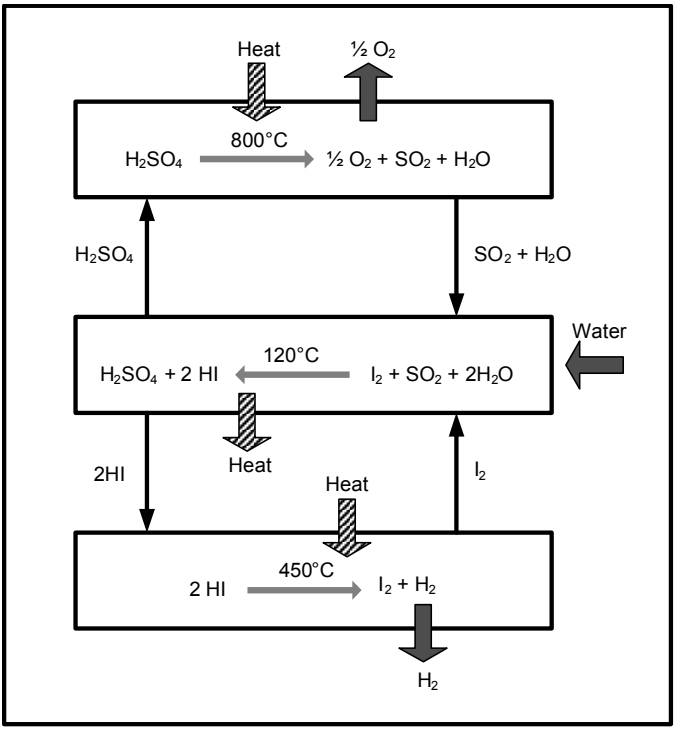

Figure 1.5 – Scheme of the thermo-chemical hydrogen production based on the I-S cycle.

The scheme of this cycled process is shown in Figure 1.5 and is composed of three steps:

- ✓ The thermo-chemical decomposition of the sulphuric acid (at 800°C ca.) in SO_2, H_2O and O_2, the last one representing a secondary product.
- ✓ The reaction, called *Bunsen Reaction* (exothermic at 120°C ca.), of iodine with SO_2 and H_2O to produce again H_2SO_4 (re-circulating) and HI.

The thermo-chemical decomposition of HI (at 450°C ca.) to produce iodine (re-circulating) and H_2.It is possible to notice that the net reaction is represented by the water thermo-chemical decomposition, carried out at a much lower temperatures than those involved in the thermolysis operated by means of only heat. The overall process provides O_2 as secondary product and heat at about 100°C, usable in its turn for other applications.

1.3 HYDROGEN PURIFICATION PROCESSES

On the industrial scale, the main hydrogen separation processes are essentially three:

- ✓ Pressure Swing Adsorption (PSA).
- ✓ Processes based on the use of appropriate polymeric membranes.
- ✓ Separation in cryogenic.

Each of these processes is based on different separation principles and, consequently, presents operating characteristic very different from each other. The choice of the optimal separation method is driven by not only economic considerations, but also questions concerning the flexibility in eventual future developments.

1.3.1 PRESSURE SWING ADSORPTION (PSA)

The PSA process for hydrogen purification is based on the ability of some materials of adsorbing more impurities at high gas pressures than at lower ones. Its operating principle is shown in Figure 1.6. The partial pressure of the impurities is decreased by varying the pressure in the tower between the top and the bottom by means of high-purity hydrogen, which is adsorbed in short supply. The process operates cyclically. The separation driving force is the impurities partial pressure difference and the minimum total pressure ratio between top and

bottom is about 4:1. However, also the absolute pressures are important, especially for the hydrogen recovery. In refinery applications the optimal feed pressure for a unit of PSA varies from 14.8 to 28.6 bar, whilst that at the bottom is set as lower as possible (from 1.14 to 1.34 bar). A bottom pressure of 1.14 bar can be used when the bottom gas has to be compressed, whereas 1.34 bar is preferred when it has to be directly burn, like, for example, for applications in steam reforming. Anyway, the process is more dependent on the bottom pressure than the feed one, as shown in Figure 1.7 [1.13]. Two main advantages of the PSA are its ability to remove even a very small amount of impurities (up to few ppm) and the production of high purity hydrogen (99.0-99.999-vol%).

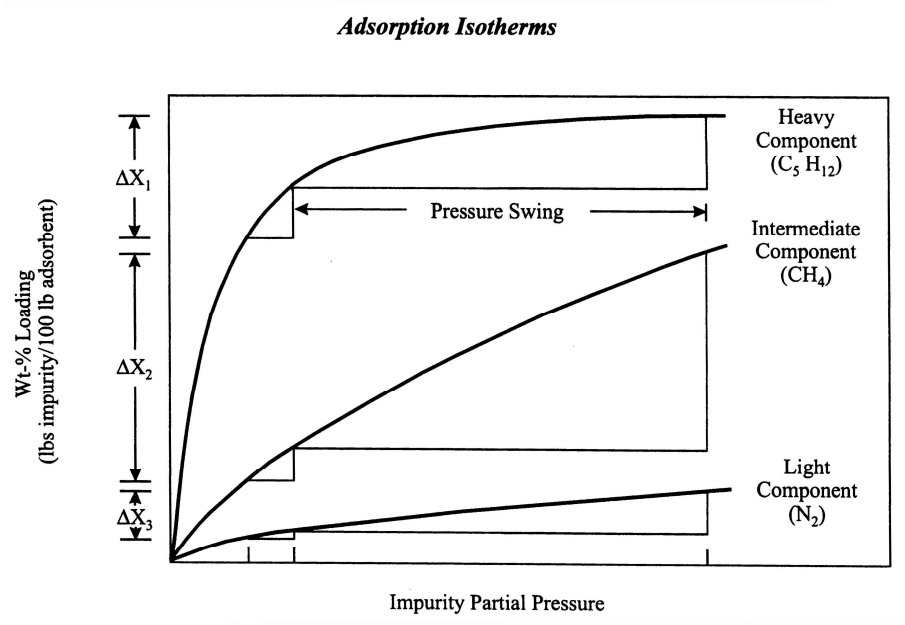

Figure 1.6 – Operating principle of the PSA. UOP 3111 [1.13].

Table 1.4 – Relative adsorption strength of the most common impurities. UOP 3111 [1.13].

Non-adsorbed	*Light*	*Intermediate*	*Heavy*
H_2	O_2	CO	C_3H_6
He	N_2	CH_4	C_4H_{10}
	Ar	C_2H_6	C_{5+}
		CO_2	H_2S
		C_3H_8	NH_3
		C_2H_4	BTX
			H_2O

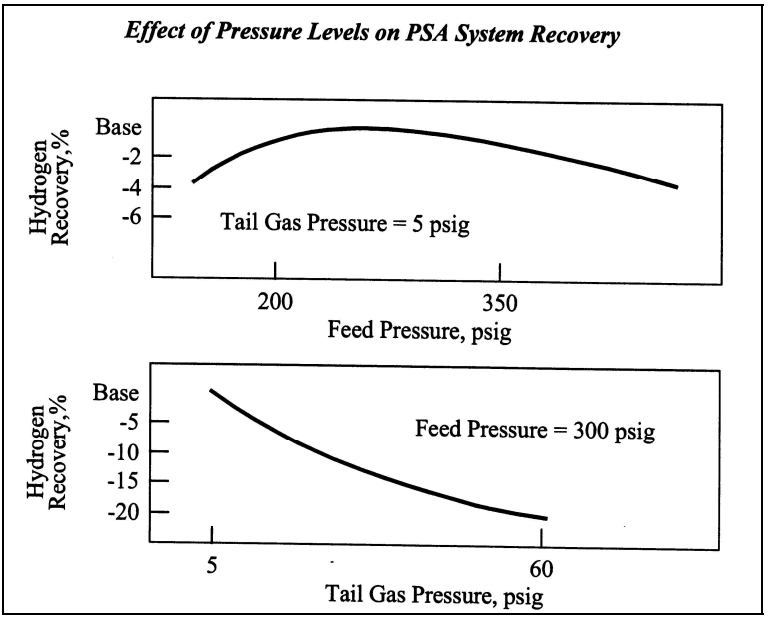

Figure 1.7 – Effect of the operating pressures on the PSA process. UOP 3111 [1.13].

Furthermore, a CO and CO_2 removal level up to 0.1-10 ppm is reached. The PSA is chromatographic-wise process, in the sense that the most strongly adsorbed impurities are separated as last ones with respect to the most weakly adsorbed impurities (Table 1.4) [1.13].

1.3.2 MEMBRANE-BASED HYDROGEN SEPARATION PROCESSES

Membrane separation processes are based on the ability of a mean (the membrane) to be more permeable towards some compounds rather than others. This ability is called perm-selectivity and is responsible of the separation effectiveness. Since this argument will be the specific topic of the Chapter 2, here only a quite general description of the process is provided. In general, a membrane module is composed of two distinct zones separated by the membrane.

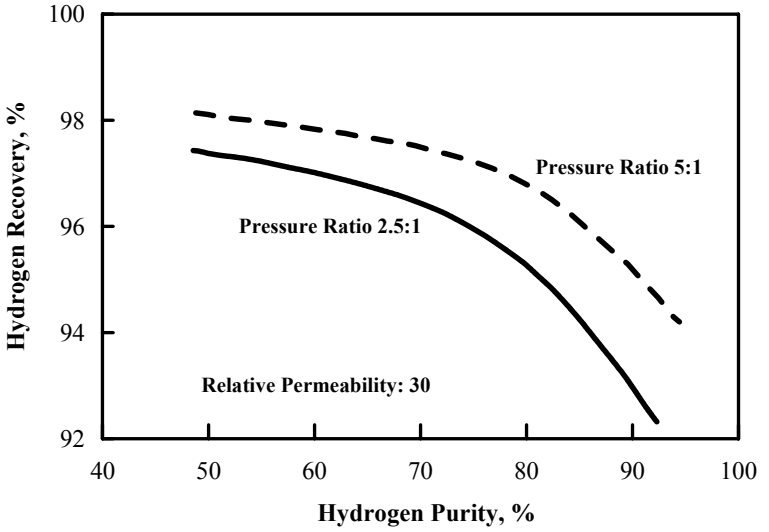

Figure 1.8 – Hydrogen recovery as function of the hydrogen purity. UOP 3111 [1.13].

The stream to be separated is fed in the first one (upstream side), where the least permeable compounds are preferably retained, whilst the second one is richer of the most permeable compounds (downstream side). The streams at the outlet of the upstream and downstream

side are called retentate and permeate, respectively. Usually, in this type of systems the higher the selectivity the lower the transmembrane flux, the higher the permeate purity and the lower recovery of the key-species (hydrogen in this case). This situation is clearly shown in Figure 1.8, where it can be noticed that a purity decrease from just 98 to 95-vol% corresponds to a recovery increase of about 25%. Furthermore, as the hydrogen recovery increases, the membrane area increases exponentially. Generally speaking, the performances of a membrane system depend mainly on the ratio of up- and down-stream pressures rather than on their absolute values, whilst the membrane area is inversely proportional to the feed pressure. This is the reason why, in order to obtain the necessary transmembrane pressure, it is preferable to compress the feed gas rather than the one in the permeate [1.13].

At the moment, two types of hydrogen separation membranes are commercially used: the asymmetric membranes and the composite ones. The first ones are composed of two layers of a single polymer: one (dense) is responsible of the separation, whereas the other one (micro-porous) has to provide the necessary mechanical resistance. On the contrary, the composite membranes are made of two different polymers, each one having the same role as shown for the asymmetric membranes. Moreover, even in the large industrial plants the amount of selective polymer is quite low, and, thus, expensive polymers can be used without increasing significantly the costs in time. The above-described membranes are made in shape of hollow fibres or flat sheets, and both of these types are packed in appropriate modules allowing the standardization of such equipments and the reduction of the volume plant in comparison to the other conventional technologies [1.13].

1.3.3 HYDROGEN SEPARATION IN CRYOGENIC

The processes in cryogenic are those processes carried out at very low temperature and exploiting the boiling point difference of the fed species to be separated. Since hydrogen has a higher volatility than the hydrocarbons and the majority of the impurities, the simplest version of the separation in cryogenic is a partial condensation to remove the required amount of impurities. The gaseous feed is firstly pre-cooled in a series of multi-step heat-exchangers

made of aluminium, whereas the main refrigeration is partially achieved by the Joule-Thompson effect (caused by a contraction-expansion of the liquid hydrocarbons condensed) and partially by external utilities or turbo-expansion of the hydrogen produced (if necessary). Figure 1.9 shows a typical flow-sheet for the partial condensation where a hydrocarbons-hydrogen feed stream, appropriately pre-treated, is sent to a cryogenic unity [1.13].

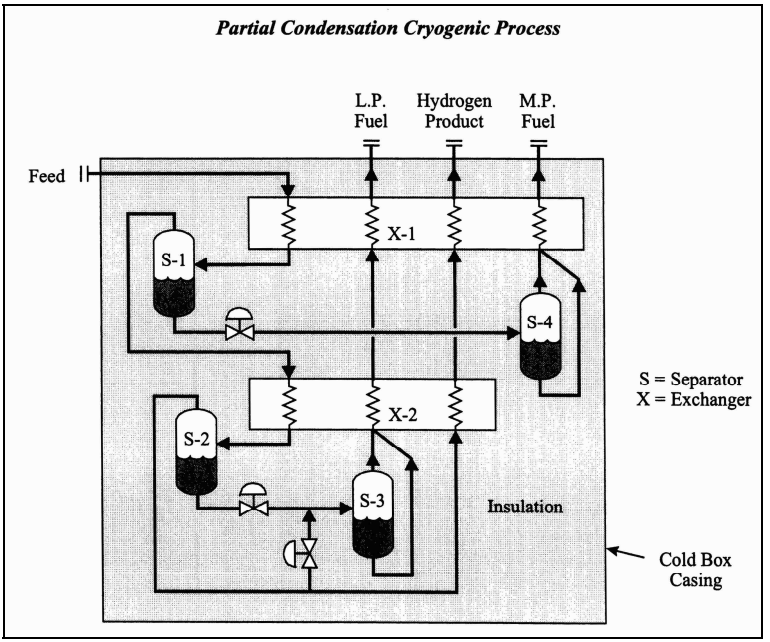

Figure 1.9 – Scheme of a cryogenic process for hydrogen purification. UOP 3111 [1.13].

The feed is cooled down in the heat-exchanger X-1 up to reach a temperature at which the majority of the hydrocarbons (C_{2+}) condense. Then, the biphasic stream is separated in the separation unity S-1, from which the H_2-CH_4 vapour mixture is sent to the exchanger X-2, where is cooled down to a low enough temperature to obtain the requested hydrogen purity. Successively, the cool stream passes through the separator S-2, which hydrogen exits in form

of vapour after being heated. The rich stream of liquid hydrocarbons is sent to the exchanger X-1, where its pressure is determined by the desired vaporization level. This stream can be removed as secondary product at its maximum pressure or mixed at low pressure with the retentate of the membrane process. The pressure of the methane-enriched liquid coming from S-2 is set in order to reach its boiling point, providing the heat necessary for the feed to be cooled at the temperature of S-2, which decides the hydrogen purity controlling the amount of methane in vapour phase.

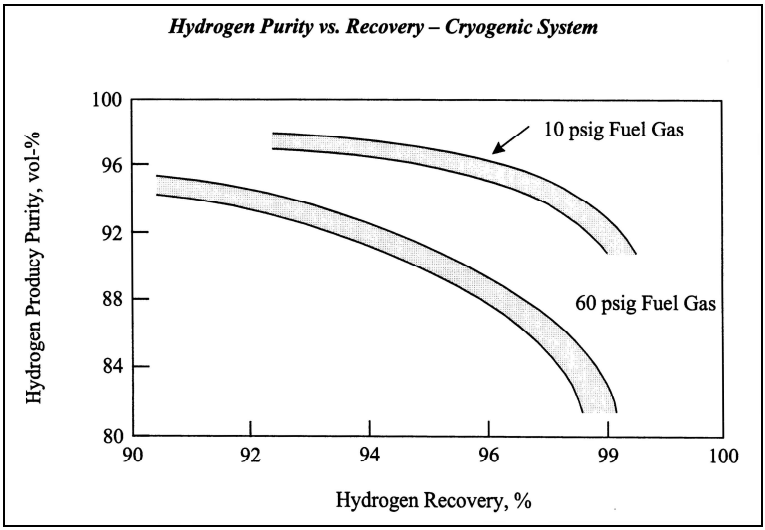

Figure 1.10 – Typical performance relation of the cryogenic processes. UOP 3111 [1.13].

Often it is necessary to send a part of the produced hydrogen in the fuel stream in order to reduce the methane partial pressure and, thus, decrease the boiling point of the same fuel stream. The amount of hydrogen to spill into the fuel stream depends on the requested purity and fuel pressure. The relation between purity, recovery and fuel pressure can be visualized in Figure 1.10. The additional separators S-3 and S-4 (Figure 1.9) are necessary for a good distribution of liquid and vapour in the multiple steps of the exchangers. If there are no

hydrocarbons or the only Joule-Thompson effect is not sufficient to provide adequate refrigeration, an external refrigeration unit must be used. If the feed is significantly composed of low-boiling point compounds, like CO or N_2, a column of liquid methane used to sweep away the impurities from the produced hydrogen. Thermodynamically speaking, the separation in cryogenic is more efficient than other processes (like PSA), reaching quite simply a high hydrogen recovery (92-97%) and a purity of about 95%.

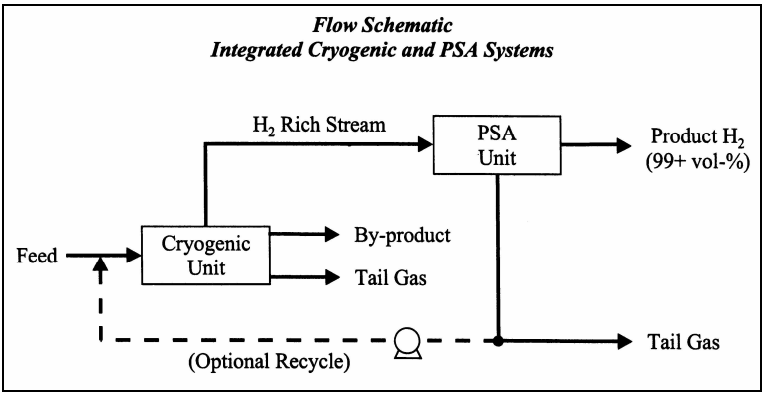

Figure 1.11 – Example of integrated process for hydrogen separation [1.13].

In general, since each of the separation/purification processes described till here presents specific advantages, an optimal design of separation systems could be represented by integrated systems where the different unities operate in synergy, as shown, for example, in Figure 1.11 [1.13].

1.4 LITERATURE CITED

[1.1] Internet link: "http://itpromegialli.provincia.so.it/Idrogeno/produzione.htm".

[1.2] Natta G. and Pasquon I., 1993. *Principi della Chimica Industriale, Vol I*. Città Studi, Milan.

[1.3] Giacobbe F. and Villante R., 1997. Method of carrying out an endothermic reaction and a reactor for carrying out the method. *International Patent: WO9726985*.

[1.4] Larson E.D. and Katofsky R.E., 1993. Production of Hydrogen and Methanol via Biomass Gasification. *Advances in Thermochemical Biomass Conversion*, A.V. Bridgwater, U.K., 495-510.

[1.5] Stucki S., 2002. *La Produzione di idrogeno-Settore Energia Generale Paul Scherrer Institut, Villigen PSI*. Internet link: http://www.poweron.ch/upload/cms/user/34 Laproduzionediidrogeno.pdf .

[1.6] Romer A., Internet link: "https://atlserver.pv.infn.it/negri/public/Corso/Part3.Produzione. Trasporto/Biomassa/1D.Romer.Energia_da_biomassa.pdf".

[1.7] Benson S.W., 1968. *Thermochemical Kinetics*. Wiley, New York.

[1.8] Altshuller V.S., 1955. *Methods of Intensification of Industrial Gas Generators Fossil Fuels Institute*. Nauka Publishers, Moscow.

[1.9] Schilling G.D., Bonn B. and Kraus U., 1986. *Coal Gasification*. Nedra Publishers, Moscow (Russian edition).

[1.10] Puri P.S., 1996. Membranes for gas separation: current status. Paper presented in the *Seminar of the Ecological Applications of Innovative Membrane Technology in the Chemical Industry*, Cetraro (CS, Italy), 1-4 May.

[1.11] Belyaev A.A., Yampolskii Y.P., Starannikova L.E., Polyakov A.M., Clarizia G., Drioli E., Marigliano G., Barbieri G., 2003. Membrane air separation for intensification of coal gasification process. *Fuel Processing Technology*. **80**: 119-141.

[1.12] Romanello V., 2003. Analisi di alcune peculiari potenzialità degli HTR: la produzione di idrogeno ed il bruciamento degli attinidi. *Master Degree Thesis*. The University of Studies of Pisa, Pisa.

[1.13] Miller G.Q. and Stoecker J., 1999. *Selection of a Hydrogen separation Processes*. Address: "UOP LLC, 25 East Algonquin Road, Des Plaines IL 60017-5017".

CHAPTER 2

MEMBRANES FOR GAS SEPARATION

2.1 GENERAL CONCEPTS

A membrane can be defined as a discontinuity region between two phases, usually characterized by a quite high ratio surface/thickness. The most important peculiarity of a membrane is its ability to allow the selective permeation (the so-called "*perm-selectivity*") of some chemical species under an appropriate driving force. Generally, for the i^{th} species in a mixture, the permeation driving force is the difference of chemical potential between the membrane sides, usually expressed as concentration or pressure difference.

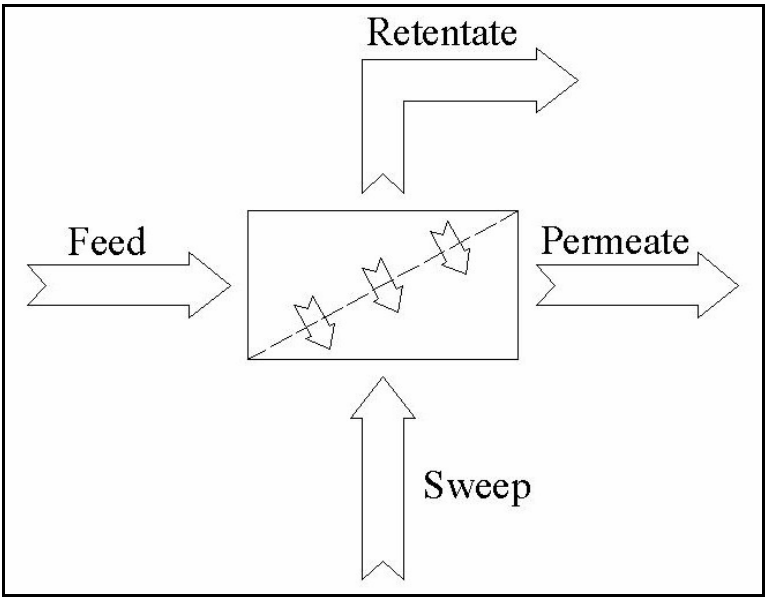

Figure 2.1 – General scheme of a membrane separation process.

A general scheme of a membrane separation process is shown in Figure 2.1, where on the high-pressure side (upstream) the stream of feed and retentate are present, whilst on the low-pressure one there are the permeate and sweep stream, this last one being optional in dependence on the particular process carried out. As said above, the membrane is the

separation mean through which some components pass more easily than others, so that retentate and permeate are richer of the least and most permeable compounds, respectively. On a physical point of view, the transmembrane mass flux of a species increases with the driving force and decreases with the membrane thickness, since a higher resistance is found. Hence, the simplest law that it is possible to write for the permeating flux is reported in Eq. 2.1, where Pe_i [mol$_i$ m^{-1} s^{-1} Pa^{-1}], π_i [mol$_i$ m^{-2} s^{-1} Pa^{-1}], ΔP_i^{TM} [Pa] are the membrane permeability, permeance and Driving Force (DF) of the ith species, respectively, whereas δ [m] is the membrane thickness.

$$J = \frac{Pe_i}{\delta}\Delta P_i^{TM} = \pi\,\Delta P_i^{TM} \tag{2.1}$$

It is very important to underline that, once an appropriate DF has been chosen, this equation represents in fact only the definition of the permeability/permeance, which has to be calculated in relation to the specific DF. In practise, in most the cases the choice of DF falls down to the simple partial pressure (gases) or concentration (liquids) difference, since, when there are no particular phenomena, the chemical potential difference can be expressed in terms of these quantities. However, in some particular cases, like, for example, the Pd-based membranes, the correct DF is represented by an expression of the type reported in Eq. 2.2, where the partial pressures are raised to a real exponent n.

$$J = \pi\left(P_{i,Upstream}^{n} - P_{i,Downstream}^{n}\right) \tag{2.2}$$

Strictly speaking, the permeability is an intrinsic property of the material constituting the membrane, whilst the permeance is an intrinsic property of a specific membrane. This means that, in order to compare the permeative performances of two different materials the permeability should be used. On the contrary, for evaluating the effectiveness of two membranes in terms of permeating flux, the permeance should be considered, since it takes

into account the different membrane thickness. Considering the general scheme in Figure 2.1, when the pressure drops along the axial direction of the upstream and downstream zone are negligible, the pressure difference at the inlet and outlet of the separation module are the same (Eq. 2.3). When the two zones are not perfectly mixed, it should be more correct to express the pressure drop by means of an arithmetic or logarithmic mean (Eqs. 2.4, 2.5, respectively).

$$\Delta P_i^{TM} = \begin{cases} P_i^{Feed} - P_i^{Sweep} = P_i^{Retentate} - P_i^{Permeate}, & \text{Co - current} \\ \\ P_i^{Feed} - P_i^{Permeate} = P_i^{Retentate} - P_i^{Sweep}, & \text{Counter - current} \end{cases} \tag{2.3}$$

$$\Delta P_{i,AM}^{TM} = \frac{\left(P_i^{Feed} + P_i^{\text{Retentate}}\right) - \left(P_i^{\text{Sweep}} + P_i^{\text{Permeate}}\right)}{2} \tag{2.4}$$

$$\Delta P_{i,LM}^{TM} = \frac{\left(P_i^{Feed} - P_i^{Sweep}\right) - \left(P_i^{Permeate} - P_i^{Retentate}\right)}{ln\left(\frac{P_i^{Feed} - P_i^{Sweep}}{P_i^{Permeate} - P_i^{Retentate}}\right)} \tag{2.5}$$

The total amount of feed permeating through the membrane is indicated by the so-called "*Stage-Cut*" θ (Eq. 2.6, where F and Q indicate the molar and volumetric flow rate, respectively).

$$\theta = \frac{F^{Permeate}}{F^{Feed}} = \frac{Q^{Permeate}}{Q^{Feed}} \tag{2.6}$$

In order to have a measure of the separation degree of a species i with respect to species j, a "*Separation Factor*" (SF_{ij}) or selectivity is opportunely defined. Two definitions are

available: one, referring to an ideal case (Eq. 2.7) and the other defined in actual cases (Eq. 2.8). A very important quantity to measure is the amount of a certain species recovered in the permeate with respect to the total amount of the same species in the feed. For this aim, an appropriate "*Recovery Factor*" RF_i for a species i is introduced (Eq. 2.9).

$$_{ideal}SF_{i,j} = \frac{Permeance_i}{Permeance_j} \tag{2.7}$$

$$_{actual}SF_{i,j} = \frac{\left(\frac{x_i}{x_j}\right)^{\text{Permeate}}}{\left(\frac{x_i}{x_j}\right)^{\text{Feed}}} \tag{2.8}$$

$$RF_i = \frac{F_i^{Permeate}}{F_i^{Feed}} = \frac{Q_i^{Permeate}}{Q_i^{Feed}} = \frac{x_i^{Permeate}}{x_i^{Feed}}\theta \tag{2.9}$$

2.2 MEMBRANES CLASSIFICATION

The membranes can be classified basing on several different criteria, which can consider, for example, the composition material, internal structure, physical properties, their applications and/or the transport mechanism which they have to obey. Among all these different aspects, a classification can be made considering the materials of which the membranes are made. Hence, they can be divided into:

- ✓ Polymeric membranes.
- ✓ Inorganic membranes (ceramic and metallic).
- ✓ Hybrid membranes.

In the in-coming sections, the main characteristics of all these types will be exhaustively described.

2.2.1 POLYMERIC MEMBRANES

The polymeric membranes can be divided basing on their structure in:

- ✓ Symmetric membranes.
- ✓ Asymmetric membranes.
- ✓ Composite membranes.

The symmetric membranes are made of a quite thick layer of homogeneous material (polycarbonate or polyester) and are generally characterized by cylindrical shaped pores laid out perpendicularly and randomly on the surface. Considering for example an aqueous solution, these membranes allow the permeation of only those solutes having a dimension smaller than the pores' diameter. Commercially speaking, several materials are available, like PVC, PVDF, PTFE, cellulose-derived polymers, polyammides and polypropylene. However, this market is always in development and many other innovative materials are being considered.

The asymmetric membranes are composed of two adjacent layers made of the same materials having different characteristics (porosity in particular) achieved by different preparation methods. For example, the cellulose-acetate membranes belong to this category and are massively used in process of inverse osmosis and ultra-filtration. The composite membranes are asymmetric membranes on whose surface a dense or porous thin film of another material is spread out. This film is the selective layer and is responsible of the out-and-out separation. Several under-laying layers are possible, like, for example, membranes supported by polyester, with an intermediate layer of polysulphone and selective layer in polyammide. A different classification of the polymeric membranes can be made considering the "state" of the polymers:

- ✓ Glassy polymers.
- ✓ Rubbery polymers.

A polymer is said glassy or rubbery when the operating temperature is under or over its glassy transition point (T_g). For this reason, it should be spoken more correctly about "glassy or rubbery state" of polymer instead of "glassy or rubbery polymers". However, in literature this last expression has by now became very common and in practise the two expressions assume the same meaning. The glassy state is characterized by a relative rigidity of the polymeric network and, thus, the physical and mechanical properties are more similar to a crystal than to a rubber, the structure being more fragile. On the contrary, the rubbery state shows a certain flexibility of the reticular internal structure, caused by the mobility of the polymeric chains. Hence, its behaviour is more liquid- than solid-like, and, for this reason, a rubbery polymer is able to relax the external stresses more rapidly than in the glassy state, which is characterized by higher resistance to strains and to become fragile.

2.2.2 INORGANIC MEMBRANES

In the last three decades the inorganic membranes have been successfully tested in many separation processes, so that a great interest has been developed in the research field, especially as concerns the potential applications in processes presenting drastic operating conditions. In fact, an inorganic material usually is much more stable exposed at high temperatures, at ionizing radiations and at certain chemical environments than common polymeric materials. Some other advantages of these membranes are:

- ✓ Chemical resistance.
- ✓ Mechanical resistance even at transmembrane pressure higher than 3 MPa.
- ✓ High durability in time.
- ✓ Simplicity of cleaning.

However, they present also several drawbacks, like:

- ✓ Fragility, this one requiring appropriate supports.
- ✓ High costs.
- ✓ Limited morphologies and geometries that can be used.
- ✓ Low ratios Membrane Area / Module Volume.

A classification can be made depending on several factors like:

- ✓ Internal structure of the selective layer (dense or porous).
- ✓ Type of the selective layer material (metallic, zeolitic, perovskitic, etc.).
- ✓ Type of the support material (ceramic, metallic, etc.)
- ✓ Atomic structure (amorphous, semi-crystalline or crystalline).

The most common characteristic to consider among the just-described ones is that concerning the internal structure of the selective layer, dividing the inorganic membranes in two great classes:

- ✓ Dense membranes.
- ✓ Porous membranes.

However, for the structural complexity of the available membranes, it is not possible to provide a univocal classification for them.

2.2.2.1 DENSE METALLIC MEMBRANES

The metallic membranes are used in almost all the cases in processes involving gas separation. At the beginning of the development of such membranes, membranes made of pure metals were used. Although they showed a quite high selectivity, they were characterized by very low permeance values. Furthermore, in order to reach an acceptable mechanical resistance, it was necessary to adopt high selective layer thicknesses, this fact representing a serious limitation to a large-scale use of these membranes because of the high material cost (noble metals in most the cases). Hence, the necessity arose of preparing membranes with as this as possible thicknesses and presenting at the same time a good mechanical and thermal resistance. In order to fulfil the two requirements, in the course of the technological development membranes have been prepared with some techniques allowing the deposition of a thin metallic film on the surface of an appropriate porous support. Such a system metal-support permits to exploit fully the best characteristics of each two phases, as shown in Table 2.1. Hence, the technological goal has been and is still represented by the ability to use preparation techniques allowing to make membranes with a dense selective layer as thin as possible deposited on a porous

support. This one has to be chosen with good mechanical resistance, for increasing the resistance of the selective layer to high pressure gradients and tensional states, and good thermal stability, as well as being simple to prepare and with moderate costs. Anyway, since the membrane type is chosen depending on the process to be carried out and in this specific case the interest is focussed on the hydrogen production and purification, a special attention will be paid to the Pd-based membranes, which have the peculiarity of being infinitely selective towards hydrogen with respect to all the other chemical species.

Table 2.1 – Advantages of the supported membranes with respect to the self-supported ones.

Support	Pure metal membranes		Supported metallic membranes
Null Selectivity	Very high selectivities		Very high selectivities
High permeance	Quite low permeances	⇒	High permeances
Low costs	High costs		Moderate costs
Good thermal stability	High thermal stability		High thermal stability
Good mechanical stability	High mechanical stability		High mechanical stability

2.2.2.1.1 PD-BASED DENSE MEMBRANES

The Pd-based membranes show important potentialities on an industrial point of view, presenting the particular property to retain completely all the chemical species except hydrogen, which can permeate through the dense layer by a mechanism that will be described exhaustively in Chapter 3. The other chemical compounds can pass only if the membrane presents some defects in the structure large enough to allow the permeation by viscous or Knudsen transport. Hence, these membranes show an infinite selectivity towards hydrogen and usually several Pd-alloys are considered in their preparation, like Pd-Ru, Pd-Ni, Pd-Zr or other metals belonging to VI, VII and VIII group. Today, for the considerations made in Section

2.2.2.1, selective layer thicknesses as thin as possible, deposited on appropriate ceramic (glass, alumina, etc) [2.1] or metallic (SS, Ni, Fe, etc.) [2.2] supports, are used.

2.2.2.1.2 PALLADIUM HYDROGEN SYSTEM

Below its critical temperature (300°C), the system Pd-H presents a miscibility gap in which two phases with different composition (in terms of H atoms over Pd ones) co-exist: α-phase and β-phase, which have the same reticular symmetry but very different specific volumes. At room temperature (20°C) α-phase is characterized by a ratio n_H/n_{Pd} of 0.008 and is poorer of hydrogen atoms, whereas for β-phase this ratio is 0.607. In these conditions, the hydrogen partial pressure in equilibrium with the two phases is about 0.07 atm.

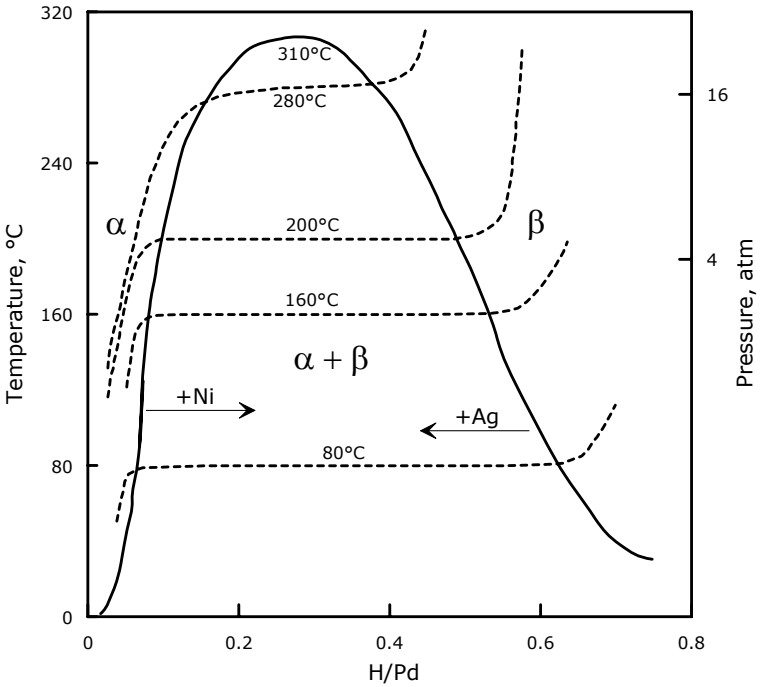

Figure 2.2 – Phase diagram of the H-Pd system [2.3].

The phase diagram of this system is shown in Figure 2.2 [2.3]. The phase transition $\alpha \rightarrow \beta$ generates a volume increase of about 1.57 $cm^3\ mol_H^{-1}$, corresponding to a situation in which in α-phase only one H atom is found out of 125 Pd atoms, whilst in β-phase there are 76 H atoms out of the same number of Pd atoms. Hence, the reticular parameter passes from 0.3894 nm to 0.4025 nm, causing deformations generating internal stresses able to lead up to breaks inside the metallic bulk. Hence, two extreme (or idealized) cases exist, one in which the stresses are not at all relieved and the other in which all stresses are relieved. This gives rise to two kinds of equilibrium and, hence, to two kinds of phase diagrams the coherent and the incoherent equilibrium diagrams. It is emphasized that these are idealizations and that in practice a phase distribution of mixed character is achieved, the degree of stress relief being dependent on details of the experimental procedure. In the idealized coherent equilibrium between two phases of a metal-hydrogen system one phase has grown within the parent phase without any diffusive motion of the metal atoms and without any plastic deformation. Hence, the lattice lines are continuous (although not straight) between the two phases and their interface is characterized by a change of composition and an inflection point in the lattice parameter-distance variation. The resulting coherency stresses change the chemical potential of the dissolved hydrogen in both phases along the principles described in a previous section, so that the compositions of the coexisting phases in equilibrium with a given hydrogen gas fugacity have values different from those that would exist in the absence of stresses at the same hydrogen gas fugacity. Furthermore, for a single crystal with free surfaces the compositions of coherent coexisting α- and β-phases would be functions of the shape of the crystal. This results from the coherency stresses, which are functions of the image forces at the free surfaces. For a long thin wire, the effect of coherency stresses is negligible so that the compositions of coexisting coherent phases would be the same as for a fully incoherent equilibrium. The coherent equilibrium is in general a meta-stable condition of higher free energy (caused by elastic energy) than that of the corresponding incoherent equilibrium. The change from coherency to incoherency necessitates the nucleation of dislocations which can move the matrix atoms, by slip, away from the neighbourhood of the coherent second-phase

particle to free surfaces or to grain boundaries. The nucleation cannot occur until enough coherency elastic energy has accumulated by the growth of the coherent particles to "pay" for the self-energy of the dislocations. In general, coherency is lost by the formation of dislocations at the interface between the α- and β-phases and by the generation of dislocations which ideally should carry metal atoms to the free surface or to grain boundaries.

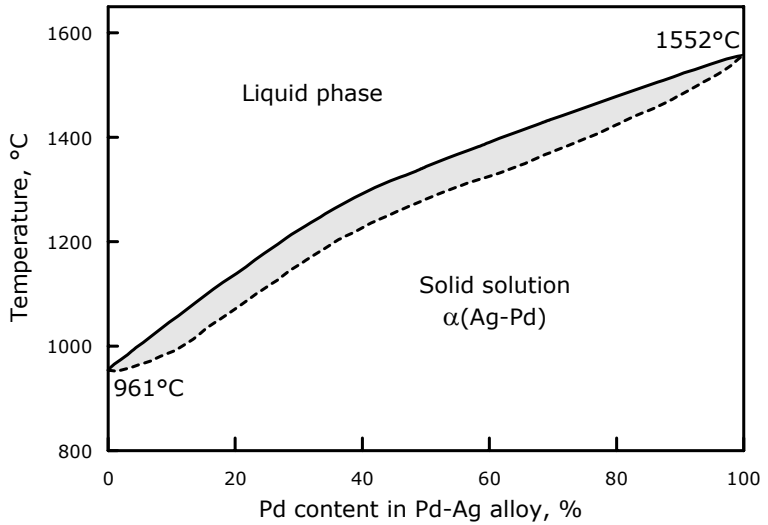

Figure 2.3 – State diagram of the H-Pd system.

However, this transport is never complete, so that the system usually ends up with large dislocation densities distributed throughout the metal grains. Although the excess free energy in the coherent equilibrium is considerably reduced by the transition to incoherence, it is not totally removed since the dislocations represent a free energy excess over the dislocation-free state. The coherence-incoherence transformation is the chief reason for the well-known hysteresis observed when trying to establish phase boundaries in metal-hydrogen systems. Coherency stresses and their reduction by dislocation generation occur in hydrogen charging/discharging into/form a metal whenever more than one phase is produced by the

ingress or egress of hydrogen. The generated dislocations modify the mechanical properties and can affect micro-cracking of the metal [2.4]. The problem of the phase transition $\alpha \rightarrow \beta$ can be overcome operating above the critical temperature 300°C, where only β-phase is present.
As demonstrated by Gryaznov [2.5], a good mechanical stability can be achieved by using Pd-alloys, like Pd-Ag, leading up to a reduction of the temperature at which α- and β-phase co-exist, allowing to work at lower temperatures without embrittlement phenomena [2.5-2.7].
As the Ag-content increases, an increase of the hydrogen solubility and a reduction of its diffusion coefficient occur. Because of these two opposite tendencies, the hydrogen permeability in a Pd-Ag alloy reaches its maximum value whenever the Ag-content is about 23% [2.8]. Furthermore, the alloy melting point decreases as function of the Ag composition according with the phase diagram in Figure 2.3, but the working temperature has to be kept quite below the values shown in figure because of the presence of permeating hydrogen.

2.2.2.1.3 POISONING AND INHIBITION PHENOMENA IN PALLADIUM AND ITS ALLOYS

The surface of pure palladium and its alloys can be reduced by the physical (reversible) and/or chemical (irreversible) adsorption of some species present as impurities in the gaseous streams, causing a decrease of the hydrogen permeating flux and, thus of the performance of membranes. In dealing with this argument, it is necessary to distinguish the poisoning phenomena from the inhibition ones. In fact, the first ones occur whenever the impurities and metallic surface are bonded permanently and irreversibly, causing in time the complete de-activation of the adsorption sites responsible of the permeation.
On the contrary, inhibition occurs whenever these bonds are reversible, causing only a temporary reduction of the active surface, whose complete activity can be restored by setting appropriate operating conditions (e.g. increasing temperature). As concerns Pd-alloys, the impurities of highest interest are represented by CO (inhibitor) and sulphur compounds (poisons), especially H_2S.

SURFACE EFFECTS OF CO ON PD-ALLOYS.

At room temperature, CO is physically adsorbed on Pd-alloy surfaces with a sticking coefficient of about 1, whilst in the same conditions that of hydrogen is about 0.6. Let us remember that the sticking coefficient is the ratio between the number of molecules effectively adsorbed and the total number of molecules colliding with the surface. Hence, at low temperatures, the CO amount adsorbed is higher than that of hydrogen. In particular, CO tends to occupy different positions on the surface: first, the "bridge-sites", i.e. the space between four adjacent Pd atoms, and, then, the "top-sites", i.e. the space just over one Pd atom, although all of these sites are considered energetically equivalent [2.9]. As temperature increases, the CO adsorption is less favoured than that of hydrogen, since the bonds are weaker. This phenomenon was studied by Chabot *et al.* [2.10] considering a gaseous mixture of H_2, CO, CO_2 and CH_4 in the CO concentration range of [0.2-9%-vol], providing the following results:

- ✓ In the range [0.2-2%-vol] the reduction in hydrogen permeation becomes appreciable only at temperatures lower than 200°C.
- ✓ In the range [4.3-9%-vol] the inhibition occurs below 300°C, increasing rapidly as temperature decreases and becoming practically total at 150°C.

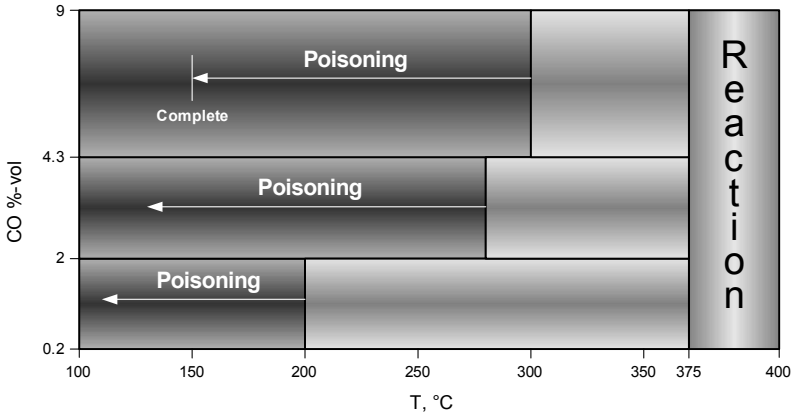

Figure 2.4 – Palladium inhibition degree by CO as function of CO concentration and temperature.

If working in the temperature range of [300-375]°C, no problem is found for any CO concentration value.Above 375°C the most of CO present in the mixture reacts with hydrogen to form CH_4, CO_2 and H_2O, and the analysis loses its validity. A graphical summary of the just-described results are shown in Figure 2.4. Successive regeneration tests showed the temporary character of the CO inhibition, leading the Pd-surface up to the initial performances by means of heating under vacuum at higher temperature than 250°C. The inhibition by CH_4 and CO_2 was demonstrated to have a much less significant influence than that by CO, being appreciable only at temperatures below 150°C.

SURFACE EFFECTS OF SULPHUR-BASED SPECIES ON PD-ALLOYS.

The gaseous compounds containing sulphur-based species, like H_2S or SO_2, poison the Pd-based surfaces by forming deposits of pure sulphur [2.11]. In particular, H_2S dissociates forming atomic hydrogen and sulphur according with Eq. 2.10.

$$H_2S \rightarrow 2H + S \tag{2.10}$$

The hydrogen atoms normally diffuse through the metal bulk, whilst the sulphur atoms create permanent bonds with the Pd-alloy surface, preventing new hydrogen molecules to be adsorbed. A similar effect occurs also with SO_2, although the phenomenon is much less important than with H_2S.

2.2.2.1.4 PREPARATION METHODS OF PD-ALLOY MEMBRANES

At the moment, several techniques for the thin metallic layers' deposition on porous supports are available. The choice of the most appropriate one is always the result of different necessities depending on the chemi-physical of substrate and support, as well as on the application which the membrane has to be involved in. The control of the deposition process is a typical problem not only of the chemical process, but also of the electronic one.

The most commonly used techniques are:

- ✓ Electroless Plating, EP.
- ✓ Magnetron Sputtering, MS.
- ✓ Spray pyrolysis, SP.
- ✓ Chemical Vapour Deposition, CVD.
- ✓ Electrochemical Vapour Deposition, EVD.
- ✓ Physical Vapour Deposition, PVD.
- ✓ Solvated Metal Atom Deposition or Co-condensation, SMAD.
- ✓ Vacuum Electro-Deposition, VED.
- ✓ Sol-Gel process, SG.
- ✓ Cold Rolling and Diffusion Welding, CR-DW.

The order of magnitude of the minimum thicknesses achievable by several different techniques is reported in Figure 2.5.

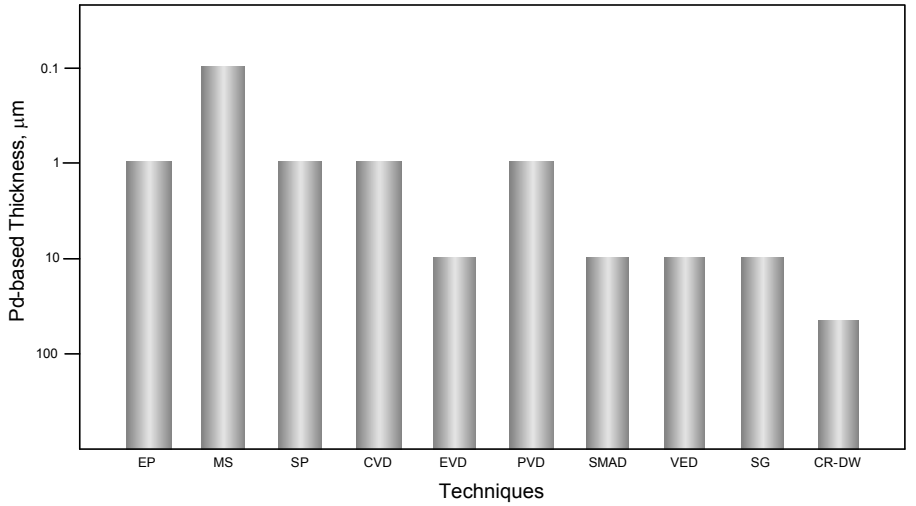

Figure 2.5 – Minimum thickness obtainable by means of several deposition techniques.

ELECTROLESS PLATING (*EP*).

This deposition technique is constituted of several steps, some of which consist in a simple cleaning and some others in support preparation and in out-and-out deposition of the metal required. The main steps are described as follows:

1) First, the support is cleaned by means of common detergents; then, a warm washing in CCl_4 followed by several cold washing in acetone, ethylic alcohol and water.
2) In order to remove eventual impurities traces, a washing in a solution of HNO_3-HCl (30-70%-vol) and a final washing in NH_3 are carried out.
3) Then, the support is immersed in a solution of $SnCl_2 \cdot 2H_2O$ (5 g L^{-1}) with a small amount of HCl making the solution a bit acid. This step aims to make the surface adapt for the deposition of the first metallic (palladium in this case) particles. After this immersion, the surface is washed in distilled water.
4) The support is immersed in a solution containing 0.12 g L^{-1} of $Pd(NH_3)_4Cl_2$ with a small quantity of HCl. In this step the first palladium particles, which represent the active centres for the successive deposition, are deposed on the surface. A washing in water is then carried out.
5) The steps 3) and 4) are repeated several times (usually five times). In case of alumina supports ten iterations are necessary.
6) The support is then immersed in a solution of: 0.8 g of $PdCl_2$, 300ml of NH_4OH (28%-vol), 42 g of $C_{10}H_{14}O_8N_2Na_2 \cdot 2H_2O$, 6 mL of hydrazine (1 M). The whole solution is successively led up to a volume of 600 mL. The operating temperature and pH must be about 40°C and 11, respectively. The deposition time takes about 2 hours.

During the deposition of a Pd-layer up to 1-2 μm can be achieved. Several depositions are necessary to increase the thickness of the metallic layer. Shu *et al.* [2.12] carried out the co-deposition of a Pd-Ag alloy on a SS porous support, Govind and Atnoor [2.13] deposited pure Pd on an Ag porous substrate, and Uemiya *et al.* [2.14] made a deposition of Pd on a porous glass tube using a solution of $[Pd(HN_3)_4]Cl_2$+2Na·EDTA+NH_4OH+H_2NNH_2. Before being immersed in this solution, the substrate is activated in solutions of $SnCl_2$ and $PdCl_2$ in order to

ensure the auto-catalytic deposition. The reduction velocity depends on the surface activation, on the concentration of metallic salt and reducing agent, on temperature and pH. This technique allows a low defects concentration and quite homogeneous surface, permitting to lead thicknesses up to about 1 μm. The main drawback is that several problems arise in the control of the film thickness and because of decomposition phenomena causing loss of the material to depose.

MAGNETRON SPUTTERING (*MS*).

In this technique metal particles are deposed on a target surface by means of sputtering. The substrate is placed in a vacuum chamber (< 1 Pa) of an inert gas (usually argon) and is covered by a target material (atoms or negative ions) [2.15]. The positive ions of the metal strike the surface removing the target material. It is also possible to do two consecutive depositions of two different metals. In order to obtain good quality Pd-Ag alloys, it is necessary to have a sufficient ionization closely to the substrate, a high density of ions' current on the substrate (> 1 mA cm^{-1}) and high deposition velocity. In this way, the film is uniformly deposed with the almost complete absence of surface defects. As the distance of the target substrate increases, the ions' current strongly decreases, hence, in order to keep an appropriate deposition velocity, it is necessary to increase the ionization by means of a magnetic field of a permanent magnet. A drawback of this method is that the metallic film is not bonded very strongly to the substrate on which it is deposed.

SPRAY PYROLYSIS (SP).

This technique requires the sputtering of a solution of the metal salts into a heated gas stream, where a pyrolysis occurs. This method can be used to fabricate Pd-Ag membranes whenever a high purity is not requested, since, in general, the selectivities of the membranes made by means of this technique are considerably lower than those made by means of the above-described techniques.

Nevertheless, Gryaznov *et al.* [2.7] used this technique obtaining a quite high selectivity towards hydrogen by means of a deposition of binary and ternary alloys of Pd with Mn, Co, Ru,

Sn, Pb, carried out in an argon atmosphere with a variable pressure from 0.1 to 1 Pa. In these conditions, the deposition velocity was kept at about 1 $\mu m\ min^{-1}$.The substrates utilized were constituted of asymmetric polymeric membranes, porous steel and metallic oxides.

CHEMICAL VAPOUR DEPOSITION (*CVD*).

This method consists in the low pressure vaporization of an organic compound of the metal to depose. In the contact, the organo-metallic compounds decompose, leaving the metal on the pores' surface. The compound containing the metal can be a hydride, halide or an organo-metallic complex. The most of the CVD processes operate in a pressure ranges from some hundreds Pascal to the atmospheric pressure.

The energy required is usually provided by a thermal source, but sometimes also photons or electric discharges are used. Since many chemical reactions can be adopted in CVD, this technique is characterized by a high flexibility and versatility for the production of thin films or dielectric means. For this reasons, it is massively used also in the micro-electronic industry, but not for preparing membrane to be used at high temperature. However, it is thought that it could be successfully applied also to make membranes suitable for this aim.

ELECTROCHEMICAL VAPOUR DEPOSITION (*EVD*).

This technique is principally used for the deposition of metals on other metals, like, for example, the plating processes. It is a process very simple to set up, requiring only a continuous electric current sources and a bath where the temperature and the concentration of the electrolyte can be kept fixed. The porous substrate separates a chlorate vapours mixture (ZCl_3, YCl_3, etc.) from an oxygen source (water vapour or oxygen).

Initially, the reactants back-diffuse, forming a solid oxide. When the pores are completely closed by the solid, the ions of oxygen are carried through the oxides. In this way, the growth of the oxide film increases on the side where the chlorate compounds are present. The use of the EVD after a preliminary deposition allows to reach relatively high thicknesses in a controlled way and without particular difficulties, but only if the first metallic layer is strongly bonded to the surface. This technique cannot be adopted in a so simple way when thin films have to be

deposed on ceramic or glassy substrates, for which a preliminary metal deposition by means of other techniques is necessary.

PHYSICAL VAPOUR DEPOSITION (*PVD*).

The name of this technique includes a large class of methods in which a material is converted in vapour phase and successively condensed in vacuum conditions on a target surface. It can be used to depose several types of materials:

- ✓ Metals (Ag, Au, Pt, Pd, etc.).
- ✓ Ceramic materials.
- ✓ Alloys.
- ✓ Semi-conductors.
- ✓ Glasses.
- ✓ Polymers.

This method allows to reach layer thicknesses in the range [1-50 μm]. The vaporization can be done by means of electric resistances and this ensures a deposition velocity of about 1 g m^2 s^{-1}.

SOLVATED METAL ATOM DEPOSITION (*SMAD*) *OR CO-CONDENSATION.*

In this technique, the palladium is placed in a melting pot and vaporized by means of energy provided by an electric arc. The Pd-vapours, which are weakly bonded to an appropriate coordination solvent (1-esene or mesistilene), are condensed in a glassy tank at a typical temperature of the liquid nitrogen. During the co-condensation, a simply oxidable organo-metallic compound is formed, which for this reason is handled in argon atmosphere. The solution, containing the Pd, is heated up to room temperature and put in contact with the porous substrate, releasing the organo-metallic compound from palladium, which is deposed on the porous surface. This method was originally adopted to depose metallic catalytic particles [2.16], but later on was used to depose metallic films on porous supports. This technique allows to make ultra-thin thicknesses (of the order of 0.1 μm), which make the so-made membranes very fragile and not enduring.

VACUUM ELECTRO-DEPOSITION (*VE*).

The electro-deposition of metallic alloys includes the migration of positive metallic ions towards the cathode made of a membrane substrate by means of an electric field. The ions accept the electrons and are deposed on the cathode as metallic atoms formed at the Pd-anode, which is immersed in a solution of metallic complexes. This method seems very effective for reducing the superficial roughness of the surface. Furthermore, if vacuum conditions are adopted during the electro-deposition of metallic alloys on mesoporous substrates, the covering solutions is allowed to penetrate inside the pores, creating a film bonded very strongly to the substrate.

COLD ROLLING AND DIFFUSION WELDING (*CR-DW*).

The cold rolling is commonly used also in industrial scale to prepare metallic foils and papers. This technique permits to increase the hardness and the resistance to traction, whilst a reduction in lengthening is shown. When it is applied to Pd-alloys foils, a reduction in layer thickness is achieved. In the laboratory of the Italian national research centre "*ENEA*" – "*Ente per le Nuove tecnologie, l'Energia e l'Ambiente*" (*Frascati, Rome*) – two types of composite Pd-based membranes were prepared:

- ✓ Supported membranes with a porous metallic substrate (grid or pierced foil) bonded to a Pd-Ag foil by the diffusion welding method. In these membranes the thin Pd-based foil ensures a high hydrogen permeability, whereas the metallic support resists to the pressure differences which the membrane is subjected to.
- ✓ Metallic rolled membranes with a thin Pd-Ag covering was deposed on foil made of several metals (Nb, Ta, V). In this case, an appropriate thickness of non-noble metals is able to ensure the necessary mechanical resistance, absence of defects (fractures and/or micropores) and an infinite selectivity towards hydrogen.

In a rolled membrane, the principal role of the ceramic support is to prevent the contact between Pd-based membrane and a catalytic bed of an eventual membrane reactor. The addition of some bonding element to palladium improves the mechanical resistance, but, because of this fact, the rolling become more complicated, especially when the metallic foil

thickness goes down 120 μm. In order to obtain always more thin thicknesses several rolling-welding cycles are necessary, but, when the thickness is very thin, the presence of impurities becomes a very important fact to avoid. In fact, traces of specific elements (C, S, Si, Cl, O, etc.) can have a significant influence on both the mechanical properties of the metallic foil and hydrogen permeability. Hence, a base-condition to obtain high performance commercial Pd-based foils (1-10 μm thick) is the extreme purity of the starting materials.

2.2.2.1.5 PEROVSKITES

The perovskites are complex inorganic solids that can be chemically indicated by the empirical formula ABO_3, where the cationic sites "A" are usually occupied by metals belonging to the rare earths group, whilst in sites "B" the transition metals with different valencies are placed. Some perovskites exhibit an high conductivity of electrons and oxygen-ions and, for this reason, are being studied for "Solid Oxides Fuel Cells" ("*SOFCs*") applications, as oxygen sensors, batteries and oxygen-permeable membranes [2.17].

2.2.2.2 POROUS CERAMIC MEMBRANES

The porous ceramic membranes can be divided into the following three categories according with their mean pore diameter:

- ✓ Microporous membranes.
- ✓ Mesoporous membranes.
- ✓ Macroporous membranes.

Figure 2.6 shows the ranges corresponding to each category. However, it has to be underlined that the boundaries of these ranges are quite flexible and, thus, this classification represents only a rough indication distinguishing the different groups. Very recently, a new category of porous materials has been classified: the so-called "nano-materials", which are characterized by very ordered internal structure and by pore diameters with a magnitude order in the range of the nanometric scale.

Although this type of materials can be naturally included in the microporous materials group, it is very common in literature to use the adjective "nanoporous" to classify them. However, it is necessary to keep in mind that, actually, the two adjectives (micro and nanoporous) are completely equivalent to each other and can be used indifferently. In the whole group of the inorganic oxides being studied to be used as porous membranes, the most important are:

- ✓ Titania.
- ✓ Silica.
- ✓ Alumina and zeolites.
- ✓ Vycor-glass.

In applications concerning the catalytic membrane reactor, the porous membranes used are essentially composite ceramic, zeolitic or made of Vycor-glass with very small pores. Although continuous efforts are aimed to prepare inorganic oxide-based membranes, these ones do not present infinite selectivities towards a sole gas as, on the contrary, occurs in case of Pd-based membranes. Microporous membranes of γ-alumina supported on macroporous materials like α-alumina were developed to separate H_2 from CO_2 [2.18]. These membranes showed a good thermal stability, since the modifications of the alumina γ-phase towards the other crystalline phases occur at about 600°C.

It was demonstrated that it is possible to use other oxides to prepare membranes with smaller pores than those of γ-alumina, even though the best commercial membranes operate with pores of 4 nm. Unluckily, this diameter is not sufficient to obtain good selectivities, since pores less than 1 nm would be necessary, but this value was reached only in experimental laboratory scale [2.18]. Some progresses have been got basing on the innovative concept of "*Chemical Valve Membranes*", which represent a new membranes group made of V_2O_3 or V_2O_5 whose permeability can be tuned by acting on the redox properties of the gas phase [2.19]. An important application of this characteristic consists in the possibility of a controlled addition of a reactant along the axial direction of a membrane reactor. For example, in the partial oxidation of the alkanes the progressive conversion of the reactants towards the reactor outlet causes the ratio alkane/oxygen to decrease progressively. This type of membranes allows to control

the oxygen concentration in side the reactor in such a way to improve the efficiency of the process and keep the reactants ratio to the optimal value [2.19]. An important characteristic of the ceramic membranes is their ability to be used at quite high temperatures, even higher than 1000°C.

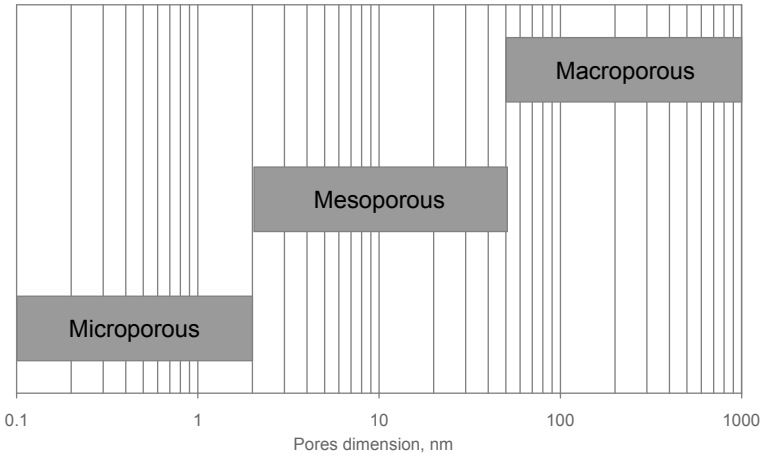

Figure 2.6 – Classification of the porous membranes according to the dimension of the pores.

Furthermore, it must be highlighted that they can operate also with radioactive gas mixtures, this aspect being very important if thinking about radioactive tracers or other uses in the nuclear industry. The main limitation is the difficulty to prepare microporous films arranged in shape of hollow fibres, fact that would improve the packing density (surface area/volume) with a consequent reduction of the costs. Nevertheless, a relatively new type of ceramic membranes, the zeolitic membranes, could overcome this problem, developing more sophisticated methods for deposing thin ceramic films on cylindrical shaped macroporous substrates.

2.2.2.2.1 ZEOLITIC MEMBRANES

The name "*zeolite*" (form Greek "*zeo lithos"*, "boiling stone") was introduced in 1756 by the Swedish mineralogist A.F. Cronsted, who observed that when these minerals (the stilbite, in particular) are heated, bubbles are formed because of the release of the interstitial water. The zeolites represent a very promising class of microporous materials, used massively in ionic interchanges, as adsorbent means and molecular sieves, and play an important role in the heterogeneous catalysis. Their properties are an immediate consequence of their crystalline structure, whose relation with the macroscopic characteristics can be directly observed.

The theoretical and applicative interest for zeolites is continuously increasing, indicated by the progressive expansion of the synthesis procedures for preparing new zeolitic materials. At the beginning, zeolites were used mostly as cationic exchangers for the water sweetening and even now are utilized in detergents in place of the phosphates, which cause serious environmental problems. In nature at least 40 different zeolites exist, but in the course of the years their number has been increased much by means of synthetic procedures.

INTERNAL STRUCTURE AND COMPOSITION.

The zeolites are a class of materials related to feldspars and feldspathoids. They are alumino-silicates presenting crystalline structures made of tetrahedra TO_4 (T=Si, Al, etc.), whose oxygen atoms are shared with the adjacent tetrahedra. Their general formula is represented by Eq. 2.11, where cations "M" of valency "*n*" neutralize the negative charges on the alumino-silicate lattice.

$$M_{\frac{x}{n}}\left[\left(AlO_2\right)_x\left(SiO_2\right)_y\right]\cdot mH_2O \qquad (2.11)$$

The fundamental units of zeolites are tetrahedral units of $[SiO_4]^{4-}$ and $[AlO_4]^{5-}$ bonded together by the sharing one vertex for each couple of tetrahedra, creating non-linear oxygen bridges. Since the values of the "T-O-T" angles are distributed in a range of about [125°-180°], the tetrahedra can be arranged in several different structures, forming rings with a variable number

of units (4, 5 or 6 tetrahedra). The structure of many zeolites is based of a unit made of 24 tetrahedra of Si or Al, which is called "*sodalitic unit*" (β-cage). The bond "Si-O-Al" is relatively rigid and the cations do not belong to the structure and, hence, are often called as "interchangeable cations". The variation of the ratio Si/Al causes a variation of the cations content in the lattice, since the lower Al atoms, the less number of exchangeable cations. A high content of Si causes the zeolite to be more hydrophobic, showing a certain affinity towards the hydrocarbons.

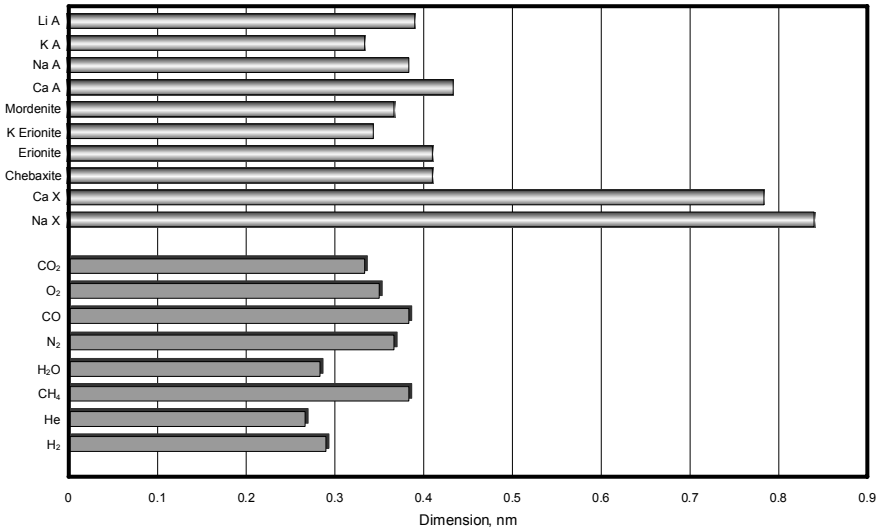

Figure 2.7 – Comparison between the characteristic dimensions of some zeolites and kinetic molecular diameters of some chemical species.

CLASSIFICATION.

According with the channels structure, the zeolites can be distinguished in the following groups:

- ✓ Fibrous zeolites.
- ✓ Lamellar zeolites.
- ✓ Framework zeolites.

The first ones are composed of several chains linked to each other by oxygen bridges. A typical example of fibrous zeolite is the edingtonite, which have a characteristic shape of chain linked to a regular repetition of five tetrahedra. The lamellar zeolites are frequently found in the sedimentary rocks, like the fillipsite, whose channels are parallel to the crystallographic axis "*a*". The third type of zeolites presents channels developing along the three dimensions (for example, the zeolite-A). Usually, the dimensions of the cage's windows are included in the range [0.3-1 nm], from which the name of "*molecular sieve*" arises. In Figure 2.7 the pores' dimensions of some zeolites are compared with the molecular diameter of some molecules, highlighting the attitude of these materials to be used as selective means in gas separation.

PREPARATION METHODS

The zeolites are prepared from starting solutions of silicates and aluminates at high pH obtained by using the hydroxide of an alkaline metal or an organic base. The common method to prepare these materials occurs in one step, during which the synthesis mixture is put in contact with the target support in an autoclave. However, in order to prepare very thin and defect-free membranes, the promising technique of the so-called "*secondary growth*" is to be used. This technique consists in separating the nucleation step from the one of crystal growth, being able to optimize independently the operating conditions of the two steps. In this method, first the nucleation seeds are prepared apart ("*primary growth*") and then the secondary growth is carried out in an appropriate thermal system. Vroon *et al.* [2.20] prepared membranes of zeolite MFI on α-alumina supports by means of several hydro-thermal treatments, in each of which the support is placed in an autoclave and put in contact with synthesis mixtures having each time the same composition but different temperature. The so-obtained membranes presented a thickness of 4 μm thick, which showed crannies during the calcination.

Another method consists a) in deposing some precursors of the zeolitic phase (with or without nucleation seeds) on the target surface, b) in drying step and c) in the growth of the zeolitic layer in vapour phase. For example, Tsay and Chiang [2.21] sowed a gel containing zeolite seeds on a ceramic support, successively introduced in an environment saturated of water

vapour. In these conditions the water condensed between the zeolitic particles dissolves and causes the growth of the zeolite. Balkus *et al.* [2.22] developed the "*Pulse Laser Ablation*" method, in which a laser makes zeolites fragments evaporate going onto an appropriate support kept at low temperature. Successively, the support with the zeolitic film is placed into a mixture synthesis for the generation of a homogeneous and compact layer whose thickness can be easily controlled. At the beginning of this decade several types of zeolitic membranes were prepared, orienting the zeolitic film on both dense and porous supports. Among these membranes, let us recall the zeolite MFI [2.21] and the zeolite A [2.23]. An oriented film can present some advantages since a) the number of defects decreases if crystals grow uniformly along the same direction; b) when the crystals are oriented in along the flux direction, the less tortuosity increase the permeability keeping high value of selectivity.

SOL-GEL PROCESS

This process allows to prepare high purity and homogeneity ceramic materials by means of techniques different from the traditional methods based on the oxides fusion. First, a gel is formed by means of a co-polymerization process of the silicate and aluminate ions and, then, is heated at 60-100°C in a closed tank for about 2 days (hydro-thermal conditions), producing a condensed zeolite, whose characteristics depend on the operating conditions and mechanical agitation. In general, the process is carried out in liquid solution of organo-metallic compounds, which lead up to the formation of a new phase (Sol) generated by hydrolysis and condensation reactions (Eq. 2.12).

$$\begin{aligned} &M-O-R+H_2O \rightarrow M-OH+R-OH, && \text{(Idrolisi)} \\ &2M-OH \rightarrow M-O-M+H_2O, && \text{(Water condensation)} \\ &MO\text{-}R+M\text{-}OH \rightarrow M\text{-}O\text{-}M+R\text{-}OH, && \text{(Alcoholic condensation)} \\ &(M=Si,\ Zr, Ti) \end{aligned} \tag{2.12}$$

The Sol phase is composed of solid particles with a diameter of few hundreds of nanometres suspended in the liquid phase. Successively, the particles condense in the Gel phase, where a solid macromolecule is placed in a liquid phase (solvent). Drying the gel phase by appropriate thermal treatment (25-100°C), it is possible to obtain solid porous matrices, called "*Xerogel*".

The principal advantage of the Sol-Gel process consists in being able to prepare ceramic material at room temperature. In Figure 2.8 some potential applications of this process are shown, highlighting its flexibility and versatility.

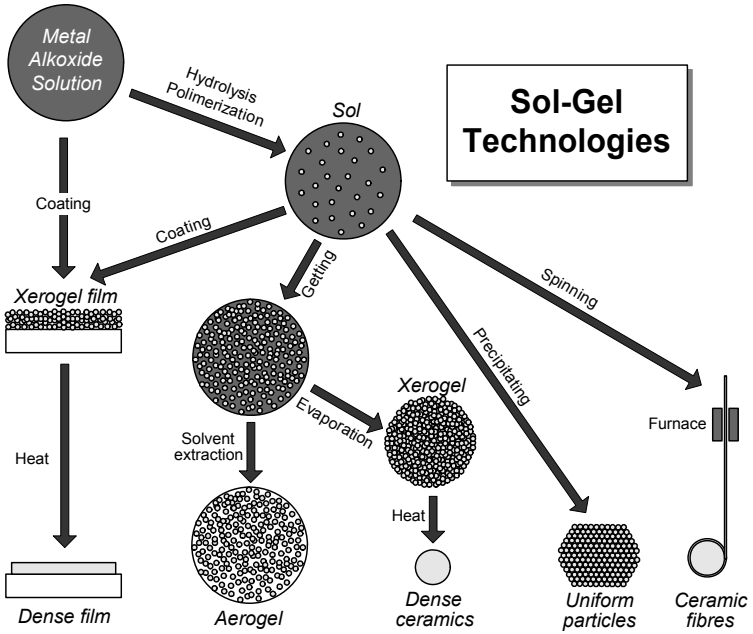

Figure 2.8 – Potential applications of the Sol-Gel process.

2.3 LITERATURE CITED

[2.1] Basile A., Criscuoli A., Santella F. and Drioli E., 1996. Membrane reactor for water gas shift reaction, *Gas Separation and Purification*, **10:** 243-254.

[2.2] Shu J., Grandjean B.P.A., Van Neste A. and Kaliaguine S., 1991. Catalytic Palladium-based Membrane Reactors: A Review. *Canadian Journal of Chemical Engineering*, **69**: 1036-1060.

[2.3] Lewis F.A., 1967. *Palladium Hydrogen System*. Academic Press, London, New York.

[2.4] Oriani R.A., 1993. The Physical and Metallurgical Aspects of Hydrogen in Metals. *Proceeding Acts of ICCF4, Fourth International Conference on Cold Fusion*. Lahaina, Maui: Electric Power Research Institute 3412 Hillview Ave., Palo Alto, CA 94304.

[2.5] Gryaznov V. M., Ermilova V.M., Morozova L.S., Orekhova N.V., Polyakova V.P., Roshan N.R., Savitsky E.M. and Parfenova N.I., 1983. Palladium alloys as hydrogen permeable catalysts in hydrogenation and dehydrogenation reactions. *Journal of the Less Common Metals*, **89**: 529-535.

[2.6] Gryaznov V.M., Vedernikov V.I. and Gul'yanava S.G., 1986. Participation of oxygen diffused through the silver membrane catalyst during heterogeneous oxidations. *Kinetika i Kataliz*, **27**: 142-146. Coden: KNKTA4, ISSN: 0453-8811. Russian.

[2.7] Gryaznov V.H., Serebryannikova O.S., Serov Y.M., Ermilova M.M., Karavanov A.N., Mischenko A.P. and Orekhova N.V., 1993. Preparation and catalysis over palladium composite membranes. *Applied Catalysis. A: General*, **96**: 15-23.

[2.8] Amandusson H., Ekedahl L.G. and Dannetun H., 2001. Alcohol dehydrogenation over Pd versus Pd-Ag membranes. *Applied Catalysis A: General*, **217**: 157-164.

[2.9] Ertl G. and Koch J. 1971. Adsorption studies with a Pd(111) Surface. *Adsorption-Desorption Phenomena: Proceeding Acts of II International Conference*, 345-357.

[2.10] Chabot J., Lecomte I., Grumet C. and Sannier J., 1988. Fuel clean-up system: Poisoning of palladium-silver membranes by gaseous impurities. *Fusion Technology*, **14**: 614-618.

[2.11] Albers P., Pietsch J. and Parker S.F., 2001. Poisoning and Deactivation of Palladium Catalyst. *Journal of Molecular Catalysis A: Chemical*, **173**: 275-286.

[2.12] Shu J., Grandjean B.P.A., Kaliaguine S., 1993. Simultaneous deposition of palladium and silver on porous stainless steel by electroless plating. *J. Mem. Sci.*, **77:** 181-195.

[2.13] Govind R. and Atnoor D., 1991. Development of a composite palladium membrane for selective hydrogen separation at high temperature. *Industrial & Engineering Chemistry Research.* **30**: 591-594.

[2.14] Uemiya S., Sato N., Ando H., Matsuda T. and Kikuchi E., 1991. Steam Reforming on Methane in a Hydrogen Permeable Membrane Reactor. *Applied Catalysis.* **67**: 223-230.

[2.15] Gobina E., Hou K. and Hughes R., 1995. Equilibrium-shift in alkane dehydrogenation using a high temperature catalytic membrane reactor. *Catalysis Today*. **25**: 365-370.

[2.16] Capannelli G., Bottino A., Gao G., Grosso A., Servida A., 1993. Characterisation of catalytic membrane reactors using the hydrogenation of benzene. *Proceeding Acts of First Conference on Chemical and Process Engineering*, AIDIC, Milano. 796.

[2.17] Mukasyan A.S., Costello C., Sherlock K.P., Lafarga D. and Varma A., 2001. Perovskite membranes by aqueous combustion synthesis: synthesis and properties, *Separation and Purification Technology*. **25**: 117-126.

[2.18] Ross J.R.H., Erzeng X., 1995. Catalysis with membranes or catalytic membranes?. *Catalysis Today*. **25**: 291-301.

[2.19] Uhlhorn R.J.R., Keizer K. and Burggraaf A.J., 1989. Gas and surface diffusion in modified γ-alumina systems. *Journal of Membrane Science.* **46**: 225-241.

[2.20] Vroon Z.A.E.P., Keizer K., Burgraaf A. J., and Verweij H., 1998. Preparation and characterization of thin zeolite MFI membranes on porous supports. *Journal of Membrane Science*. **144**: 65-76.

[2.21] Tsay C.S. and Chiang A.S.T., 2000. Supported zeolite membrane by vapor-phase regrowth. *AICHE Journal*. **46**: 616-625.

[2.22] Balkus K.J., Munoz T. and Gimon-Kinsel M.E., 1998. Preparation of Zeolite UTD-1 Films by Pulsed Laser Ablation: Evidence for Oriented Crystal Growth. *Chemistry of Materials*. **10**: 464-466.

[2.23] Huang L., Wang Z., Sun J., Miao L., Li Q., Yan Y., and Zhao D., 2000. Fabrication of Ordered Porous Structures by Self-Assembly of Zeolite Nanocrystals. *Journal of American Chemical Society*. **122**: 3530-3531.

CHAPTER 3

MODELLING OF HYDROGEN PERMEATION THROUGH SUPPORTED PD-BASED MEMBRANES*

*Some contents of this chapter have been already published [6.5, 6.15-6.17].

3.1 INTRODUCTION

It is well-known that Pd-based membranes show an infinite selectivity towards hydrogen with respect to the other chmical species. Thus, these membranes are usually employed in processes requiring the selective removal of hydrogen from the reactive zone, like de-hydrogenation reactions (propane, iso-butane/n-butane, ethyl-benzene, etc.) or processes to produce pure hydrogen (methane or methanol steam reforming and water-gas-shift reaction) for PEM fuel cells, preventing chemical equilibrium from being established. For this reason, an adequate modelling of hydrogen permeation through such a kind of membranes is necessary to optimize the operating conditions of these reactive processes.

Since two decades the relatively high costs of palladium and the necessity to increase hydrogen permeability have been driving more efforts to fabricate ever thinner membranes, which need for supports for acquiring the necessary mechanical resistance. However, the presence of the support and the effect of external mass transfer in the gaseous films – the so called Concentration Polarization, which will be dealt with in next chapter – represent additional resistances to hydrogen permeation, determining a more or less significant decrease of membrane performance in terms of permeating flux. In general, on a physical point of view, the permeation of a species through a membrane can be viewed as a series of resistances to be overcome by an appropriate driving force. As regards the Pd-based membranes, it can be demonstrated that, when the transport through the metallic bulk is slow enough to be the permeation rate-determining step, the hydrogen transmembrane flux can be described by the Sieverts' law (Eq. 3.1).

$$J = \pi \left(P_{H_2,Upstream}^{0.5} - P_{H_2,Downstream}^{0.5} \right) \tag{3.1}$$

Thanks to the simplicity of Eq. 3.1, similar empirical expressions (Eq. 3.2) are massively used in literature by only replacing the original Sieverts' exponent (n=0.5) with another one (see, for example, the papers [3.3-3.9]).

$$J = \pi\left(P^n_{H_2,Upstream} - P^n_{H_2,Downstream}\right) \tag{3.2}$$

The problem of this approach is that the exponent n assumes a precise physical meaning just only when the transport in the Pd-based membrane bulk is the limiting step, representing otherwise only an empirical parameter to be estimated by means of a statistical analysis of available experimental data. Furthermore, it is not possible to recognize the relative contribution of each transport and kinetic phenomenon involved in the permeation process by only considering the empirical Sieverts' exponent, which is clearly inadequate to describe the effects of many interacting phenomena. In fact, the increase of the driving force exponent with respect to the value of 0.5 can be due to the surface phenomena as well as to the external mass transfer in support and/or in gaseous film adjacent to the membrane sides. Moreover, the value of this exponent is commonly estimated by means of a statistical-type analysis (usually a non-linear regression), whose inevitable fitting errors represent another degree of uncertainty. For all these reasons, a deviation from the original Sieverts' law (n =0.5) may have different explainations and there is no unequivocal conclusion to be drawn from this. Furthermore, the value of this exponent could change even along the same membrane equipment. In fact, in membrane reactors and/or contactors, significant changes in partial pressure of the target-component or in temperature can cause a shift from a permeation rate-determining step to another one. In all cases, the empirical approach is able to describe correctly the system behaviour only if these changes are not important, fact that does not occur, for example, in the highly exothermic and/or endothermic reactions, for which the temperature differences are significant. For these reasons, it is necessary to have an adequate model to identify the individual effect of each phenomenon occurring in hydrogen permeation through the Pd-based membranes. Ward and Dao [3.1] have already introduced such a model by accounting for several elementary steps, but they did not consider the presence of any support and, furthermore, their approach to the external mass transfer appears inadequate (binary mixture approach) to deal with actual systems. Hence, in this chapter a new model is developed by taking into account different elementary steps, paying a special care to the transport in a

multilayered porous support and to external mass transfer, both based on the multicomponent Stefan-Maxwell equations. Since the present approach is similar to that of Ward and Dao [3.1], their article is set as a reference work to improve the mathematical modelling.

Table 3.1 – Permeation elementary steps of the present model and comparison with the one of Ward and Dao [3.1].

Target	Present model	Ward and Dao [3.1]
Membrane	Supported	without support
Differences in physical approach		
Feed Side	Multicomponent mixture	Hydrogen as the only species
Permeate Side	Multicomponent mixture	H_2-N_2 Binary Mixture
In the multilayered porous support	Multicomponent mixture	N.A.
Differences in mathematical approach		
Feed Side	Stefan-Maxwell theory	N.A.
Permeate Side	Stefan-Maxwell theory	Constant mass transfer coefficient
Multilayered porous support	Dusty Gas Model	N.A.
Driving force of the diffusion in the Pd-Bulk	Gradient of atomic hydrogen chemical potential along the Pd-layer	Difference between hydrogen concentrations at the Pd-bulk sides
Analogies		
Adsorption and Desorption	King and Wells' equations [3.2] (as Ward and Dao [3.1])	
"Surface to Bulk" and "Bulk to Surface"	Ward and Dao's approach [3.1]	

The description of the present model and the differences and analogies with Ward and Dao [3.1] are reported in Table 3.1. As indicated in Table 3.1, this model is able to describe the

transport in supported membranes, on the contrary to what done by Ward and Dao, which consider only self-supported ones. The transport in the support is described by means of the Dusty Gas Model, accounting for Knudsen, Poiseuille and ordinary diffusion.

For transport through the Pd-alloy layer, the gradient of the hydrogen chemical potential is used as the driving force for the diffusion. On the contrary, Ward and Dao [3.1] consider pure hydrogen on the feed side and a binary mixture on permeating side, using constant mass transfer coefficients to describe the external mass transfer. For all these reasons, the model developed here, missing in the open literature, represents a useful tool for analyzing H2 permeation through supported membranes in order to:

- Evaluate the hydrogen profiles along the membrane top-layer, in the layers of the asymmetric porous support and in the gas-phase layers adjacent to the supported membrane, describing the mass transport in a more exhaustive way.
- Calculate quantitatively the influence of each step on the whole permeation process, in order to identify the rate-determining steps as a function of the operating conditions.
- Enlarge the range of applicability of the mathematical description.
- Design the membrane to maximize the transmembrane flux by minimizing the resistance of each elementary step. This can be done a) by decreasing the Pd-based layer thickness as regards the diffusion in the Pd-layer; b) by modifying the fluid-dynamic flow regime (as turbulent as possible) for the transport in the films; c) by decreasing the resistance of the support (adopting a larger mean pore diameter, a higher porosity and/or a less thickness) for the transport in the support.

3.2 DESCRIPTION OF THE MODEL

The physical and schematic representation of the target system are shown in Figure 3.1, where a) an SEM photo of a multilayered Pd-based membrane, b) the scheme of membrane considered here and c) the mechanism rate of each elementary step involved in the permeation, are reported. The Pd-based layer is supported by an asymmetric support

characterized by several (five) layers, each one having different thicknesses and pore sizes.This study describes the transport in the orthogonal direction to the membrane surface and no axial profiles are considered.

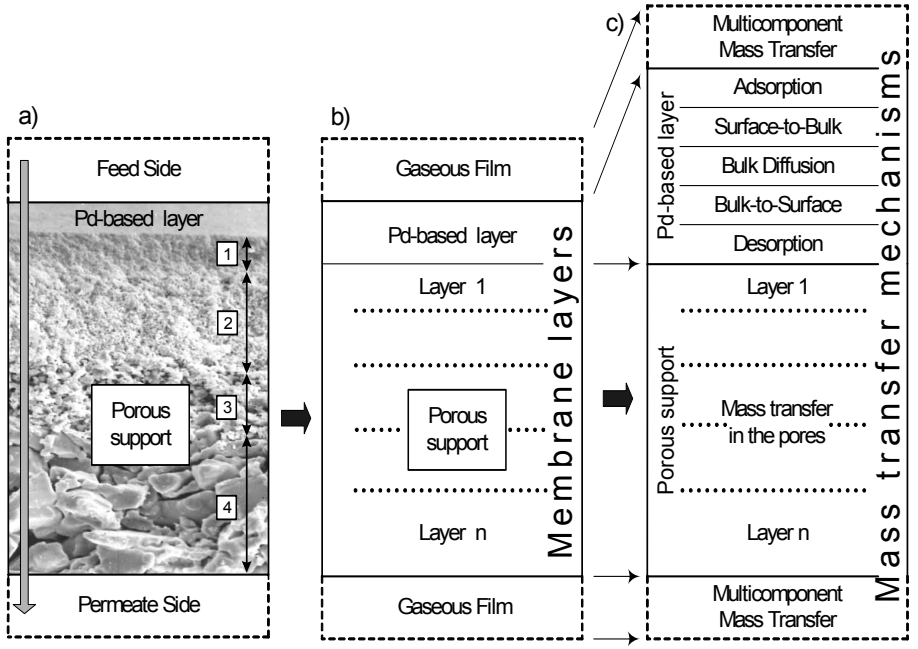

Figure 3.1 – a) Example of a multilayered Pd-based membrane (adapted from Höllein *et al.* [3.9]. b) Scheme of the multilayered membrane considered here. c) Mass transfer mechanisms of all the elementary steps involved in the permeation process.

Therefore, the scheme proposed can be used to describe the permeation, e.g., in a continuous stirred system or in each abscissa of tubular systems. The whole permeation mechanism has been divided into the following elementary steps:

1) On the retentate side:
   a. Mass transfer in the fluid phase of the film just near the interface.
   b. Adsorption: hydrogen decomposition in atoms on the Pd-alloy surface.

2) Inside the Pd-alloy layer:
   a. Surface to Bulk: atomic hydrogen transition from Pd-alloy surface to Pd-alloy bulk.
   b. Diffusion: transport in the Pd-alloy bulk.
   c. Bulk to Surface: atomic hydrogen transition from Pd-alloy bulk to Pd-alloy surface.
3) On the permeate side:
   a. Desorption: Hydrogen atomic recombination on the Pd-alloy surface.
   b. Mass transfer in the fluid phase of the multilayered porous support.
   c. Mass transfer in the fluid phase of the film just near the interface.

In the following sections, the detailed mathematical form of the above described physical model is provided.

3.2.1 MASS TRANSFER IN THE FLUID PHASES ON RETENTATE AND PERMEATE SIDE

The transport of the gas mixtures is modelled by using the Stefan-Maxwell multicomponent theory. In the simplest case of a binary mixture and for slow mass transfer velocity, the partial pressure of a component at a solid interface can be related to its flux by Eq. 3.3 [3.10].

$$N_1 = \frac{1}{RT} Kc \left(P_1^{Bulk} - P_1^{Surface} \right) + \frac{N_{Total}}{P_{Total}} P_1^{Surface} \tag{3.3}$$

The quantities of the other components are known by the difference, since the total pressure is constant. In the film theory, the mass transfer coefficient is related to the diffusivity and to the transfer film thickness according with Eq. 3.4.

$$Sh = \frac{Kc\ l}{\mathfrak{D}_{12}} = g(Re) Sc^q \tag{3.4}$$

where $g(Re)$ is an appropriate function of Reynolds number, q is a real number and l is a characteristic dimension of the mass transfer equipment, which in this case can be represented

by the equivalent diameters in the feed and permeate side, respectively. In the more complex case of multicomponent mixtures, Toor [3.11] and Stewart and Prober [3.12] proposed the same approach, based on the Stefan-Maxwell transport theory, by simply transforming some dimensionless scalar groups into corresponding dimensionless matrix groups. According with these considerations, the expression for the fluxes is given by Eq. 3.5 [3.13].

$$\vec{N} = \frac{1}{RT}\{Kc\}\cdot\{Z\}\cdot\left(\vec{P}^{Bulk} - \vec{P}^{Surface}\right) + \frac{N_{Total}}{P_{Total}}\vec{P}^{Surface} \tag{3.5}$$

All the vectors and matrices, indicated with "→" and "{ }", have a dimension of (n-1) and (n-1) by (n-1), respectively, since the profiles of one component can be calculated by the others. $\{Kc\}$ is the matrix of the mass transfer coefficients and $\{Z\}$ is that of correction factors for taking into account the high transfer rates. Using the film theory, $\{Kc\}$ is expressed by Eq. 3.6.

$$\{Kc\} = \frac{\{Sh\}\cdot\{D\}}{d_{Equivalent}} \tag{3.6}$$

In analogy to the scalar case, the Sherwood matrix can be expressed by semi-empirical correlations
(Eq. 3.7) [3.13]:

$$\{Sh\} = g(Re)\{Sc\}^{q} \tag{3.7}$$

In this analogy the function of Reynolds' number remain scalar, while Schmidt's number becomes a matrix, given by Eq. 3.8.

$$\{Sc\} = \nu\{D\}^{-1} \tag{3.8}$$

The matrix $\{D\}$ is the matrix of the multicomponent diffusivities, calculated according with the Stefan-Maxwell theory (Eq. 3.9) [3.13], where the index 'n' marks the nth specie of the mixture.

$$\{D\} = \{B\}^{-1},\ B_{ii} = \frac{x_i}{\mathfrak{D}_{in}} + \sum_{\substack{k=1 \\ k \neq i}}^{N^{Species}} \frac{x_k}{\mathfrak{D}_{if}},\quad B_{ij} = -x_i\left(\frac{1}{\mathfrak{D}_{ij}} - \frac{1}{\mathfrak{D}_{in}}\right) \tag{3.9}$$

According with the film theory, the expression for the matrix $\{Z\}$ is given by Eqs. 3.10-3.11 [3.13].

$$\{Z\} = \{\varphi\}\left(e^{\{\varphi\}} - \{I\}\right)^{-1} \tag{3.10}$$

$$\{\varphi\} = \frac{RT\,N_{Total}}{P_{Total}}\{Kc\}^{-1} \tag{3.11}$$

In this calculation, the expression for $\{Z\}$ was trunk at second order, as indicated in Eq. 3.12.

$$\{Z\} \cong \{I\} - \frac{1}{2}\{\varphi\} + \frac{1}{12}\{\varphi\}^2 \tag{3.12}$$

Finally, once the semi-empirical correlation has been chosen, Eq. 3.13, which provides the mass transfer coefficients matrix, is obtained.

$$\{Kc\}d_{Equivalent} = \nu^r g(Re)\{D\}^{1-q} \tag{3.13}$$

The matrix power is calculated by the approximation of Alopaeus *et al.* [3.14]. The vector of the transmembrane fluxes is indicated in Eq. 3.14, where the fluxes of all the other components are zero because only hydrogen can pass through the membrane.

$$\vec{N} = \begin{bmatrix} N_1 & 0 & \cdots & 0 \end{bmatrix} \tag{3.14}$$

$$N_{Total} = \sum_{i=1}^{N^{Species}} N_i = N_1 = N_1^{Surface} \tag{3.15}$$

The value of transmembrane flux is to be considered known, since, as will be explained in Section 3.3, a shooting method carried out by means of a Newton-Raphson algorithm is adopted to solve the problem. The important fact to be underlined here is that once the flux value is known, the vectors of the pressures just adjacent to the membrane can be calculated for both retentate and permeate side from Eq. 3.5. The semi-empirical correlation $g(Re)$ used in Eqs. 3.7 and 3.13 are the following [3.15]:

$$g(Re) = \begin{cases} 1.62\left(\dfrac{d_{Equivalent}}{L} Re\right)^{\frac{1}{3}}, & Re \le 2100 \\ 0.026\, Re^{0.80}, & Re > 2100 \end{cases} \tag{3.16}$$

3.2.2 DISSOCIATIVE ADSORPTION AND RE-COMBINATIVE DESORPTION

Analogously to Ward and Dao [3.1], the adsorption and desorption rates were described by the expressions introduced for the first time by King and Wells [3.2] for the adsorption of nitrogen on tungsten and used by Behm *et al.* [3.16] for hydrogen adsorption on palladium. Hydrogen adsorption on palladium surfaces involves a bi-atomic dissociation, while desorption involves a superficial recombination of two hydrogen atoms to form one molecule. The adsorption rate is given by Eqs. 3.17-3.18, where Γ is the molecular bombardment rate and $S(\theta)$ is the sticking

coefficient, depending on the surface coverage θ and $P_{H_2}^{Surface}$ is the hydrogen partial pressure in the fluid just near the interface fluid-solid.

$$r_{Adsorption} = 2\Gamma S(\theta) \tag{3.17}$$

$$\Gamma = \frac{P_{H_2}^{Surface}}{\sqrt{2\pi M_{H_2} RT}} \tag{3.18}$$

$S(\theta)$ can be modelled by the quasi-chemical equilibrium approximation of King and Wells [3.2] (Eqs. 3.20 and 3.19). The same procedure leads to the following expressions for the desorption rate (Eqs. 3.21 and 3.22).

$$S(\theta) = \frac{S_0}{1 + K_w\left(\frac{1}{\theta_{oo}} - 1\right)} \tag{3.19}$$

$$\theta_{oo} = 1 - \theta - \frac{2\theta(1-\theta)}{1 + \sqrt{1 - 4\theta(1-\theta)\left[1 - e^{\left(\frac{w}{RT}\right)}\right]}} \tag{3.20}$$

$$r_{Desorption} = 2\,K_{Desorption}^{0}\; e^{\left(-\frac{2E_{Desorption}}{RT}\right)} N_S^2\, \theta_{HH} \tag{3.21}$$

$$\theta_{HH} = \theta - \frac{2\theta(1-\theta)}{1+\sqrt{1-4\theta(1-\theta)\left[1-e^{\left(\frac{w}{RT}\right)}\right]}} \tag{3.22}$$

3.2.3 TRANSITIONS "SURFACE-TO-BULK" AND "BULK-TO-SURFACE"

As indicated by Ward and Dao [3.1], the atomic hydrogen transition rates from the surface to the bulk state and *vice-versa* can be given by Eq. 3.23 and 3.24, respectively, where ξ is the atomic hydrogen concentration adjacent to the Pd-surface.

$$r_{SurfaceToBulk} = N_S\, N_b\, K^0_{SurfaceToBulk}\, e^{\left(-\frac{E_{SurfaceToBulk}}{RT}\right)}\, \theta\, (1-\xi) \tag{3.23}$$

$$r_{BulkToSurface} = N_S\, N_b\, K^0_{BulkToSurface}\, e^{\left(-\frac{E_{BulkToSurface}}{RT}\right)}\, \xi\, (1-\theta) \tag{3.24}$$

The two kinetic constants are functions of the temperature and the surface coverage, as shown by the Eq. 3.25 [3.1]:

$$\begin{cases} K^0_{BulkToSurface} = \dfrac{\Gamma_{j0}}{3N_b(1-\theta)} \\ K^0_{SurfaceToBulk} = \dfrac{K^0_{BulkToSurface}(\theta,T)T^{0.25}}{10.154}\dfrac{1-\theta}{\theta}\sqrt{\dfrac{\theta_{HH}\, S_0}{S(\theta)}} \\ E_{SurfaceToBulk} = E_{BulkToSurface} + \dfrac{\Delta E_{Adsorption} - \Delta E_{SurfaceToBulk}}{2} \end{cases} \tag{3.25}$$

3.2.4 DIFFUSION THROUGH THE PD-BASED BULK

The diffusion of the atomic hydrogen in the Pd-bulk is described by the irreversible thermodynamics theory, for which the atomic hydrogen flux can be given by Eq. 3.26, where *l* is the generic abscissa along the Pd-thickness. The thermodynamic factor Γ_H takes into account the deviation from the ideal case (ξ<<1). When the hydrogen concentration is high, Γ_H can be expressed as shown in Eq. 3.27.

$$J_H = -N_b D_H \Gamma_H \frac{\partial \xi}{\partial l} \tag{3.26}$$

$$\Gamma_H = 1 + \xi \frac{\partial \, ln \, \gamma_H}{\partial \xi} \tag{3.27}$$

The activity coefficient γ_H is related to the atomic hydrogen chemical potential in the palladium lattice μ_H as shown in Eq. 3.28, where μ_H can be expressed according with Eq. 3.29.

$$\frac{\partial \mu_H}{\partial \xi} = RT \frac{\partial \, ln(\xi \gamma_H)}{\partial \xi} = \frac{RT}{\xi}\left(1 + \xi \frac{\partial \, ln \, \gamma_H}{\partial \xi}\right) = \frac{RT}{\xi}\Gamma_H \Rightarrow \Gamma_H = \frac{\xi}{RT}\frac{\partial \mu_H}{\partial \xi} \tag{3.28}$$

$$\mu_H = \mu_H^0 + RT \, ln\left(\frac{\xi}{1-\xi}\right) + 2\xi W_{HH} - \overline{V}_H \sigma \tag{3.29}$$

The quantity μ_H^0 is the chemical potential at the standard state (infinite dilution, $\xi \rightarrow 0$). The last term takes into account the crystalline lattice deformation due to the stress caused by the atomic hydrogen passage. This deformation (elastic) becomes ever stronger as the hydrogen concentration increases, being negligible for dilute systems. The term σ can be expressed according with Eq. 3.30 [3.17]:

$$\frac{\partial \sigma}{\partial l} = -\frac{2\,\mathrm{Y}\,\overline{\mathrm{V}}_{\mathrm{H}} N_b}{3}\frac{\partial \xi}{\partial l} \tag{3.30}$$

From the previous expressions, the atomic hydrogen flux shown in Eq. 3.31 is obtained. The diffusion of hydrogen in palladium D_{H} can be described as an activated process (Eq. 3.32) [3.15].

$$J_{\mathrm{H}} = -N_b D_{\mathrm{H}}\left(\frac{1}{1-\xi} + \frac{2\mathrm{W}_{\mathrm{HH}}}{RT}\xi + \frac{2\mathrm{Y}\,\overline{\mathrm{V}}_{\mathrm{H}}^2 N_b}{3RT}\xi\right)\frac{\partial \xi}{\partial l} \tag{3.31}$$

$$D_{\mathrm{H}} = D_{\mathrm{H}}^0 e^{\left(-\frac{E_{Diffusion}}{RT}\right)} \tag{3.32}$$

If the flux expression is integrated along the palladium thickness up to a generic abscissa by setting a constant mean value for $\overline{\mathrm{V}}_{\mathrm{H}}$ (see Table 3.4), Eq. 3.33 is obtained.

$$J_{\mathrm{H}} = \frac{N_b\, D_{\mathrm{H}}}{l}\left[\ln\left(\frac{1-\xi_1}{1-\xi}\right) + \left(\frac{\mathrm{W}_{\mathrm{HH}}}{RT} + \frac{N_b \mathrm{Y}\,\overline{\mathrm{V}}_{\mathrm{H}}^2}{3RT}\right)\left(\xi_1^2 - \xi^2\right)\right] \tag{3.33}$$

Integrating for the entire palladium thickness, Eq. 3.33 becomes Eq. 3.34.

$$J_{\mathrm{H}} = \frac{N_b\, D_{\mathrm{H}}}{\delta^{\mathrm{Pd-Layer}}}\left[\ln\left(\frac{1-\xi_1}{1-\xi_2}\right) + \left(\frac{\mathrm{W}_{\mathrm{HH}}}{RT} + \frac{N_b \mathrm{Y}\,\overline{\mathrm{V}}_{\mathrm{H}}^2}{3RT}\right)\left(\xi_1^2 - \xi_2^2\right)\right] \tag{3.34}$$

For dilute systems (ξ<<1) is $\Gamma_{\mathrm{H}} \cong 1$ and the flux expression can be simplified as shown in Eq.3.35, which is the same expression as used by Ward and Dao to describe the hydrogen flux in the metallic lattice [3.1]. It can be demonstrated that when the diffusion through the Pd-bulk

is the only rate-determining step and the other steps can be considered at the equilibrium, the latter relation leads to a theoretical demonstration of the Sieverts' law.

$$J_{\mathrm{H}} \cong -D_{\mathrm{H}} N_b \frac{\xi_1 - \xi_2}{\delta^{\mathrm{Pd-Layer}}} \tag{3.35}$$

3.2.5 TRANSPORT THROUGH THE SUPPORT POROUS LAYERS

The transport through the multilayered porous support is described by means of the Dusty Gas Model [3.18].

$$\sum_{j=1}^{n} \frac{x_j N_i - x_i N_j}{C_{Total}\, D_{ij,effective}^{MaxwellStefan}} + \frac{N_i}{C_{Total}\, D_{i,effective}^{Knudsen}} = -\frac{x_i}{RT} \nabla_{T,P} \mu_i + \\ -\frac{x_i \overline{\mathrm{V}}_i}{RT} \nabla P - x_i \frac{B_0}{\eta\, D_{i,effective}^{Knudsen}} \nabla P, \quad B_0 = \frac{d_{pore}^2}{32} \tag{3.36}$$

The mathematical expression used to analyze each layer is shown in Eq. 3.36, where the factor B_0 is calculated considering the support pore as cylindrical.

Since the components are considered as ideal gases, Eq. 3.36 can be expressed by Eq. 3.37, which is the final relation used in the simulation. The calculations of the physical properties for the fluid phases are reported in Appendix A (Section 3.7.1).

$$\sum_{j=1}^{n} \frac{x_j N_i - x_i N_j}{C_{Total}\, D_{ij,effective}^{MaxwellStefan}} + \frac{N_i}{C_{Total}\, D_{i,effective}^{Knudsen}} = -\nabla x_i + \\ -\frac{x_i \overline{\mathrm{V}}_i}{RT} \nabla P - x_i \frac{B_0}{\eta\, D_{i,effective}^{Knudsen}} \nabla P \tag{3.37}$$

3.3 STRATEGY FOR THE NUMERICAL SOLUTION

Once all the equations characterizing the system have been formalized, they need to be solved by means of an appropriate method. However, before doing this, it is also necessary to choose a solution strategy, in order to achieve the results as simply and rapidly as possible. The scheme of the chosen strategy is shown in Figure 3.2, where it is taken into account that a different number of species can be present in retentate and permeate.

According with this strategy, once a first guess for the hydrogen flux has been set, the procedure solves all the steps in sequence by starting first from the bulk on the retentate side and, then, from the bulk on the permeate one. In the scheme, the quantities calculated in correspondence of each step are indicated just near it. For example, from the calculation in the external mass transfer in the retentate (or in permeate), the vector of the partial pressures just adjacent to the membrane surface on retentate (or permeate) is obtained.

When solving the adsorption step, the surface coverage on the surface in retentate (θ^{Ret}) is achieved, and so on up to the boundary between the first layer of the support and the Pd-based surface on permeate side, where the two calculation sequences meet themselves and two values of hydrogen partial pressure are obtained. The difference of these two values justly represents the quantity to set to zero by means of an appropriate numerical method, chosen to be the Newton-Raphson routine. In general, the strategy adopted belongs to the category of the "*shooting*" methods, which need for an initial guess of the unknown variable, i.e., the permeating flux (N_{H2} in the figure).

Although the solution of only an equation in only one unknown variable is to be determined, nevertheless at the beginning of the simulation, the solving method presented some problems related to the fact that some "*intermediate*" variables (θ or ξ) assume a physical meaning only in range [0,1], providing no acceptable solution otherwise. Since not all the hydrogen flux values determine acceptable values of the intermediate variables, some constraints were to be set in order to avoid the undesired solution and make the method as robust as possible.

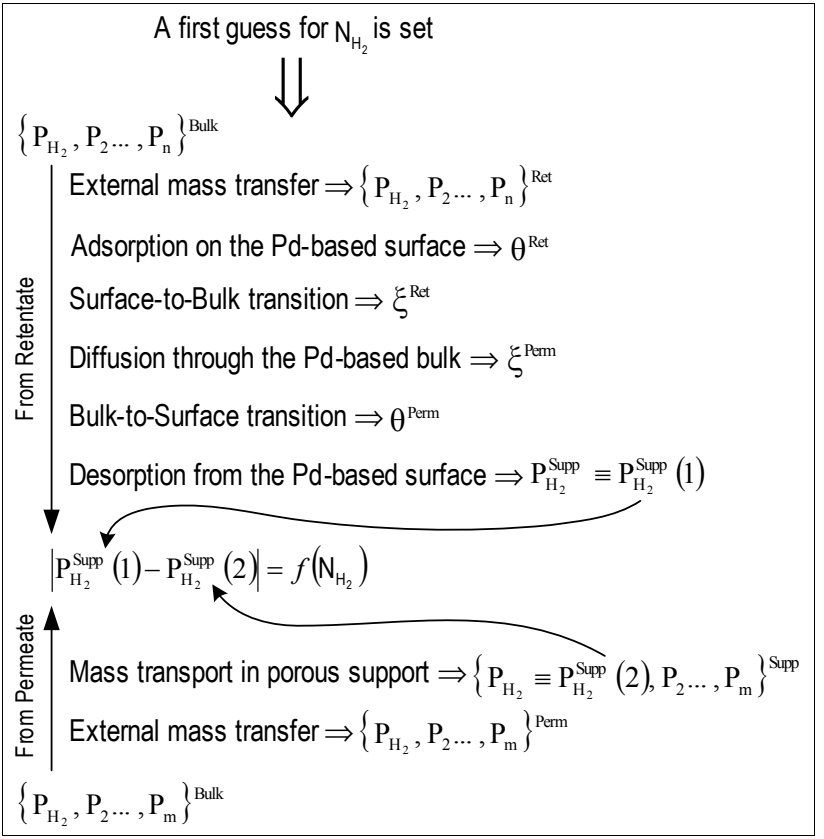

Figure 3.2 – Scheme of the strategy adopted for the numerical solution of the model.

The numerical solution was obtained by means of a home-made numerical procedure implemented in the program language Java 2®, dealing with post-processing using appropriate macros developed in Visual Basic 6®.

3.4 RESULTS AND DISCUSSION

The following tables report the operating conditions (Table 3.2), the geometrical parameters (Table 3.3) and physical and kinetic constants used in the simulation (Table 3.4).

Table 3.2 – Operating conditions considered in the simulation.

Side	Pressure, kPa							Reynolds' Number	Total flow rate, mmol/s
	H_2	N_2	O_2	CO_2	H_2O	CO	Total		
Feed	600	75	75	50	50	25	875	1700 - 800* 4600 - 2500**	100
Permeate	100	80	20	-	-	-	200	1900 - 950* 6400 - 3200**	20
Temperatures, °C = {250; 300; 350; 400; 500; 600}									

* Laminar regime. **Turbulent regime.

Table 3.3 – Geometrical data of the Pd-alloy supported membrane considered in the simulation.

Pd-alloy layer thickness, μm = {1, 10}				
Multilayered porous support				
Layer	Thickness, μm	Mean pore Diameter, nm	Porosity, -	Tortuosity, -
1*	1	5	0.5	1.2
2	50	100	0.5	1.2
3	100	1,000	0.5	1.2
4	500	10,000	0.5	1.2
5	850	50,000	0.5	1.2
Total	≅ 1.5 mm	-	-	-

* In contact with the Pd-alloy surface

Table 3.4 – Physical and kinetic constants of the model. Data taken from open literature.

$\Delta E_{Adsorption}$ [J mol^{-1}]	83,680 [3.16]	K_w [-]	0.05 [3.1]
$E_{Desorption}$ [J mol^{-1}]	41,840 [3.16]	$E_{BulkToSurface}$ [J mol^{-1}]	22,175 [3.1]
$K^0_{Desorption}$ [s^{-1}]	4.80 10^{17} [3.16]	D^0_{H} [m^2 s^{-1}]	2.90 10^{-7} [3.19]
$E_{Diffusion}$ [J mol^{-1}]	22,175 [3.19]	Υ [Pa]	1.84 10^{11} [3.17]
$\mathrm{W_{HH}}$ [J mol^{-1}]	-23,400 [3.1]	S_0 [-]	1 [3.16]
Γ_{j0} [s^{-1}]	2.30 10^{13} [3.1]	$\Delta E_{SurfaceToBulk}$ [J mol^{-1}]	16,736 [3.1]
N_b [mol$_{Pd}$ m^{-3}]	1.13 10^5 [3.1]	$\overline{\mathrm{V}}_{\mathrm{H}}$ [m^3 mol^{-1}]	1.77 10^{-6} [3.17]
N_s [mol$_{Pd}$ m^{-2}]	2.80 10^{-5} [3.1]	w [J mol^{-1}]	2,092 [3.1]

In this section two cases will be examined: permeation in laminar (Section 3.4.1) and turbulent (Section 3.4.2) regime, respectively, in order to analyze the role of the external mass transfer in the permeation process. Then (Section 3.4.3) an overall comparison between both cases will be done.

3.4.1 LAMINAR FLOW CONDITIONS

Figure 3.3 shows the transmembrane hydrogen partial pressure profiles for all permeation steps at different temperatures for a palladium thickness of 1 μm. In this and other figures of this type virtual thicknesses are introduced in the graphical representation of the following steps: adsorption, desorption, surface-to-bulk and bulk-to-surface, in order to visualize the system behaviour. In fact, these phenomena are interfacial and do not take place in a layer, but on a surface.

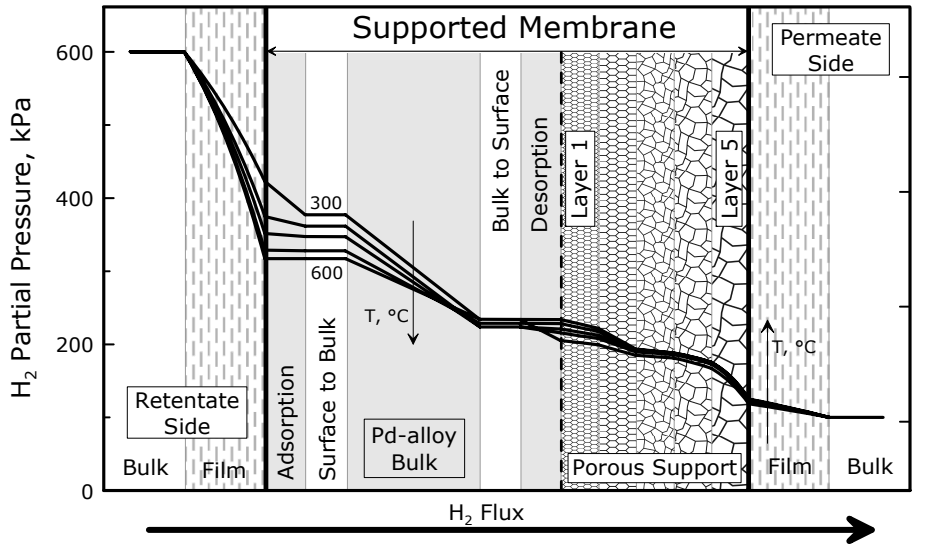

Figure 3.3 – Calculated hydrogen partial pressure profiles through the membrane and in the fluid phases adjacent to the membrane for different temperatures in laminar regime at $\delta^{Pd\text{-}layer}$ = 1 μm. The lengths of the permeation steps are not to scale. See Table 3.2 for the other operating conditions.

Thus, the lines connecting the initial and final pressure values of these virtual domains are not profiles, because only the boundary points have a physical meaning. In order to compare immediately the profiles inside the selective layer with the ones in the fluid phases (gaseous films and porous support), the surface coverage (on the surfaces) and atomic hydrogen concentration (in the Pd-based bulk) are expressed in terms of equivalent pressures. Furthermore, the domains of each permeation step are not drawn to scale to avoid visualization problems. Considering the case at 300°C, starting from the bulk on retentate side, a quite significant pressure drop is found for hydrogen profile in the upstream film. In the adsorption and desorption step the pressure drop is low but non-negligible, whilst both the transitions surface-to-bulk and bulk-to-surface do not show any appreciable contribution so that they could be considered at equilibrium. The diffusion in Pd-bulk and transport in porous support provide important pressure drops, especially when considering the first two porous layers, which show

important resistances even if their thicknesses are very thin (Table 3.3). The effect of external mass transfer is also appreciable in permeate side, even though not so as in retentate one. At higher temperatures, the mass transfer influence becomes more relevant in both gaseous film and in the support, whereas the surface phenomena (adsorption and desorption) and diffusion in the Pd-based layer got to be more rapid steps. Hence, in these conditions it is not possible to recognize only a unique rate determining step, because several elementary steps are able to affect the permeation. However, it is possible to notice that the mass transfer in film on retentate side and the one in support are slower than diffusion in the palladium, this effect being larger as higher temperatures are considered. This is due to the different nature of the processes. In fact, the diffusion in the Pd-based layer is an activated process and becomes more rapid as temperature increases.

On the contrary, the other two steps are non-activated and their resistance to mass transfer assumes progressively more importance. Analyzing the situation in the porous support, at temperatures higher than about 300°C, all the layers, even the ones with large mean pore diameters, offer little but non-negligible pressure drops. The reasons why the polarization in the film on retentate side and in the support is very strong in these conditions are to be searched in the very little Pd-based layer thickness used (1 μm), which makes the diffusion in the metal bulk very rapid (low resistance).

In order to identify the rate-determining steps and quantify their influence on the permeation rate, in Figure 3.4 the relative resistance of each permeation step and the normalized overall resistance are shown as functions of temperature in the same conditions of Figure 3.3. The definition of these resistances is provided in Appendix B (Section 3.7.2), where the temperature reference value for the overall resistance is chosen to be 350°C. At low temperature the surface phenomena control the process, but their contributions rapidly decrease as the temperature increases. At about 280°C, surface phenomena, diffusion in the palladium, film on retentate side and support provide comparable contributions in terms of resistance and it is not possible to recognize only one rate determining step.

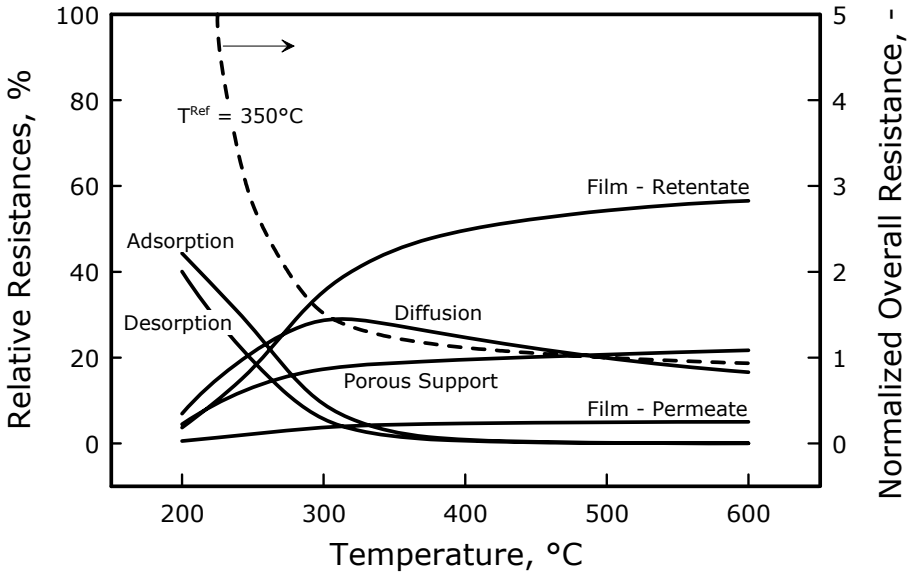

Figure 3.4 – Relative resistance of each permeation elementary step as a function of temperature in laminar flow conditions (see Table 3.2). $\delta^{Pd\text{-}layer}$ = 1 μm. The non-reported steps do not provide any appreciable contribution.

Considering higher temperatures (300-600°C), the contribution of mass transfer in the film on retentate side and in the support increases, providing contributions of about 50-60% and 20-25%, respectively, whilst the diffusion in metallic bulk becomes more rapid. Again, the three contributions are comparable and it is necessary to consider all of them in a permeation law. As concerns the normalized overall resistance, its profile is an indication of the fact than the hydrogen partial pressure drop increases significantly up to about 400°C, the differences becoming negligible when considering higher temperatures. For analyzing the effect of the Pd-based layer thickness on the rate-determining steps, in Figure 3.5 the same situation as Figure 3.3 is shown, but with a Pd-based layer thickness of 10 μm. The difference with the previous case is significant. In fact, the diffusion in metallic bulk shows a more important influence than before, because the resistance provided by the Pd-based layer is larger.

Obviously, this affects the relative importance of the transport in films and in support, which provide less resistance than before. From the figure, it possible to notice that the polarization in the film on retentate side is influenced by the Pd-layer thickness much more than the one in the support and in the permeate side.

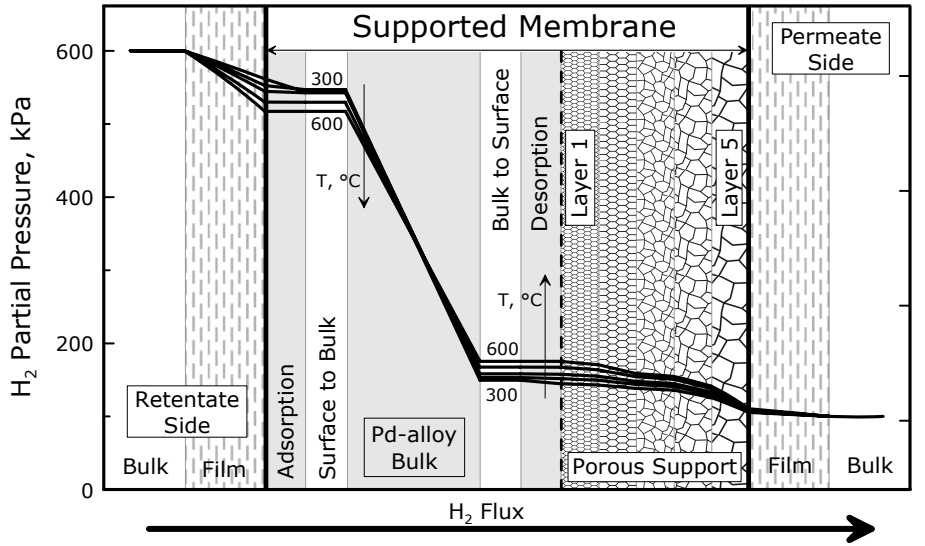

Figure 3.5 – Calculated hydrogen partial pressure profiles through the membrane and in the fluid phases adjacent to the membrane for different temperatures in laminar regime at $\delta^{Pd\text{-}layer}$ = 10 μm. The lengths of the permeation steps are not to scale. See Table 3.2 for the other operating conditions.

This effect is due to lower permeating flux and to the relative position of the resistances with respect to the flux direction. In this case, the use of the original Sieverts' law provides an error surely less than before, since the diffusion in the Pd-based layer is very slow in comparison to the other steps. This situation is more clearly shown in Figure 3.6, where in the range 300-600°C the diffusion provides a relative resistance of about 70-80%, whilst the sum of the resistance in support and in film on retentate side is about 20-25%. The normalized overall

resistance is here more sloped at high temperature than before, this indicating that the permeation process is more controlled by activated processes than in the case of 1 μm.

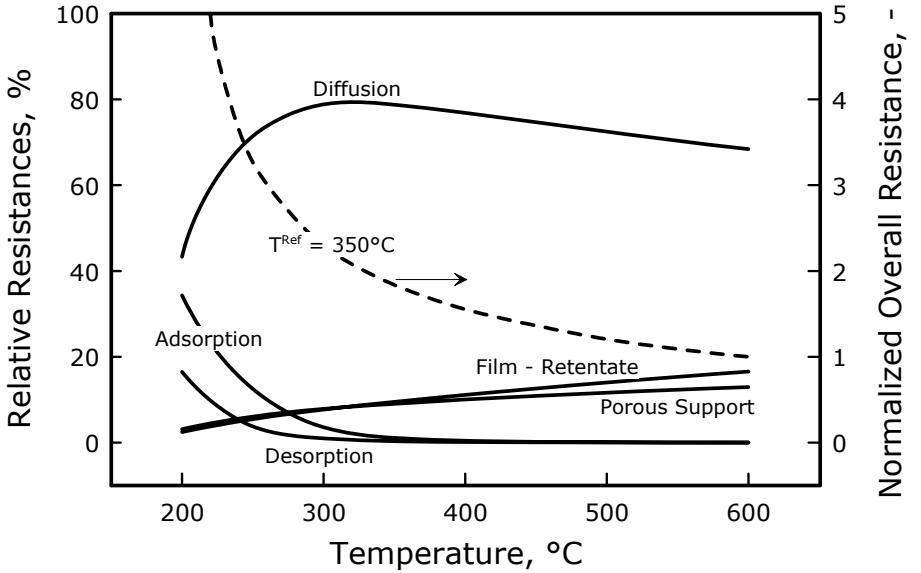

Figure 3.6 – Relative resistance of each permeation elementary step as a function of temperature in laminar flow conditions (see Table 3.2). $\delta^{Pd\text{-}layer}$ = 10 μm. The non-reported steps do not provide any appreciable contribution.

3.4.2 TURBULENT FLOW CONDITIONS

Once the permeation has been analyzed considering laminar regimes for both up- and downstream, the same system is studied in turbulent conditions. This change in fluid-dynamic conditions reflects directly on the external transport in films, but also affects indirectly the other permeation steps. Except for the flow regime, the figures presented in this section are obtained in the same operating conditions as their respective ones in the previous section. Figure 3.7 shows the transmembrane hydrogen partial pressure profiles calculated at different temperatures for a Pd-alloy thickness of 1 μm in turbulent regime case. The first thing to

highlight is that, on the contrary of what seen in the previous section, the pressure drop related to the transport in the films – especially the one on the retentate side – can be neglected with respect to the other permeation steps, owing to the fact that the mass transfer is made more rapid by the improved fluid-dynamic conditions. At about 300°C, the pressure drop in the adsorption and desorption steps is low but not negligible.

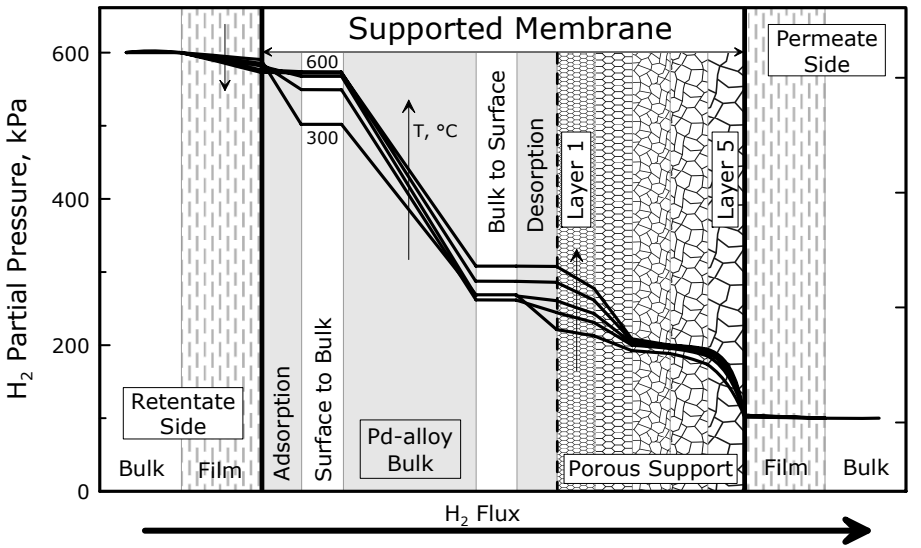

Figure 3.7 – Calculated hydrogen partial pressure profiles through the membrane and in the fluid phases adjacent to the membrane for different temperatures in turbulent regime at $\delta^{Pd\text{-}layer}$ = 1 μm. The lengths of the permeation steps are not to scale. See Table 3.2 for the other operating conditions.

The largest resistance is concentrated in the Pd-alloy layer and in multilayered porous support, where the layers 5, 4, 2 and 1 provide the most of resistance. The importance of the support is more significant at higher temperature (~500°C) and even the presence of the thinnest support layers has an appreciable influence on the permeation. At higher temperatures, the rate of the surface phenomena increases and their slopes decrease, whereas the transport resistance is concentrated in the Pd-alloy layer and in the support. In this case, the increase of the pressure

drop in the support – especially in the first layers – is relevant and is due to the Knudsen mechanism, which exceeds the other two diffusional mechanisms considered in the support (Poiseuille and ordinary diffusion). The mass transfer in the external films is rapid and provides an appreciable effect only in the film on retentate side.

Similarly to what done in the previous section, Figure 3.8 shows the relative resistances of each step and the normalized overall resistance of the whole membrane determined in the same conditions as Figure 3.7. In particular, the importance of the porous support is clear, since it provides a relevant increasing contribution from about 250°C onwards. This occurs since the transport in the pores is a non-activated process, which is not favoured by the temperature increase.

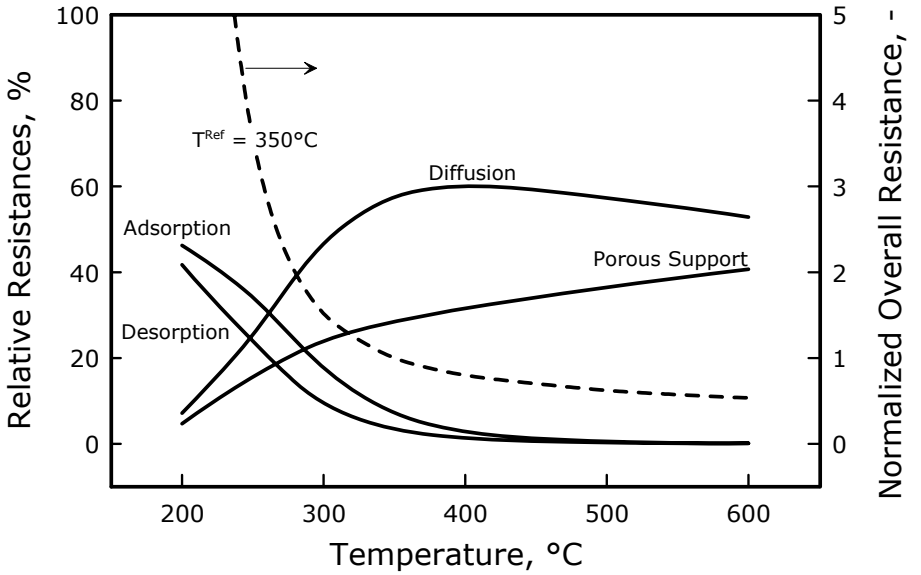

Figure 3.8 – Relative resistance of each permeation elementary step as a function of temperature in turbulent flow conditions (see Table 3.2). $\delta^{Pd\text{-}layer}$ = 1 μm. The non-reported steps do not provide any appreciable contribution.

At 300-320°C the situation is quite complex and it is not possible to recognize only one rate-determining step, since there are four steps controlling the process, whereas at high temperatures (> 350°C ca.), only diffusion in the Pd-layer and transport in the support limit the permeation. The normalized overall resistance decreases very weakly from 400°C onwards, since there is a shift from the controlling steps characterized by high activation energies (the surface phenomena) to non-activated ones (transport in the support) or ones having lower activation energy (the diffusion in the Pd-layer). At low temperature (< 250°C ca.) the surface phenomena control the process with a small contribution from the diffusion in the Pd-layer and less from the support. As seen for the laminar case, when a higher Pd-layer thickness (10 μm) is considered (Figure 3.9), a very different situation is found. In fact, at higher temperatures, the diffusion in the palladium influences the process much more than at 1 μm, because the resistance provided by the Pd-alloy layer is larger.

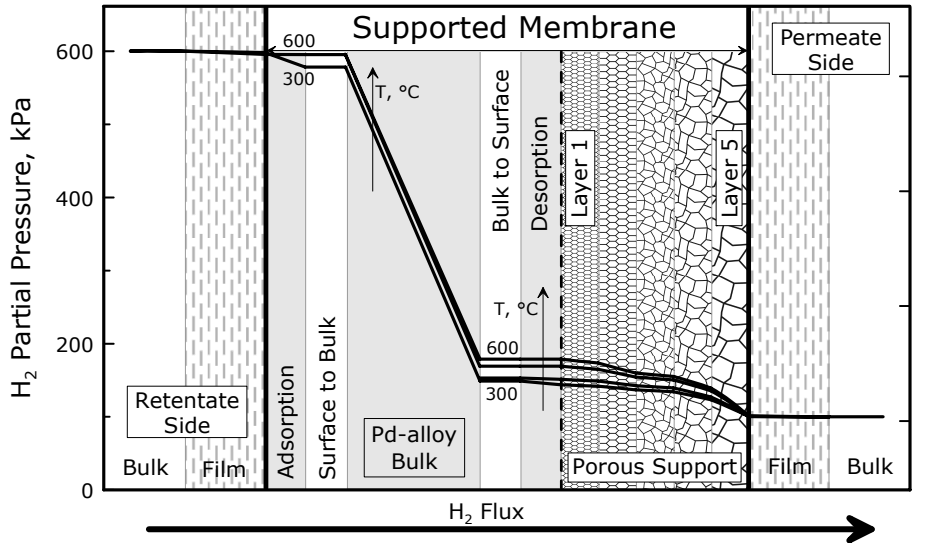

Figure 3.9 – Calculated hydrogen partial pressure profiles through the membrane and in the fluid phases adjacent to the membrane for different temperatures in turbulent regime at $\delta^{Pd\text{-}layer}$ = 10 μm. The lengths of the permeation steps are not to scale. See Table 3.2 for the other operating conditions.

For the same reason, the influence of the diffusion in the Pd-alloy cannot be neglected neither at low temperatures (200-250°C). In this case, the influence of the film on the retentate side is negligible even at high temperatures, and the pressure profiles in the support do not show such a large slope as before. Analyzing the relative resistances of each elementary steps and the normalized overall resistance in Figure 3.10, it is found that the decreasing rate of the normalized overall resistance is larger than before.

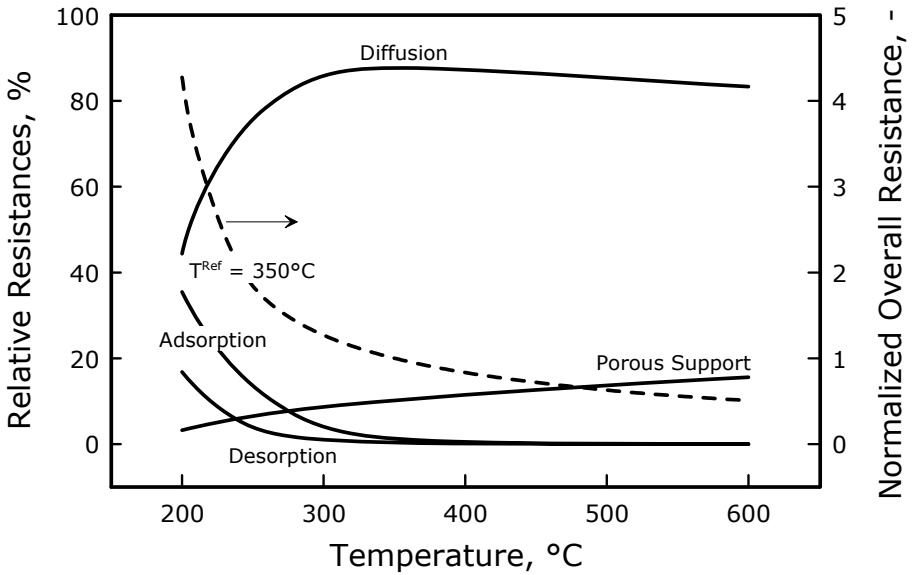

Figure 3.10 – Relative resistance of each permeation elementary step as a function of temperature in turbulent flow conditions (see Table 3.2). $\delta^{Pd\text{-}layer}$ = 10 μm. The non-reported steps do not provide any appreciable contribution.

The relative resistance of the support is much lower than before in the whole temperature range considered, arriving at a value of about 20% at 350°C, against 80% ca. of that of the Pd-based layer. Thus, the influence of the support is less relevant than before, but cannot be neglected. Only whenever higher Pd-based layer thicknesses are considered, the influence of

the support can be ignored. Anyway, the high-performance membranes are those characterized by a very thin Pd-based layer and, thus, they represent the objects of this study.

3.4.3 LAMINAR VS. TURBULENT REGIME

At this point, let us analyze the difference in performance between the two flow regimes in terms of the most important quantity characterizing a membrane: the permeating flux. In this direction, this quantity is shown in Figure 3.11 as function of temperature.

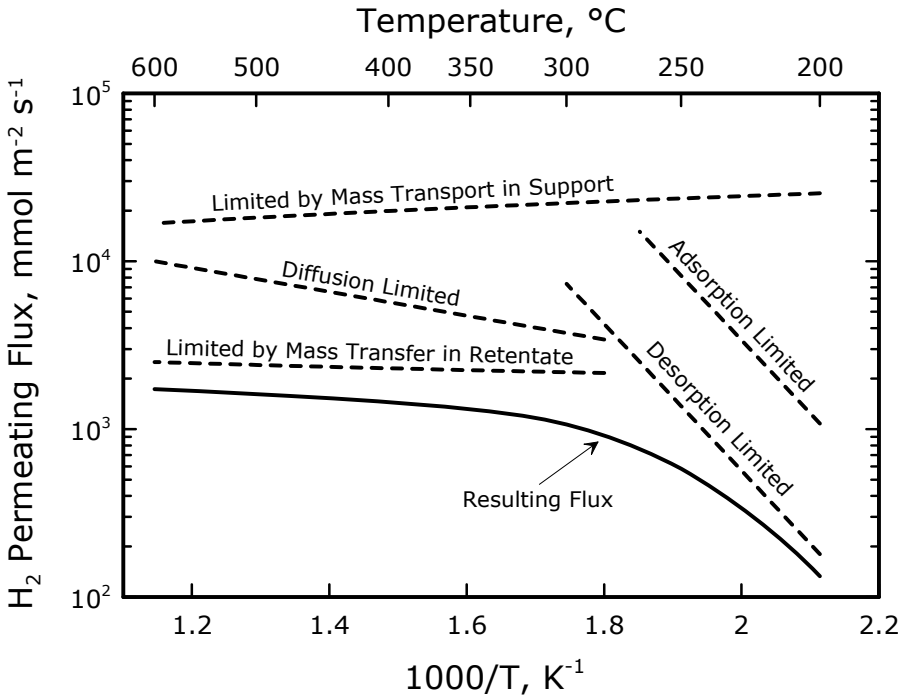

Figure 3.11 - Step-limited fluxes (dashed lines) and overall resulting flux (continuous line) as functions of temperature in laminar conditions. $\delta^{Pd\text{-}layer}$ = 1 μm. The fluxes corresponding to the non-reported steps are very high and, thus, are not shown. See Table 3.2 for the other operating conditions.

In this figures the overall resulting flux (the actual flux) is plotted together with the step-limited fluxes (dashed-line), each of which is calculated considering a certain step as the only rate-determining one and all the others at the equilibrium. Hence, they consider each time the effect of only one step, whilst the overall resulting flux takes into account the influence of all the steps. In particular, the upper curves correspond to more rapid steps that the downer ones. However, the influence of the steps is not directly related to their distance from the overall resulting flux. Examining the details of the figure, among the activated processes, the adsorption and desorption steps have a decreasing slope larger than diffusion, but obviously in both cases the temperature has a positive effect on the flux. The slopes relative to these steps are proportional to their respective activation energies. On the contrary, the curve of the transport in the film on the retentate side is almost flat, whereas the one relative to the transport in the support has even an increasing profile. This means that this last step is not favoured by the temperature and, hence, that Knudsen-wise transport prevails on the Poiseuille-wise one and on ordinary diffusion, the Knudsen diffusivity decreasing with temperature. Anyway, the mass transport in the fluid films and the one in the support are not activated processes and, hence, are characterized by a non-linear behaviour in this type of plots.

In figures like Figure 3.11, the effect of each permeation step on the overall resulting flux can be evaluated by looking its slope, since the overall flux tends to assume point-by-point the same slope as the controlling steps. For example, at temperatures higher than about 350°C, the permeation is mostly influenced by the external mass transfer in the film on retentate and, thus, the slope of the resulting flux tends to be similar to the one of the flux limited by the external mass transfer. Analogously, at low temperatures (< 250°C ca.) the surface phenomena limit the process and, hence, the slope of the resulting flux is more similar to the one of adsorption and desorption (equal). It is important to highlight that in this case the flux limited by the mass transfer is located downer than the one limited by the diffusion and by the transport in the support. The situation is completely different when considering Figure 3.12, where, thanks to more favourable fluid-dynamic conditions due to turbulent flow regime, the flux limited by the external mass transfer is higher than the others. This is a clear indication that

at high enough temperature (350°C ca.) the resulting flux is mostly affected by transport in the support and by diffusion in the Pd-based layer. Since, as seen before (Figure 3.8), the influence of the second step is more significant than that of the first one, the slope of the resulting flux is more similar to the one of the corresponding diffusion-limited curve, even though at higher temperatures (> 400°C ca.), its slope tends to be similar to the one of the support-limited flux.

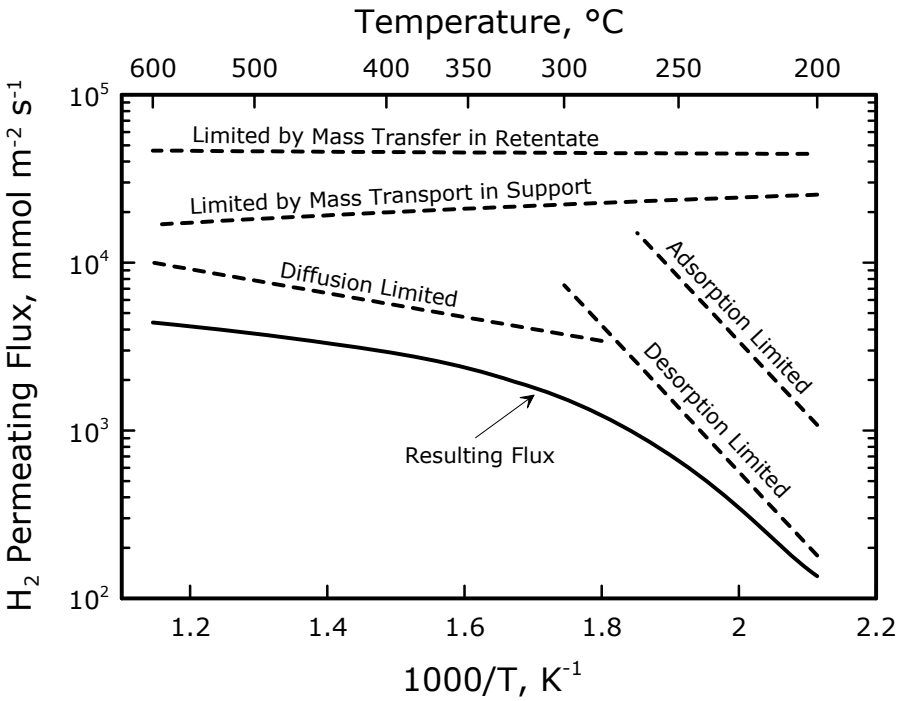

Figure 3.12 – Step-limited fluxes (dashed lines) and overall resulting flux (continuous line) as functions of temperature in turbulent conditions. $\delta^{Pd\text{-}layer}$ = 1 μm. The fluxes corresponding to the non-reported steps are very high and, thus, are not shown. See Table 3.2 for the other operating conditions.

Similarly, in the temperature range of 200-350°C, the transition from the surface phenomena-limited flux to the diffusion-limited one is characterized by a significant slope change. It has to

be underlined that in this figure the other step-limited fluxes remains so as seen before, since they are not affected by external mass transfer, being considered at equilibrium. In order to make a direct comparison between all the cases examine up to this point, in Figure 3.13 the hydrogen flux is shown as function of temperature for the two flow regimes and Pd-based thicknesses considered (1 and 10 μm).

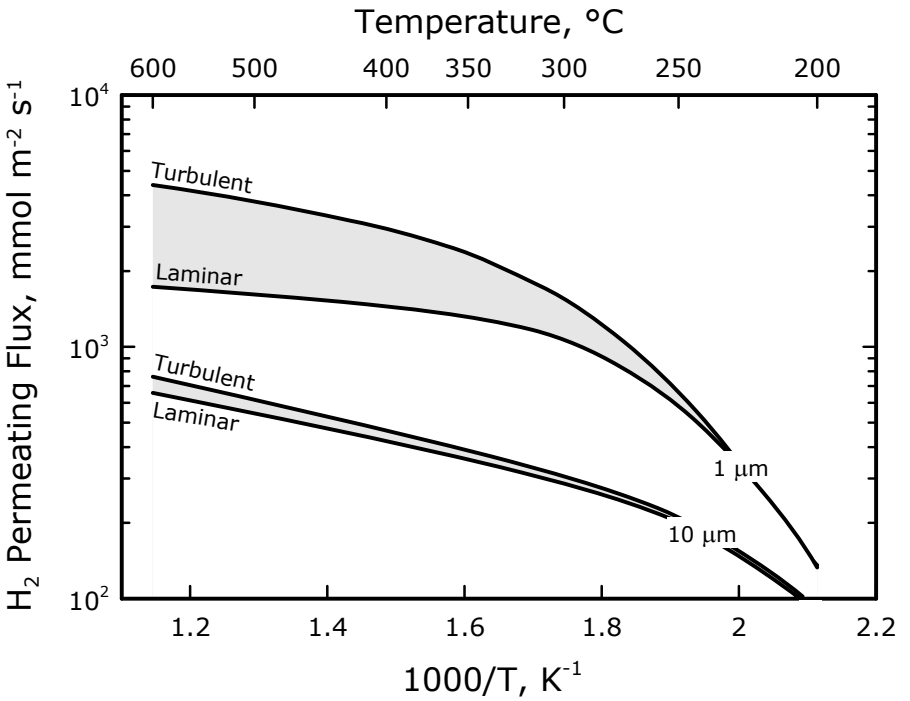

Figure 3.13 – Hydrogen flux as a function of temperature for two Pd-based thicknesses and flow regimes. See Table 3.2 for the other operating conditions.

Looking at 1 μm case, the significant difference between laminar and turbulent regime is remarkable, especially at high temperature, where it has been shown that the influence of mass transfer in laminar conditions is higher. When considering lower temperatures, this

difference becomes less, other limiting steps taking the place of external mass transfer. The gap between laminar and turbulent flow decreases significantly as a thicker Pd-layer (10 μm) is considered, since the diffusion in the metallic bulk is predominant with respect the other steps and, hence, the relative importance of the external mass transfer become smaller. All these considerations have demonstrated that this model is very useful for evaluating and predicting the membrane behaviour in those conditions in which it is not possible to recognize only one rate determining step (the most common situation). Now, in the next section, this model will be applied to actual cases in order to provide a validation of the whole analysis.

3.5 COMPARISON WITH LITERATURE

3.5.1 COMPARISON WITH WARD AND DAO'S SIMULATION

The comparison is made in the same operating conditions used by Ward and Dao [3.1] (see Table 3.5) in presence of external mass transfer resistance only on permeate side (Figure 3.14). Without the external mass transfer (absence of polarization) and in these conditions, the two approaches lead up to very similar results, as demonstrated in Section 3.2.4. The difference is very small in the whole temperature range considered for $\delta^{Pd\text{-}Layer}$ of 100 μm, because the transport in the Pd-bulk limits the process. For thinner membranes, the effect of the external mass transfer is stronger, thus the behaviour of the two models becomes increasingly different.

Table 3.5 – Operating conditions considered by Ward and Dao [3.1] in their simulations.

Side	Pressure, kPa		Reynolds' number
	H_2	N_2	
Retentate	101.3	-	Not influent
Permeate	0	101.3	≅ 10
No support, T = [100, ..., 800]°C, $\delta^{Membrane}$ = [1, 10, 100] μm			

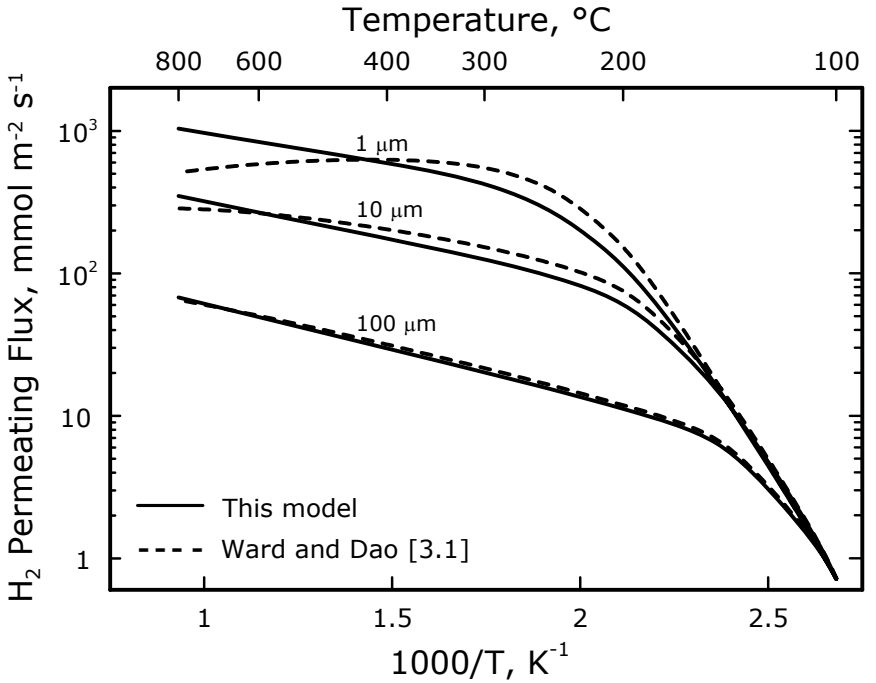

Figure 3.14 – Comparison between the simulation results of the present model and those obtained by Ward and Dao in the same operating conditions (see Table 3.5).

The most important difference is that in Ward and Dao's simulation there is a maximum value in the profiles at 1 and 10 μm, whilst in present analysis the profile continuously increases with the temperature. This difference is due to the constant value of mass transfer coefficient considered by Ward and Dao [3.1], a condition removed in the present approach. Their expression for external mass transfer in the permeate side is given by Eq. 3.38 (in terms of concentration) and 3.39 (in terms of pressures), this last one being achieved by using the ideal gas law. As a consequence, their model establishes that in the case in which the external mass transfer is the rate-determining step, the permeating flux is inversely proportional to the temperature (decreasing profile).

$$J_{H_2} = Kc\left(C_{H_2}^{Surface} - C_{H_2}^{Bulk}\right)\Big|^{Permeate\ Side} \tag{3.38}$$

$$J_{H_2} = \frac{Kc}{RT}\left(P_{H_2}^{Surface} - P_{H_2}^{Bulk}\right)\Big|^{Permeate\ Side} \tag{3.39}$$

This behaviour – flux decreasing with temperature – does not seem to have a physical justification for auto-supported membranes. On the contrary, the present model provides a monotonic behaviour as a result, because the dependence of the mass transfer matrix on temperature and pressure was taken into account. A flux decreasing with temperature can be found only when a porous support is considered and at the same time the influence of the Knudsen diffusion in the porous support is much larger than the other diffusion mechanisms.

3.5.2 MODEL VALIDATION

In Figure 3.15, the results of the model are compared with some experimental data from the literature relative to supported Pd-based membranes in different operating conditions. In particular, the comparison was made with appropriate literature data from:

1) Dittmeyer *et al.* [3.4], who measured hydrogen flux as a function of the temperature for several feed pure hydrogen pressures.
2) Liang and Hughes [3.3], for taking into account the behaviour of the model at changing sweep-gas flow rate.

The tortuosity and porosity (not specified in the two papers considered), are set as 1.2 and 0.4, respectively. Figure 3.15 shows good agreement with experimental data taken from different sources. In particular, it can be noticed in the second plot (Liang and Hughes [3.3]) that the permeating flux increases with the sweep rate only from 0 to ca. 0.5 mmol s^{-1}, whereas remains at an almost constant value (about 55 mmol m^{-2} s^{-1}) for higher sweep rates. This occurs because an increase of the sweep rate in the permeate side produces a decrease of the hydrogen partial pressure, reaching negligible values for very high sweep rate.

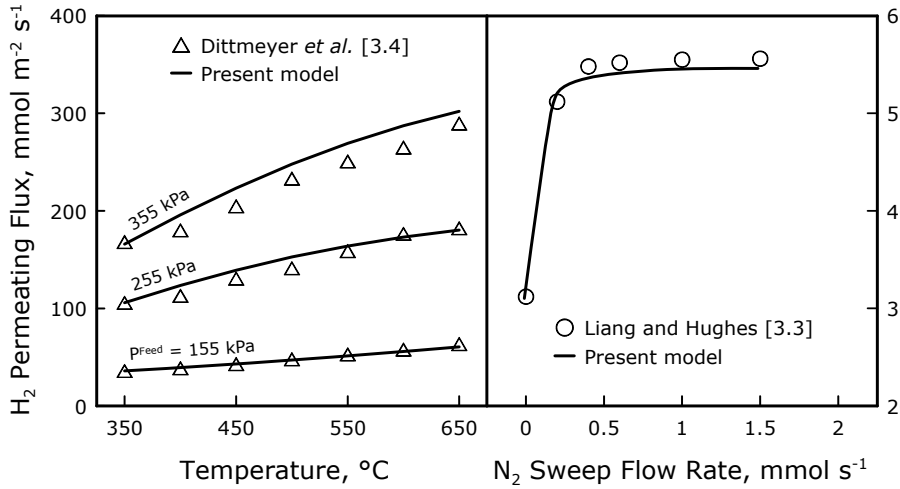

Figure 3.15 – Comparison with some literature experimental data. The values of kinetic parameters used for simulation are that reported in Table 3.4.

In their experimental analysis, Dittmeyer *et al.* [3.4] found that the membrane behaviour did not follow the original Sieverts' law. In order to investigate about the reasons for this discrepancy, the relative resistances of the permeation steps in their membrane were calculated by means of the present model, whose results are reported in Figure 3.16. The only relevant contributions are those of the diffusion in the Pd-based layer and the transport in the support. This means that, as in the present model, the explanation for the difference from the original Sieverts' law is due to the presence of the support, whose resistance increases with the temperature. This type of evaluation is an example of the applicability of the present model to actual experimental cases. Since these evaluations cannot be made by the Ward and Dao's model [3.1] (where no support is considered), this model represents a new tool to carry out the correct interpretation of the data analysis for the supported Pd-based membranes. However, it must be underlined that not all the Pd-alloy membranes have the same kinetic parameters, since the physical and chemical membrane properties strictly depend on the preparation method.

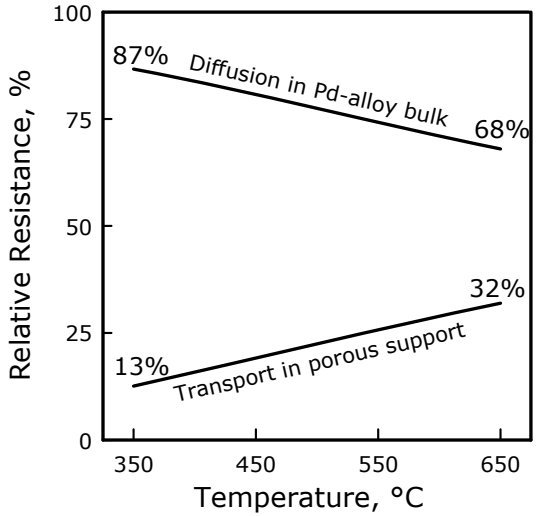

Figure 3.16 – Resistances of permeation steps calculated by the present model for the experimental system of Dittmeyer *et al.* [3.4]. P^{Feed} = 255 kPa. The non-reported steps do not provide any appreciable contribution.

Thus, the general procedure for applying the present model to actual cases consists in obtaining the necessary kinetic and transport parameters from experimental data in terms of permeance (pure hydrogen test), using them to predict the membrane behaviour in different conditions of interest.

3.6 CONCLUSIONS

The hydrogen permeation through supported Pd-alloy membranes was described by means of a detailed model, which involves several elementary steps: multicomponent mass transfer in the fluid phases adjacent to the membrane sides, transport in a multilayered porous support, surface phenomena (adsorption and desorption), dissolution from the Pd-based surface into metal lattice and vice-versa ("surface-to-bulk" and "bulk-to- surface" transitions) and the diffusion through the Pd-based bulk. The model prediction shows a good agreement with the experimental literature data in a quite large range of operating conditions. The hydrogen partial

pressure profiles in the Pd-alloy thickness, in the porous support and in the adjacent gaseous films were calculated as functions of temperature and membrane thickness and fluid-dynamic conditions, evaluating the relative importance of each permeation elementary step and the hydrogen flux. The analysis shows that, for a membrane thickness of 1 μm, at temperatures included in the range of interest (350-500°C), the diffusion in the metallic bulk and the transport in the porous support are the rate determining steps. For a thicker membrane (10 μm), the diffusion in the Pd-alloy bulk is the rate determining step in the whole temperature range considered (relative resistance of ca. 85%).

The simulation based on the present model was also compared with that of Ward and Dao [3.1] (in terms of flux vs temperature) for self-supported membranes. The results of the present model showed that the hydrogen permeating flux is an increasing function of the temperature, whereas the model of Ward and Dao [3.1] establish the flux profiles to be non-monotone with temperature (owing to the use of constant mass transfer coefficients, removed in the present model). The results showed that the model developed here demonstrated its ability in quantifying the influence of each permeation step, especially the one of the multilayered porous support. Hence, it represents a powerful tool to improve the flux prediction and optimize the performance of a Pd-based membranes and, thus, of actual separation systems which the supported thin Pd-based membranes are involved in.

3.7 APPENDICES

3.7.1 APPENDIX A: CALCULATION OF THE PHYSICAL PROPERTIES

3.7.1.1 VISCOSITY OF SINGLE GAS

The viscosity of a single gaseous component is calculated by the kinetic theory of gas developed independently by Chapman and Enskog. For relatively low densities, Eq. 3.40 is valid. The collision integral Ω_μ is a function of the group kT/ε_i and its values are provided in form of tables [3.20]. However, for the calculations, the tabled values were transformed into a continuous function, adopting the functional expression indicated by Eq. 3.41. The values

calculated for the parameters {a_1…f_1} reported in the Table 3.6 provide a correlation coefficient practically equal to unity in the range kT/ε_i = {0.30…10}, which covers completely the target range for the Pd-based membrane operations (up to 800°C).

$$\eta_i = \beta_1 \frac{\sqrt{M_i T}}{\sigma_i^2 \Omega_\mu} \tag{3.40}$$

$$\Omega_\mu = \frac{a_1 \varsigma^3 + b_1 \varsigma^2 + c_1 \varsigma}{\varsigma^3 + d_1 \varsigma^2 + e_1 \varsigma + f_1}, \qquad \varsigma \equiv \frac{kT}{\varepsilon_i} \tag{3.41}$$

Table 3.6 – Correlation parameters for the calculation of Ω_μ and η_i.

β_1	a_1	b_1	c_1	d_1	e_1	f_1
2.67E-05	0.427	58.13	55.89	73.30	-4.765	2.754

3.7.1.2 VISCOSITY OF MIXTURE

For calculating the viscosity of a multicomponent gas mixture, the Wilke semi-empirical correlation [3.10] was used (Eq. 3.42-3.43).

$$\eta_{mix} = \sum_{i=1}^{N^{Species}} \frac{x_i \eta_i}{\sum_{j=1}^{n} x_j \Phi_{ij}} \tag{3.42}$$

$$\Phi_{ij} = \frac{1}{2\sqrt{2}} \left(1 + \frac{M_i}{M_j}\right)^{-0.5} \left[1 + \left(\frac{\eta_i}{\eta_j}\right)^{0.5} \left(\frac{M_j}{M_i}\right)^{0.25}\right]^2 \tag{3.43}$$

3.7.1.3 BINARY MIXTURE DIFFUSIVITIES

The binary mixture diffusivities were calculated by the relation shown in Eq. 3.44.

$$\mathfrak{D}_{ij} = \beta_2 \frac{T^{1.5}\left[\frac{1}{M_i}+\frac{1}{M_j}\right]^{0.5}}{P_{Total}\,\sigma_{ij}^2\,\Omega_d} \tag{3.44}$$

By analogy to the case of the viscosity calculation, a continuous expression for Ω_d was adopted (Eq. 3.45). The values for ε_{ij} σ_{ij} and can be obtained from those of pure compounds (Eq. 3.46) [3.10].

$$\Omega_d = \frac{a_2\varsigma^3 + b_2\varsigma^2 + c_2\varsigma}{d_2\varsigma^3 + e_2\varsigma^2 + f_2\varsigma + g_2}, \qquad \varsigma \equiv \frac{kT}{\varepsilon_{ij}} \tag{3.45}$$

$$\varepsilon_{ij} = \sqrt{\varepsilon_i \varepsilon_j}, \quad \sigma_{ij} = \frac{1}{2}\left(\sigma_i + \sigma_j\right) \tag{3.46}$$

Table 3.7 – Parameters of the correlation for Ω_μ and $\mathfrak{D}_{ij}$ calculation.

β_2	a_2	b_2	c_2	d_2	e_2	f_2
1.86E-03	0.404	36.30	35.79	49.29	-0.974	1.107

3.7.1.4 KNUDSEN DIFFUSIVITY

The Knudsen diffusivities (conventional and effective) are calculated by Eqs. 3.47 and 3.48, respectively.

$$D_i^{Knudsen} = 4850\,\bar{d}_{pore}\sqrt{\frac{T}{M_i}} \tag{3.47}$$

$$D_{i,effective}^{Knudsen} = D_i^{Knudsen} \frac{\varepsilon^{Support}}{\tau} \tag{3.48}$$

3.7.2 APPENDIX B: CALCULATION OF THE PERMEATION RELATIVE RESISTANCES

3.7.2.1 RELATIVE RESISTANCES OF THE ELEMENTARY STEPS

The relative resistance of each step was calculated by Eq. 3.49, where $\Delta P_{H_2}^{(j)}$ is the hydrogen partial pressure drop in the jth step and $\Delta P_{H_2}^{Total}$ is the hydrogen partial pressure drop between the retentate and permeate fluid bulks.

$$\text{Relative Resistance}\left(\text{j}^{\text{th}}\text{Step}\right) = \frac{\Delta P_{H_2}^{(j)}}{\Delta P_{H_2}^{Total}} \tag{3.49}$$

3.7.2.2 NORMALIZED OVERALL RESISTANCE

The overall resistance in membrane at a generic temperature T is the inverse of the permeance (Eq. 3.50).

$$Flux\big|_T = \pi\big|_T \Delta P = \frac{1}{R\big|_T} \Delta P \tag{3.50}$$

In order to compare the values at different temperatures, the overall resistance has been normalized with respect to its value calculated at T^{Ref}. Thus, Eq. 3.51 is obtained.

$$\text{Normalized Overall Resistance} = \frac{\text{Overall Resistance at } T}{\text{Overall Resistance at } T^{\text{Ref}}} = \frac{\text{Permeance at } T^{\text{Ref}}}{\text{Permeance at } T} \tag{3.51}$$

In this specific case a T^{Ref} of 350°C was chosen in the calculations.

3.8 LIST OF SYMBOLS

B_0	geometrical factor [m^2]
C	molar concentration, mol m^{-3}]
$d_{equivalent}$	equivalent diameter [m]
D_{H}	diffusion coefficient of atomic hydrogen in Pd-bulk [m^2 s^{-1}]
$\mathfrak{D}_{ij}$	binary diffusivity [m^2 s^{-1}]
D_{ij}	multicomponent diffusivity [m^2 s^{-1}]
$\overline{d}_{Pore}$	mean pore diameter in the support layers [m]
E	activation energy [J mol^{-1}]
$\Delta E_{Adsorption}$	heat of adsorption on the Pd-surface [J mol^{-1}]
$\Delta E_{SurfaceToBulk}$	heat of absorption in the Pd-bulk [J mol^{-1}]
$\mathrm{E}_{\mathrm{Young}}$	Young's modulus of palladium [Pa]
J_{H}	flux of atomic hydrogen [mol_H m^{-2} s^{-1}]
K	kinetic constant [m^2 mol_H^{-1} s^{-1}]
k	boltzmann constant [J $mole^{-1}$ K^{-1}]
Kc	mass transfer coefficient [m s^{-1}]
K_w	probability constant [-]
Γ_{H}	non-ideality correction factor [-]
Mw	molecular weight [kg mol^{-1}]
N	molar flux [mol m^{-2} s^{-1}]
N_b	octahedral sites concentration in Pd-bulk [mol_{Pd} m^{-3}]
N_S	superficial sites concentration on Pd-surface [mol_{Pd} m^{-2}]
P	pressure [Pa]
R	ideal gas constant = 8.31451 J mol^{-1} K^{-1}]
$Re = \frac{\rho v D_{eq}}{\eta}$	Reynolds' number [-]

$S(\theta)$	sticking coefficient [-]
S_0	clean sticking coefficient [-]
$Sc = \frac{\nu}{D_{12}}$	Schmidt number [-]
T	temperature [K]
$Sh = \frac{Kc}{\delta^{Film} D_{12}}$	Sherwood number [-]
$\overline{\mathrm{V}}_{\mathrm{H}}$	hydrogen partial molar volume in Pd-bulk [m^3 mol^{-1}]
w	pairwise Interaction energy [J mol^{-1}]
W_{HH}	interaction energy of two adjacent hydrogen atoms in the Pd-bulk [J mol^{-1}]
x	molar fraction [-]
$Y = \frac{\mathrm{E}_{\mathrm{Young}}}{1-\nu_P}$	stress parameter [Pa]
Z	high transport correction matrix [-]
Greek symbols	
Γ	molecular bombardment rate [mol m^{-2} s^{-1}]
Γ_{j0}	jump frequency [s^{-1}]
γ_{H}	hydrogen activity coefficient [-]
δ	thicknesses [m]
$\varepsilon^{Support}$	porosity of the support [-]
ε_i , σ_i , ε_{ij} , σ_{ij}	Lennard-Jones parameters: ε [K], σ [Å]
η	viscosity [Pa s]
μ_H	hydrogen chemical potential in palladium [J mol^{-1}]
$\nu = \frac{\eta}{\rho}$	cinematic viscosity [m^2 s^{-1}]
ν_P	Poisson's ratio [-]
θ	surface coverage [-]

θ_{HH}	probability of two adjacent filled sites [-]
θ_{OO}	probability of two adjacent empty sites [-]
π	permeance [mol m^{-2} s^{-1} Pa^{-n}]
ρ	density [kg m^{-3}]
σ	hydrostatic pressure in the metal lattice [Pa]
τ	tortuosity [-]
ξ	atomic hydrogen concentration [mol_H mol_{Pd}]
Ω	collision integrals [-]

3.9 LITERATURE CITED

[3.1] Ward T. and Dao T., 1999. Model of hydrogen permeation behaviour in palladium membranes. *Journal of Membrane Science*, **153**: 211-231.

[3.2] King D.A. and Wells M.G., 1974. Reaction Mechanism in chemisorption kinetics: nitrogen on the {1 0 0} plane of tungsten. *Proceedings of the Royal Society of London, Series A,* **339**: 245.

[3.3] Liang W. and Hughes R., 2005. The effect of diffusion direction on the permeation rate of hydrogen in palladium composite membranes. *Chemical Engineering Journal,* **112**: 81-86.

[3.4] Dittmeyer R., Hollein V. and Daud K., 2001. Membrane reactors for hydrogenation and dehydrogenation processes based on supported palladium. *Journal of Molecular Catalysis A: Chemical,* **173**: 135-184.

[3.5] Gielens F.C., Tong H.D., Vorstman M.A.G. and Keurentjes J.T.F., 2007. Measurement and modeling of hydrogen transport through high-flux Pd membranes. *Journal of Membrane Science*, **289**: 15-25.

[3.6] Guazzone F., Engwall E.E. and Ma Y.H., 2006. Effects of surface activity, defects and mass transfer on hydrogen permeance. *Catalysis Today*, **118**: 24-31.

[3.7] Tong J. and Matsumura Y., 2004. Thin Pd membrane prepared on macroporous stainless steel tube filter by an in-situ multi-dimensional plating mechanism. *Chemical Communications*, **21**: 2460-2461.

[3.8] Tong J., Su L., Haraya K. and Suda H., 2006. Thin and defect-free Pd-based composite membrane without any interlayer and substrate penetration by a combined organic and inorganic process. *Chemical Communications*, **10**: 1142-1144.

[3.9] Höllein V., Thornton M., Quicker P. and Dittmeyer R., 2001. Preparation and characterization of

palladium composite membranes for hydrogen removal in hydrocarbon dehydrogenation membrane reactors. *Catalysis Today*, **67**: 33-42.

[3.10] Bird R.B., Stewart W.E. and Lightfoot E.N., 1960. *Transport Phenomena,* J. Wiley & Sons Inc.

[3.11] Toor H.L., 1964. Solution of the linearized equations of multicomponent mass transfer. *American Institute of Chemical Engineering Journals*, **10**: 460-465.

[3.12] Stewart W.E. and Prober R., 1964. Matrix Calculation of Multicomponent Mass Transfer in Isothermal Systems. *Industrial and Engineering Chemistry, Fundamentals*, **3**: 224-235.

[3.13] Krishna R. and Taylor R., 1993. *Multicomponent Mass Transfer.* Wiley & Sons.

[3.14] Alopaeus V. and Nordèn H. V., 1999. A calculation method for multicomponent mass transfer coefficient correlations. *Computers & Chemical Engineering*, **23**: 1177-1182.

[3.15] Cussler E.L., 1997. *Diffusion – Mass Transfer in Fluid Systems.* Cambridge University Press, Cambridge, UK. pp 226-227.

[3.16] Behm R.J., Christmann K. and Ertl G., 1980. Adsorption of hydrogen on Pd (1 0 0). *Surface Science*, **99**: 320.

[3.17] Adrover A., Giona M., Capobianco L., Tripodi P. and Violante V., 2003. Stress-induced diffusion of hydrogen in metallic membranes: cylindrical vs. planar formulation. I. *Journals of Alloys and Compounds*, **358**: 268-280.

[3.18] Krishna R., 1987. Diffusion in Multicomponent Electrolyte Systems. *Chemical Engineering Journal*, **35**: 19-24.

[3.19] Holleck G.L., 1970. Diffusion and solubility of hydrogen in palladium and palladium-silver alloys. *The Journal of Physical Chemistry*, **74**: 503.

[3.20] Hirschfelder J.O., Bird R.B. and Spotz E.L., 1949. *Chemical Reviews*, **44**: 205.

CHAPTER 4

CONCENTRATION POLARIZATION IN SELF-SUPPORTED PD-BASED MEMBRANES*

*Some contents of this chapter have been already submitted for publication [6.3].

4.1 INTRODUCTION

Since the last decades, the hydrogen production from industrial processes like hydrocarbons oxidation, steam reforming and water gas shift, has been continuously increasing and is estimated to increase in the future. This is one of the main reasons why hydrogen could represent a good candidate to be used as energy carrier [4.1, 4.2]. Furthermore, high purity hydrogen could have concrete applications for the civil and/or military [4.3] transport in Proton Exchange Membrane Fuel Cells (PEM-FC), which provide an energetic efficiency much higher than the traditional engines with a very low impact on the environment in terms of pollution. As seen in the previous chapter, the Pd-based membranes can be very useful to be adopted in hydrogen purification process and several Pd-alloys have been used to improve the characteristics of the selective layer. In particular, the addition of other metals (e.g. Ag) can strongly limit the embrittlement of the material caused by the hydrogen permeation in the metallic lattice, as well as can provide a good resistance against the chemical species causing poisoning/inhibition phenomena on the metal surface – the Pd-Cu membranes are quite resistant to the contamination of S-, Cl- and Hg-based compounds, especially of H_2S [4.4]. Moreover, the techniques to make very thin selective Pd-based layers have been improving continuously. For example, some researchers in their recent works [4.5-4.7] were able to make Pd-membranes having thicknesses from 1.2 to 5 μm ca., showing very high performances in terms of permeating flux, although in these last cases the influence of the concentration polarization was found to be relevant, as shown in detail in previous chapter. Let us recall that the concentration polarization occurs in principle in all membrane-based separation processes because of the perm-selectivity of the same membrane. This phenomenon consists in a reduction of the transmembrane driving force of the most permeable species, due to the presence of the least permeable ones, which reduce in this way the overall process performance. Historically speaking, the first field where the concentration polarization was well analyzed was the liquid separation membrane processes, such as ultra-filtration and reverse osmosis, for which its causes and effects have been massively studied since the 1960s [4.8]. On the contrary, concerning the gas separation, in the same period it had been generally

accepted the polarization to have only a negligible effect on the membrane performance because of the low permeating flux and, at the same time, of the gas diffusivities, 4-5 order of magnitude higher that those of the liquids [4.8]. However, the progresses obtained in the last three decades in the field of membrane preparation for gas separation allowed to increase significantly the trans-membrane flux of the key-species to separate, decreasing in this way the influence of the selective layer resistance. When this situation occurs, the external mass transfer can affect seriously the membrane performances up to become one of the slowest elementary steps which the whole permeation process is composed of. In this case, concerning Pd-alloy membranes, the Sieverts' law (valid just in case of intra-lattice hydrogen diffusion to be the only rate-determining step) cannot be used for modelling the hydrogen permeation, as shown in the previous chapter and elsewhere [4.9,4.10].

In the field of gas separation, several studies have been carried out in order to quantify the influence of the concentration polarization at different operating conditions. Lüdtke *et al.* [4.11] considered the effect of the concentration polarization on the separation of n-butane/nitrogen in a composite (three layers) polymeric membrane. They found that the relative resistance in the boundary layer is significant as much as to exceed that in the membrane at a high enough feed total pressure. He *et al.* [4.8] used a binary mixture-based film model to carry out a theoretical analysis on the concentration polarization in a generic membrane. They defined a concentration polarization coefficient for both the two species involved in the separation as the ratio of the actual flux to the ideal one (without polarization), quantifying the polarization effect by means of the ratio of the actual fluxes of the components. Although this is a simplified approach, which cannot be generalized to multicomponent systems, nevertheless, in some operating conditions, the authors predicted an important influence of the external mass transfer on the process. A phenomenon apart, marginally related to the concentration polarization, is represented by the permeation inhibition due to carbon monoxide, affecting more or less all the Pd-alloy membranes. The effect of this factor was object of study of several researchers. In particular, Hara *et al.* [4.12] analyzed theoretically and experimentally the effect of the polarization in presence of CO in a Pd-membrane reactor where water gas shift reaction was

carried out, highlighting the decrease in performances due to the hydrogen radial gradients. More recently, Barbieri *et al.* [4.13] investigated the decrease of the Pd-based membrane permeance due to the presence of carbon monoxide in the upstream mixture, putting in evidence that its actual effect is a reduced permeance due to a decrease of the metal surface suitable for the H_2 dissociative adsorption. Many other researchers used complex 3D-models to study specific systems involving Pd-based membranes [4.14,4.15] in order to take into account the polarization phenomena, but their attention is highly paid towards a specific process and, thus, it is very difficult to achieve and extrapolate general considerations about. In this sense, the aim of this chapter is properly to analyze the influence of the polarization phenomenon on the performances of Pd-alloy membranes involved in hydrogen separation processes in several different operating conditions. In order to do this, a model already introduced in Chapter 3 will be used, dividing the hydrogen permeation process into several different steps. Such a model is able to calculate the transmembrane hydrogen partial pressure profile and, hence, the level of the polarization, which will be evaluated by means of an appropriately-defined Concentration Polarization Coefficient (CPC). Such an approach will be used here in order to take into account the effects due to the presence of many components in the upstream mixture. This is necessary, since the hydrogen concentration in the mixture to be purified significantly varies during the separation process. In the course of this chapter, after a brief description of the physical system, the concentration polarization coefficient will be opportunely defined, showing its relation with the permeance and with the corresponding driving force. Then, several working maps will be build up in order to evaluate qualitatively and quantitatively the amount of the polarization in dependence on actual operating conditions typical of these kinds of system.

4.2 DESCRIPTION OF THE SYSTEM

Figure 4.1 shows the reference system for this analysis, which, as mentioned above, is focussed on Pd-based defect-free membranes, permeable towards only hydrogen. In the scheme, three different permeation stages can be recognized: 1) the mixture side, whose bulk is perfectly mixed and the whole resistance to the external mass transfer is entirely

concentrated in the gaseous film; 2) the Pd-based membrane, i.e. the selective layer, and 3) the pure-component (hydrogen) side, where no resistance due to the external mass transfer occurs. In the successive analysis, both the permeations a) from (dashed line) and b) towards (continuous line) the pure hydrogen side will be considered, in order to make the analysis more complete. It is highlighted that the gap between the bulk (or membrane) hydrogen partial pressures is a direct graphical indication of the permeation driving force, whose functionality will be made explicit later.

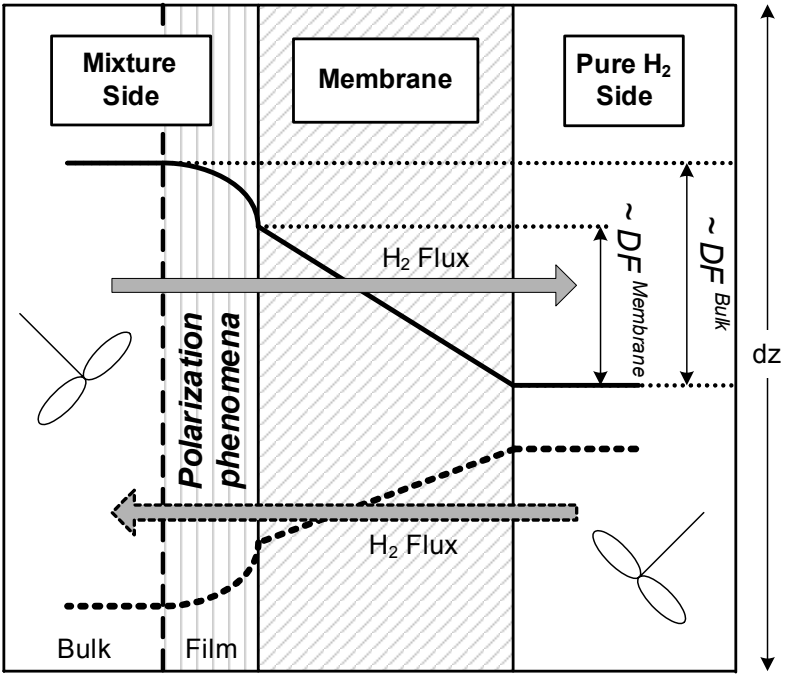

Figure 4.1 – Schematic representation of hydrogen permeation in a generic point of a tube-in-tube permeator (Figure 4.2). The solid and dashed lines indicate the forward and backward permeation case, respectively. The profiles are intended to be those of the hydrogen partial pressure, even in the membrane, where the concentration of the atomic hydrogen is expressed in terms of equivalent pressure.

Form this point on, the driving force of membrane (between the membrane surfaces) and of bulk (between the bulks) are indicated by means of the superscripts "*Membrane*" and "*Bulk*", respectively, as indicated in the figure. The just described system can be viewed also as a generic element of infinitesimal length "dz" of a tube-in-tube membrane equipment (Figure 4.2), whose behaviour during the separation process will be represented in the coming figures by means of the here-called "separation paths". These paths are thick lines indicating the typical decrease (or increase, in case of back-permeation) of hydrogen molar fraction $x\{H_2\}$ in mixture side. However, it must be pointed out that these paths are not to be intended as continuous curves, but as composed of a series of points close to each other, each one corresponding to a perfectly mixed system.

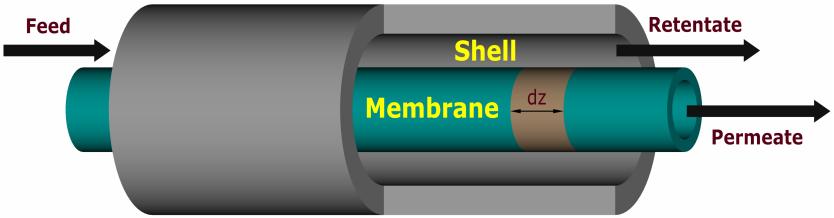

Figure 4.2 – Scheme of a Pd-based membrane permeator in tube-in-tube configuration. The element of the equipment indicated by "dz" identifies the target volume used in Figure 4.1 for the mass transport analysis.

The reason why a multicomponent mixture is considered instead of a simple binary one is to study a system as close as possible to actual cases.

For the flux calculation through the membrane, the model introduced in the previous chapter is used, adopting the kinetic and transport parameters reported in (Table 3.4). If different Pd-alloys were to be analyzed, it would be necessary to acquire the data of the specific membrane considered – for instance in terms of permeance measured in pure H_2 test – like done here in Section 4.4.3 regarding the model validation.

4.3 CONCENTRATION POLARIZATION COEFFICIENT

The effect of the concentration polarization will be evaluated by means of an appropriate coefficient, whose definition requires a particular attention to be paid.

Table 4.1 – The most common definitions of concentration polarization coefficient in open literature.

Reference	Concentration polarization coefficient	Range
Zhang *et al.* [4.15]	defined for one component: $\frac{N_1}{N_1^0}$,	(0, 1)
	defined for a binary mixture: $\frac{N_1}{N_2}$	(0, ∞)
Wijmann *et al.* [4.16] Yeom *et al.* [4.17, 4.18]	$\left.\frac{C_i^{Film}}{C_i^{Bulk}}\right\vert^{Feed}$	(0, 1)
Zhao *et al.* [4.19]	$\left.\frac{x_i^{Film}}{x_i^{Bulk}}\right\vert^{Feed\ and\ Permeate}$	(0, 1)
Wang *et al.* [4.20]	$\left.1-\frac{x_i^{Film}}{x_i^{Bulk}}\right\vert^{Feed}$	(0, 1)
Haraya *et al.* [4.21] Takaba *et al.* [4.22]	$\frac{x_{i,Feed}^{Film}-x_{i,Permeate}^{Bulk}}{x_{i,Feed}^{Bulk}-x_{i,Permeate}^{Bulk}}$	(0, 1)

C = Concentration, x = molar fraction, N = Flux, N^0 = Flux without polarization.

In open literature, it is possible to find several definitions, whose the most used ones are summarized in Table 4.1. As it is possible to see, all the coefficients refer to a key-species permeating through the membrane. In particular, if considering that there is no variation of the total pressure along the flux direction, the definition of Wijmann *et al.* [4.16] and Yeom *et al.* [4.17, 4.18] is in fact coincident to that of Zhao *et al.* [4.19], who used a coefficient per each membrane side in order to take into account also the polarization in the down-stream side. However, in this case, as the polarization becomes more important, the coefficient tends to be closer to zero, going towards the unitary value in the opposite situation (no polarization). On the contrary, Wang *et al.* [4.20] defined a coefficient in such a way that it is close to one when the polarization is significant. In order to link the polarization effect to the selectivity of a membrane, Zhang *et al.* [4.15] used the permeating fluxes in the definition of the coefficient, as shown in the table. However, this does not seem a good choice, since the approach is valid only for a binary mixture and the overall coefficient is not embedded between zero and one.

A more useful definition was provided by Haraya *et al.* [4.21] and Takaba *et al.* [4.22], who considered a unique coefficient for accounting the polarization on both the membrane sides (Table 4.1). The problem with this and other expressions is that the quantity explicitly related to the permeation does not appear, like the driving forces (usually the difference between the partial pressures) and/or the permeances of the species to be separated. In fact, the expressions involving the molar fractions are equivalent to those expressed as function of the partial pressure only if the total pressures of upstream and downstream are equal, thing that does not generally occur.

Hence, in this work the Concentration Polarization Coefficient (CPC) is defined as a function of appropriate permeation Driving Forces (DF) of bulk and membrane (see the sketch shown in Figure 4.1) having a precise physical meaning (Eq. 4.1). According with this definition, when the external resistance is negligible, CPC approaches to zero (very low polarization), whereas it goes towards the unitary value in the opposite case (total polarization), as highlighted in Table 4.2. In this particular case, the DF is related to only hydrogen, which is the only species able to permeate generally through the Pd-based membranes.

$$CPC = 1 - \frac{DF^{Membrane}}{DF^{Bulk}}$$

$$\Downarrow \qquad (4.1)$$

$$DF^{Membrane} = (1 - CPC)\,DF^{Bulk}$$

This definition is used since CPC should indicate properly the amount of polarization, i.e. the distance from the ideal case in correspondence of which the bulk DF^{Bulk} is equal to $DF^{Membrane}$ ($CPC \approx 0$).

Table 4.2 – Limit values of CPC as defined in the present analysis.

Parameter	*Value*	*Physical meaning*
CPC	0	No Polarization
	1	Total Polarization

At this point, it is necessary to explicit the functionality of the generic DF used in Eq. 4.1. For this aim, it has to be considered that, when the other permeation elementary steps (external mass transfer and surface phenomena of adsorption and desorption) are rapid enough, the diffusion through the Pd-based membrane becomes the only rate-determining step [4.9, 4.10] and, hence, the permeation can be described by means of the Sieverts' law (Eq. 4.2).

$$J_{H_2} = \pi\, DF \equiv \pi \left(\sqrt{P_{H_2}^{Upstream}} - \sqrt{P_{H_2}^{Downstream}} \right) \equiv \pi\, \Delta \sqrt{P_{H_2}} \qquad (4.2)$$

Since the conditions in which the Sieverts' law is valid are the most desirable ones (no polarization), they represent the ideal case to which a Pd-based membrane system has to tend. Hence, the Sieverts' DF is chosen to be the reference DF by means of which expressing CPC (Eq. 4.3). Thus, from this point on, DF will indicate the Sieverts' driving force.

$$CPC = 1 - \frac{\left[\Delta\sqrt{P_{H_2}}\right]^{Membrane}}{\left[\Delta\sqrt{P_{H_2}}\right]^{Bulk}} \tag{4.3}$$

Relating CPC with permeance (π) and flux (J_{H_2}), some considerations have to be done. In a generic membrane-based operation, and, thus, also in gas separation carried out in membrane equipments, once an appropriate permeation DF characteristic of the process has been chosen, the hydrogen permeating flux can be expressed as the product of this DF and the corresponding π (Eq. 4.4).

$$J_{H_2} = \pi \; DF \tag{4.4}$$

The left hand side of Eq. 4.4 is the actual value of transmembrane flux (measurable), whilst the right one represents a simplified model by means of which to describe what occurs in a membrane system. As a consequence of this definition, the permeance is strictly linked to a specific DF, and it is possible to define different permeances corresponding to different driving forces. Two main choices are available (Eq. 4.5), since one can choose to consider the DF establishing 1) between the membrane surfaces or 2) between the fluid bulks of the upstream and downstream. Both the solutions present advantages and drawbacks. In fact, in the first case the membrane permeance (named $\pi^{Membrane}$) is quite simple to be evaluated (e.g. in pure single gas measurements or in perfectly mixing conditions), whilst it is more complicated to measure the actual DF between the two interfaces ($DF^{Membrane}$).

$$\begin{aligned} J_{H_2} &= \pi^{Membrane} \; DF^{Membrane} \\ &= \pi^{Bulk} \; DF^{Bulk} \end{aligned} \tag{4.5}$$

In the second case, the DF of bulk is direct obtained from the operating conditions, whereas the bulk permeance (named π^{Bulk}) is very difficult to be correctly estimated, it being a function of mixture composition and of mixing degree. These are the reasons why it is more convenient to express the permeating flux in terms of the most simply valuable quantities, which are the bulk driving force and the membrane permeance (Eq. 4.7).

$$\left(1-CPC\right)\pi^{Membrane}=\pi^{Bulk}$$

or (4.6)

$$CPC=1-\frac{\pi^{Bulk}}{\pi^{Membrane}}=1-\frac{DF^{Membrane}}{DF^{Bulk}}$$

$$J_{H_2}=\left(1-CPC\right)\pi^{Membrane}DF^{Bulk} \tag{4.7}$$

For being a membrane intrinsic property, $\pi^{Membrane}$ does not depend on the fluid-dynamics in the upstream side, but only on the temperature and the membrane thickness and is measurable by pure H_2 tests. Hence, the variation of π^{Bulk} with the external conditions is directly related to that of CPC, which provides a direct measure of the difference between the two defined permeances (Eq. 4.6). This aspect will be explained in more details in the Section 4.4.1 (see Figure 4.3).

As concerns the effective evaluation of CPC, the model already introduced in Chapter 3 is used. In particular, once the bulk conditions have been set, the H_2 flux is calculated taking into account all the elementary permeation steps. As a result, the model provides also the value of $DF^{Membrane}$, which, together with H_2 flux, allows to evaluate both $\pi^{Membrane}$ and CPC. Hence, this procedure permits to calculate CPC in different operating conditions and investigate the effect of several variables like temperature, pressures, membrane thickness, etc.

4.4 RESULTS AND DISCUSSION

The operating conditions considered in the simulation are reported in Table 4.3. In mixture, six gaseous species are considered, whilst on the other membrane side only hydrogen is present.

Table 4.3 – Operating conditions for the simulation.

Side	*Molar Fraction, -*						*Total Pressure, kPa*	*Reynolds' number*
	H_2	N_2	O_2	CO_2	H_2O	CH_4		
Mixture	{0 ... 1}	0.2 ... 0 (for each species)					{100 ... 1000}	≈ 2100 - 8000
Pure H_2	1	Not present					{100 ... 800}	Not influent
Temperatures, °C = {300, 350, 400, 450, 500}, Membrane Thicknesses, μm = {1, 5, 15, 50, 150}								

As shown in the table, the molar fractions of the other species except hydrogen are equal to each other in mixture, their total sum being equal to $(1- x\{H_2\})$. In the course of this chapter, the quantities relative to the mixture and pure H_2 sides will be indicated by means of the superscript "Mixture" and "Pure", respectively.

4.4.1 INFLUENCE OF THE PERMEANCE ON CPC

In Figure 4.3 both the bulk and membrane permeances and the hydrogen flux are reported as functions of $x\{H_2\}$ for different membrane thicknesses in certain operating conditions. In particular, a Reynolds' number of about 5200 is considered, which indicates a turbulent flow regime. This choice will be done also concerning the other investigations up to Figure 4.7, after which the influence of Reynolds' number will be analyzed and discussed in detail (Figure 4.8-9). Coming back to Figure 4.3, the permeance behaviour (of bulk and membrane) can be explained by the following considerations. As mentioned above (Eq. 4.6), $\pi^{Membrane}$ is independent of what occurs in the films and, hence, of partial pressures in mixture (constant behaviour in the figure).

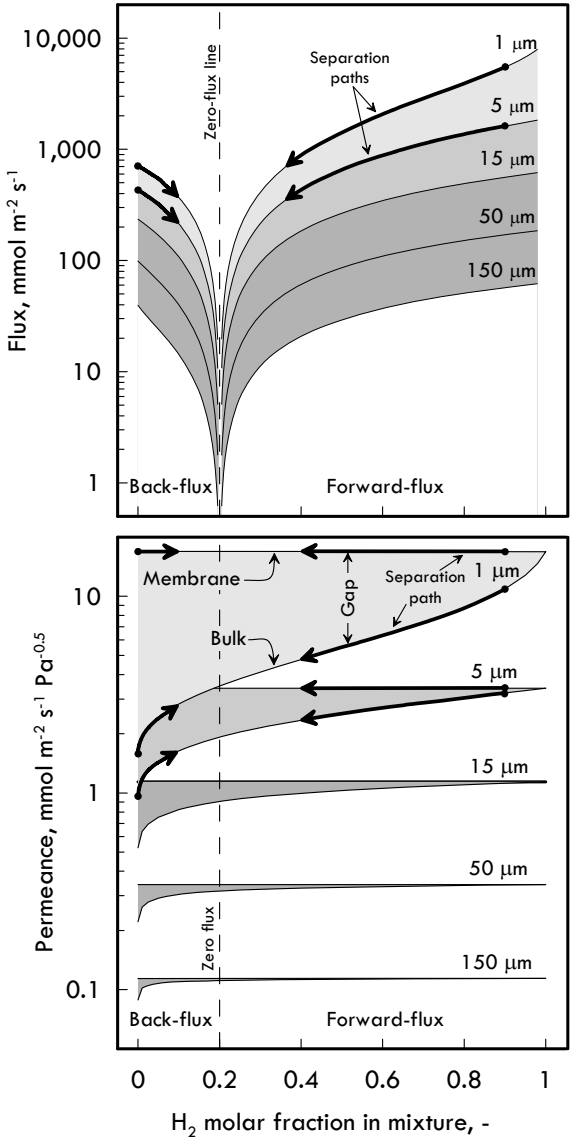

Figure 4.3 – Hydrogen permeating flux and both permeances (of bulk and membrane) as a function of the H_2 molar fraction in mixture for different membrane thicknesses at 500°C. The thicker arrows at 1 and 5 μm indicate the separation paths. $P^{Mixture}$ = 1000 kPa and P^{Pure} = 200 kPa, $Re \approx 5200$.

On the contrary, π^{Bulk} is highly affected by the external mass transfer, which in turn is influenced by the partial pressures of all the components in the mixture. Both forward and back-permeation cases are considered in figure, for which the above-mentioned separation paths (indicated in terms of $x\{H_2\}$ by means of thicker arrows on the flux and permeance curves) are also shown for a separation occurring i) from a $x\{H_2\}$ of 0.9 to 0.4 in forward flux case and ii) from 0 to 0.1 in the other case.

Following the path at 1 μm in forward flux case, during the separation process both the flux and bulk permeance decreases in the same qualitative manner for high value of $x\{H_2\}$, but approaching to the zero-flux point the behaviour is different. In particular, while the flux tends to zero, the bulk permeance tends to a finite value, which is the same one found for the back-flux case. The physical meaning of this important aspect is that a membrane has two characteristic values of permeance. The first one, obtainable in pure hydrogen permeation test, is, as said before, a property of the specific membrane and is the maximum permeance reachable, whilst the second one is a characteristic proper of both membrane and fluid-dynamic conditions. From a physical point of view, two contrasting effects caused by an increase of $x\{H_2\}$ are present. In fact, on one hand, the flux becomes more significant, causing the mass transfer resistance to be more important, but, on the other hand, the hydrogen content is higher and, thus, the external resistance tends to decrease, increasing in this way π^{Bulk}.

The overall result of these two contrasting factors is that at low $x\{H_2\}$ the first tendency is high, whereas at high $x\{H_2\}$ the effect of the second one is more important. This is the reason why the curves are provided with inflection point recognizable in their shape. At higher membrane thicknesses the behaviour is analogous, but the gap between the two permeances decreases for the polarization influence to be lower because of the higher resistance in the membrane.

In order to quantify the amount of the polarization, CPC is reported as a function of the bulk and membrane permeance (Figure 4.4) for different values of thickness and $x\{H_2\}$. The limits considered for the permeances are typical values of literature.

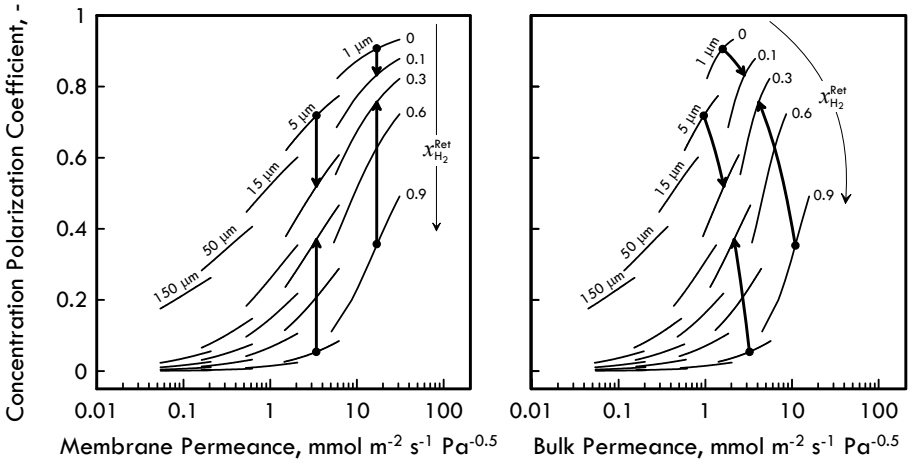

Figure 4.4 – Concentration polarization coefficient (CPC) as a function of H_2 permeance of bulk and membrane for different membrane thicknesses and hydrogen molar fractions in mixture. The thicker arrows at 1 and 5 μm indicate the separation paths. $P^{Mixture}$ = 1000 kPa and P^{Pure} = 200 kPa, *Re* ≈ 5200.

In the figure, some separation paths are indicated at 500°C for two different membrane thicknesses in back- (molar fractions from 0 to 0.1) and in forward-flux (from 0.9 to 0.3) cases. Since $\pi^{Membrane}$ does not depend on the flow regime, the paths are vertical in this plot, whereas π^{Bulk} is affected by the polarization and, hence, is subjected to a certain decrease when considering the forward-flux case, increasing its value in the opposite back-flux situation.

As regards the behaviour of CPC, it is in both the cases qualitatively analogous, hence the $\pi^{Membrane}$ case will be analyzed. The first very interesting fact to notice is that CPC is not a univocal function of the permeance, two different values being recognized in correspondence of a certain permeance. This behaviour is not surprising, since several combinations of different factors can provide same values of permeance, but not of CPC. In the specific case, as the permeance can vary with both the membrane thickness and temperature, a same value of it can be obtained with a thin membrane at low temperature and with a thicker membrane in higher temperature conditions. However, CPC is differently influenced by each of these factors,

thus only the permeance is not sufficient to evaluate the polarization effect. Only at low permeances CPC can be considered as a sole function of the permeance with good approximation, but usually these ranges of values are not interesting, since they corresponds to quite low fluxes and the polarization is negligible. Analyzing the case of $x\{H_2\}$=0.9, CPC increases with permeance for all the thicknesses, since, once set the other operating conditions, a higher permeance means a higher flux and, hence, a higher resistance to transport. For lower $x\{H_2\}$, the polarization effect becomes more significant, for the dilution influence to be higher than that of the decreasing flux.

4.4.2 POLARIZATION MAPS

In this section, the effect of the operating conditions on CPC is analyzed in details, creating some maps useful to determine the amount of the polarization in some situations. The influence of six different system variables is considered: 1) temperature, 2) membrane thickness, 3) total pressure of mixture, 4) total pressure in pure H_2 side side (in this case equal to the hydrogen partial pressure), 5) hydrogen molar fraction in mixture $x\{H_2\}$ and 6) the Reynolds' number, which indicates the fluid-dynamic conditions. In Figure 4.5, CPC is shown as a function of $x\{H_2\}$. In the plot, the separation path corresponding to the $x\{H_2\}$ axial profile in the permeator considered in Figure 4.1 during the separation process is also shown by means of thicker curved arrows for two cases. Furthermore, the dashed line, relative to the case that the permeation driving force is null, is shown. About this last particular limit condition, some comments have to be made concerning the definition of CPC. On a mathematical point of view, when $x\{H_2\}$ approaches to the zero-flux value, DF^{Bulk} and $DF^{Membrane}$ tend to be equal to each other and, thus, both approach to zero with the same "velocity". This means that, in the limit case of null driving forces, a finite value of CPC is obtained. However, on a physical point of view, if there is no permeation, it has no sense speaking about polarization, since this phenomenon is properly related to a permeating flux.

For all these reasons, the points in the plot corresponding to a null driving force (marked with a white circle) have to be considered as virtual values of CPC having no physical meaning.

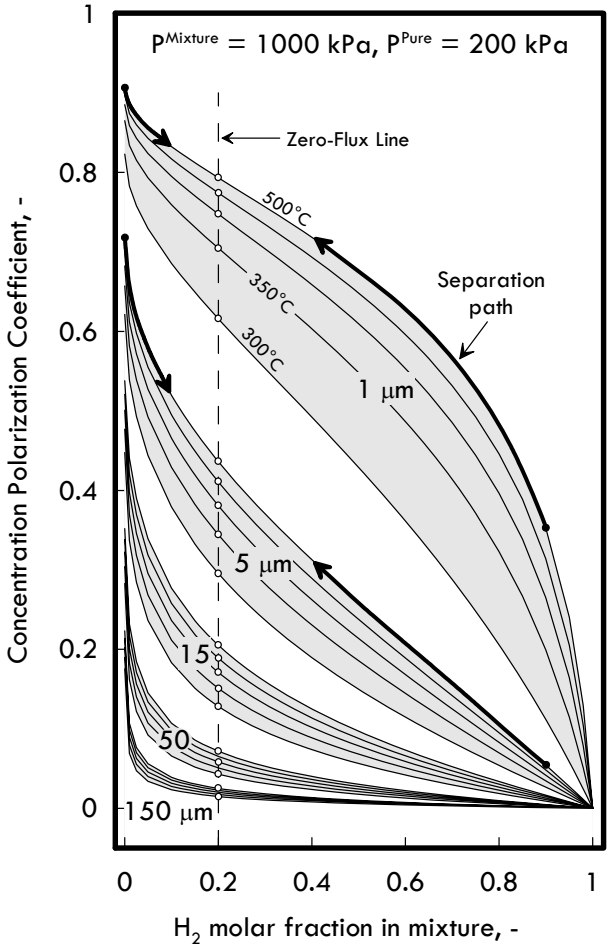

Figure 4.5 – CPC as a function of the H_2 molar fraction in mixture for different temperatures and membrane thicknesses. The temperatures at higher thicknesses are the same as for 1 μm in the same order. The thicker arrows at 1 and 5 μm indicate the separation paths. *Re* ≈ 5200.

Examining the situation at 1 μm and 500°C, the curves monotonically decrease with $x\{H_2\}$, first with a certain rapidity, then more slowly and then again more rapidly, causing the sign of the second derivative to change from a positive to a negative value. The presence of an

inflection point in all the curves can be explained by means of the following considerations. Going back from the unitary value of $x\{H_2\}$ to zero, the amount of polarization on one hand tends to increase for the larger composition of other components, but on the other hand it tends to decrease for the smaller hydrogen permeating flux. Until the first tendency prevails, the second derivative of the curve is negative, whilst it becomes positive in the opposite situation. This inflection point can be found in correspondence of a higher abscissa as lower temperature is considered. At high contents of hydrogen in mixture ($x\{H_2\}$ close to unitary value), the polarization tends to be zero, even for high fluxes, because of the absence of other species creating a composition gradient. Thus, there are two factors determining CPC: the flux and the stream composition. This is due to the fact that at lower temperatures the resistance in the Pd-based membrane is higher and the incidence of the polarization is relatively lower. Hence, the contribution of the presence of other components is less important than that of the higher flux. The behaviour at higher thicknesses is the same, even though it is not completely recognizable from the figures because the inflection points are closer to the unitary value. In these conditions, the resistance in the membrane controls more significantly the entire permeation process and, consequently, the influence of the polarization becomes smaller. This aspect is reflected also on the small effect of the temperature on CPC at high thicknesses, insomuch as at 150 μm its functionality can be considered negligible with temperature.

All these considerations are useful in order to understand the functioning of a Pd-based membrane permeator, which is in this contest the target equipment whose performances need to be optimized by means of an efficient design. In fact, considering what occurs along the axial upstream direction of such a kind of equipment during a hydrogen purification process, the polarization could provide a significant effect, since, as the purification process goes on, $x\{H_2\}$ decreases, causing an increase of the CPC as higher as thinner is the membrane. In order to analyze in a more detail the effect of the mixture total pressure, CPC is reported at a temperature of 500°C (which is a typical operating temperature for these membranes) and a pure H_2 pressure of 200 kPa (Figure 4.6). The first thing to notice is that the effect of the pressure on CPC is qualitatively similar to that of temperature. This occurs for two orders of

things. In fact, the higher is the pressure (higher driving force), the higher is the permeating flux (higher hydrogen composition gradient). Furthermore, the diffusivities of the species are almost inversely proportional to the total pressure.

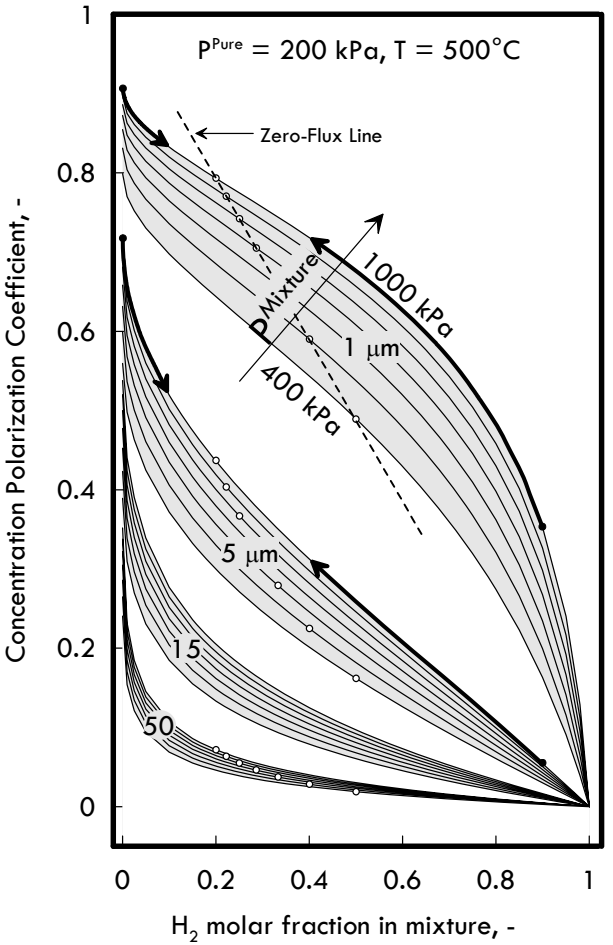

Figure 4.6 – *CPC* as a function of the H_2 molar fraction in mixture for different total pressures of mixture and membrane thicknesses. The total pressures for the higher thicknesses are the same as for 1 μm in the same order. The thicker arrows at 1 and 5 μm indicate the separation paths. *Re* ≈ 5200.

This causes the external mass transfer to be slower as the pressure increases, determining in this way a higher CPC.

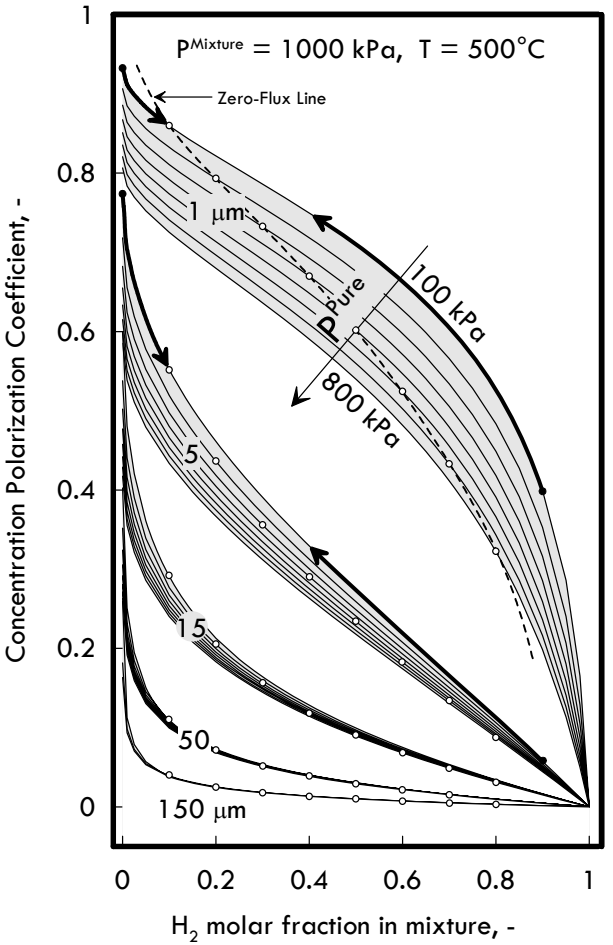

Figure 4.7 – Polarization maps as a function of the H_2 molar fraction mixture for different total pressures of pure H_2 and membrane thicknesses. The thicker arrows at 1 and 5 μm indicate the separation paths. Re ≈ 5200.

The other variable to study is the total pressure of pure H_2 (Figure 4.7), where only hydrogen is considered to be present, a mixture total pressure being 1000 kPa. Other cases corresponding to other mixture total pressures are qualitatively similar to this one and, hence, are not reported. For all the membrane thicknesses, as the pure H_2 pressure increases, CPC decreases. The explanation of this behaviour is due only to the lower flux determined by the decrease of the permeation driving force. In fact, in the pure H_2 side no concentration polarization occurs (only hydrogen) and, thus, the compositions and all of the physical properties remain constant in the mixture side. As thicker membranes are considered, the influence of pure H_2 pressure becomes lower, up to be negligible from about 15 μm on. Thus, in a first approximation, it is possible to assume that for a thickness higher than 15 μm the CPC is actually independent of the pure H_2 pressure, whilst in the more important field of very thin membranes, its effect should be taken into account. Another important effect which remains to be evaluated is that of the fluid-dynamic conditions of the system (Figure 4.8). Since the behaviour of each single profile has been already analyzed in some of the previous figures, let us pay attention only to the variation with *Re*. Considering the case at 5 μm (quite thin thickness), a significant influence of *Re* on the CPC is found, providing the quantitative results of the qualitative fact that, as *Re* increases, the external mass transfer is more facilitated (decreasing CPC). Extremizing this situation, for *Re* tending to infinite, CPC has to go towards zero. Considering the case of higher thicknesses, the influence of *Re* becomes smaller for the resistance in the membrane to be more significant. This situation is examined in terms of hydrogen flux in Figure 4.9, where the normalization was done basing on different reference fluxes, whose values are those evaluated in pure hydrogen conditions. In the figure, both regions of flux and back-flux (negative one) can be recognized. In the back-flux region, the flux decreases (in absolute value) as the hydrogen composition increases, approaching to zero when the decreasing permeation driving force becomes null, whilst in the other zone the opposite behaviour is found. Considering the case at 5 μm, the variation of the flux with Reynolds' number is quite relevant, whereas as thicker membranes are considered, the influence of the fluid-dynamic conditions becomes less significant.

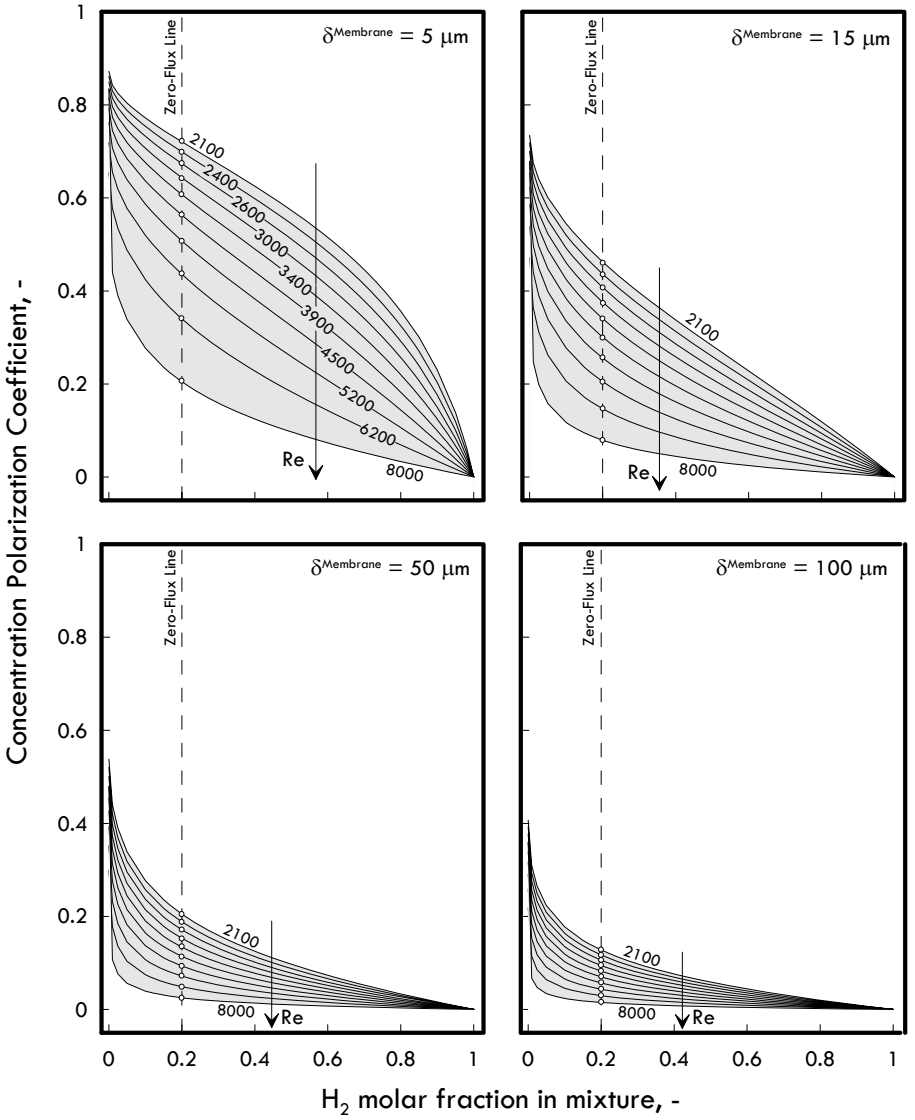

Figure 4.8 – Polarization maps as a function of the H_2 molar fraction in mixture for different Reynolds' number and membrane thicknesses at 500°C, $P^{Mixture}$ = 1000 kPa and P^{Pure} = 200 kPa. The intermediate curves between 2100 and 8000 for 15, 50 and 100 μm correspond to the same values of Re as indicated in the case of 5 μm.

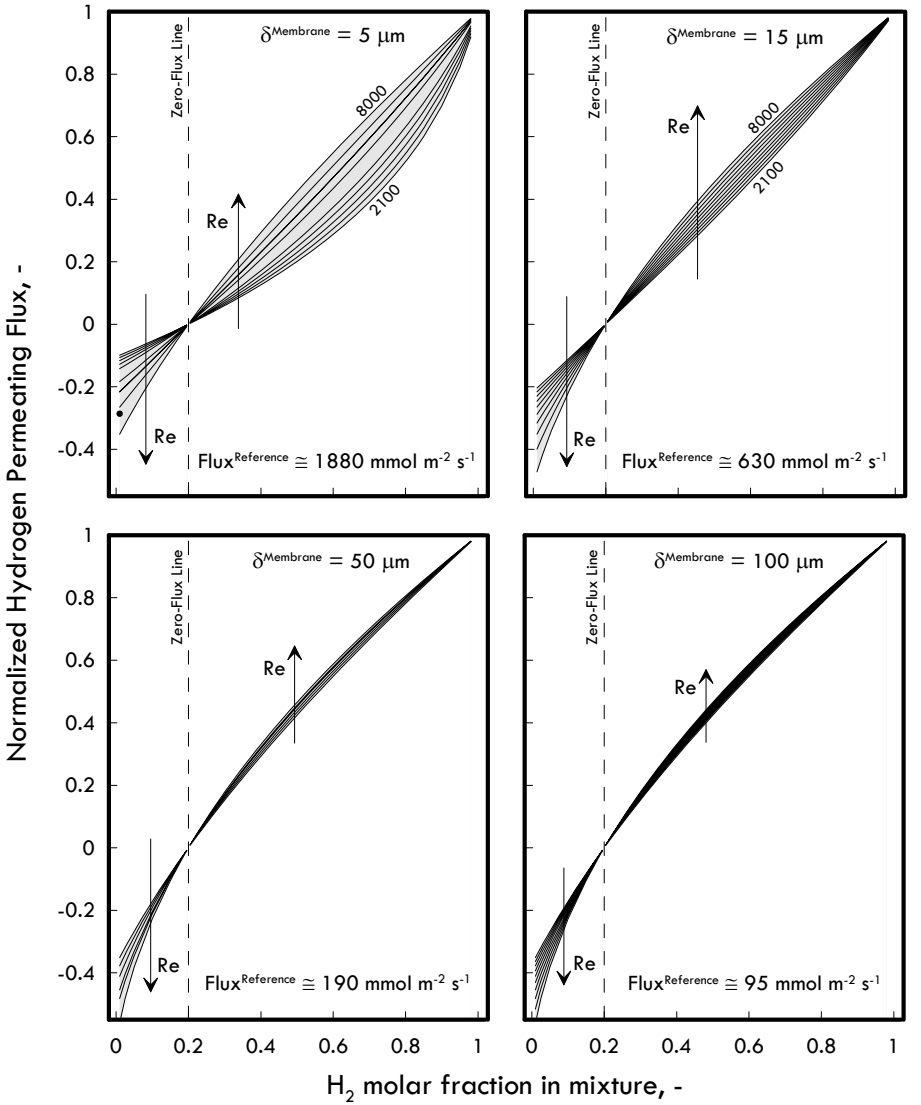

Figure 4.9 – Normalized hydrogen permeating flux as a function of the H_2 molar fraction in mixture for different Reynolds' number and membrane thicknesses at 500°C, $P^{Mixture}$ = 1000 kPa and P^{Pure} = 200 kPa. Each flux reference value by which the normalization is made is reported in the respective plots. The curves at 15, 50 and 100 μm correspond to the same values as indicated at 5 μm.

This indicates that the concentration polarization has to be minimized in those target conditions providing high fluxes. Thus, it is necessary to choose appropriately the operating conditions in order to exploit the membrane as much as possible. However, the process performances depend also on how a high Reynolds' number is reached.

4.4.3 MODEL VALIDATION

In order to provide a validation to the analysis presented above, some data taken from literature were used. In this specific case, the work of Peters *et al.* [4.5] was considered, since the effect of the polarization phenomenon at quite high feed pressures was specifically studied on the performance of an ultra-thin Pd-Ag membrane (77-23wt%, 2.2 μm thick), whose permeance obtained from pure H_2 permeation tests was used in the model calculation. Thus, the results of the model are validated by means of experimental data of H_2 flux obtained in mixture conditions, whose some main operating conditions are recalled in Table 4.4. The results of the validation are shown in Figure 4.10, where the hydrogen flux and CPC are reported as a function of the total pressure in the feed, which is a binary mixture H_2:N_2 having a hydrogen molar fraction of 0.5. Considering the plot of flux, it is possible to notice the good agreement with the experimental data considered. However, some details about the model calculation are to be provided.

Table 4.4 – Operating conditions for the validation.

Test Type	*Conditions*
Pure H_2 permeation ⇒	$\delta^{Membrane}$ = 2.2 μm
	T = 400°C
Concentration Polarization Case ⇒ (Binary mixture H_2:N_2 at 50:50)	P^{Feed} = [3, ..., 26] bar
	$P^{Permeate}$ = 1.01 bar

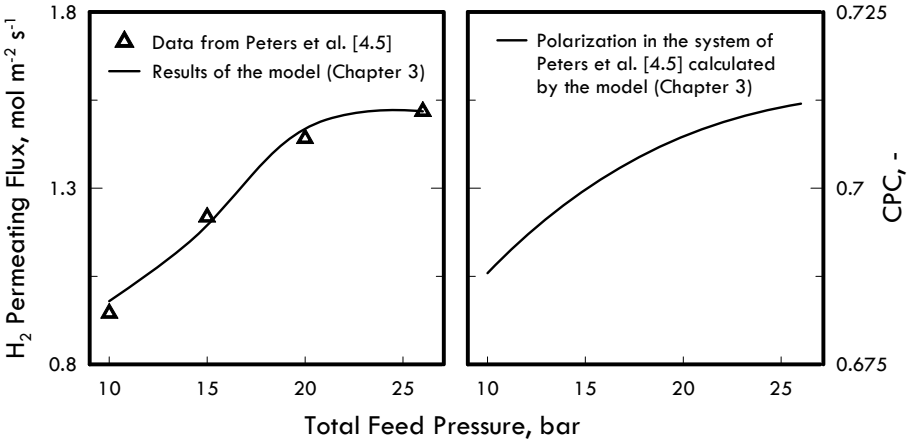

Figure 4.10 – Comparison between the results obtained from the present model and some experimental data taken from literature [4.5] in terms of hydrogen permeating flux. The values of CPC for the experimental system are calculated by the present model. The experimental data are appropriately re-elaborated.

In fact, Peters *et al.* [4.5] found a certain amount of hydrogen partial pressure depletion (4-7%) along the membrane length during the permeation tests (carried out in counter-current configuration and using a sweep gas). This caused the permeation driving force at the inlet of the module to be different from that at the outlet, also because the permeate side progressively enriches itself with hydrogen. For this reason, their permeator cannot be fully considered as a concentrated parameters system. Therefore, each point of the model was calculated as arithmetic mean of the two fluxes evaluated at the inlet and outlet of the membrane module. In the figure relative to CPC, the model was used to evaluate the polarization amount in the experimental system of Peter *et al.* [4.5], who clearly estimated in their paper a very high influence (78-83%) of the concentration polarization expressed in terms of relative resistance (= pressure drop due to polarization over the total transmembrane one). In order to compare their estimations to the model results, it would be necessary to convert the relative resistance (measured in $Pa \cdot Pa^{-1}$) into CPC values (measured in $Pa^{0.5} \cdot Pa^{-0.5}$). However, as concerns the specific case, this conversion cannot be made because of the uncertainty due to the hydrogen

partial pressure axial depletion. Nevertheless, it is reasonable to think that the level of the polarization effect predicted by the model is close to the one estimated in the experimental system considered, since in both cases quite significant values are found.

4.5 CONCLUSIONS

In this chapter the effect of the concentration polarization was analyzed in hydrogen permeation through self-supported Pd-alloy membranes by means of the model introduced in the previous chapter and here-validated in terms of permeating flux by means of some literature data [4.5] with good agreement. First, the effect of the permeating flux and both membrane and bulk permeances on the polarization was considered, highlighting the fact that these quantities are able to identify unambiguously the amount of polarization only at quite low values. Then, the concentration polarization coefficient was investigated in different operating conditions, showing that it decreases with the up-stream hydrogen molar fraction, membrane thickness, downstream total pressure and turbulence level (at higher Reynolds' number), whereas increases with temperature and upstream total pressure. The results achieved in the validation section highlighted that the concentration polarization can sometimes represent the most important phenomenon occurring in the hydrogen permeation, covering up to 70% of the relative transmembrane pressure drop, especially in presence of very thin membranes (< 3 μm). In this direction, the methodology proposed here allows to calculate quantitatively the amount of the polarization by means of the here-developed polarization maps. These diagrams can be built once the fluid-dynamic conditions and the membrane permeation parameters have been known, using them in such a way to avoid as much as possible the inefficiencies of a membrane separation process.

4.6 LIST OF SYMBOLS

J	permeating flux [mol m^{-2} s^{-1}]
P	pressure [Pa]
Re	Reynolds' number [-]
T	temperature [K]
x	molar fraction [-]
	Greek Symbols
δ	thickness [m]
π	permeance [mol m^{-2} s^{-1} $Pa^{-0.5}$]
	Acronyms
CPC	Concentration Polarization Coefficient [-]
DF	permeation Driving Force [Pa or $Pa^{0.5}$]

4.7 LITERATURE CITED

[4.1] Morreale B.D., Ciocco M.V., Enick R.M., Morsi B.I., Howard B.H., Cugini A.V. and Rothenberger K.S., 2003. The permeability of hydrogen in bulk palladium at elevated temperatures and pressures. *Journal of Membrane Science*, **212**: 87-97.

[4.2] Ciocco M.V., Morreale B.D., Rothenberger K.S., Howard B.H., Cugini A.V., Killmeyer R.P. and Enick R.M., 2002. High-pressure, high-temperature hydrogen permeability measurements of supported thin-film palladium membranes. *Proceeding Acts of 19th Pittsburgh Coal Conference*, paper **49**-3.

[4.3] *Fuel Cell Handbook* (Seventh Edition), EG&G Technical Services, Inc., 2004.

[4.4] Howard B.H., Killmeyer R.P., Rothenberger K.S., Cugini A.V., Morreale B.D., Enick R.M. and Bustamante F., 2004. Hydrogen permeance of palladium-copper alloy membranes over a wide range of temperatures and pressures. *Journal of Membrane Science*, **241**: 207-218.

[4.5] Peters T.A., Stange M., Klette H. and Bredesen R., 2008. High pressure performance of thin Pd-23%Ag/stainless steel composite membranes in water gas shift gas mixtures; influence of dilution, mass transfer and surface effects on the hydrogen flux. *Journal of Membrane Science*, **316**: 119.

[4.6] Mekonnen W., Arstad B., Klette H., Walmsley J.C., Bredesen R., Venvik H. and Holmestad R., 2008. Microstructural characterization of self-supported 1.6μm Pd/Ag membranes. *Journal of Membrane Science*, **310**: 337-348.

[4.7] Mejdell A.L., Klette H., Ramachandran A., Borg A. and Bredesen R., 2008. Hydrogen permeation of thin, free-standing Pd/Ag23% membranes before and after heat treatment in air. *Journal of Membrane Science*, **307**: 96-104.

[4.8] He G., Mi Y., Yue P.L. and Chen G., 1999. Theoretical study on concentration polarization in gas separation membrane processes. *Journal of Membrane Science*, **153**: 243-258.

[4.9] Caravella A., Barbieri G. and Drioli E., 2008. Modelling and Simulation of Hydrogen Permeation through Supported Pd-based Membranes with a Multicomponent Approach. *Chemical Engineering Science*, **63**: 2149-2160.

[4.10] Ward T. and Dao T., 1999. Model of hydrogen permeation behaviour in palladium membranes, *Journal of Membrane Science*, **153**: 211-231.

[4.11] Lüdtke O., Behling R.D. and Ohlrogge K., 1998. Concentration polarization in gas permeation. *Journal of Membrane Science*, **146**: 145-157.

[4.12] Hara S., Sakaki K. and Itoh N., 1999. Decline in Hydrogen Permeation Due to Concentration Polarization and CO Hindrance in a Palladium Membrane Reactor. *Industrial & Engineering Chemistry Research*, **38**: 4913-4918.

[4.13] Barbieri G., Scura F., Lentini F., De Luca and Drioli E., 2008. A novel model equation for the permeation of hydrogen in mixture with carbon monoxide through Pd–Ag membranes. *Separation and Purification Technology*, **61**: 217-224.

[4.14] Tiemersma T.P., Patil C.S., van Sint Annaland M., Kuipers J.A.M., 2006. Modelling of packed bed membrane reactors for autothermal production of ultrapure hydrogen. *Chemical Engineering Science*, **61**: 1602-1616.

[4.15] Zhang, J., Liu D., He M., Xu H. and Li W., 2006. Experimental and simulation studies on concentration polarization in H2 enrichment by highly permeable and selective Pd membranes. *Journal of Membrane Science*, **274**: 83-91.

[4.16] Wijmann J.G., Athayde A.L., Daniels R., Ly J.H., Kamaruddin H.D. and Pinnau I., 1996. The role of boundary layers in the removal volatile organic compounds from water by pervaporation. *Journal of Membrane Science*, **109**: 135-146.

[4.17] Yeom C.K., Lee S.H., Lee J.M. and Song H.Y., 2002. Modeling and evaluation of boundary layer resistance at feed in the permeation of VOC/N_2 mixtures through PDMS membrane. *Journal of Membrane Science*, **204**: 303-322.

[4.18] Yeom C.K., Lee S.H., Lee J.M. and Song H.Y., 2002. A characterization of concentration polarization in a boundary layer in the permeation of VOCs/N_2 mixtures through PDMS membrane. *Journal of Membrane Science*, **205**: 155-174.

[4.19] Zhao S., Li Z., Liu Y. and Wang L., 2008. Simulation of binary gas separation in hollow fiber membrane-acetylene dehydration. *Desalination*, **233**: 310-318.

[4.20] Wang R., Liu S. L., Lin T. T. and Chung T. S., 2002. Characterization of hollow fiber membranes in a permeator using binary gas mixtures. *Chemical Engineering Science*, **57**: 967-976.

[4.21] Haraya K., Hakuta T. and Yoshitome H., 1987. A study of concentration polarization phenomenon on the surface of a gas separation membrane. *Separation Science and Technology*, **22**: 1425-1438.

[4.22] Takaba H. and Nakao S., 2005. Computational fluid dynamics study on concentration polarization in H_2/CO separation membranes. *Journal of Membrane Science*, **249**: 83-88.

CHAPTER 5

DEVELOPMENT OF IMPROVED CONFIGURATIONS FOR STAGED PD-BASED MEMBRANE REACTORS. CASE STUDY: METHANE STEAM REFORMING*

*Some contents of this chapter have been already published or submitted for publication [6.1-6.2, 6.4, 6.9-6.10].

5.1 INTRODUCTION

Processes operated in membrane equipments are very versatile, as emphasized by Dittmeyer *et al.* [5.1] in their review; thus, they have been massively studied and analyzed since more than two decades. The reason of this great interest is their feature to combine reactive and separative processes in one step. The consequence is a considerable reduction of the plant volumes, according with the guide-lines of the process intensification strategy, whose main aim is to substitute traditional processes with innovative ones, obtaining, in this way, the same or higher performances in more compact and modular equipments [5.2].

The features of the membrane equipments can be exploited in many industrial chemical processes, like, for example, in reactions where the conversion is limited by the thermodynamic equilibrium (hydrocarbons partial oxidation, de-hydrogenation reactions, steam reforming of hydrocarbons, etc.). One of these processes is methane steam reforming to produce hydrogen, it being an endothermic reaction typically carried out on a Ni-based catalyst in tubular reactors. In order to produce acceptable amounts of hydrogen in traditional reactors it is necessary to operate at high temperature (about 800-850°C) with considerable energy requirements. The use of Pd-based membrane reactors allows to overcome this problem, causing the shift of the reaction towards the products, thanks to their well-known ability to be permeable for only hydrogen, as already discussed in Chapter 3 and 4.

Moreover, this allows a purer hydrogen stream on the permeate side and, hence, leads up to a significant decrease of separation costs after the reaction stages. In this direction, many researchers were and are still interested in the integration of the membrane technology in processes involving the steam reforming of hydrocarbons, developing many more or less complex models to simulate and predict the behaviour of the so-assembled membrane equipments. In literature, the influence of several operating variables has been studied, like feed and sweep pressure, temperature, membrane thickness and sweep ratio [5.3-5.6]. In particular, Koukou *et al.* [5.3] analyzed the role of non-ideal flow in those membrane reactors, showing the importance of taking into account the radial profiles when a high radial dimension is considered. A similar study was carried out by Assabumrungrat *et al.* [5.4] in their paper on

the oxidative dehydrogenation of n-butane in a porous membrane reactor, where the effect of several other factors like furnace temperature, air/n-butane feed ratio and reactor size is analyzed. Some of other simulation studies were carried out in parallel with experimental analyses. Some of these operating variables have been studied in comparison with experimental data by Kim *et al.* [5.7] and Gallucci *et al.* [5.8]. The effect of energy transport between the sides of a Pd-membrane reactor was studied by Marigliano *et al.* [5.9], whilst Lin *et al.* [5.10] simulated the effect of incipient removal of hydrogen. Oklany *et al.* [5.11] investigated on a numerical point of view the performance difference of the methane steam reforming reaction carried out first in a Pd-based membrane reactor and then a microporous membrane-based one, whereas Adris *et al.* [5.22] carried out the same process in a fluidized-bed membrane reactor at high temperature.

Very recently, Chiappetta *et al.* [5.23] highlighted in their work the importance of the catalyst axial distribution on the temperature hot spot along a packed bed Pd-membrane reactor for the Water Gas Shift reaction. In their paper, they considered three different axial distributions: constant, linear and exponential, finding that it is more useful to adopt a linear catalyst distribution in order to control the hot spot. Actually, the role of the catalyst distribution can be very important not only to regulate the behaviour of a reactive system, but also to improve its performances. However, despite the vastness of the literature on the subject (membrane reactors), to our knowledge, there are no studies dealing with the importance of the catalyst and membrane area axial distribution on the reactor performances. In fact, it cannot be taken for granted that a conventional packed bed membrane reactor, i.e. the one with only one simultaneous reactive/permeative stage, represents an optimal configuration.

Actually, depending on the particular process, some reactor zones may exist where the membrane area and/or the catalyst are wasted simply for the reaction and/or permeation rate to be too slow or fast. For instance, it can be considered that the membrane area at the beginning of the reactor is wasted, since the small amount of produced hydrogen leads to a negligible permeation, it being useless for increasing the reaction rate. Furthermore, in those zones where the local equilibrium conversion has been approached, it can be observed that

the catalyst is not optimally utilized unless hydrogen is significantly removed by permeation. In all the cases, the amount of the wasted area strictly depends on the relative importance of the permeation with respect to the reaction rate and, thus, it is necessary to adopt appropriate distributions to avoid these negative factors or make them as negligible as possible. On a qualitative point of view, it is reasonable thinking that the higher the reaction rate, the higher the wasted membrane area and catalyst. However, an optimization procedure is required to quantify effectively the waste level and determine in this way the optimal distributions of catalyst and membrane area.

The aim of this chapter justly consists in analyzing the effects of the catalyst and membrane area axial distribution for the methane steam reforming process, considering two different staged Pd-based membrane reactors, named here as follows:

- ✓ "*Permeative Stage Membrane Reactor*", PSMR.
- ✓ "*Inert Stage Membrane Reactor*", ISMR.

Although the detailed description of these reactors will be provided in the following sections, some their aspects have to be underlined here to explain the reasons why just these two different reactors has been chosen to be analyzed. The first one of them (PSMR) is a staged membrane reactor in which packed bed traditional reactors and membrane permeators are laid out in an alternated disposition, so that, differently than in conventional Membrane Reactors (MR), the key-species (hydrogen in this case) is produced and separated in distinct stages. Hence, the effect of the reaction and separation can be distinguished and distinctly analyzed. The second one (ISMR) consists in a staged membrane reactor where reactive zones are followed by inert ones alternatively, with the membrane being present in both the zones. In this reactor, the effect of the permeation rate on the axial catalyst distribution can be studied, specifying that the shape of the distribution is determined by the lengths of the reactor stages.

The whole analysis will be carried out in the following sections by analyzing first the PSMR and then ISMR. Both reactors will be appraised in terms of methane conversion x, hydrogen Recovery Factor RF and hydrogen Recovery Yield RY, comparing their performances with some appropriate reactors (conventional MR and, for only the PSMR, with TR). As concerns

the PSMR, once the number of stages have been fixed, three axial distributions will be investigated, one of which is the equi-sized distribution. The other two distributions will be determined by optimizing two different objective functions: x and RF, introducing the overall criterion of the highest RY to choose the best one. Regarding the ISMR, two kinds of aspects will be studied. First, analogously to what done for the PSMR, some optimal distributions will be achieved, keeping the number of stages fixed. Then, this last hypothesis will be removed and the role of the stages' number and catalyst amount will be analyzed.

5.2 CASE STUDY I: PERMEATIVE STAGE MEMBRANE REACTOR

5.2.1 DESCRIPTION OF THE SYSTEM

In this section, methane steam reforming is considered to be carried out in the above-mentioned Permeative Stage Membrane Reactor (PSMR), whose descriptive scheme is shown in Figure 5.1. It is composed of five reactive stages in an alternated series with four Pd-based permeative stages. The total length of the reactor and the number of stages are chosen in order to simulate a laboratory-scale system with a significant enough stages' length. In particular, the choice of the stages' number (nine, totally) is made in order to set a reference system in which too long or too short stages are avoided.

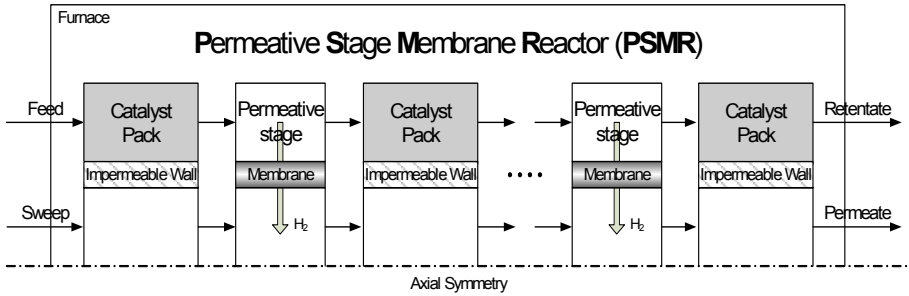

Figure 5.1 – Scheme of the Permeative Stage Membrane Reactor (PSMR) considered.

Furthermore, the assumption of a reactive last stage is made since, as mentioned earlier, two objective functions are considered and it is not possible to know *a-priori* whether or not that stage is convenient for the process. The usefulness of the last reactive stage will be determined by the optimization procedure below described, which is able to indicate whether or not a stage can be neglected. This aspect will be clarified later, when the PSMR optimization procedure will be explained in details. A nitrogen sweep-gas is considered in a co-current configuration. Thus, the permeate stream is more enriched by hydrogen as approaching to the end of the reactor. The catalyst is located in the shell side of the reactive stages and the inner tube in the permeative stages is the membrane, supported by 1 mm of porous stainless steel. The entire system is situated inside a furnace providing the necessary heat. The performances of the PSMR will be compared with those of a Membrane Reactor (MR) and a Traditional Reactor (TR) in the same configuration, geometry and working conditions. Schemes of these reactors are shown in Figure 5.2.

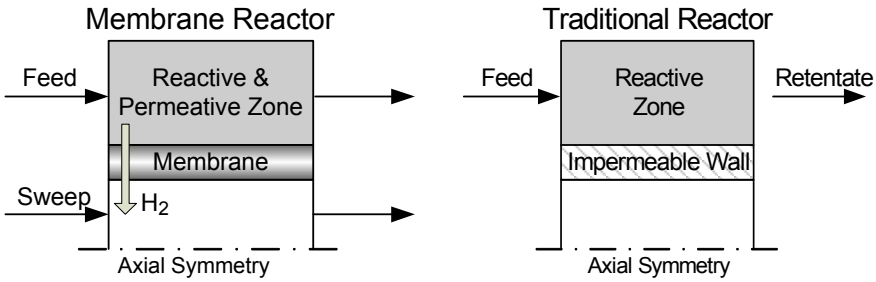

Figure 5.2 – Scheme of the Membrane Reactor (MR) and Traditional Reactor (TR).

In the results' representation, different total length for PSMR (= membrane length + catalytic bed length) and for MR and TR (= membrane length = catalytic bed length) are considered. The choice of different reactor lengths is due to the necessity to keep in the comparison the same conditions between the PSMR and MR, which means the same amount of catalyst and the same membrane area. In fact, in the MR the catalytic bed and membrane area occupy the

same volume and, obviously, have the same length. On the contrary, in the PSMR they are laid out as stages in series and, therefore, the length of the PSMR is double with respect to that of MR in the same conditions. However, in this way the heat exchange area of the PSMR is double compared to that of MR and TR. Although the effective amount of heat exchanged between the PSMR and the furnace does not only depend on the heat exchange area (the temperature difference profile has much more importance), the PSMR could have a certain advantage with respect to MR and TR. This aspect will be discussed later in Section 5.2.4.4. Hence, in a first time the PSMR (so as proposed) will be analyzed and compared with the MR and TR, since on a technical point of view represents the most logical solution of staged reactor. At the end of this analysis, a PSMR with the same furnace-to-retentate heat exchange area as the MR will be considered, evaluating the eventual advantages/disadvantages. The mechanism of the methane steam reforming on Ni-based catalyst is taken from Xu and Froment [5.12] (Eq. 5.1).

$$\begin{aligned} &CH_4 + H_2O \Leftrightarrow CO + 3H_2 && \Delta H_r^0 = 206\ \text{kJ/mol} \\ &CO + H_2O \Leftrightarrow CO_2 + H_2 && \Delta H_r^0 = -41.4\ \text{kJ/mol} \\ &CH_4 + 2H_2O \Leftrightarrow CO_2 + 4H_2 && \Delta H_r^0 = 165\ \text{kJ/mol} \end{aligned} \qquad (5.1)$$

The reaction rates corresponding to this mechanism are reported in Appendix A (Section 5.5.1) together with the kinetic and thermodynamic parameters.

5.2.2 MATHEMATICAL MODEL

The model has been developed considering 1D steady-state mass, momentum and energy balances in a tube-in-tube reactor. Reactive and permeative terms can be enabled or disabled depending on the reactor considered or the kind of stage in the PSMR. Non-isothermal conditions are taken into account, including the dependences of the gas properties, kinetics and permeance upon the temperature. Hydrodynamics is assumed as plug flow, since the

reactor diameter to length ratio is much smaller than unity. The co-current configuration considered allows to formulate the problem as an initial value problem. In the reaction rate the influence of the internal resistances to diffusive transport is small for the catalytic particle diameter less than 250 μm ca. [5.12].

5.2.2.1 SET OF EQUATIONS

From the above mentioned hypotheses and assumption, the mathematical system is characterized by non-linear ordinary differential equations and their respective initial conditions (Eq. 5.2-5.12).

5.2.2.1.1 MASS BALANCES

REACTIVE STAGES OF PSMR AND TR:

$$\frac{dF_i^{Ret}}{dz} = R_i \; A^{Ret}, \qquad \frac{dF_i^{Perm}}{dz} = 0 \tag{5.2}$$

PERMEATIVE STAGES OF PSMR:

$$\frac{dF_i^{Ret}}{dz} = -\frac{dF_i^{Perm}}{dz} = -N_i^{Mem} \, \pi \, D_m^{Mem} \tag{5.3}$$

MR:

$$\frac{dF_i^{Ret}}{dz} = R_i \; A^{Ret} - N_i^{Mem} \, \pi \, D_m^{Mem}, \quad \frac{dF_i^{Perm}}{dz} = N_i^{Mem} \, \pi \, D_m^{Mem} \tag{5.4}$$

with

$$N_i^{Mem} = \begin{cases} 0, & i \neq \mathrm{H_2} \\ N_{\mathrm{H_2}}, & i = \mathrm{H_2} \end{cases} \tag{5.5}$$

where F_i^{Ret} and F_i^{Perm} are the axial molar flow rate of the ith species of the retentate and permeate, respectively, R_i is the reaction rate of the ith species and N_{H_2} is the H_2 permeating flux through the Pd-alloy membrane. The permeation law (Eq. 5.6) is taken from Roy [5.13], where T^{Mem} is the membrane temperature.

$$N_{H_2} = \frac{\kappa}{\delta^{Mem}} exp\left(-\frac{E_d}{RT^{Mem}}\right)\left[\left(P_{H_2}^{Ret}\right)^n - \left(P_{H_2}^{Perm}\right)^n\right] \tag{5.6}$$

From a 2-D numerical simulation T^{Mem} was demonstrated to be almost the same as the temperature of the gaseous mixtures (very similar between each other) and, hence, it was calculated as arithmetical mean of the retentate and permeate temperatures. The values of the parameters in the Eq. 5.6 are reported in Table 5.1.

Table 5.1 – Permeation law parameters from Roy [5.13].

κ, mol m^{-1} s^{-1} Pa^{-n}	E_d, J mol^{-1}	n, -
1.7 10^{-10}	6.17 10^3	0.72

5.2.2.1.2 ENERGY BALANCES

REACTIVE STAGES OF PSMR AND TR:

$$\frac{d}{dz}\left(\sum_{i=1}^{n} F_i^{Ret}\,\Delta H_i^{Ret}\right) = U^{Ext}\pi\, OD^{Shell}\left(T^{Furnace} - T^{Ret}\right) + \\ - U^{Mem}\pi\, OD^{Tube}\left(T^{Ret} - T^{Perm}\right) \tag{5.7}$$

$$\frac{d}{dz}\left(\sum_{i=1}^{n} F_i^{Perm}\,\Delta H_i^{Perm}\right) = U^{Mem}\pi\left(T^{Ret} - T^{Perm}\right) \tag{5.8}$$

PERMEATIVE STAGES OF PSMR AND MR:

$$\frac{d}{dz}\left(\sum_{i=1}^{n} F_i^{Ret}\,\Delta H_i^{Ret}\right) = U^{Ext}\pi\, OD^{Shell}\left(T^{Furnace} - T^{Ret}\right) + \\ -U^{Mem}\pi\, OD^{Mem}\left(T^{Ret} - T^{Perm}\right) - \pi\, D_m^{Mem} N_{H_2}^{Mem}\Delta H_{H_2}\Big|_{T^{Ret}} \tag{5.9}$$

$$\frac{d}{dz}\left(\sum_{i=1}^{n} F_i^{Perm}\,\Delta H_i^{Perm}\right) = U^{Mem} OD^{Mem}\pi\left(T^{Ret} - T^{Perm}\right) + \\ +\pi\, D_m^{Mem} N_{H_2}^{Mem}\Delta H_{H_2}\Big|_{T^{Ret}} \tag{5.10}$$

where T indicates the temperatures, ΔH_i is the molar enthalpy, U^{Ext} is the heat transfer coefficients between the shell and the furnace and U^{Mem} the one between the retentate and permeate side, respectively. The procedures for evaluating the physical properties and the heat transfer coefficients are reported in Appendices B and C (Sections 5.5.2 and 5.5.3), respectively.

5.2.2.1.3 PRESSURE VARIATION

REACTIVE STAGES OF PSMR, MR AND TR:

In order to describe the total pressure drop along the catalyst bed, an Ergun's equation modified for the annular bed was used [5.14], where P is the pressure and v_c^{Ret} is the effective inter-particles velocity corrected with a correction factor f_c, which is calculated as indicated by Sodrè and Parise [5.14].

$$\frac{dP^{Ret}}{dz} = -\frac{v_C^{Ret}}{d_p}\frac{1-\varepsilon_{Bed}}{\varepsilon_{Bed}^3}\left(\frac{150\left(1-\varepsilon_{Bed}\right)\mu^{Ret}}{d_p} + 1.75\, v_C^{Ret}\rho^{Ret}\right) \tag{5.11}$$

PERMEATIVE STAGES OF PSMR AND PERMEATE SIDE OF THE MR AND PSMR:

The total pressure in the part of the reactors where there is no catalyst was considered constant.

$$\frac{dP^{Ret}}{dz} = 0, \qquad \frac{dP^{Perm}}{dz} = 0 \tag{5.12}$$

The system of coupled differential equations was solved by a Matlab® routine specific for stiff problems, since it belongs to this category of problems. The routine used, "ode15s", is a variable order solver based on the numerical differentiation formulas (NDFs) [5.15].

5.2.2.1.4 EVALUATION OF THE CATALYST EFFECTIVENESS FACTOR

In modelling a chemical reactor, a very important role is played by the effectiveness factor of the catalytic pellets involved in the reaction. In this study, a constant effectiveness factor was considered, estimating it by solving preliminarily the mass and energy balances (Eqs. 5.13-5.16) inside the generic spherical pellet (Figure 5.3) in correspondence of three zones (inlet, outlet and centre) of the reactors (both PSMR and ISMR).

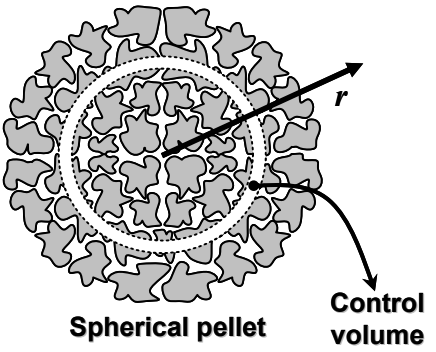

Figure 5.3 – Sketch of the generic spherical catalytic pellet considered for the effectiveness factor evaluation.

Mass balance on the ith species:
$$\frac{\partial N_i^{Cat}}{\partial r} + \frac{2}{r} N_i^{Cat} - R_i = 0 \quad (5.13)$$

Stefan-Maxwell equations:
$$\sum_{\substack{j=1 \\ j \neq i}}^{n} \frac{p_j^{Cat} N_i^{Cat} - p_i^{Cat} N_j^{Cat}}{P_T D_{ij,eff}^{MS}} + \frac{N_i^{Cat}}{D_{i,eff}^{K}} = -\frac{1}{RT} \frac{\partial p_i^{Cat}}{\partial r} \quad (5.14)$$

Energy balance:
$$\sum_{i=1}^{n} R_i \Delta \widetilde{H}_i - \frac{q^{Cat}}{k_{mix}} \sum_{i=1}^{n} N_i^{Cat} \widetilde{C} p_i + 2 \frac{q^{Cat}}{r} + \frac{\partial q^{Cat}}{\partial r} = 0 \,, \quad (5.15)$$

Fourier's equation:
$$q^{Cat} = -k_{mix} \frac{\partial T^{Cat}}{\partial r} \quad (5.16)$$

Evaluation of the effectiveness factor:
$$\eta_{Pellet} = \frac{3 \int_0^{r_p} R_i \, r^2 dr}{r_p^3 \, R_i^{Surf}} \quad (5.17)$$

The solution of Eqs. 5.13-5.17 was obtained by means of the Matlab® function "bvp4c", using the collocation method to solve a boundary value problem. Since an effectiveness factor close to 0.7 was achieved from these calculations, this value was used as constant in the simulations, where the same catalyst geometrical data as the ones adopted for the model validation (see Table 5.2 in Section 5.2.2.2) were utilized.

5.2.2.2 MODEL VALIDATION

The model has been validated by means of some literature experimental data taken from Tong *et al.* [5.16]. It must be specified that the authors did not indicate in their paper the catalyst data, which are necessary for evaluating the effectiveness factor and, hence, for the correct model

validation. Nevertheless, these data was provided by one of the authors by a private communication [5.17], in which he specified the data reported in Table 5.2, according to which an effectiveness factor of about 0.03 was calculated. This very low value is not surprising, since the pellet diameter is very large compared to the very high reaction rate of methane steam reforming in the process conditions considered [5.16]. Furthermore, a proof of effectiveness factors of this order of magnitude was also provided by Xu and Froment [5.18], who calculated in their work values in the range [0.01-0.06].

Table 5.2 – Catalyst geometrical data used in the calculation [5.17].

Mean pellet diameter	Porosity	Tortuosity (estimated by the authors)	Material density	BET surface area
3.175 mm	0.4482	5.5	5,075 kg m^{-3}	115,300 m^2 kg_{Cat}^{-1}
The pellets have the shape of an equi-lateral cylinder				

The comparison with the experimental data is showed in Figure 5.4, which reveals a very good accordance between the model and the experimental data. The Pd-based membrane (supported) used by Tong *et al.* [5.16] has permeation law parameters different from those of the membrane considered for the simulation in the present analysis. In particular, they found that their supported membrane (6 μm thick) obeys a modified Sieverts' law with a driving force exponent n very close to 1. This fact indicates that the permeation through the membrane is mainly controlled by the transport in the support. If a higher membrane thickness is considered, the permeation law of Tong *et al.* [5.16] is no longer valid, since the relative influence of the controlling mechanisms change because of a more important contribution of the transport in the Pd-based layer (if the transport in the Pd-based layer is the only rate-determining step, the driving force exponent is 0.5, which corresponds to the original Sieverts' law). Since in this chapter the role of the membrane thickness is also investigated, a permeation law accounting for the presence of both the transport mechanisms (transport in the support and in palladium) is required.

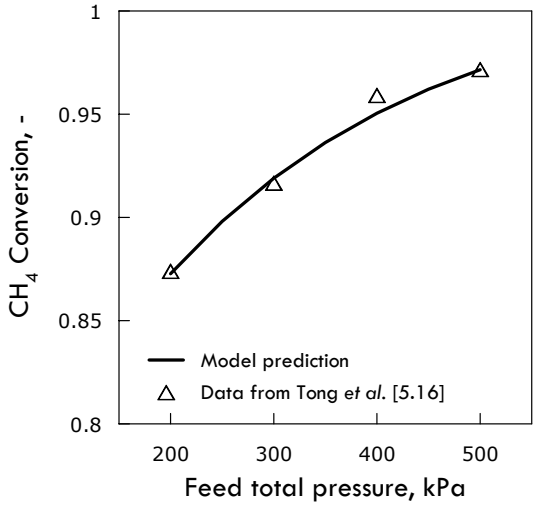

Figure 5.4 – Comparison between the model and some experimental data from Tong *et al.* [5.16].

In this sense, the permeation law from Roy [5.13] is chosen, as done also by other authors in literature (e.g., see the work of Tiemersma *et al.* [5.6]).

5.2.3 OPTIMIZATION PROCEDURE

In this section, two different objective functions are chosen to be maximized: methane (limiting reactant) conversion and hydrogen (the only permeating species) recovery factor, both defined in Table 5.3 together with the hydrogen recovery yield. All these three parameters are used to measure the performances of the systems considered here. The factor "4" at the denominator in the definition of RY is the maximum number of H_2 moles produced per mole of methane reacted according to mechanism stoichiometry. The choice of these objective functions is driven by the fact that almost always these two parameters are used in literature to evaluate the performances of a membrane reactor for H_2 production. The reason why two different objective functions are considered arise from the consideration that in general it is not possible to know *a priori* whether or not the two criteria are equivalent, that is, whether or not the maximum x corresponds to the maximum RF and vice-versa. In this study, the length of the

stages are set as decisional variables with respect to which the optimization is carried out, keeping the total catalyst amount and membrane area as constant.

From a mathematical point of view, the optimization problem for the two objective functions considered is formulated as reported in Eq. 5.18-5.22, where l_i^R and l_i^P are the lengths of the ith Reactive ("*R*") and Permeative ("*P*") stage, respectively and l^{Min} represents the minimum length that a stage can reach. The variables l^{Cat} and l^{Mem} are the catalyst bed length and membrane length, respectively, and are both equal because of the system considered. The presence of a minimum length arises from the necessity of each stage to have a non-zero integration domain. Anyway, the fact that the procedure provides as result one or more stages of the order of l^{Min}, indicates that these stages can be neglected. The optimization procedure was developed in Matlab® [5.15], using the function "*fmincon*" that finds a minimum of a constrained multivariable function.

Table 5.3 – Factors used to analyze the performances of the reactors considered here.

Factor	Description	Formal Definition	Mathematical Definition
x	CH_4 Conversion	$\frac{CH_4 \text{ Converted}}{CH_4 \text{ Fed}}$	$1-\frac{F_{CH_4}}{F_{CH_4}^0}$
RF	H_2 Recovery Factor	$\frac{H_2 \text{ Recovered in the Permeate Side}}{H_2 \text{ Produced}}$	$\frac{F_{H_2}^{Perm}}{F_{H_2}^{Ret}+F_{H_2}^{Perm}}$
RY	H_2 Recovery Yield	$\frac{H_2 \text{ Recovered in the Permeate Side}}{\text{Maximum } H_2 \text{ Produced at total } CH_4 \text{ Conversion}}$	$\frac{F_{H_2}^{Perm}}{4F_{CH_4}^0}$

$$\max_{l_i} x \quad or \quad \max_{l_i} RF \tag{5.18}$$

s.t.:

$$\sum_{i=1}^{n^R} l_i^R = l^{Tot}, \qquad \sum_{i=1}^{n^P} l_i^P = l^{Tot} \tag{5.19}$$

$$l^{Min} < l_i^R, \; l_i^P < l^{Tot} \tag{5.20}$$

$$\underline{l} = \left\{ l_1^R, \ldots, l_{n^R}^R, l_1^P, \ldots, l_{n^P}^P \right\}$$

with: (5.21)

$$l^{Tot} = l^{Mem} = l^{Cat}$$

In order to use this Matlab® function, the problems (Eq. 5.18) are re-formulated as indicated by Eq. 5.22, subjected to the same constraints as before. Since the problem is complicated by strong non-linearities and may exhibit multiple local minimum points, several initial guess vectors are used to find the global minimum.

$$\min_{l_i} \left\{ 1 - x \right\} \quad or \quad \min_{l_i} \left\{ 1 - RF \right\} \tag{5.22}$$

5.2.4 RESULTS AND DISCUSSIONS

The geometrical data and the operating conditions of the reactor considered in this study are summarized in Table 5.4 and Table 5.5.

Table 5.4 – Operating conditions.

Side	Pressure, kPa							Total flow rate, mmol/s
	H_2	CH_4	CO_2	H_2O	CO	N_2	Total	
Feed	-	200	-	600	-	-	800	8
Sweep	-	-	-	-	-	120	120	1
T^{FUR}, °C = {400; 500; 600}, ε_{Bed} = 0.50, ε_{Supp} = 0.40								

Table 5.5 – Geometrical data of the system.

ID^{Tube}, mm	δ^{Mem}, μm	δ^{Supp}, mm	ID^{Shell}, mm	OD^{Shell}, mm	l^{Mem}, cm	d_p, mm
10	{1; 10; 50}	1	30	32	50	0.25

5.2.4.1 EQUI-SIZED STAGES.

The first configuration considered is the most intuitive one: the equi-sized configuration, in which the stage lengths of reactive stages are equal to each other, the same holding for the permeative ones. Figure 5.5 shows the partial pressure profiles of some of the components involved in the process considering a furnace temperature of 600°C and a membrane thickness of 1 μm. In the reaction side only the limiting species (CH_4) and the component to recover (H_2) are reported, whereas the hydrogen and the sweep-gas are shown in the permeate side. In the reactive stages (non-permeable) the CH_4 partial pressure profile decreases and the H_2 one increases continuously, whereas in the other side of the reactor nothing occurs to the N_2 and H_2 profiles (flat profiles) because the reaction side is insulated.

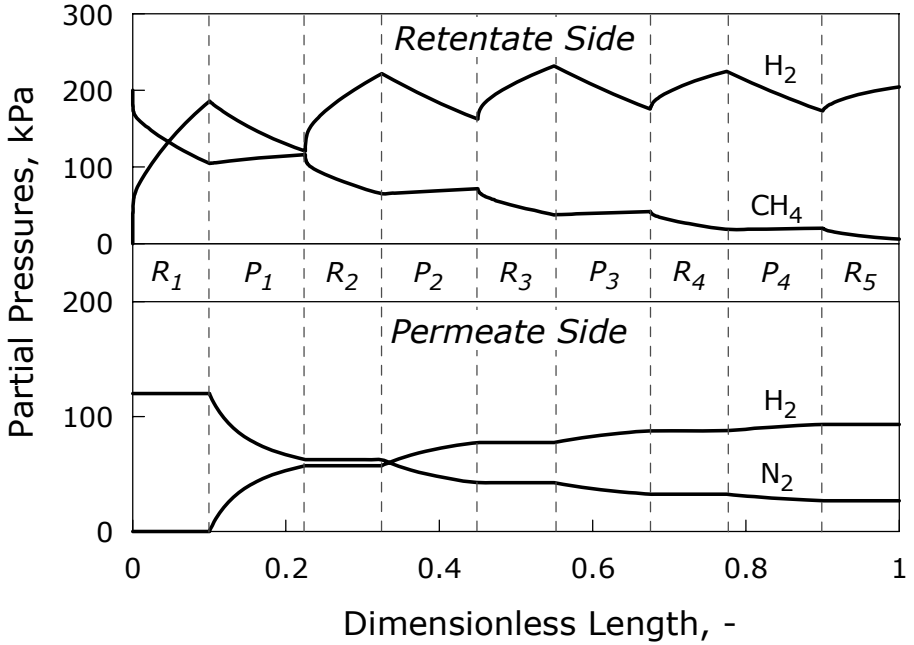

Figure 5.5 – Partial pressure profiles of some of the species involved in the process at T^{Fur} = 600°C and $\delta^{Pd\text{-}layer}$ = 1 μm with an equi-sized reactive and permeative stages. The other operating conditions are specified in Table 5.4. The vertical dashed-lines show the boundaries of each stage. The letters "R" and "P" respectively indicate "Reactive" and "Permeative" stage and the subscripts are the progressive numbers of the stage.

In the permeative stages, H_2 flows through the membrane and its partial pressure decreases along the retentate side and increases along the permeate side. Therefore, the plot shows a typical saw-teeth shape. Since in these stages the total pressure is constant along the sides, the CH_4 partial pressure increases and the N_2 one decreases.

As regards the temperature profiles, an analogous situation (Figure 5.6) can be observed. In the retentate side of the reactive stages the temperature exhibits a minimum as a result of two contrasting phenomena: the heat absorbed by the reaction and the heat transferred from the furnace and the permeate side. Due to the decreasing reaction rate, this minimum tends to the

furnace temperature moving toward the end of the reactor. The energy transfer affects also the temperature of the permeate side and its profile presents a minimum. In the permeative stages, the profiles of both sides increase monotonically, tending to the furnace temperature. In order to have an idea of the performances of the PSMR in these operating conditions, x and RF are shown in Figure 5.7 and Figure 5.8, where also the comparison with the MR is made for different membrane thicknesses. Concerning the PSMR, the first two stages present the same behaviour for all the thicknesses considered, since there is no membrane in the reactive stages and, thus, the permeative stages do not affect the methane conversion.

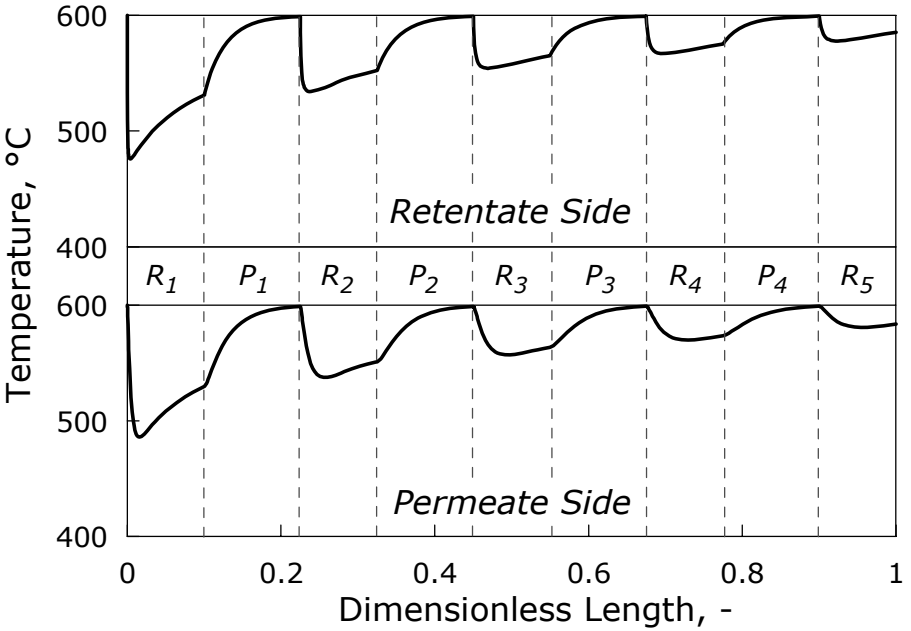

Figure 5.6 – Temperature profiles at T^{Fur} = 600°C and $\delta^{Pd\text{-}layer}$ = 1 μm with an equi-sized reactive and permeative stages. The other operating conditions are specified in Table 5.4. The vertical dashed-lines show the boundaries of each stage. The letters "R" and "P" respectively indicate "Reactive" and "Permeative" stage and the subscripts are the progressive numbers of the stage.

The differences arise from the third stage on, where the smaller amount of H_2 in the reaction side due to the presence of the membrane in the second stage determines a larger reaction rate than those of the thicker Pd-alloy layers considered. This effect increases more when the last stages are considered. In the MR, the largest differences are toward the reactor end, whereas at the beginning the behaviour of the reactor for all of the thicknesses is very similar. This is due to the reaction rate of the process involved that is much higher than the hydrogen permeation rate at the beginning of the reactor. Therefore, the influence of the permeation on x is negligible. When the reaction rate decreases (toward the end of the reactor), the permeation rate plays a leading role in determining a high conversion, this effect being larger as thinner thicknesses (high permeating fluxes) are considered. By making a comparison in the most favourable cases (membrane thickness of 1 μm) for both reactors considered in the figure, a certain advantage is found in terms of x using the PSMR instead of the MR (0.968 vs 0.928).

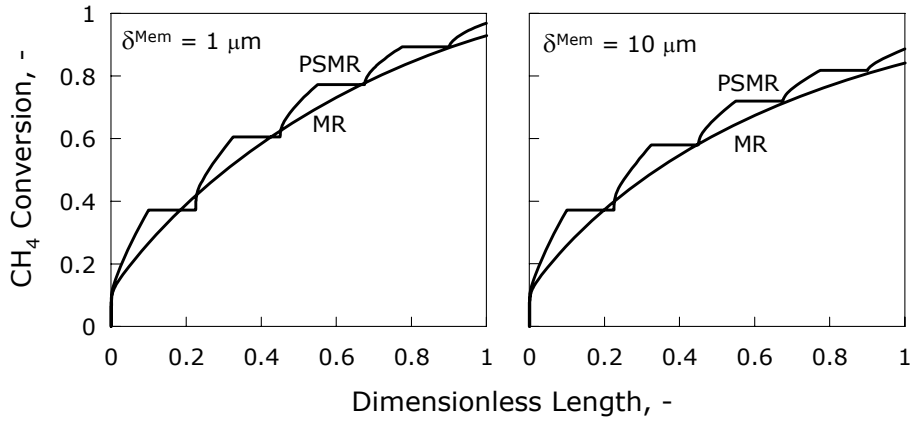

Figure 5.7 – CH_4 conversion profiles at T^{Fur} = 600°C for different values of $\delta^{Pd\text{-}layer}$ with an equi-sized catalyst and membrane distribution. The other operating conditions are specified in Table 5.4.

Before conclusions are drawn on the performance of the PSMR compared with the MR, it necessary to analyze the other parameter useful to check the performances of a membrane reactor, i.e. RF (Figure 5.8).

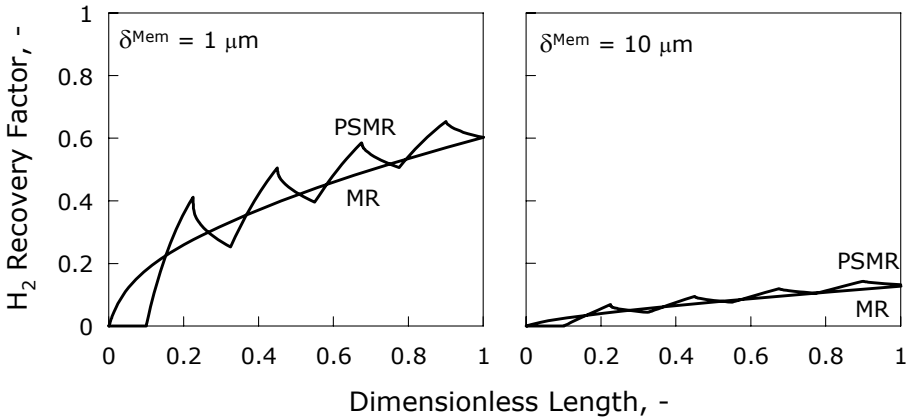

Figure 5.8 – RF profiles at T^{Fur} = 600°C for different values of $\delta^{Pd\text{-}layer}$ with an equi-sized catalyst and membrane area distribution. The other operating conditions are specified in Table 5.4.

Whereas the conversion increases monotonically in the reactive stages and is constant in the permeative ones, RF increases in the permeative stages and continuously decreases in the reactive ones (except for the first stage, where it is set to zero by convenience). This is due to RF definition, being the ratio of the hydrogen permeated to that produced by reaction. In the reactive stages the amount of H_2 produced increases and RF decreases, since the amount permeated is constant. As a general trend, the final RF is almost equal for the two reactors.

5.2.4.2 OPTIMIZATION OF METHANE CONVERSION

In Figure 5.9 and Table 5.6 the lengths of the optimal distributions calculated by maximizing the conversion x are reported for several different membrane thicknesses. It is interesting to notice the remarkable difference of the behaviour at 1 μm with respect to 10 and 50 μm. In fact, while in all cases the permeative stages are of the same order of magnitude, the first four reactive

stages at low permeating fluxes (10 and 50 μm) are very small compared to the corresponding ones at 1 μm. This trend can be explained by means of the following considerations. Let us assume, for simplicity, the systems with high membrane thicknesses to be impermeable, so that the permeative stages act only as heaters. It shall be noticed that high temperatures promote the reaction kinetics and, at the same time, lead to an increased equilibrium conversion. Hence, the system tends to assume the highest possible temperatures in the reactive stages. Due to the endothermicity and elevated reaction rate, the maximum temperature reductions occur at the beginning of each reactive stage.

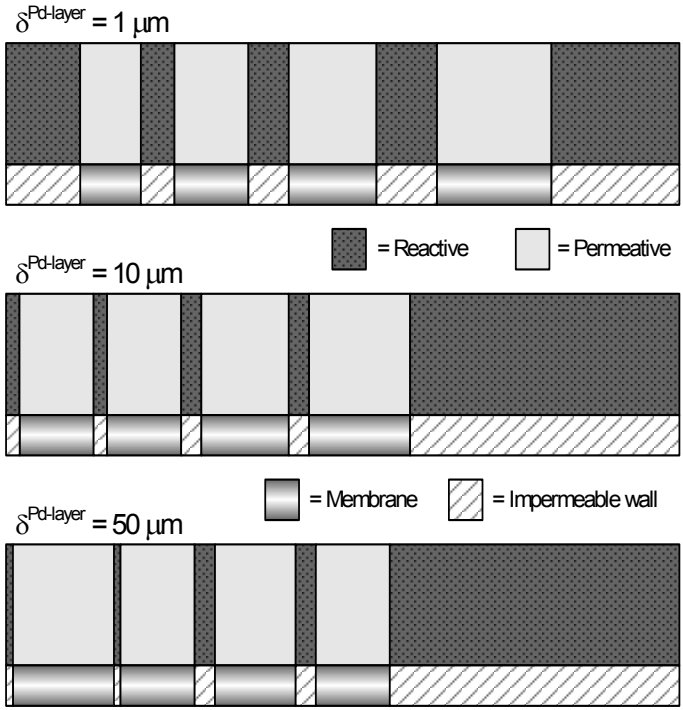

Figure 5.9 – Shape of the optimal distributions with maximized conversion for several membrane thicknesses at T^{Fur} = 600°C. The other operating conditions are specified in Table 5.4.

Table 5.6 – Optimal lengths' distribution for the maximum conversion compared with the equi-sized case. The letters "R" and "P" indicate "Reactive" and "Permeative" stage, respectively.

$\delta^{Pd\text{-}layer}$, μm	Stages Lengths, %								
	R_1	P_1	R_2	P_2	R_3	P_3	R_4	P_4	R_5
1	11	9	5	11	6	13	9	17	19
10	2	11	2	11	3	13	3	15	40
50	1	15	1	11	3	12	3	11	43
Equi-sized:	10	12.5	10	12.5	10	12.5	10	12.5	10

Therefore, to maximize the reaction rate, a permeative (i.e. heating) stage is inserted after each small reaction volume in the optimized system. The results of this situation are shown in Figure 5.10 in terms of conversion profiles along with those of the MR.

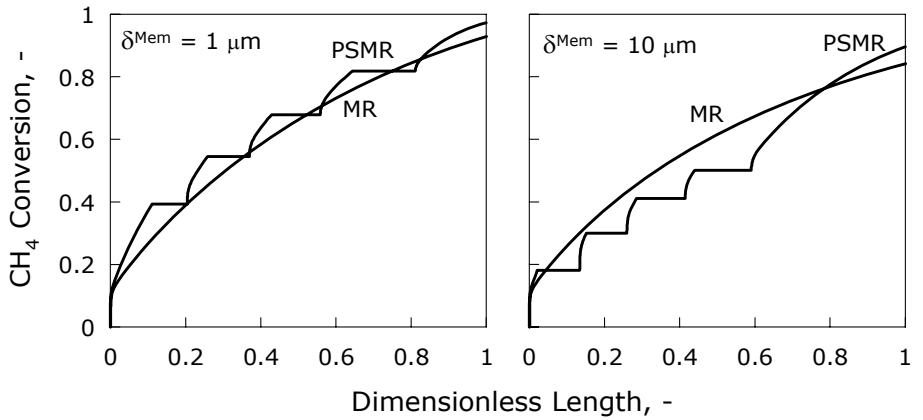

Figure 5.10 – CH_4 conversion profiles at T^{Fur} = 600°C for different values of $\delta^{Pd\text{-}layer}$ with the catalyst and membrane area distribution optimized with respect to the maximum conversion. The other operating conditions are specified in Table 5.4.

Table 5.7 – Comparison among the CH_4 conversions in the different membrane reactors (T^{Fur} = 600°C).

$\delta^{Pd\text{-}layer}$, μm	Equi-sized PSMR	Optimized PSMR (Maximum x)	MR	Optimized PSMR vs MR
1	0.968	0.973	0.928	+ 4.9 %
10	0.886	0.896	0.842	+ 6.4 %
50	0.875	0.884	0.832	+ 6.3 %

The qualitative behaviour of these conversion profiles is the same as that shown in Figure 5.7, but in this case the conversions for the three thicknesses considered are a little higher than earlier (see Table 5.7). Figure 5.11 shows a comparison of the conversions of the optimized PSMR, MR and TR for all the furnace temperatures and membrane thicknesses considered.

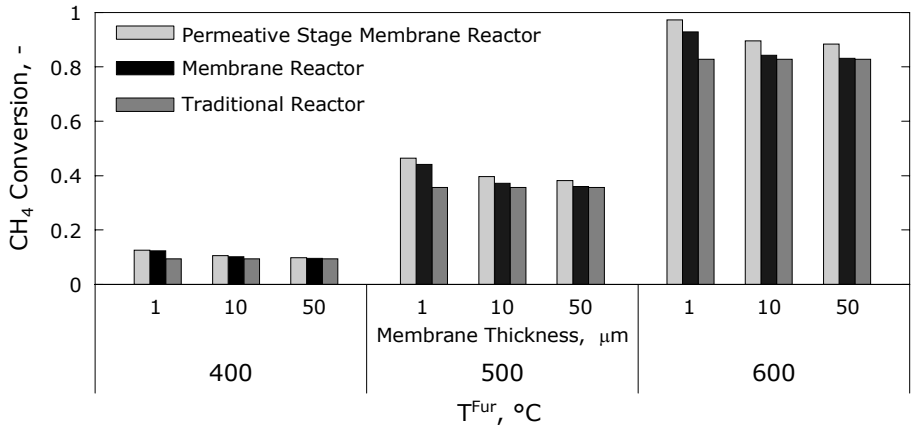

Figure 5.11 – Comparison among the CH_4 conversion of a PSMR (with the catalyst and membrane area distribution optimized with respect to the maximum conversion), MR and TR as function of $\delta^{Pd\text{-}layer}$ and T^{Fur}. The other operating conditions are specified in Table 5.4.

For 500 and 600°C at higher thicknesses (10 and 50 μm) the conversions in MR and TR are very close, while the PSMR exhibits a significant improvement. At 400°C the performances of the three reactors are comparable, but very low. It is interesting to notice that even at high membrane thicknesses the conversion in the PSMR is still higher than the MR and TR, these two having similar behaviour, due to the above mentioned beneficial effects of the heat exchange in the permeative stages. In Figure 5.12 the profiles of RF are reported. It can be noticed that the performances of the MR are higher than those of PSMR for all the thicknesses considered, differently from the equi-sized case (Figure 5.8).

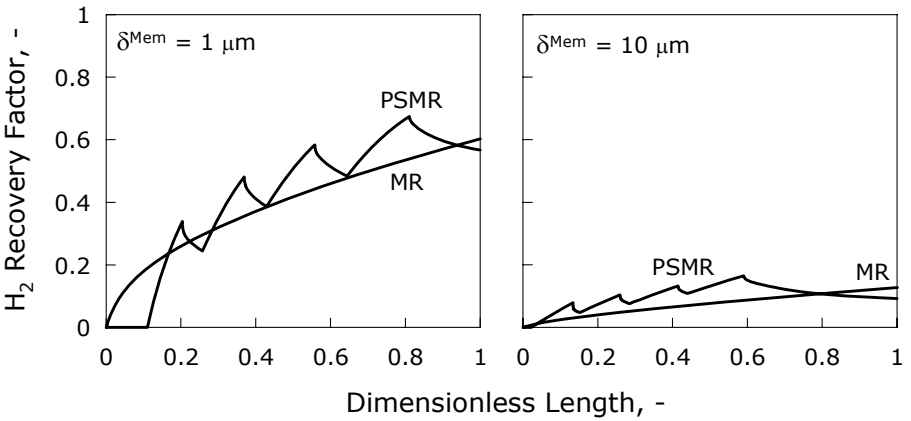

Figure 5.12 – RF profiles at T^{Fur} = 600°C for different values of $\delta^{Pd\text{-}layer}$ with the catalyst and membrane area distribution optimized with respect to the maximum conversion. The other operating conditions are specified in Table 5.4.

This result is particularly significant as it shows that maximizing x does not necessarily mean maximizing RF, making the choice of the objective function a crucial point for this kind of analysis. In fact, the increase of x and the simultaneous decreases of RF are caused by the last reactive stage, whose presence is due to the optimum criterion considered. Before considering another objective function, let us verify the uniqueness of the solution by checking whether similar maximum conversions are reached with different lengths' distributions, starting

with different initial guesses. Some of the optimal distributions are shown in Figure 5.13, where x and RF profiles are reported.

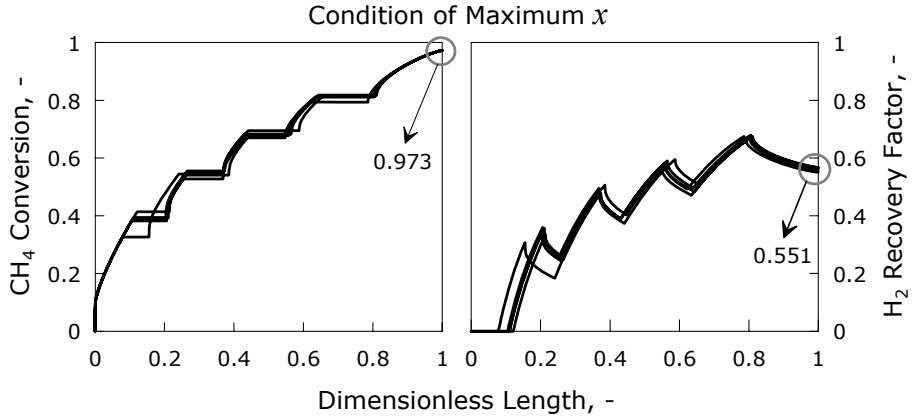

Figure 5.13 – Comparison among the profiles of several optimal distributions by imposing the maximum conversion criterion. $\delta^{Pd\text{-}layer}$ = 1 μm and T^{Fur} = 600°C. The other operating conditions are specified in Table 5.4.

While the differences in the final conversion are in all cases less than a prescribed tolerance of $5 \cdot 10^{-4}$, the differences among the final RF s are small enough (3% at most) to consider a unique final mean value. In order to find the maximum performance improvement achievable by an optimized PSMR it is useful to evaluate the "optimized" distribution corresponding to the minimum x. Applying the same numerical procedure and setting the minimum x criterion at T^{Fur} of 600°C and 1 μm membrane thickness, the results shown in Figure 5.14 are found, where also the maximum x case is reported for comparison. As expected, the procedure provides a distribution corresponding to only one reactive stage followed by only one permeative stage. Interestingly, the difference between the two situations considered in Figure 5.14 is very significant, moving from a conversion of 0.973 (maximum x) to a conversion of 0.832 (minimum x). This means that in the same operating conditions, with the same amount of catalyst and

membrane area, there is a considerable range of conversions (spanning 15.6% with respect to the mean value) uniquely due to the distribution. This fact demonstrates the importance of the distribution as a parameter to improve the system performance, also considering that it is a variable relatively easy to change without affecting other aspects of the process.

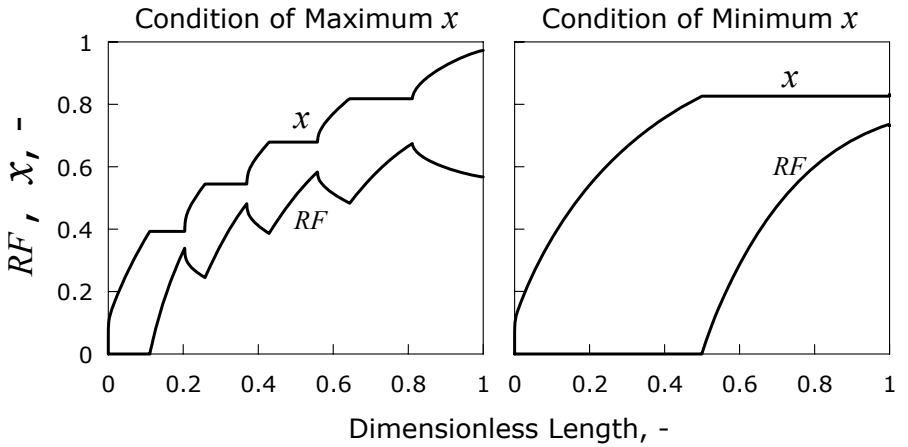

Figure 5.14 – Profiles of x and RF in PSMR calculated by imposing the maximum and minimum conversion, respectively. T^{Fur} = 600°C, $\delta^{Pd\text{-}layer}$ = 1 μm. The other operating conditions are specified in Table 5.4.

5.2.4.3 OPTIMIZATION OF H_2 RECOVERY FACTOR

The other objective function considered is RF, whose distributions for 1 and 10 μm are shown in Figure 5.15 and reported in Table 5.8. It is possible to notice that for all the membrane thicknesses considered, the last reactive stage presents the lowest length allowed. This means that the initial choice of placing a reactive stage at the end of the PSMR does not influence the final result of the optimization procedure. In the cases of 10 μm and higher thicknesses (not reported) the system is reduced to only two stages (one reactive and one permeative), whilst at 1 μm the intermediate permeative stages are very small compared to the last ones, but not negligible.

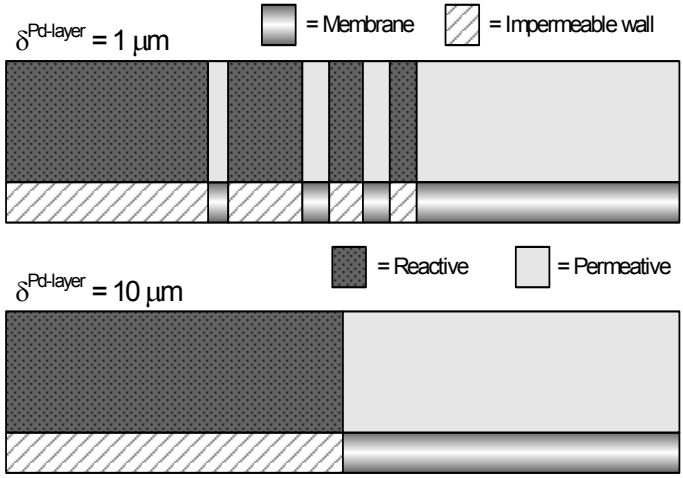

Figure 5.15 – Shape of the optimal distributions with maximized recovery factor for two membrane thicknesses at T^{Fur} = 600°C. The operating conditions are specified in Table 5.4.

Table 5.8 – Optimal lengths' distribution for the maximum RF compared with the equi-sized case. The letters "R" and "P" indicate "Reactive" and "Permeative" stage, respectively.

$\delta^{Pd\text{-}layer}$, μm	Stages Lengths, %								
	R_1	P_1	R_2	P_2	R_3	P_3	R_4	P_4	R_5
1	30	3	11	4	5	4	4	39	≈ 0
10	27	≈ 0	15	≈ 0	8	7	≈ 0	43	≈ 0
Equi-sized:	10	12.5	10	12.5	10	12.5	10	12.5	10

In terms of x, a significantly different situation with respect to Figure 5.10 is found (Figure 5.16), because in this case the conversion of the PSMR is lower than that of the corresponding MR. In this case, the situAt 10 and 50 μm the profiles are nearly coincident (the 50 μm case was not reported)

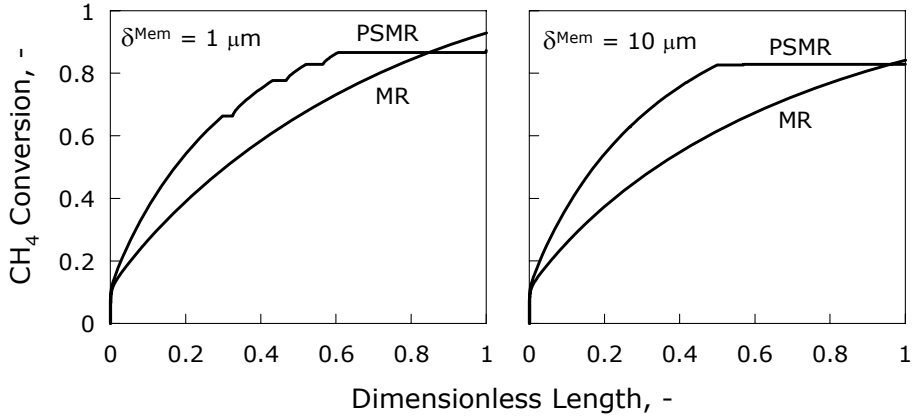

Figure 5.16 – Profiles of x for different values of $\delta^{\text{Pd-layer}}$ with the catalyst and membrane area distribution optimized with respect to the maximum RF. T^{Fur} = 600°C. The other operating conditions are specified in Table 5.4.

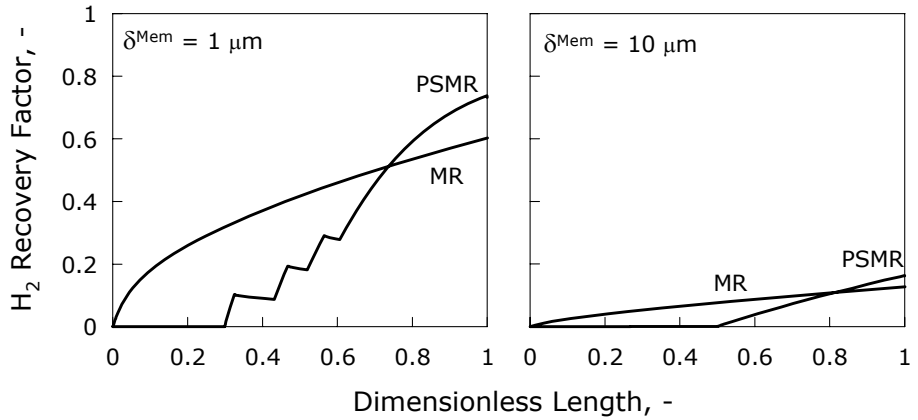

Figure 5.17 – Profiles of RF for different values of $\delta^{\text{Pd-layer}}$ with the catalyst and membrane area distribution optimized with respect to the maximum RF. T^{Fur} = 600°C. The remaining operating conditions are specified in Table 5.4.

As far as RF is concerned, it is possible to observe in Figure 5.17 that higher performances can be achieved using the PSMR than using the MR (RF = 73% vs. 60% at 1 μm). An

interesting thing to remark is that the minimum x criterion (Figure 5.14) leads to a RF value very close to that obtained by using the maximum RF criterion (about 0.73 in both cases), but quite different values of x (0.83 vs 0.87, respectively). This confirms that the two variables considered as objective functions are evidently independent.

At this point it is useful to summarize the performances of the PSMR for the two optimum criteria considered, comparing them with the performances of the MR in the most favourable conditions (Figure 5.18). Considering the maximum conversion, the PSMR exhibits a higher x and lower RF than the MR.Analogously, when the maximum RF condition is set, a higher RF and lower x than the MR is found. Which of the two criteria gives the best results of all depends on plant-scale economical considerations (e.g. separation costs) rather than on the sole reactor performances.

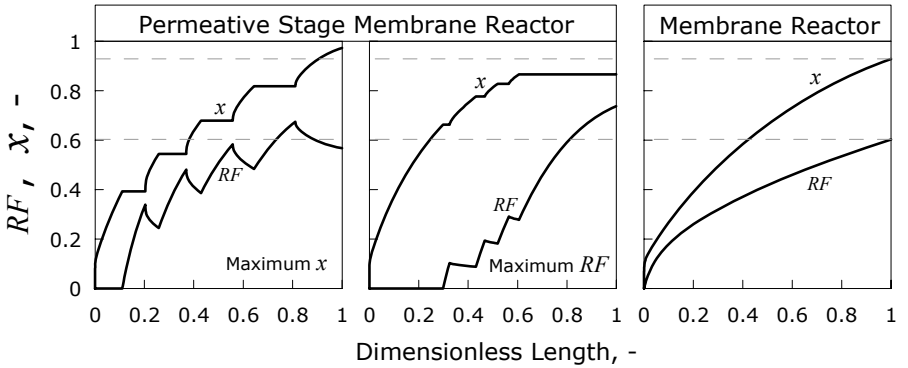

Figure 5.18 – Comparison among the performances of PSMR and MR. $\delta^{Pd\text{-}layer}$ = 1 μm, T^{Fur} = 600°C. The dashed lines indicate the MR values. The remaining operating conditions are specified in Table 5.4.

5.2.4.4 ON THE ROLE OF THE HEAT EXCHANGE AREA IN THE PSMR, MR AND TR

In Section 5.2.1, the question about the different heat exchange area between the PSMR and the MR has been temporarily held in reserve. In this section, this question is re-considered and studied in details. For setting in both the cases the same exposed area to the furnace, a PSMR

having adiabatic permeative stages is analyzed. Once the heat exchange area of the PSMR is set, the optimization procedure is carried out by maximizing one-by-one x and RF.

The results of the procedure are showed in Figure 5.19. In Table 5.9 the final values of x and RF are showed for the PSMR with adiabatic permeative stages, for the MR and also for the PSMR with no adiabatic stages (previously considered).

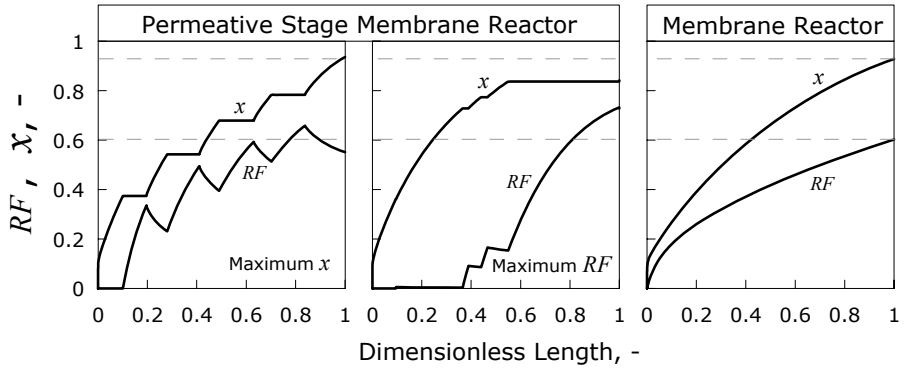

Figure 5.19 – Comparison among the performances of PSMR for which adiabatic permeative stages are considered and MR. $\delta^{Pd\text{-}layer}$ = 1 μm, T^{Fur} = 600°C. The dashed lines indicate the MR values. The remaining operating conditions are specified in Table 5.4.

This analysis shows that, when adiabatic permeative stages are considered, the advantage of the PSMR with respect to the MR decreases in terms of conversion, but substantially remains of the same order of magnitude in terms of RF. In particular, looking at the condition of maximum *RF*, an *RF* of about 21% higher than that of the MR is found for both the two PSMRs considered, independently of the different exchange areas. In this sense, only when the conversion is taken as objective function, the double exchange area of the PSMR without adiabatic stages gives a certain advantage compared to the PSMR with adiabatic permeative stages (0.973 vs 0.936 in terms of x), whereas the advantage becomes negligible carrying out the maximization of RF (0.732 vs 0.728 in terms of RF).

Table 5.9 – Comparison between x and RF in the different cases considered. $\delta^{Pd\text{-}layer}$ = 1 μm and T^{Fur} = 600°C. The values in parentheses are differences in percentage with respect to the values of MR.

Performance indices	Optimized PSMR with no adiabatic stages		Optimized PSMR with adiabatic permeative stages		MR
	Maximum x	Maximum RF	Maximum x	Maximum RF	
x	0.973 (+4.8%)	0.873 (-5.9%)	0.936 (+0.9%)	0.841 (-9.4%)	0.928
RF	0.567 (-5.8%)	0.732 (+21.6%)	0.551 (-8.5%)	0.728 (+20.9%)	0.602

Another aspect which needs to be considered is that different exchange areas could affect the amount of power transferred from the furnace to the retentate side. Table 5.10 reports this power evaluated for each reactor considered.

Table 5.10 – Power exchanged between furnace and retentate for the distributions considered. $\delta^{Pd\text{-}layer}$ = 1 μm, T^{Fur} = 600°C. The values in parentheses are differences in percentage with respect to the value of MR.

	Optimized PSMR with no adiabatic stages		Optimized PSMR with adiabatic permeative stages		MR	TR
	Maximum x	Maximum RF	Maximum x	Maximum RF		
Power exchanged [W] Furnace → Retentate	657 (+6%)	592 (-4%)	625 (+1%)	557 (-10%)	618	551 (-11%)

From the table, it is clear that the transferred power is not only related to the exchange area. In fact, the MR and the TR, which have the same exchange area, are characterized by very different values of power. Furthermore, even the exchanged power in the PSMR with no adiabatic stages is higher or lower than that of the MR in dependence on the objective function considered. The same occurs for the PSMR with adiabatic permeative stages, as a result of the particular temperature difference profile in the equipment. This means that the most important

factor is not as much the amount of exchange area, but rather how the system exploits this area in order to fulfil the design requirements.

5.2.4.5 CHOICE OF THE "MOST CONVENIENT" OBJECTIVE FUNCTION

Since the impact of the conversion and recovery factor on the process economy is not included in the present analysis, it is chosen here to consider the "best" distribution the one providing the highest recovery yield RY., which represents an indication of the hydrogen productivity with respect to the limiting reactant.

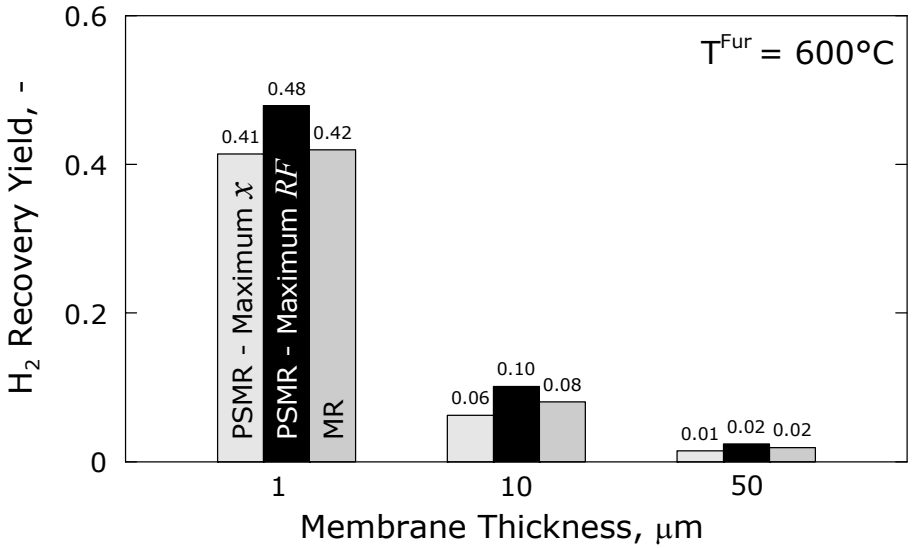

Figure 5.20 – Hydrogen permeate molar flow rate for the PSMR (in the two optimization criteria considered) and MR at T^{Fur} = 600°C for all the $\delta^{Pd\text{-}layer}$ considered. The other operating conditions are specified in Table 5.4.

In fact, by definition, RY represents the amount of hydrogen recovered in the permeate side divided by the maximum amount of hydrogen that can be theoretically produced according to the reaction scheme (Eq. 5.1). In Figure 5.20 RY is reported as a function of the membrane

thickness at 600°C for the MR and the two optimized PSMRs. At 1 μm RY in the RF-optimized reactor is larger of about 14% than in the other two systems. The same behaviour can be observed at 10 and 50 μm, for which the relative differences increase. In accordance with these results, the maximization of RF appears superior for all the thicknesses examined.

5.3 CASE STUDY II: INERT-STAGE MEMBRANE REACTOR

5.3.1 OPTIMIZED STAGE LENGTHS

The other membrane reactor considered is the ISMR, shown in Figure 5.21. As already mentioned, several reactive stages are in alternative series with the same number of inert stages.

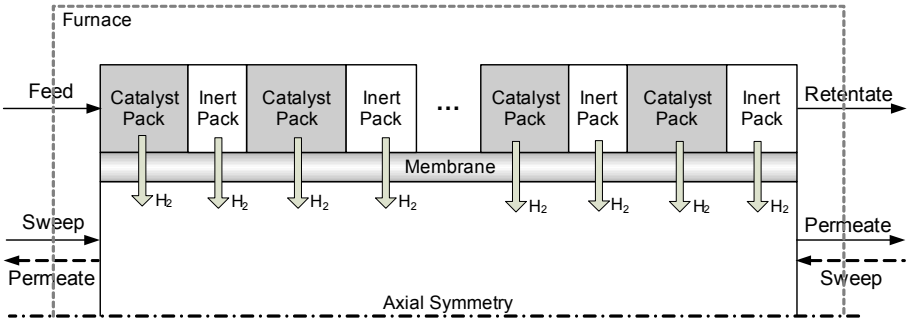

Figure 5.21 – Scheme of the Staged Membrane Reactor (SMR) considered.

The whole equipment is located in a furnace, whose temperature is considered to be the same as that of the shell external wall. In this section, a two-stage reactor (with one reactive and one inert stage) and two ten-stage ones (five reactive and five inert stages) are compared to each other, choosing to set the total catalyst bed length as one half of the total membrane length. The inert zones can be viewed as void or filled of inert pellets having the same physical properties as the catalytic ones. If, on one hand, this fact causes an increase of the pressure drops along the reactor, on the other hand it leads up to very flexible equipment, where the

length of each stage can be easily modified without more complicated connections. The choice of ten stages is related to the necessity of considering not too long or too short stages. The membrane here-considered, present in both reactive and inert zones, is a supported Pd-based membrane, whose permeation characteristics are taken from the experimental work of Tong *et al.* [5.16]. The reactor performances are studied in both co- and counter-current configurations, comparing its performances to those of the analogous staged traditional reactor in the same geometry and configuration, as shown in Figure 5.22.

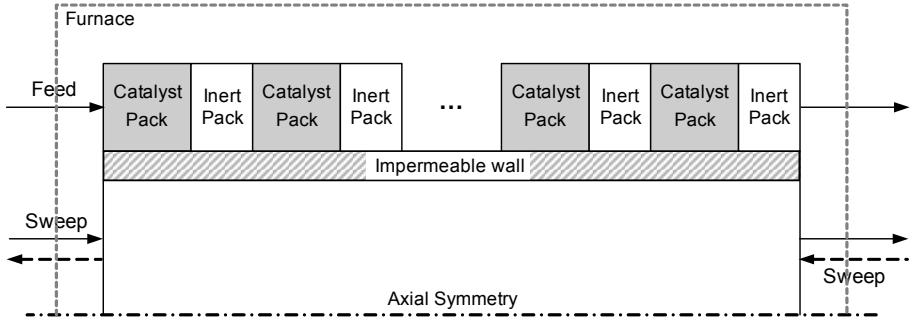

Figure 5.22 – Scheme of a Staged Traditional Reactor (STR) with the same catalyst distribution as the SMR shown in Figure 5.21.

5.3.2 MATHEMATICAL MODEL

The hypotheses of the model and its validation are the same as reported in Section 5.2.2.2. Modifications are related to the presence of the counter-current configuration, improved correlation for heat transfer (see Appendix A in Section 5.5.3 for the details) and other minor changes.

5.3.2.1 SET OF EQUATIONS

The equations relative to the mass balances for both reactive and inert stages are shown in the Eq. 5.23, where the same notation as the PSMR case is used.

$$\frac{dF_i^{Ret}}{dz} = R_i \; A^{Ret} - N_i^{Mem} \, \pi \, D_m^{Mem}, \qquad \frac{dF_i^{Perm}}{dz} = N_i^{Mem} \, \pi \, D_m^{Mem} \tag{5.23}$$

with

$$N_i^{Mem} = \begin{cases} 0, & i \neq \mathrm{H_2} \\ N_{\mathrm{H_2}}, & i = \mathrm{H_2} \end{cases} \tag{5.24}$$

$$N_{\mathrm{H_2}} = \frac{\kappa}{\delta^{Pd-layer}} exp\left(- \frac{E_d}{RT^{Mem}} \right) \left[\left(P_{\mathrm{H_2}}^{Ret} \right)^n - \left(P_{\mathrm{H_2}}^{Perm} \right)^n \right] \tag{5.25}$$

Table 5.11 – Permeation law parameters from Tong *et al.* [5.16].

κ, mol m^{-1} s^{-1} Pa^{-n}	E_d, J mol^{-1}	n, -
2.4 10^{-10}	17563	1

As mentioned above, the permeation law used here (Eq. 5.25) is taken from the paper of Tong *et al.* [5.16], whose parameters assume the value reported in Table 5.11. The reasons why this membrane is not in accordance with the Sieverts' law can be various, as shown in Chapter 3 and also reported elsewhere [5.25-5.26]. The energy balances for the retentate and the permeate side are represented by Eq. 5.26 and 5.27, respectively.

$$\begin{aligned} &\frac{d}{dz}\left(\sum_{i=1}^{n} F_i^{Ret} \, \Delta H_i^{Ret} \right) = U^{Ext} \pi \, OD^{Shell} \left(T^{Furnace} - T^{Ret} \right) + \\ &- U^{Mem} \pi \, OD^{Tube} \left(T^{Ret} - T^{Perm} \right) - \pi \, D_m^{Mem} N_{\mathrm{H_2}}^{Mem} \Delta H_{\mathrm{H_2}} \Big|_{T^{Ret}} \end{aligned} \tag{5.26}$$

$$\begin{aligned} &\frac{d}{dz}\left(\sum_{i=1}^{n} F_i^{Perm} \, \Delta H_i^{Perm} \right) = U^{Mem} OD^{Mem} \pi \left(T^{Ret} - T^{Perm} \right) + \\ &+ \pi \, D_m^{Mem} N_{\mathrm{H_2}}^{Mem} \Delta H_{\mathrm{H_2}} \Big|_{T^{Ret}} \end{aligned} \tag{5.27}$$

Their shape for the reactive and inert stages is the same, since the heat lost for reaction characterizing the reaction side is included in the enthalpy variation. The pressure drops along the reactor are evaluated in the same way as described above for the PSMR. The same holds for the permeation side where the pressure is considered constant.

5.3.2.2 OPTIMIZATION PROCEDURE

Analogously to what done for the PSMR, also in this case two objective functions are chosen: methane conversion x and hydrogen recovery yield (RY).

$$\max_{\underline{l}} x \quad or \quad \max_{\underline{l}} RY \tag{5.28}$$

s.t.:

$$\sum_{i=1}^{n^R} l_i^R = \frac{l^{Tot}}{2}, \quad \sum_{i=1}^{n^I} l_i^I = \frac{l^{Tot}}{2} \tag{5.29}$$

$$l^{Min} < l_i < \frac{l^{Tot}}{2} \tag{5.30}$$

Here, RY is chosen instead of RF as one of the objective functions, since in this case the aspect of the hydrogen productivity is highlighted more than the one of hydrogen recovery. Hence, the optimization problem is mathematically represented as reported in Eqs. 5.28-5.30, where l_i^R and l_i^I are the lengths of the ith Reactive ("*R*") and Inert ("*I*") stage, respectively. As for PSMR, the maximization problem has been converted in a minimization one, solved in Matlab® by means of the "*fmincon"* function [5.15] by using the same methods to find the global minima.

5.3.3 RESULTS AND DISCUSSIONS

In the following sections, several different cases will be analyzed. In Section 5.3.3.1 a distribution having a catalyst mass entirely laid out at the beginning of the reactor. This particular distribution as the reference one, to which the other distributions, achieved by maximizing x and RF (Sections 5.3.3.2 and 5.3.3.3, respectively), will be compared. The operating conditions and the geometrical data of the equipments analyzed are summarized in Table 5.12 and Table 5.13.

Table 5.12 – Operating conditions.

Side	Pressure, kPa						Total flow rate, mmol/s
	H_2	CH_4	CO_2	H_2O	CO	Total	
Feed	-	125	-	375	-	500	8
Sweep	-	-	-	120	-	120	8
T^{Funace} = 600°C, ε_{Bed} = 0.40							

Table 5.13 – Geometrical data of the system.

ID^{Tube}, mm	$\delta^{Pd\text{-}layer}$, μm	δ^{Supp}, mm	ID^{Shell}, mm	OD^{Shell}, mm	L^{Tot}, cm	dp, μm
10	6	1.2	30	32	100	400

5.3.3.1 CASE 1: THE CATALYST MASS ENTIRELY PLACED AT THE REACTOR INLET

The first distribution analyzed has the whole amount of catalyst concentrated at the beginning of the reactor (at the feed inlet). This configuration will be set as the reference one in the comparison carried out in the subsequent sections. In all of the following figures, the abscissas are expressed in dimensionless form, whose reference length is that of the reactor. Furthermore, let us specify that, from this point on and if not differently specified, the reference

system for reading the figures is the one following the versus of the feed stream, even in the permeate side of the counter-current case. Hence, when a curve is said to increase or decrease, it is always done with respect to the positive versus of the feed stream (from 0 to 1 in the figures). In Figure 5.23, the hydrogen partial pressure profiles are shown in co- and counter-current flow on both reactor sides.

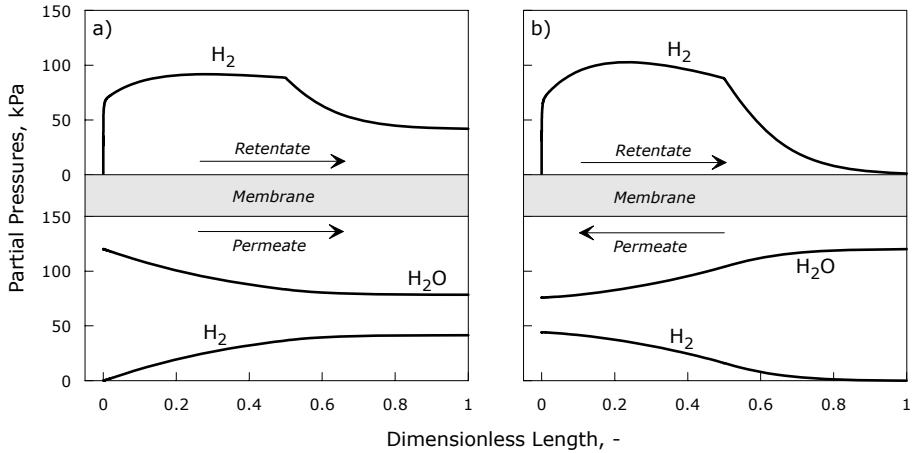

Figure 5.23 – H_2 and H_2O (permeate only) partial pressure profiles along the reactor length in the reference configuration in a) co- and b) counter-current flow. The arrows indicate the versus of the stream flow. The operating conditions are specified in Table 5.12.

Up to the end of the catalyst bed – i.e., up to an abscissa of 0.5 – hydrogen is produced and selectively removed through the membrane at the same position. When the reaction is rapid enough (at the beginning of the reactor), the permeation process has not much influence on hydrogen profiles in retentate and very high partial pressure gradients are found. As the reaction rate decreases and the amount of produced hydrogen increases, the permeation rate becomes comparable to the reaction one and, hence, the slope of the hydrogen profile in the reaction side decreases. In the inert zones only permeation occurs, causing the hydrogen pressures to decrease in the retentate and increase on the other side. In the co-current case,

the hydrogen profile in the reactive zone is flatter than the one in counter-current, whilst in the inert zone, its decrease is much higher in the second flow configuration than in the first one, allowing an almost complete hydrogen recovery in the counter-current case (Figure 5.23b). These important differences, that significantly influence the reactor performances, can be analyzed in more details by referring to Figure 5.24, where the hydrogen permeation Driving Force (DF) and transmembrane flux profiles are shown.

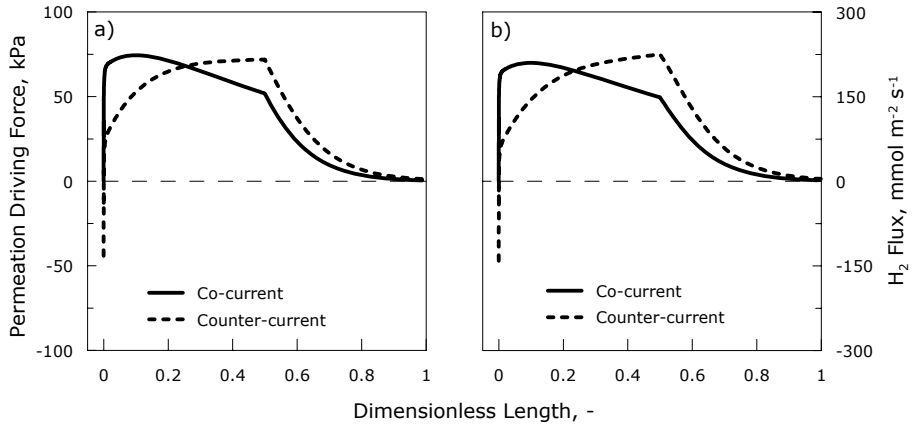

Figure 5.24 – a) Hydrogen permeation driving force and b) transmembrane flux profiles (positive from reaction to permeation side) along the reactor length in the reference configuration in co- and counter current flow. The operating conditions are specified in Table 5.12.

The peculiarity of the counter-current configuration is to present a part of the reactor where a negative DF and, consequently, a back-permeation from the permeate to the reaction side is found. This occurs since the hydrogen fed at the inlet is zero, whereas the permeate has accumulated a certain amount of hydrogen. Hence, a condition is created in which the DF is higher in those reactor zones where the reaction rate is slow, determining a better membrane exploitation. On the contrary, in co-current the DF is higher at the beginning of the reactor, where the kinetics is still fast and the presence of the membrane has a little influence on the process. The importance of the DF distribution is proved by the fact that the DF maximum in

co-current is higher than the maximum in counter-current, but this apparent advantage becomes vain because being positioned in a reactor zone where it cannot be fully exploitable. However, in terms of methane conversion, the advantage of the counter-current configuration disappears, as shown in Figure 5.25, where the two profiles reported can be hardly distinguished. The analysis of the other performance indexes allows to appreciate the differences between the co- and counter-current flow (Figure 5.26).

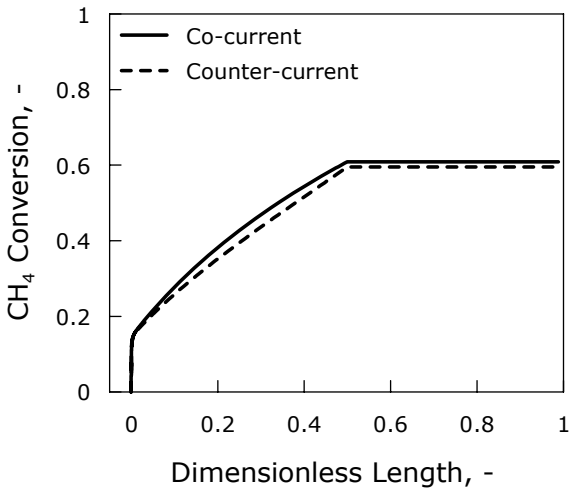

Figure 5.25 – Conversion profiles along the reactor length in the reference configuration in co- and counter-current flow. The operating conditions are specified in Table 5.12.

Along with the performance of the staged membrane reactors, also that of the staged traditional reactor (Figure 5.22) is reported for comparison in terms of conversion, since no indexes indicating a hydrogen recovery degree can be defined for this equipment. It is important to highlight that, when comparing the traditional staged reactor performances, a traditional reactor with the same distribution as the corresponding SMR is considered in all of the subsequent sections. Referring to Figure 5.26, although the conversion does not depend on the flow configuration (nor does it for the staged TR), this does influence RY and, more

strongly, RF. In particular, from the co- to counter-current flow, RY increases by 9% ca., whilst the improvement in terms of RF is about 12%, reaching an almost complete hydrogen recovery. As concerns the comparison with the equivalent stage TR the advantage is doubtless.

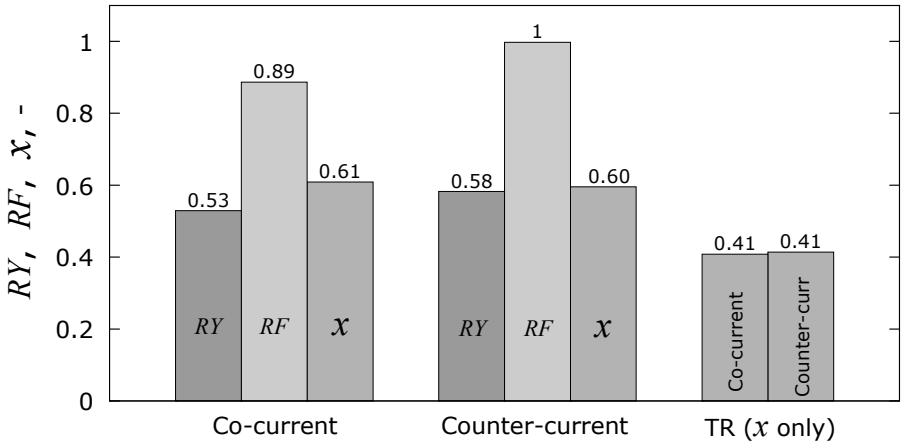

Figure 5.26 – Reactor performances in terms of RY, RF and x in co- and counter-current flow in the reference catalyst distribution. The conversion of the corresponding staged TR is also reported for comparison in both the flow configurations. The operating conditions are specified in Table 5.12.

In fact, in the case where the reaction and the permeation rate are comparable, the SMR permits an important increase of conversion, allowing also an important selective hydrogen recovery, which can be achieved even when the reaction is much faster than permeation. Furthermore, the very high value of RF (virtually the maximum achievable) could demonstrate that the distribution considered in this section is that one corresponding to the maximum RF. This is in analogy to what was found in a previous investigation, where the maximization procedure of RF applied to a co-current permeative-stage membrane reactor provided a distribution having almost the whole catalyst mass concentrated at the beginning of the reactor.

5.3.3.2 CASE 2: MAXIMIZATION OF THE METHANE CONVERSION

Once the SMR in the reference distribution has been analyzed, an optimization procedure has been carried out by setting the methane conversion as objective function. Carrying out the optimization procedure in analogy to what done in the previous section, the distributions shown in Table 5.14 and Figure 5.27 (in terms of stages' lengths) are obtained.

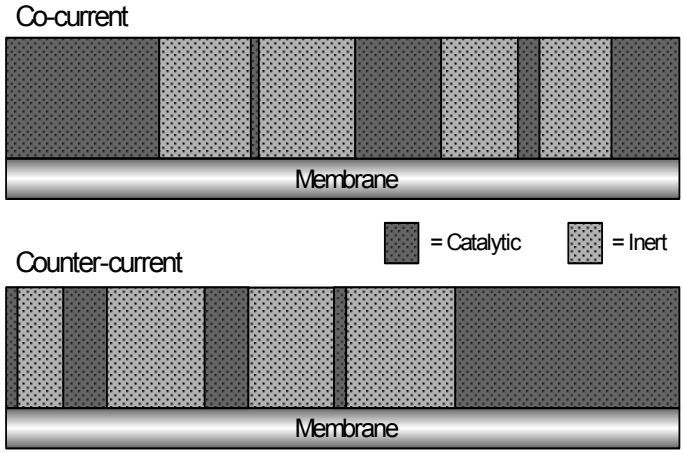

Figure 5.27 – Shape of the optimal distributions with maximized conversion. The operating conditions are specified in Table 5.12.

Table 5.14 - Optimal lengths distribution for the maximum conversion criterion in co- and counter-current flow. The letters "R" and "I" indicate "Reactive" and "Inert" stages, respectively.

Flow Configuration	*Stage lengths, % of the total reactor length*									
	R_1	I_1	R_2	I_2	R_3	I_3	R_4	I_4	R_5	I_5
Co-current	22.7	13.6	1.2	14.3	12.8	11.4	3.2	10.7	10.1	≈ 0
Counter-current	1.6	6.8	6.5	14.5	6.5	12.6	1.9	16.1	33.5	≈ 0

The corresponding profiles are shown in Figure 5.28 (in terms of partial pressure) and in Figure 5.29 (in terms of conversion). In co-current flow, a distribution with a very large first reactive stage is achieved, whilst, at the same time, that in counter-current presents a large last reactive stage. In both the cases, a negligible last inert stage is found. This fact, with the conversion as objective function, is somehow expected. The same cannot be said when maximizing RY, since in that case also the last inert stage plays an active role in increasing the RF.

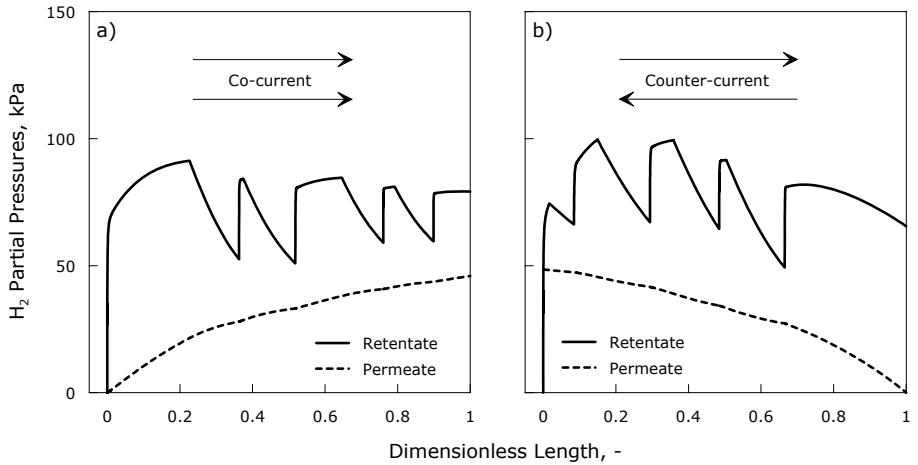

Figure 5.28 – H_2 and H_2O partial pressure profiles along the reactor length for the distribution obtained from the maximization of the CH_4 in a) co-current and b) counter-current flow. The arrows indicate the versus of the stream flow. The operating conditions are specified in Table 5.12.

As regards the reason why the largest stage in co-current is found in an opposite position with respect to the one in counter-current, a possible explanation can be provided by looking at the temperature profiles (Figure 5.30). Generally speaking, it is reasonable to think that the system "tries" to place the largest catalyst packs in those zones where it is easier to acquire the energy required by the reaction, i.e., where the temperature difference is as large as possible.

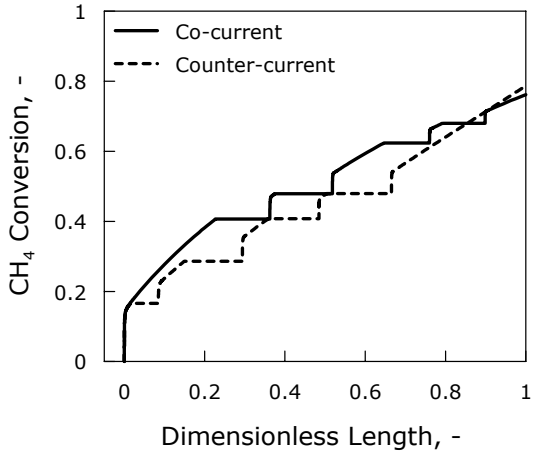

Figure 5.29 – Conversion profiles along the reactor length for the catalyst distribution obtained by maximizing conversion in co- and counter-current. The operating conditions are specified in Table 5.12.

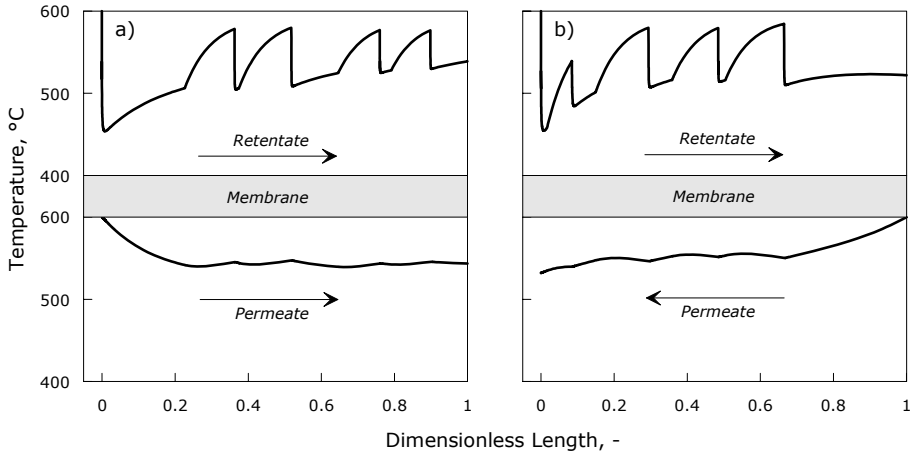

Figure 5.30 – Temperature profiles along the reactor length for the catalyst distribution obtained from the maximization of the CH_4 conversion in a) co- and b) counter-current flow. The arrows indicate the versus of the stream flow. The operating conditions are specified in Table 5.12.

In the co-current flow this occurs towards the beginning of the reactor, where the sweep stream enters the reactor at the highest temperature. On the contrary, in counter-current flow this occurs towards the end, and, hence, the system exploits these favourable conditions as well as possible by "placing" a large catalyst pack. However, any other speculation on the particular lengths' values of the obtained distributions risks of resulting vain, since the length of a stage is necessarily influenced by the others. Hence, at least until now, there are no precise rules allowing to predict the shape of an optimal distribution, but only qualitative guide-lines.

Analyzing the performance indexes for this case (Figure 5.31), a quite different situation with respect to the previous cases is found. The first thing to remark is that the conversions in co- and counter current are more different between each other (0.76 vs. 0.79) than RF (0.86 vs. 0.87). On the contrary, as concerns the RY, the difference is still significant (about +10% for counter-current flow). The conversions of the traditional staged reactors are always independent of the flow configuration.

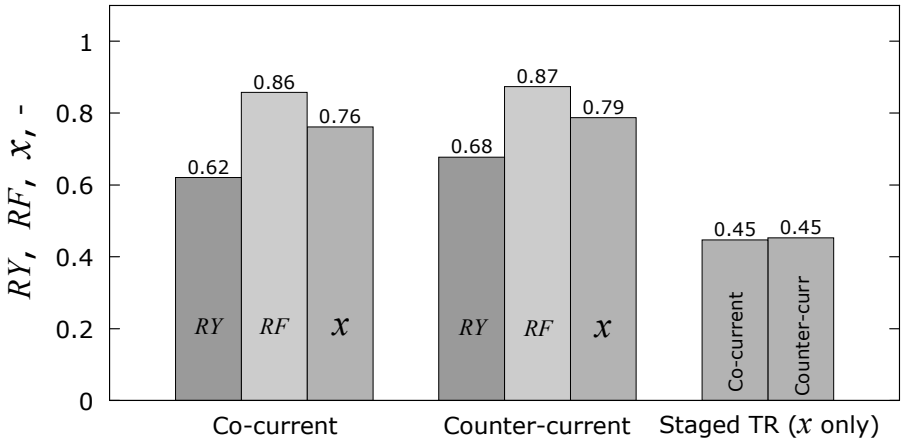

Figure 5.31 – Reactor performances in terms of RY, RF and x in co- and counter-current flow for the catalyst distribution obtained from the maximization of x. The conversion of the corresponding staged TR is also reported for comparison in both the flow configurations. The operating conditions are specified in Table 5.12.

An interesting aspect is that for the two objective functions considered, even presenting quite different distributions, the staged TRs have practically the same conversions, whereas for the reference distribution a lower value is found (0.45 vs. 0.41). This is due to the fact that, as mentioned above, in the inert stages the stream recharges itself by a certain amount of energy. Thus, the higher the number of stages, the more significant this effect. As regards the TR in reference distribution (only two stages), there is no possibility for the reacting stream to exploit the amount of energy transferred in the inert stage, since, obviously, there are no other reactive stages after it. Of course, this is a limit-case, because there are no apparent reasons to build a traditional reactor with a useless pure heating stage, but it can be useful to make understand the role of the distribution in a staged reactor. In other words, it can be said that the criterion by means of which the optimization procedure acts is an energetic criterion. At this regard, generally speaking, one can consider that the optimization procedure only redistributes the stages in such a way for the reactor to be able to acquire the necessary heat (for reaction and/or permeation) in the most efficiently manner. Hence, it represents a way for the system to use the energy in the best way accordingly to the particular objective function chosen.

5.3.3.3 CASE 3: MAXIMIZATION OF THE HYDROGEN RECOVERY YIELD

The other objective function considered is RY. Analogously to the previous case, the distribution shape is reported in Table 5.15 and Figure 5.32, where it can be observed that the optimal values can be considered, in a first approximation, as distributed in equi-sized shape.

Table 5.15 - Optimal lengths distribution for the maximum RY criterion in co- and counter-current flow. The letters "R" and "I" indicate "Reactive" and "Inert" stages, respectively.

Flow Configuration	*Stage lengths, % of the total reactor length*									
	R_1	I_1	R_2	I_2	R_3	I_3	R_4	I_4	R_5	I_5
Co-current	9.6	9.6	9.5	9.8	10.5	9.3	8.0	9.6	12.4	11.7
Counter-current	10.6	7.9	9.5	9.9	10.2	10.1	6.4	10.1	13.3	11.9

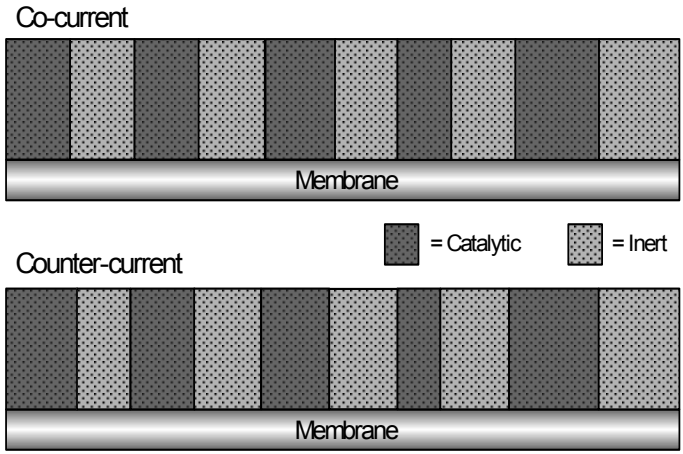

Figure 5.32 – Shape of the optimal distributions with maximized recovery yield. The operating conditions are specified in Table 5.12.

A possible explanation for this result is that maximizing RY is, by its definition, equivalent to maximize the hydrogen content in the permeate and, thus, the permeating flux. Therefore, the presence of too large reactive stages would imply the presence of other very short stages that, especially towards the end of the reactor, would not allow a large amount of hydrogen produced and, hence, separated through the membrane. In this sense, it is not casual that, in both the flow configurations, the last reactive stage is little bit larger than all the previous ones.

The resulting hydrogen profiles, corresponding to the optimal distributions (in both co- and counter-current flow) are shown in Figure 5.33. In each reactive zone, the reaction rate is very fast at the beginning and becomes slow towards the end. Considerations similar to those done in Section 5.3.3.1 concerning the hydrogen content in the retentate are valid. In fact, also in this case the hydrogen partial pressure at the end of the SMR in counter-current flow is higher than in the co-current, and, for the same reasons, the profiles in counter-current are steeper than the corresponding ones in co-current.

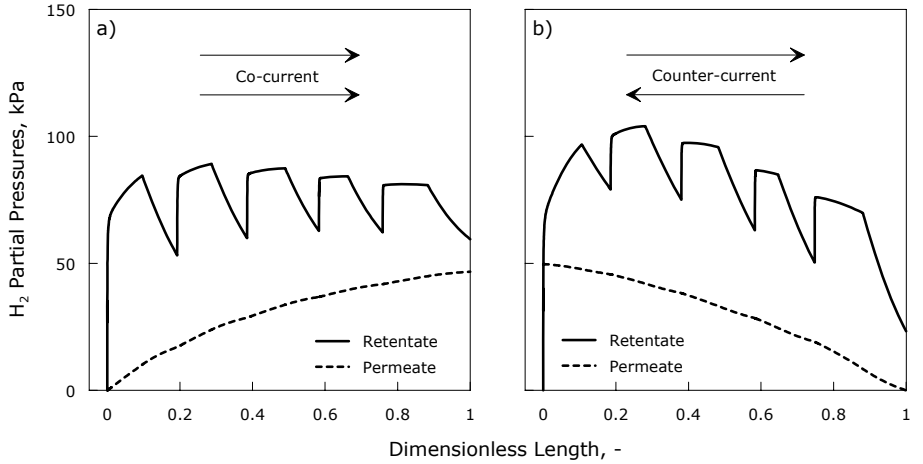

Figure 5.33 – H_2 partial pressure profiles along the reactor length on both the membrane sides for the distribution obtained from the maximization of RY in a) co- and b) counter-current flow. The arrows indicate the versus of the stream flow. The operating conditions are specified in Table 5.12.

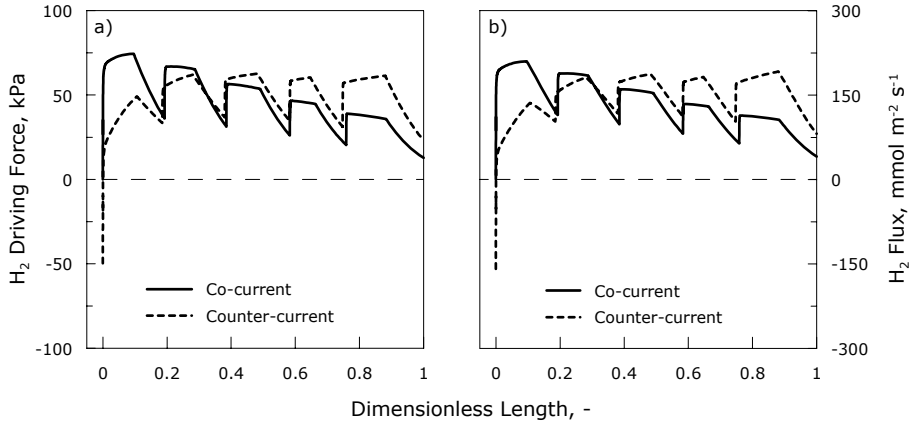

Figure 5.34 – a) Hydrogen permeation driving force and b) transmembrane flux profiles along the reactor length for the catalyst distribution obtained from the maximization of RY in co- and counter-current flow. The operating conditions are specified in Table 5.12.

This aspect becomes clear if examining the driving force and the permeating flux profiles (Figure 5.34). The figure shows that in the first part of the reactor the DF in co-current is larger than that in counter-current, but this tendency changes from a certain point on. In particular, in the reactive packs the DF profiles in co-current decrease, whilst those in counter-current increase significantly, causing a larger gap. However, this important difference does not significantly affect the performance of the reactor in terms of conversion. In fact, although the conversion profiles are quite different (Figure 5.35), the final values are practically the same.

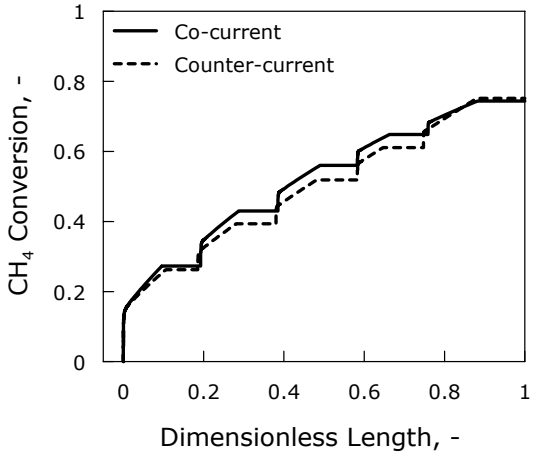

Figure 5.35 – Conversion profiles for the catalyst distribution obtained from the maximization of RY in co- and counter-current flow. The operating conditions are specified in Table 5.12.

Hence, also in this case the conversion is not influenced by the configuration flow. However, this difference is not excessively high, evidently because otherwise quasi-equilibrium conditions (very low hydrogen production) would occur at the end of these stages. Moreover, there is one more aspect to consider, namely the effect of the energy transfer. In fact, the role of the inert stages is both to "recharge" the stream once it has lost energy because of the reaction, and allow an easier permeation through the membrane. This last consideration arises from the fact that the permeating flux in an inert stage surely occurs at higher temperatures

than the previous reactive stage. Thus, in these conditions, a lower permeation driving force is compensated by higher permeance.

The question about the energy transfer is of crucial importance also for the reactive stages, which need to take heat from the furnace and, in this specific case, from the permeate side. The overall effect of all these coupled kinetic and transfer phenomena reflects on the performance indexes, as shown in Figure 5.36.

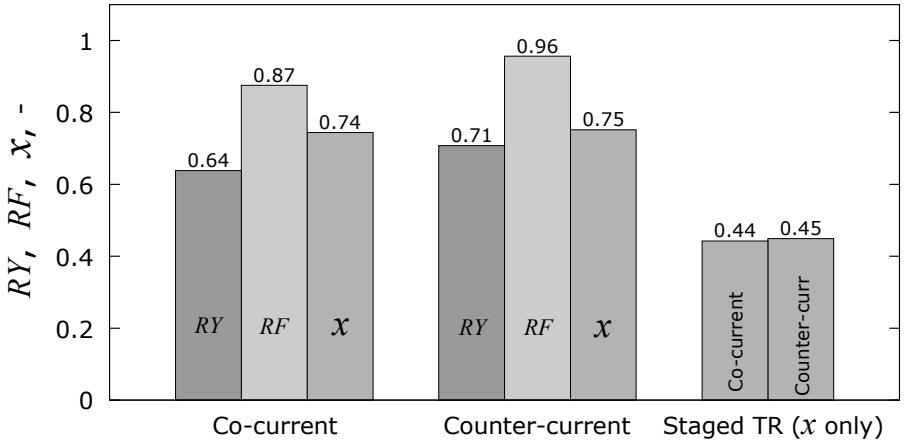

Figure 5.36 – Reactor performances in terms of RY, RF and x in co- and counter-current flow for the catalyst distribution obtained from the maximization of RY. The conversion of the corresponding staged TR is also reported for comparison in both the flow configurations. The operating conditions are specified in Table 5.12.

The first thing to notice is the significant difference in terms of RY and RF between co- and counter-current. As regards RY, the counter-current flow provides an increase of 11% ca. with respect to the co-current case, while the improvement of RF is about 10%. These large gaps are determined by the different behaviour of the system in terms of driving force and permeating flux analyzed above (Figure 5.34). The higher the permeation rate, the higher all the performance indexes related to the hydrogen recovery.

As concerns the comparison with the corresponding TRs, the improvement is evident, showing a conversion increased by a factor of 0.30. Hence, the presence of the membrane, allowing the shift of the reactor towards the products, is determinant to improve the conversion with respect to the traditional staged reactor.

5.3.3.4 COMPARISON AMONG THE DIFFERENT DISTRIBUTIONS

Once three different distributions have been analyzed, it is necessary to compare their performances in order to highlight the positive and negative aspects of each distribution. For the co-current flow, Figure 5.37 reports the performance indexes together with those of a conventional membrane reactor (MR), with the same membrane area as the SMR, but completely filled with catalyst, i.e. with an amount double with respect to the SMR.

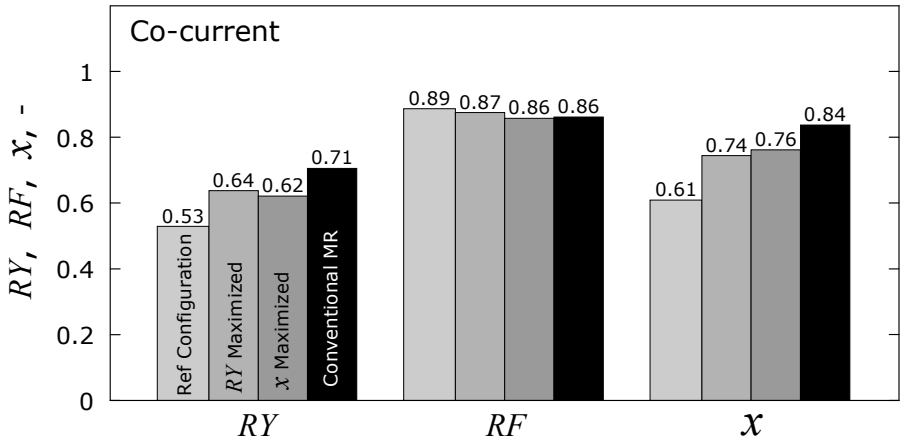

Figure 5.37 – Comparison among the SMR performances for several catalyst distributions in co-current flow. The performances of the conventional MR (with the same membrane area as the SMR but a double amount of catalyst) are also reported. The operating conditions are specified in Table 5.12 .

Obviously, a larger amount of catalyst causes the MR to overcome the performances of all the SMRs in terms of x and RY. As concerns RF, the reference distribution continues to be the

best one, even considering the MR, whilst it is the worst one in terms of RY and x. This is due to the peculiarity of the two-stage reactor, which favours the permeative factor at the expense of the reactive one, since the energy is not transferred as much to increase the reaction rate but rather to get advantage to the permeation rate. However, an RF higher than the MR is not a surprising result, since, by its definition, RF compares the hydrogen recovered in the permeate to the hydrogen produced by the reaction.

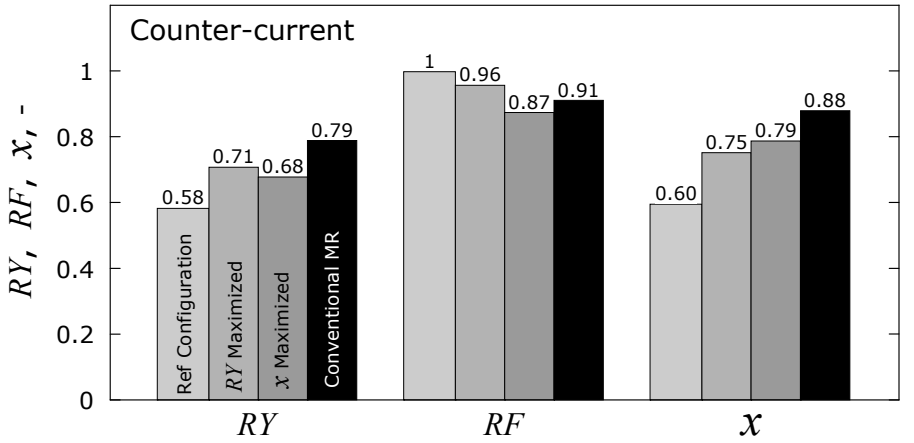

Figure 5.38 – Comparison among the SMR performances for several catalyst distributions in counter-current flow. The performances of the conventional MR (with the same membrane area as the SMR but a double amount of catalyst) are also reported. The operating conditions are specified in Table 5.12 .

Both of these quantities are variable and, thus, a reactor able to produce a large amount of hydrogen but not able to separate it, provides a smaller RF than a reactor generating a smaller amount of hydrogen but with a higher ability to remove it. In summary, the same reasons leading the two-stage SMR to be very good to recover hydrogen, lead it to just sufficient levels of x and RY. Looking at the other two distributions, they provide quite similar values of x and RY. As regards the counter-current flow (Figure 5.38), the situation is similar to the co-current from a qualitative point of view, but here the performances are generally higher than before,

except for the conversion in the reference distribution and for the maximized RY. Furthermore, in this second case, the differences between the various distributions are a little bit larger than those in previous situation. In fact, RY in the reference configuration is higher than that in MR of about 11%, against the previous value of 3.5%. A very interesting thing is that RY of the MR in co-current (Figure 5.37) is the same as the one of the SMR obtained in condition of maximum RY (Figure 5.38). This means that, only by changing the configuration flow, it is possible to achieve the same performance (at least in terms of RY) as the conventional MR with one half of the catalyst mass. This fact does not occur considering the conversion, since it is natural that, in conditions far enough from equilibrium, a larger amount of catalyst (double in this case) provides a higher conversion.

5.3.4 ON THE EFFECT OF THE STAGES' NUMBER AND CATALYST AMOUNT

In Section 5.3.1 the methane steam reforming process was considered to be carried out in an SMR with two and ten stages. In that analysis, it was highlighted the role held by different catalyst distributions achieved from the optimization of certain performance indexes (RY and x) setting the stage lengths as decisional variables and setting the number of stages and the amount of catalyst as constants for the simulation. However, what happens to the system if removing these two hypotheses? To our knowledge, the effect of this two operating parameters on the performance of a staged membrane reactor has not been yet studied specifically in literature. Nevertheless, as will be shown throughout this section, their influence on the whole process can be relevant, also in the perspective of reducing the reactor operating costs. Several research groups considered or used in their works a staged reactive system, but the number of stages was set in all the cases as a fixed parameter [5.28-5.31]. About the efficient exploitation of membrane area, Li *et al.* [5.32] carried out a simulation work for methane steam reforming investigating a staged Pd-membrane reactor, where two reactive stages and two separative ones were respectively placed in two different furnaces, each one with its own furnace temperature. In particular, they investigated the role of the amount of membrane area present in the separative stages and on the influence of some other operating variables on the

performances of the overall process, but they did not consider the possibility of increasing the number of staged to improve the performance of their equipment.

In the simulation work of Jordal *et al.* [5.33] concerning the possibility of integrating H_2 selective membrane-based technology in a gas turbine process for CO_2 capture, a reformer with five reactive stages and five separative membrane stages was considered, choosing the number of stages on the basis of computational considerations. Hence, no tests with different number of stages were carried out. The aim of this section consists properly in analyzing the role played by the stages' number and catalyst amount in changing the SMR performances.

5.3.4.1 DESCRIPTION OF THE SYSTEM

The reactor considered in this section has a similar geometrical configuration to the one shown in Figure 5.21. However, as said earlier, the hypotheses of a fixed number of stages and catalyst amount are removed. In particular, the catalyst amount is indicated here in terms of percentage ($y_{Catalyst}$) with respect to the highest amount allowable in the conventional Membrane Reactor (MR), to which corresponds the 100% (shell completely filled with catalyst).

$$\begin{aligned}
&\sum_{i=1}^{n^R} l_i^R = y_{Catalyst} \cdot l^{Tot}, && l_i^R = l_j^R \\
&\sum_{i=1}^{n^I} l_i^I = \left(1 - y_{Catalyst}\right) \cdot l^{Tot}, && l_i^I = l_j^I \\
&\frac{l_i^R}{l_i^I} = \frac{y_{Catalyst}}{1 - y_{Catalyst}}, && l_i^R \neq l_i^I \\
&n^R = n^I, && l^{Tot} = \text{constant}
\end{aligned} \tag{5.31}$$

The value of the catalyst amount and the size of the reactor stages (inert and reactive) are strictly related to each other. In fact, the term "equi-sized" stages corresponding to a certain $y_{Catalyst}$, means that all the reactive stages have the same length, whose total sum is equal to the length of the total catalyst pack. An analogous fact holds for the inert stages, which, in general, have different length than the reactive ones. The only case where the two lengths are equal is when a $y_{Catalyst}$ of 50% is considered. This situation is schematized in Eq. 5.31, where n indicates the number of stages, l the length and the superscripts "R" and "I" the "Reactive" and "Inert" stage, respectively. The question whether or not the equi-sized configuration represents the best possible configuration in order to carry out the present analysis is not important here. In fact, as the number of stages increases, an eventual optimization procedure used to find an optimal distribution becomes useless, since there is less "space" for the procedure to work.

5.3.4.2 RESULTS AND DISCUSSION

The operating conditions are summarized in Table 5.16. All the other details about the geometrical data of the equipments, the mathematical model, its validation and the definition of the performance parameters are reported in Section 5.3.1. In Figure 5.39 and Figure 5.40 the SMR performances in terms of RY, RF and x are shown as function of the number of stages for several $y_{Catalyst}$ at 600 and 500°C, respectively. The maximum number of stages considered here is 400, value that can be actually seen as an infinite number.

Table 5.16 – Operating conditions.

Side	*Pressure, kPa*						*Total flow rate, mmol/s*
	H_2	CH_4	CO_2	H_2O	CO	Total	
Feed	-	125	-	375	-	500	8
Sweep	-	-	-	120	-	120	8
T^{Funace} = { 400; 500; 600 }°C							

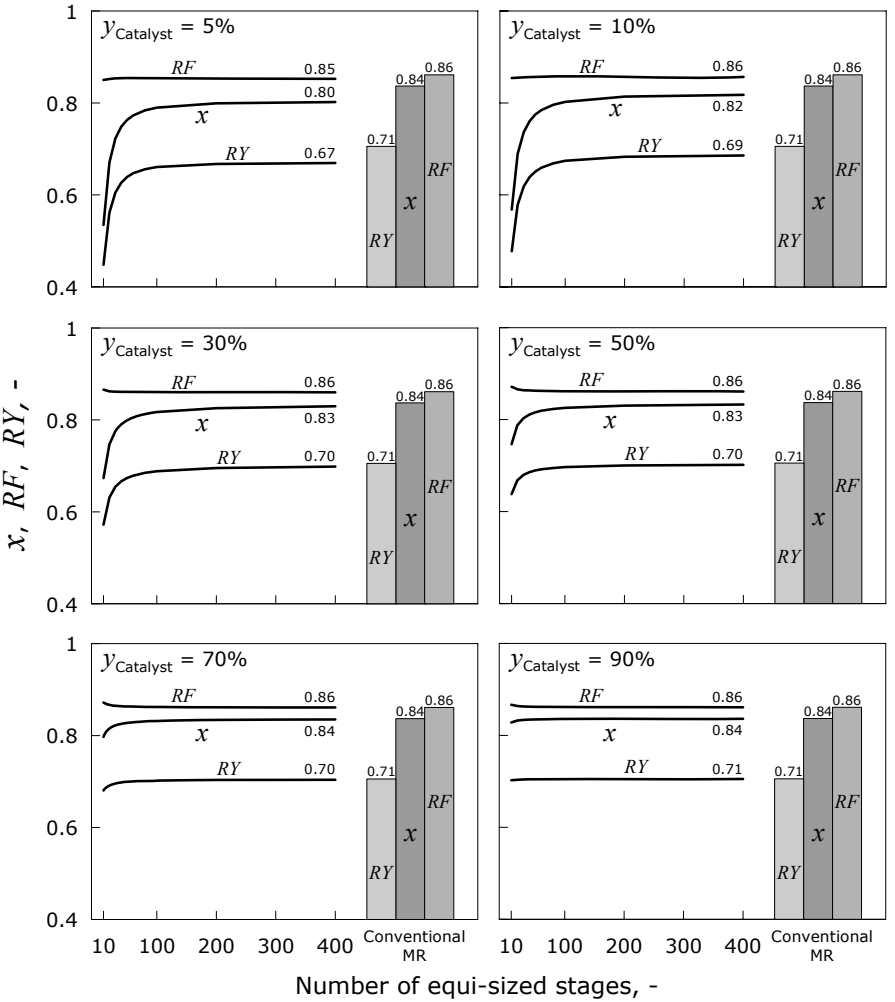

Figure 5.39 – Performances of the SMR (x, RF and RY) in co-current flow as a function of the number of equi-sized stages for different percentages of catalyst at T^{Fur} = 600°C. The performances of the conventional MR are also reported for comparison. The remaining operating conditions are specified in Table 5.16.

In order to understand the system behaviour, let us analyze first the case of 30% at 600°C (Figure 5.39). The first thing to notice is that the curves relative to x and RY continuously increase, whilst that of RF decreases, although not very strongly. This effect can be explained through the following considerations.In each couple of reaction-inert stage the upstream is involved in a thermal cycle where some heat is first consumed by reaction and then recharged (inert stages) continuously.

When considering a low number of stages (larger ones) (in the present study their minimum number is 10), in the last part of the reactive zone a certain amount of reactants is found at quite low temperature. At a higher number of stages, the reactive stream can exploit a better thermal condition, because the temperature decrease in each reactive stage is lower and the heat recharge is more frequent, causing a higher temperature to be established at the beginning of the successive reactive stage. All these facts favour the reaction rate and, thus, all the performance indexes measuring the productivity of the reactor, i.e. x, and RY.

On the contrary, the index related more to the hydrogen recovery, i.e. RF, is slightly penalized by a high number of stages, since the permeation driving force generated in this case is lower than in a configuration with lower stages. For the conversion and RY, the influence of the number of stages is relevant for a catalyst percentage less than about 50% and a number of stages up to about 100. From about 50% on, there is no an appreciable difference among low and high number of stages, since the presence of more catalyst compensate the "inefficiencies" of the system. This concept is particularly important, since the analysis shows that a designer could save a significant amount of catalyst only by acting on the catalytic pack distribution in terms of the number of stages. This aspect will be discussed in a deeper way later. Another interesting fact in the shape of the curves in Figure 5.39 and Figure 5.40 consists in the presence of plateau for all of the three performance indexes considered here. This means that, corresponding to a certain amount of catalyst, there are some performance limits whose values approaches more those of the conventional MR as the catalyst amount increases.

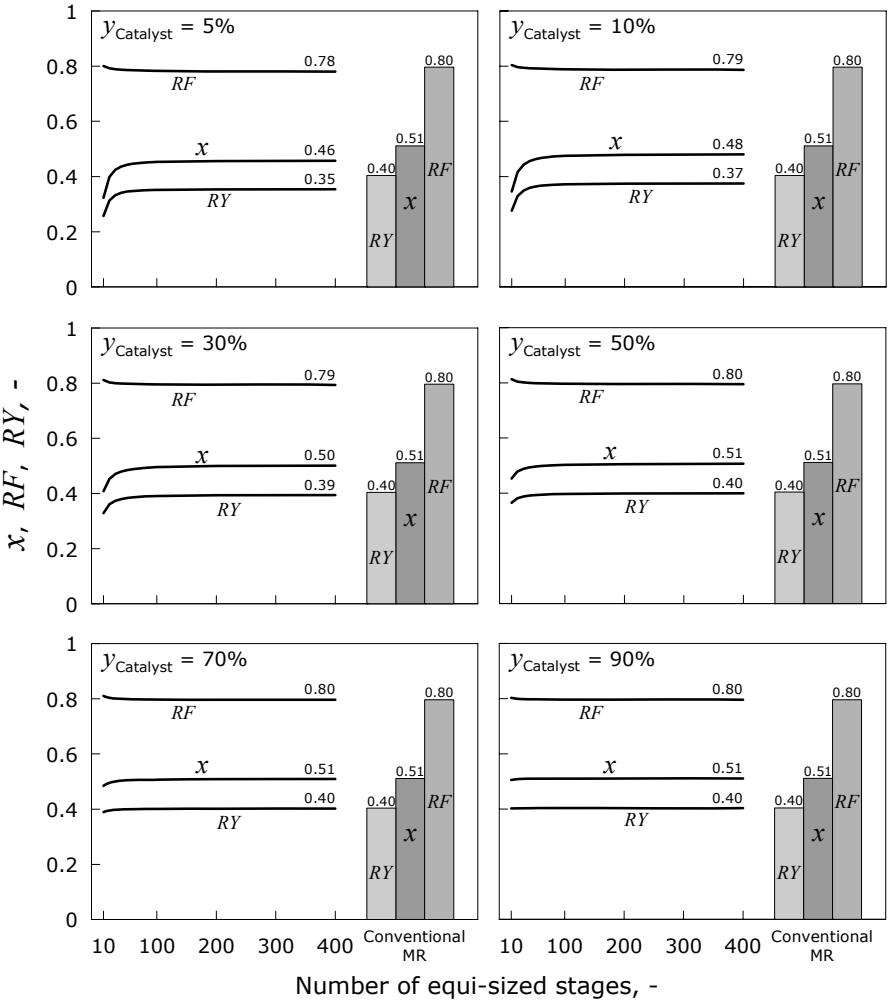

Figure 5.40 – Performances of the SMR (x, RF and RY) in co-current flow as a function of the number of equi-sized stages for different percentages of catalyst at T^{Fur} = 500°C. The performances of the conventional MR are also reported for comparison. The remaining operating conditions are specified in Table 5.16.

Considering the situation at 500°C (Figure 5.40), the qualitative behaviour of the profiles remains unchanged, but their dependence on the number of stages and on the amount of catalyst becomes less significant than the case at 600°C. This occurs because the reaction is endothermic and, thus, favoured by a high temperature. In fact, for a slower reaction rate (due to a lower furnace temperature), a certain part of advantage in using a higher number of stages and/or a larger catalyst amount for achieving higher performances is lost.

As concerns the counter-current configuration, the situation is analogous, even though the performances are higher than in co-current flow. The behaviour of the system is shown in Figure 5.41, where only the case at 30% of catalyst for 500 and 600°C is reported. The only thing to notice is that the RF is more dependent on the number of stages than before. This is due to the fact that the counter-current configuration, providing a more uniform hydrogen driving force along the reactor, favours the hydrogen recovery much more than the co-current one, making this parameter more sensitive to changes in number of stages. In order to visualize better the influence of the number of stage on the reaction rate, in Figure 5.42 the conversion profiles corresponding to two catalyst amounts (20% and 50%) and numbers of stages are reported in co-current flow (in counter-current an analogous situation is found). The number of 50 stages was chosen in this case for comparison since the variation in performance with respect to higher numbers of stages is very little. Analyzing the situation at 20%, after an initial part of reactor where the reaction is very rapid and the two configurations provide the same performances, the difference between 10 and 50 stages is significant and increases as much as going towards the end of the reactor. In particular, looking at the profiles in each stage, it is possible to see that the slope of the curve at 50 stages in the reactive stages is higher than that at 10 stages, this representing a measure of a more rapid reaction rate. When considering 50% of catalyst, the difference between the two cases decreases and the initial reactor length where the systems are in fact equivalent is larger than the previous case. As mentioned above, this happens because there is more catalyst to compensate the reaction rate decrease due to a worse configuration (lower number of stages).

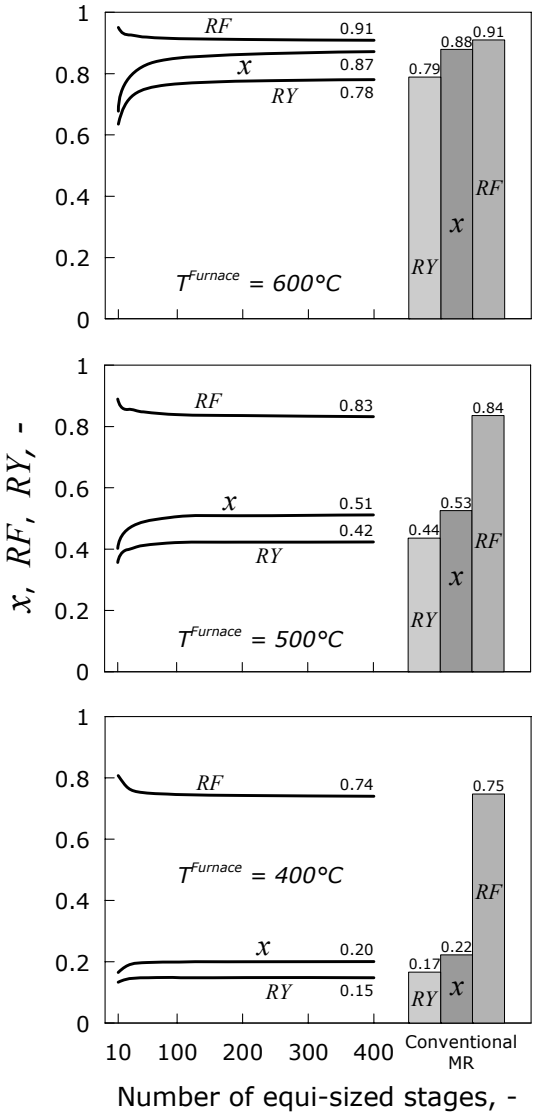

Figure 5.41 – Performances of the SMR (x, RF and RY) in counter-current flow as a function of the number of equi-sized stages for two furnace temperatures at a percentage of catalyst of 30%. The performances of the conventional MR are also reported for comparison. The remaining operating conditions are specified in Table 5.16.

Increasing the amount of catalyst in the reactor with a fixed number of stages, the performances of an SMR become closer to those of a conventional MR in the same operating conditions, this occurring more conveniently for the economy of the process adopting a higher number of stages.

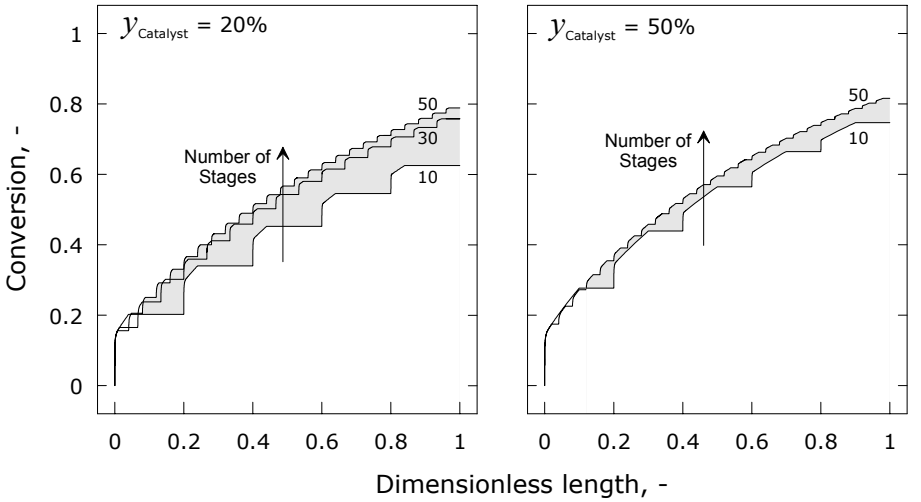

Figure 5.42 – Conversion profiles for some numbers of stages and amounts of catalyst in co-current configuration at $T^{Furnace}$ = 600°C. The remaining operating conditions are specified in Table 5.16.

5.3.4.2.1 ADVANTAGE MAPS OF THE PROCESS

At this point, it is possible to quantify the advantage in using the SMR, reporting in Figure 5.43 the performances of the system as functions of the catalyst filling the reactor at the highest number of stages considered in co- and counter-current case. The curves are evaluated in both the cases up to 90% of catalyst. All these curves present a monotonically increasing behaviour, reaching a plateau, whose value remains more or less constant from an amount of catalyst of about 30% on. This seems a very surprising fact, since this means that an SMR filled with just a part of catalyst can provide in practise the same performances as the fully filled MR.

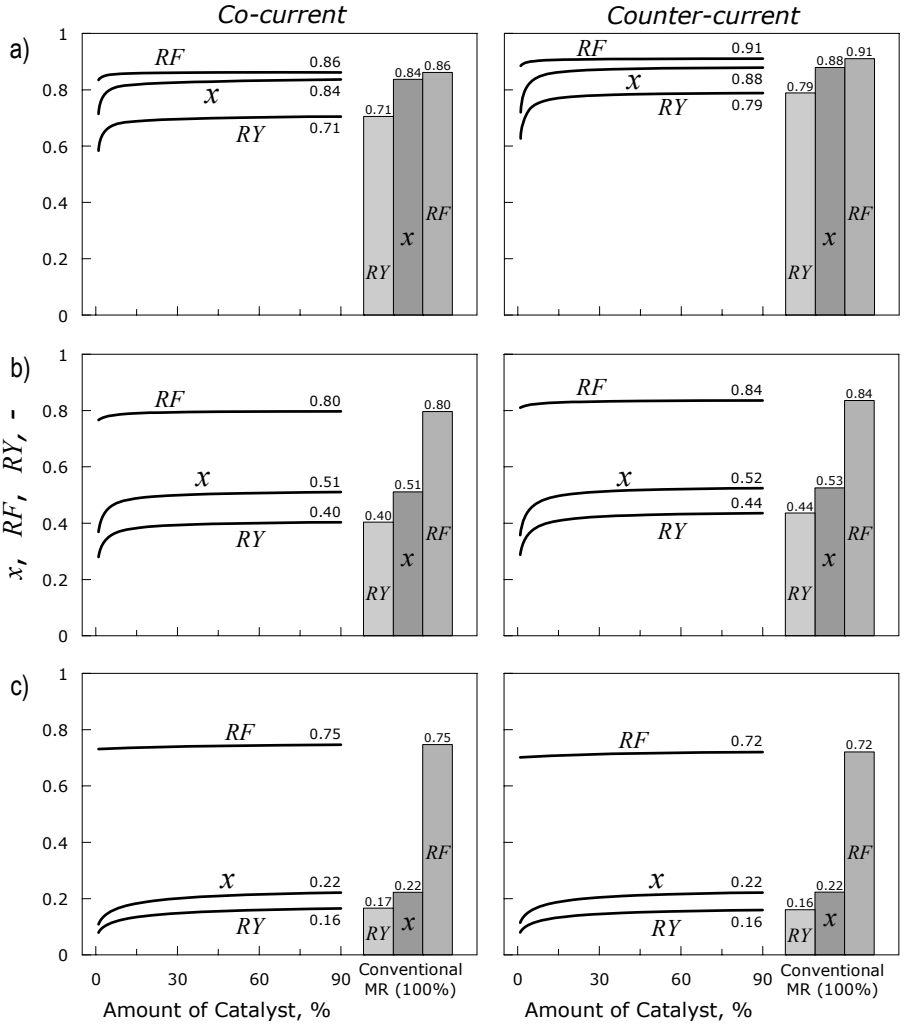

Figure 5.43 – Performances of the SMR (x, RF and RY) for $T^{Furnace}$ of a) 600°C, b) 500°C and c) 400°C in co- and counter-current flow at a "high" number of stages (> 100 ca.) as a function of the catalyst fraction of the fully-filled conventional MR, whose performances are also reported for comparison. The remaining operating conditions are specified in Table 5.16.

Dually, this means that the rest of catalyst is in fact useless. Analyzing this plot, it is evident that, from a certain point on, it is useless to add more catalyst to the SMR for improving the performances, since it will not be utilized. From another point of view, when using a membrane reactor, it is more convenient to make it staged, tuning the number of stages in order to achieve the desired level of performances, which determines the minimum amount of catalyst (from which is not convenient to add more catalyst) to use. Hence, the question arises on until which point it is convenient to save part of catalyst and lose part of performances. Figure 5.44 shows up this kind of analysis, reporting the amount of catalyst saved – in terms of percentage with respect to the total amount present in the conventional MR – as function of the performance loss at different temperatures in the two flow configuration considered. In these particular operating conditions, the qualitative behaviours of x and RY are very similar.

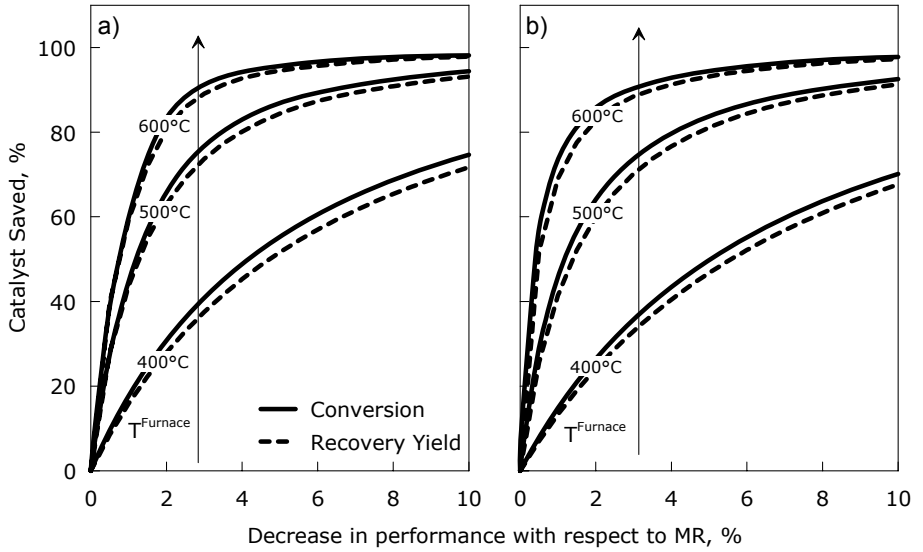

Figure 5.44 – Catalyst saved as a function of performance losses with respect to the conventional MR (in terms of x and RY) for different furnace temperatures in co- (a) and counter-current (b). The remaining operating conditions are specified in Table 5.16.

For a certain furnace temperature, (e.g. 600°C) the slope of the curves is very high for low performance losses (<2% ca.), whereas, at higher losses, it becomes almost flat. When considering lower temperatures, the slope of the curves decreases, showing a diminished advantage in the use of a SMR. Another interesting fact is that the difference between co- and counter current case is very little and, thus, one could use only one of these plots to evaluate the amount of catalyst saved. This fact cannot be predicted *a-priori* by theoretical considerations and, hence, represents an important result simplifying the evaluation of the amount of catalyst to use. In order to do this in a simpler way, a summarizing plot (here-called " advantage map", Figure 5.45) were developed, which consists in the "union" of the two plots shown in Figure 5.44. By means of this map, it is intended to provide a method to exploit more efficiently the available resources. In this sense, the indications reported in Figure 5.45 can be in principles used in two ways: 1) In a limited range, one could be interested not as much in performance losses, but rather in saving catalyst. Hence, setting the desired value of saved catalyst, it is possible to know the amount of the performance decrease; 2) on the other hand, one can directly read the indication of the saved catalyst once the performance level is set, in this way limiting to minimum the catalyst wasted. As a real example of how to use this map, let us consider the concrete case shown in figure (600°C), where, choosing that a loss of 1% in x or RY is acceptable, using an SMR it is possible to save up to 67% ca. of catalyst, reaching in practise the same performances as a conventional MR using only 1/3 of the amount of its catalyst. Considering a performance loss of 2%, the saved catalyst can reach even the value of 83%. These apparently surprising data can be explained by means of the following considerations. On one hand, it has to be considered that this specific process is highly endothermic and has a very fast kinetics. This means that the reaction rate is very high at the beginning of each catalyst pack, becoming quite slow towards the end, even if the membrane removes hydrogen. If the reactive stages (and, dually, the inert ones) are few, the reaction rate will be slow for the majority of the reactor volume. On the other hand, when considering a lot of stages, the reaction rate is meanly faster, because a larger amount of reactants remains available for the successive reactive stage at a little higher temperature. In general, the higher

the reaction rate, the less the amount of catalyst useful to obtain performances comparable to those of conventional MR.

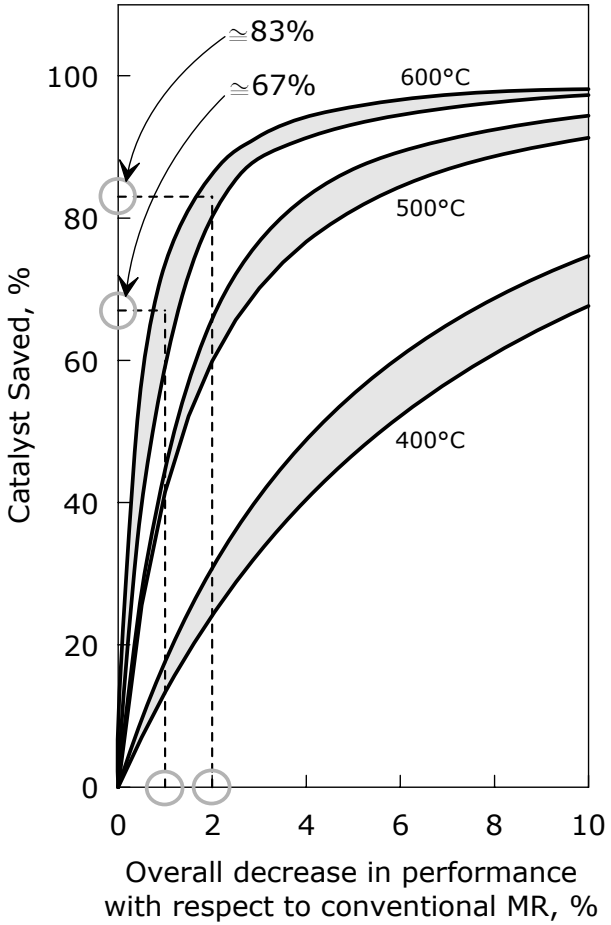

Figure 5.45 – Advantage map for methane steam reforming carried out in a Staged Membrane Reactor. The remaining operating conditions are specified in Table 5.16.

Another quantification of the advantage in adopting as many stages as possible is provided by Figure 5.46, which shows for the co-current flow the level up to which the furnace temperature can be reduced obtaining the same performance only considering an adequate number of stages. In this type of figure, the catalyst amount is fixed (30%) and a reference situation (600°C and 10 stages) is considered for both the conversion and recovery yield.

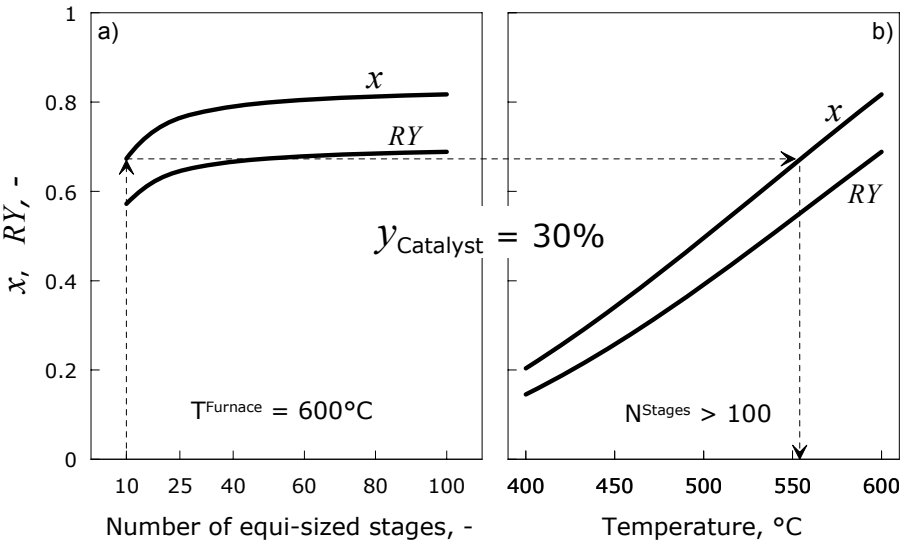

Figure 5.46 – Performance indices a) as functions of the stages' number at 600°C and b) as functions of the furnace temperature for 100 or more stages in co-current flow. The dashed arrows (drawn only for conversion) indicate how to evaluate the advantage of adopting a high number of stages in terms of lower operating furnace temperature.

Then, the furnace temperature corresponding to the reference performance index is evaluated for high stages' number (100 in this case), providing in this way the energy (in terms of temperature difference) that is possible to save with respect to the reference case. The dashed path indicated by the arrows shows this situation only for conversion, but an analogous calculation can be made for the recovery yield. If this type of evaluations is carried out for

several different catalyst amounts (Figure 5.47), a second convenience map can be drawn, showing the furnace temperature saved for conversion and recovery yield in both the flow configurations. In this map, it is shown that the relative advantage in using a high number of stages decreases continuously with the catalyst amount.

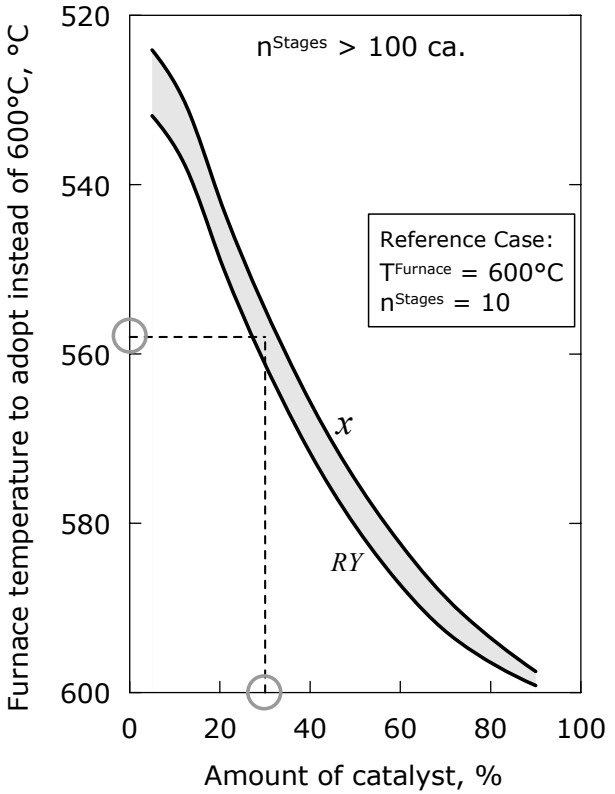

Figure 5.47 – Reduced furnace temperature that is possible to adopt instead of the one of the reference case (600°C and 10 stages) by adopting a high number of stages (>100 ca.) as function of the catalyst amount for conversion and recovery yield valid for co- and counter-current flow.

This behaviour can be explained by considering that the performance indices relative to the reference case increase with the catalyst amount, tending to assume the values of the

conventional MR (100% filled). However, the important most important fact to notice here is the significant temperature difference that is possible to save in certain conditions, reaching, for example, the value of 52°C (i.e. a furnace temperature of 548°C instead of 600°C) for a catalyst amount of about 30%. This leads up to an important energy saving, which means in turn an appreciable reduction of the reactor operating costs.

5.4 CONCLUSIONS

5.4.1 PERMEATIVE STAGE MEMBRANE REACTOR

The influence of the catalyst and membrane area axial distribution on the performances of a Permeative Stages Membrane Reactor (PSMR) was investigated for methane steam reforming at several temperatures and membrane thicknesses. Five reactive and four permeative stages of the same length were analyzed in terms of methane conversion and hydrogen recovery factor, showing that a higher conversion than in conventional membrane reactors can be achieved. On this basis, optimization of the lengths of the nine stages has been carried out using two objective functions, namely the methane conversion and the hydrogen recovery factor. Considering the most favourable conditions, in the former case the conversion can be improved from 0.93 to 0.97, while, in the latter, the recovery factor increases from 0.60 to 0.73 with respect to a conventional membrane reactor. However, the two improvements are obtained with distinct length distributions. Moreover, the influence of the heat exchange area of the reactor was studied, analyzing a PSMR having adiabatic permeative stages (with the same membrane area, amount of catalyst and heat-exchange area as the MR). The main result of this analysis is a much higher maximized recovery factor (+21% ca.) than the conventional MR. Finally, in order to select the system producing the highest amount of hydrogen in the permeate, an overall performance index, i.e. the hydrogen recovery yield, has been introduced. In this context, the stage distribution resulting by maximizing the recovery factor proves the best reactor configuration, leading to an overall recovery yield at least 14% higher than the other systems considered.

5.4.2 INERT STAGE MEMBRANE REACTOR

After studying the PSMR performance as function of several membrane area and catalyst axial distribution, the role of this last variable is investigated for an Inert Stage Membrane Reactors. Several different catalytic pack distributions were considered in both co- and counter-current flow. First, a two-stage ISMR was studied, showing that this distribution provides a high H_2 recovery factor (especially in counter-current, where its value reached almost the unity), but quite low hydrogen recovery yield and methane conversion. Then two ten-stage ISMRs were investigated, whose distributions were obtained by maximizing, with respect to the stage lengths, two different objective functions (hydrogen recovery yield and methane conversion, respectively) by means of an appropriate optimization procedure. The results showed that the counter-current flow provides always significantly better performances than the co-current one. As concerns the shape of the distribution obtained, the analysis reveals that an almost equi-sized distribution is achieved by maximizing the recovery factor in both the configuration flow, whereas, when maximizing the conversion, the optimization procedure provided a negligible last inert stage, decreasing in fact the actual number of stages. After this type of analysis, also the role of the stages number and catalyst amount was analyzed, comparing the ISMR performances to the once of a conventional MR in the same operating conditions and configurations, finding that it is possible to achieve almost the same performances as the conventional MR by using an ISMR with a catalyst amount considerably lower (up to 70% lower). Then, it was possible to evaluate the amount of saved catalyst as function of the performance losses evaluated with respect to the conventional MR, demonstrating the important result that this analysis is in practise independent of the flow configuration considered. Furthermore, the fact that the conversion and recovery yield losses showed a very similar behaviour allowed to develop a single " advantage map", on which it is possible to read directly the advantages in using an ISMR instead of an MR in dependence only on the particular process being carrying out (methane steam reforming in this case).

5.5 APPENDICES

5.5.1 APPENDIX A: PARAMETERS FOR METHANE STEAM REFORMING REACTION RATE

Table 5.17 and Table 5.18 report the controlling reaction rates expressions and the corresponding thermodynamic and kinetic parameters for methane steam reforming [5.12].

Table 5.17 – Equilibrium constants and kinetic parameters for methane steam reforming.

Reaction	Keq_j	$k_j = A_j \, exp\left(-\frac{E_j}{RT}\right)$	
		A_j	E_j
$r_1 = \frac{\frac{k_1}{P_{H_2}^{2.5}}\left(P_{CH_4}P_{H_2O} - \frac{P_{H_2}^3 P_{CO}}{Keq_1}\right)}{Den^2}$	$5.75 \cdot 10^{10}$ exp(11476/T) MPa^2	$1.336 \cdot 10^{15}$ mol MPa$^{0.5}$ g$_{cat}^{-1}$ h^{-1}	240.1 kJ mol^{-1}
$r_2 = \frac{\frac{k_2}{P_{H_2}}\left(P_{CO}P_{H_2O} - \frac{P_{H_2}P_{CO}}{Keq_2}\right)}{Den^2}$	$1.26 \cdot 10^{-2}$ exp(4639/T) -	$1.955 \cdot 10^{7}$ mol MPa^{-1} g$_{cat}^{-1}$ h^{-1}	67.13 kJ mol^{-1}
$r_3 = \frac{\frac{k_3}{P_{H_2}^{3.5}}\left(P_{CH_4}P_{H_2O}^2 - \frac{P_{H_2}^4 P_{CO}}{Keq_3}\right)}{Den^2}$	$7.24 \cdot 10^{8}$ exp(16115/T) MPa^2	$3.226 \cdot 10^{14}$ mol MPa$^{0.5}$ g$_{cat}^{-1}$ h^{-1}	243.9 kJ mol^{-1}
$Den = 1 + K_{CO}^{Adsorption} P_{CO} + K_{H_2}^{Adsorption} P_{H_2} + K_{CH_4}^{Adsorption} P_{CH_4} + K_{H_2O}^{Adsorption} \frac{P_{H_2O}}{P_{H_2}}$			

Table 5.18 – Adsorption parameters for methane steam reforming.

Adsorption Parameters: $K_i^{Adsorption} = K_i^0 \; exp\left(-\Delta H_i^{Adsorption} / RT\right)$		
$K^0_{CH_4}$ = 6.65 · 10^{-9} Pa^{-1}	$K^0_{H_2}$ = 6.12·10^{-14} Pa^{-1}	$K^0_{H_2O}$ = 1.77·10^{5}
K^0_{CO} = 8.23·10^{-10} Pa^{-1}	$\Delta H^{Adsorption}_{H_2}$ = -82.90 kJ mol^{-1}	$\Delta H^{Adsorption}_{CH_4}$ = -38.28 kJ mol^{-1}
$\Delta H^{Adsorption}_{H_2O}$ = 88.68 kJ mol^{-1}	$\Delta H^{Adsorption}_{CO}$ = -70.65 kJ mol^{-1}	

5.5.2 APPENDIX B: EVALUATION OF THE PHYSICAL PROPERTIES OF THE SYSTEM

5.5.2.1 VISCOSITY AND THERMAL CONDUCTIVITY OF PURE GASES

The viscosity (μ_i) and the thermal conductivity (k_i) of a single gaseous component are calculated from the kinetic theory of gases [5.19], where β_1 is a semi-empirical constant depending on the units used and σ_i and Cp_i are a characteristic diameter of the molecule and the specific heat of the ith species, respectively. The collision integral Ω_μ is evaluated in the same way as indicated in Section 3.7.1.1.

$$\mu_i = \beta_1 \frac{\sqrt{M_i T}}{\sigma_i^2 \Omega_\mu}, \qquad k_i = \left(\hat{C}p_i + \frac{5}{4}\frac{R}{M_i}\right)\mu_i \tag{5.32}$$

5.5.2.2 VISCOSITY AND THERMAL CONDUCTIVITY OF GAS MIXTURES

Similarly to what done in Section 3.7.1.2, the Wilke semi-empirical correlation [5.19] is used to calculate both the viscosity and the thermal conductivity of the gas mixtures in the tube and in the shell of the reactor (Eq. 5.33-5.34).

$$\mu_{mix} = \sum_{i=1}^{N^{Species}} \frac{y_i \mu_i}{\sum_{j=1}^{n} y_j \Phi_{ij}^{\mu}}, \; k_{mix} = \sum_{i=1}^{N^{Species}} \frac{y_i k_i}{\sum_{j=1}^{n} y_j \Phi_{ij}^{k}} \tag{5.33}$$

$$\Phi_{ij}^{\mu} = \frac{1}{2\sqrt{2}} \left(1 + \frac{M_i}{M_j}\right)^{-0.5} \left[1 + \left(\frac{\mu_i}{\mu_j}\right)^{0.5} \left(\frac{M_j}{M_i}\right)^{0.25}\right]^2$$
$$\Phi_{ij}^{k} = \frac{1}{2\sqrt{2}} \left(1 + \frac{M_i}{M_j}\right)^{-0.5} \left[1 + \left(\frac{k_i}{k_j}\right)^{0.5} \left(\frac{M_j}{M_i}\right)^{0.25}\right]^2 \tag{5.34}$$

5.5.2.3 MOLAR ENTHALPY OF PURE GASES

The molar enthalpy is calculated as Eq. 5.35, where the specific molar heat, Cp_i is expressed by a polynomial expression ($Cp_i = a_i + b_i T + c_i T^2 + d_i T^3$). The thermodynamic data used in the previous expressions are reported in Table 5.19.

Table 5.19 – Thermodynamic parameters of the species involved in the process.

Cp_i, J/(mol K)	ΔH_i^0, J/mol	$a \cdot 10^{-1}$	$b \cdot 10^{3}$	$c \cdot 10^{6}$	$d \cdot 10^{9}$
H_2	0	2.909	-1.915	4.001	-0.87
CH_4	-74848	1.987	50.21	12.68	-11.00
CO_2	0	2.224	59.77	-34.99	7.464
H_2O	0	3.222	1.922	10.55	-3.59
CO	-393514	2.814	1.674	5.368	-2.22
N_2	-241827	2.888	-1.570	8.075	-2.87

$$\Delta H_i\left(T\right) = \Delta H_i^0 + \int_{T_{Ref}}^{T} Cp_i\, dT\,, \quad \Delta H_i^0 = \Delta H_i\left(T_{Ref} = 298.15\,\mathrm{K}\right) \tag{5.35}$$

5.5.3 APPENDIX C: EMPIRICAL CORRELATION FOR THE HEAT TRANSFER COEFFICIENT

The expressions for the calculation of the furnace-shell (U^{Ext}) and shell-tube (U^{TM}) heat transfer coefficients are based on a series of resistances, as illustrated in the sketch reported in Figure 5.48. The temperature of the external wall is assumed equal to that of the furnace. The external and trans-membrane overall heat transfer coefficients are expressed as indicated in Eqs. 5.36-5.37, where the outer areas are set as reference values for the shell and tube side.

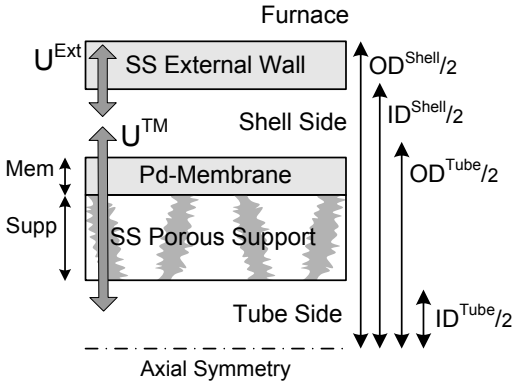

Figure 5.48 – Scheme of the porous Stainless Steel supported Pd-alloy membrane considered.

$$\frac{1}{U^{Ext}} = \frac{OD^{Shell}}{2k_{SS}} ln\left(\frac{OD^{Shell}}{ID^{Shell}}\right) + \frac{OD^{Shell}}{ID^{Shell}} \frac{1}{h^{Shell}} \tag{5.36}$$

$$\frac{1}{U^{TM}} = \frac{1}{h^{Shell}} + \frac{OD^{Tube}}{2k^{Mem}} ln\left(\frac{OD^{Tube}}{ID^{Tube} + 2\delta^{Supp}}\right) + \\ + \frac{OD^{Tube}}{2k^{Supp}} ln\left(\frac{ID^{Tube} + 2\delta^{Supp}}{ID^{Tube}}\right) + \frac{OD^{Tube}}{ID^{Tube}} \frac{1}{h^{Tube}} \tag{5.37}$$

The thermal conductivity of the porous support k^{Supp} is calculated as a weighted mean of two conductivities (Eq. 5.38), where k_{SS} and k_{Mix}^{Perm} are the thermal conductivities of the stainless steel and of the gaseous mixture in the tube (permeate) side, respectively.

$$k^{Supp} = \left(1 - \varepsilon_{Supp}\right) k_{SS} + \varepsilon_{Supp}\, k_{Mix}^{Perm} \tag{5.38}$$

5.5.3.1 CASE PSMR

Wherever a packed bed is present, the heat transfer coefficient between the fluid in the bed and the walls (membrane on one side and external wall on the other) is calculated as Eq. 5.39 [5.20], otherwise, the correlations shown in Eqs. 5.40 are used [5.21].

$$h^{Shell} = 5\frac{k_{Mix}^{Ret}}{d_p} Re_p^{0.365}, \qquad Re_p = \frac{\rho v d_p}{\mu} \tag{5.39}$$

$$h = 0.027 \frac{k_{Mix}}{D_{Eq}} Re^{0.8}\, Pr^{\frac{1}{3}} \tag{5.40}$$

5.5.3.2 CASE ISMR

Where the packed bed is present, the heat transfer coefficient between the fluid in the bed and the walls is evaluated from Eq. 5.41 [5.27], otherwise, the correlation shown in Eq. 5.42 is used.

$$h^{Shell} = 0.813 \frac{k_{Mix}^{Ret}}{D_{Eq}^{Shell}} exp\left(-\frac{6 d_p}{D_{Eq}^{Shell}} \right) Re_p^{0.9}, \qquad Re_p = \frac{\rho v d_p}{\mu} \tag{5.41}$$

$$h = 0.027 \frac{k_{Mix}}{D_{Eq}} Re^{0.8} Pr^{\frac{1}{3}} \tag{5.42}$$

5.6 LIST OF SYMBOLS

A_c	cross-sectional area [m^2]
$\widetilde{C}p_i$	specific heat [J mol^{-1} K^{-1}]
D_m	membrane mean diameter [m]
D_{Eq}	equivalent diameter [m]
d_p	mean pellet diameter [m]
E_d	permeance activation energy [J mol^{-1}]
F	molar flow rate [mol s^{-1}]
h	heat transfer coefficient [J s^{-1} m^{-2} K^{-1}]
$\Delta\widetilde{H}_i$	molar enthalpy of the ith species [J mol^{-1}]
$\Delta\widetilde{H}_i^0$	reaction molar enthalpy of the ith species at standard state [J mol^{-1}]
ID , OD	inner, outer diameter [m]
k	thermal conductivity [J s^{-1} m^{-1} K^{-1}]
k_j	kinetic constants in methane steam reforming kinetics [see Table 5.17]
K_{Eq_j}	equilibrium constants in methane steam reforming kinetics [see Table 5.17]
l	stage length [m]
L_{Mixing}	mixing length [m]

n	exponent in the H_2 permeation law [-]
n^{Ret}, n^{Perm}	number of species in the retentate and permeate side [-]
N_i	molar permeating flux of the ith species [mol m^{-2} s^{-1}]
P	pressure [Pa]
Pr	Prandtl's number [-]
r	radial coordinate (referred to a catalytic pellet) [m]
R	ideal gas constant = 8.31451 [J mol^{-1} K^{-1}]
Re	Reynolds' number [-]
Re_p	Reynolds' number for packed beds [-]
R_i	rate of formation of the ith species [mol s^{-1} m^{-3})]
T	temperature [K]
U	overall heat transfer coefficient [J h^{-1} m^{-2} K^{-1}]
v	velocity [m s^{-1}]
y_i	molar fraction of the ith species in mixture [-]
$y_{Catalyst}$	catalyst amount (fraction) [-]
x	methane conversion [-]
z	reactor abscissa [m]
Greek Symbols	
δ	thickness [m]
ε	voidage degree [-]
η	effectiveness factor [-]
Φ	Wilke's coefficient in the expression of viscosity and thermal conductivity [-]
κ	permeability pre-exponential factor [mol m^{-1} s^{-1} Pa^{-n}]

μ	viscosity [Pa s]
τ	tortuosity [-]
	Subscripts
eff	effective (velocity and diffusivity)
Mix	mixture
$Supp$	membrane support
	Superscripts
Cat	(referred to) catalytic pellet
Ext	external
Fur	furnace
K	Knudsen (referred to the diffusivity)
Mem	membrane
Min	minimum
MS	Maxwell-Stefan (diffusivity)
SS	stainless steel
Tot	total (referred to the reactor length)
TM	transmembrane
	Acronyms
MR, TR	conventional Membrane Reactor, Traditional Reactor
PSMR, ISMR	Permeative, Inert Stage Membrane Reactor
RF	H_2 recovery factor [-]
RY	H_2 recovery yield [-]

5.7 LITERATURE CITED

[5.1] Dittmeyer R., Höllein V. and Daub K., 2001. Membrane reactors for hydrogenation and dehydrogenation processes based on supported palladium. *Journal of Molecular Catalysis A: Chemical*, **173**: 135-184.

[5.2] Keil J.K., 2007. *Modeling of Process Intensification*. WILEY-VCH Verlag GmbH & Co. KGaA, Weinheim.

[5.3] Koukou M., Papayannakos N. and Markatos N., 2001. On the importance of non-ideal flow effects in the operation of industrial-scale adiabatic membrane reactors. *Chemical Engineering Journal*, **83**: 95-105.

[5.4] Assabumrungrat S., Suksomboom K., Praserthdam P., Tagawa T. and Goto S., 2002. Simulation of palladium membrane reactor for dehydrogenation of ethylbenzene. *Journal of Chemical Engineering of Japan*, **35**: 263-273.

[5.5] Fukuhara C. and Igarashi A., 2003. Two-dimensional simulation of a membrane reactor for dehydrogenation of ethylbenzene, considering heat and mass transfer. *Journal of Chemical Engineering of Japan*, **36**: 530-539.

[5.6] Tiemersma T.P., Patil C.S., van Sint Annaland M. and Kuipers J.A.M., 2006. Modelling of packed bed membrane reactors for autothermal production of ultrapure hydrogen. *Chemical Engineering Science*, **61**: 1602-1616.

[5.7] Kim J., Choi B. and Yi J., 1999. Modified simulation of methane steam reforming in Pd-membrane-packed bed type reactor. *Journal of Chemical Engineering of Japan*, **32**: 760-769.

[5.8] Gallucci F., Paturzo L. and Basile A., 2004. A simulation study of steam reforming of methane in a dense tubular membrane reactor. *International Journal of Hydrogen Energy*, **29**: 611-617.

[5.9] Marigliano G., Barbieri G. and E. Drioli, 2001. Effect of energy transport on a palladium-based membrane reactor for methane steam reforming process. *Catalysis Today*, **67**: 85-99.

[5.10] Lin Y., Liu S., Chuang C. and Chu Y., 2003. Effect of incipient removal of hydrogen through palladium membrane on the conversion of methane steam reforming: experimental and modeling. *Catalysis Today*, **82**: 127-139.

[5.11] Oklany J., Hou K. and Hughes R., 1998. A simulative comparison of dense and microporous membrane reactors for the steam reforming of methane. *Applied Catalysis. A: General*, **170**: 13-22.

[5.12] Xu J., Froment G.F. and 1989. Methane Steam Reforming, Methanation and Water-Gas Shift: I. Intrinsic Kinetics. AIChE Journal, **35**: 88-96.

[5.13] Roy S., 1998. Fluidized bed steam methane reforming with high-flux membranes and oxygen input. *PhD Thesis*. The University of Calgary, Calgary.

[5.14] Sodrè J.R. and Parise J.A.R., 1998. Fluid flow pressure drop through an annular bed of spheres with wall effects. *Experimental Thermal and Fluid Science*, **17**: 265-275.

[5.15] The MathWorks Inc., MATLAB [Online]. Internet link: http://www.mathworks.com /products/matlab/.

[5.16] Tong J., Matsumura Y., Suda H. and Haraya K., 2005. Experimental Study of Steam Reforming of Methane in a Thin (6 μm) Pd-Based Membrane Reactor. *Industrial Engineering and Chemical Research*, **44**: 1454-1465.

[5.17] Matsumura Y., 2008. *Private Communication*.

[5.18] Xu J. and Froment G.F., 1989. Methane Steam Reforming, Methanation and Water-Gas Shift: II. Diffusional Limitations and Reactor Simulation. AIChE Journal, **35**: 97-103.

[5.19] Bird R.B., Stewart W.E. and Lightfoot E.N., 1960. *Transport Phenomena. Second edition*. Wiley, New York.

[5.20] Gunn D.J. and Khalid M.K., 1975. Thermal dispersion and wall heat transfer in packed beds. *Chemical Engineering Science*, **30**: 261-267.

[5.21] Kern D.Q., Ed.1997. *Process Heat Transfer*. McGraw-Hill, New York, 103-104.

[5.22] Adris A.M., Lim C.J. and Grace J.R., 1997. The fluidized-bed membrane reactor for steam methane reforming: model verification and parametric study. *Chemical Engineering Science*, **52**:1609-1622.

[5.23] Chiappetta G., Clarizia G. and Drioli E., 2008. Theoretical analysis of the effect of catalyst mass distribution and operation parameters on the performance of a Pd-based membrane reactor for water-gas shift reaction. *Chemical Engineering Journal*, **136**: 373-382.

[5.24] Caravella A., Di Maio F.P. and Di Renzo A., 2008. Optimization of Membrane Area and Catalyst Distribution in a Permeative-Stage Membrane Reactor for Methane Steam Reforming. *Journal of Membrane Science*, **321**: 209-221.

[5.25] Ward T. and Dao T., 1999. Model of hydrogen permeation behaviour in palladium membranes. *Journal of Membrane Science*, **153**: 211-231.

[5.26] Caravella A., Barbieri G. and Drioli E., 2008. Modelling and Simulation of Hydrogen Permeation through Supported Pd-based Membranes with a Multicomponent Approach. *Chemical Engineering Science*, **63**: 2149-2160.

[5.27] Froment G.F., 1990. *Chemical reactor analysis and design*. Wiley, New York.

[5.28] Åsen K.I. and Andersen H.S., 2002. *Method for manufacturing a hydrogen and nitrogen containing gas mixture*. International Patent application no. WO 02/072470 A1.

[5.29] Birdsell S.A. and Willms R.S., 1998. Tritium recovery from tritiated water with a two-stage palladium membrane reactor. Fusion engineering and design. *Proceeding Acts of ISFNT 4: International Symposium on Fusion Nuclear Technology N°4, Tokyo, Japan*, **39-40**: 1041-1048.

[5.30] Lund C.R.F., 2001. Water-Gas Shift Kinetics over Iron Oxide Catalysts at Membrane Reactor Conditions. *Final Activity Report*. Chemical Engineering Department, University at Buffalo (SUNY-Buffalo, NY 14260-4200).

[5.31] Patil C.S., 2005. Membrane Reactor Technology for Ultrapure Hydrogen Production. *PhD Thesis*, ISBN: 9036522463. University of Twente, (Twente, The Netherlands).

[5.32] Li A., Lim C.J. and Grace J.R., 2008. Staged-separation membrane reactor for steam methane reforming. *Chemical Engineering Journal*, **138**: 452-459.

[5.33] Jordal K., Bredesen R., Kvamsdal H.M. and Bolland O., 2004. Integration of H_2-separating membrane technology in gas turbine processes for CO_2 capture. *Energy*, **29**: 1269-1278.

OVERALL CONCLUSIONS AND PERSPECTIVES

CONCLUSIONS

This dissertation was focussed on the modelling of Pd-based membranes and Pd-based membrane reactors where methane steam reforming was considered to be carried out. In particular, in Chapter 3 a detailed and complex model was developed to describe the hydrogen permeation through supported Pd-based membranes. The whole permeation mechanism was divided into several elementary steps, whose behaviour is controlled by certain mathematical equations. It was demonstrated the ability of the model in determining the contribution of each step to the total resistance to the mass transfer from the upstream to the downstream, identifying the rate-determining steps in dependence on several membrane thicknesses and operating conditions, like temperature and fluid-dynamic conditions expressed in terms of Reynolds' number. The model was finally validated by means of some experimental data obtained from the open literature showing a good agreement with them, and was compared with another one already present in literature.

Successively (Chapter 4), the same model was used to quantify the influence of the concentration polarization in self-supported Pd-based membranes as a function of several variables: hydrogen molar fraction in the upstream, temperature, total pressure of upstream and downstream, membrane thickness and fluid-dynamic conditions. After studying the relation between permeance, transmembrane flux and polarization, the here-called "polarization maps" were made, which are diagrams where, once the system conditions have been known, it is possible to recognize directly the influence of this phenomenon in terms of an opportunely-defined polarization coefficient. Moreover, a comparison with some literature data was made, demonstrating the analysis validity and indicating also that, in some conditions, this phenomenon may be such relevant to become the rate-determining step of the entire permeation process.

In the Chapter 5, an analysis of two types of staged Pd-based membrane reactors – namely PSMR ("*Permeative Stage Membrane Reactor*") and ISMR ("*Inert Stage Membrane Reactor*") – was carried out in a tube-in-tube configuration in co- (both PSMR and ISMR) and counter-current (only ISMR). After an appropriate model validation using opportune literature data, each reactor was studied. As concerns the first one, nine stages (5 reactive and 4 permeative ones) were considered, analyzing the effect of three different catalyst and membrane area axial distributions. The first one to be studied was the equi-sized distribution, whilst the other two were obtained by optimizing two different objective functions (first methane conversion and then hydrogen recovery factor) with respect to the stages' lengths. The results showed a significant improvement of the reactor performances in terms of the optimized parameter, highlighting the ability of the optimization procedure to reduce the total number of stages when the last one is useless for increasing the performance index to be optimized. Then, a choice of the best distribution among the ones obtained in all the considered cases was made by adopting the overall criterion of the highest hydrogen recovery yield. From this comparison, the distribution providing the maximum hydrogen recovery factor resulted to be the most convenient. As regards the second staged membrane reactor (ISMR), firstly, the role of the catalyst distribution was analyzed by setting the catalyst amount and the stages' number as constant, evaluating the performances related to three distributions: 1) the reference distribution (the entire catalytic pack placed at the reactor inlet) and 2-3) two distributions achieved by applying the same optimization procedure as the one used for the PSMR to methane conversion and hydrogen recovery yield (instead of recovery factor). The results showed that the reference distribution provides the highest hydrogen recovery factor, but quite modest methane conversion and hydrogen recovery yield, whilst the other two distributions determine much higher performance than the first one, the counter-current case being the best configuration in almost all the situations. Then, in a second step, the effect of catalyst amount and stages' number was studied, showing the possibility to save up to 70-75% of catalyst with respect to the conventional membrane reactor by adopting an opportune staged distribution.

PERSPECTIVES OF FUTURE WORKS

The work carried out in this dissertation is to be intended as being placed in a wider aim, consisting in the design of membrane-based plants able to reduce the plant volumes and solve (partially or totally) the problems related to the nocive and greenhouse gaseous emissions with a consequent more efficient exploitation of the raw materials. In this direction, the next steps of study are the development of the following topics:

- ✓ Integration of the new model introduced in Chapter 3 in design of reactors.
- ✓ Developing analogous models for polymeric and microporous membranes, adopting a multi-scale approach in order to reduce the number of unknown parameters.
- ✓ Considering other processes, like WGS and methanol/ethanol steam reforming, to be carried out in staged membrane reactors.
- ✓ Modelling, simulation and design of integrated membrane technology-based plant accounting for the possibility to produce energy by means of Fuel Cells, generally characterized by a high energetic efficiency with respect to the conventional engines.

Furthermore, at the moment the assembling of a laboratory-scale experimental ISMR (Inert Stage Membrane Reactor, see Chapter 5) is under development. This will allow to provide the experimental proof of the advantages in using staged membrane reactor for several processes.

LIST OF PUBLICATIONS

PUBLICATIONS ON INTERNATIONAL JOURNALS

[6.1] **Caravella A.**, Di Maio F.P. and Di Renzo A., 2008. Computational study of improved membrane reactor configurations for methane steam reforming: I. Staged Reactor with Optimized Lengths. *Submitted for publication to AIChE Journal*.

[6.2] **Caravella A.**, Di Maio F.P. and Di Renzo A., 2008. Computational Study of Improved Membrane Reactor Configurations for Methane Steam Reforming: II. Effect of the stages number and catalyst amount. *Submitted for publication to AIChE Journal*.

[6.3] **Caravella A.**, Barbieri G. and Drioli E., 2008. Concentration polarization analysis in self-supported Pd-based membranes. *Submitted for publication to Separation Purification Technology*.

[6.4] **Caravella A.**, Di Maio F.P. and Di Renzo A., 2008. Optimization of membrane area and catalyst distribution in a permeative-stage membrane reactor for methane steam reforming. *Journal of Membrane Science*, **321**: 209-221.

[6.5] **Caravella A.**, Barbieri G. and Drioli E., 2008. Modelling and simulation of hydrogen permeation through supported Pd-based membranes with a multicomponent approach. *Chemical Engineering Science*, **63**: 2149-2160.

[6.6] Brunetti A., **Caravella A.**, Barbieri G., Drioli E., 2007. Simulation study of water gas shift reaction in a membrane reactor. *Journal of Membrane Science*, **306**: 329-340.

PUBLICATIONS IN PROCEEDING ACTS OF CONGRESSES

[6.7] **Caravella A.**, Di Maio F.P. and Di Renzo A., 2008. Methane Steam Reforming in a staged membrane reactor: influence of the number of stages and amount of catalyst. *Submitted to the 9th Conference on Chemical & Process Engineering* (*ICheaP 9*). May 10-13 Rome (Italy).

[6.8] **Caravella A.**, Barbieri G. and Drioli E., 2008. Effect of the concentration polarization on the hydrogen permeation through Pd-based membranes. *Submitted to the 9th Conference on Chemical & Process Engineering* (*ICheaP 9*). May 10-13 Rome (Italy).

[6.9] **Caravella A.**, Barbieri G., Di Maio F.P. and Di Renzo A., 2008. Permeazione di idrogeno in membrane a base di palladio: Effetto della composizione di retentato sugli stadi limitanti del processo. *Proceedings Acts of the National Italian Congress on Chemical Engineering GRICU 2008 "Ingegneria Chimica: Le Nuove Frontiere"*. Le Castella (Crotone, Italy), September 14-17.

[6.10] **Caravella A.**, Di Maio F.P. and Di Renzo A., 2008. Influence of the Catalyst Axial Distribution in a Pd-based Membrane Reactor for Methane Steam Reforming, *Proceeding Acts of 18th International Congress of Chemical and Process Engineering* (*CHISA 2008*), Prague (Czech Republic) 24-28 August.

[6.11] **Caravella A.**, Barbieri G. and Drioli E., 2008. Influence of the operating conditions on the rate-determining steps of the H_2 permeation through supported Pd-based membranes. *Proceeding Acts of 18th International Congress of Chemical and Process Engineering* (*CHISA 2008*), Prague (Czech Republic) 24-28 August.

[6.12] Brunetti A., Barbieri G., **Caravella A.** and Drioli E., 2007. Membrane Reactors for Process Intensification. *Proceeding Acts of European Process Intensification Conference* (*EPIC*), Copenhagen (Denmark) 19-20 September.

[6.13] Brunetti A., **Caravella A.**, Barbieri G. and Drioli E., 2007. Effect of membrane selectivities on WGS reaction in a non-isothermal membrane reactor. *Proceeding Acts of 8Th International Conference on Chemical and Process Engineering* (*ICHEAP 8*), Ischia (Naples, Italy) 24-27 June.

[6.14] Brunetti A., **Caravella A.**, Barbieri G. and Drioli E., 2006. Simulation Study of Water Gas Shift Reaction in a Catalytic Membrane Reactor. *Proceeding Acts of First Mediterranean Congress Chemical Engineering for Environment*, San Servolo (Venice, Italy) 4-6 October.

[6.15] **Caravella A.**, Barbieri G. and Drioli E., 2006. Theoretical Study of H_2 Permeation through Supported Pd-Based Membranes. *Proceeding Acts of Euromembrane 2006*, Giardini Naxos (Taormina, Italy), 14-17 September.

[6.16] **Caravella A.**, 2006. Influence of Porous Supports on the Hydrogen Permeation through Pd-based Membranes. *Proceeding Acts of 8th Network Young Membrains* (*NYM 8*), Rende (Cosenza, Italy), 11-13 September.

[6.17] **Caravella A.**, Barbieri G. and Drioli E., 2006. H_2 Permeation through thin Pd-based Membranes Deposited on Multilayer Porous Supports. *Proceeding Acts of 9th International Conference on Inorganic Membrane* (*ICIM 9*), Lillehammer (Norway), 25-29 June.

[6.18] Scura F., Barbieri G., **Caravella A.** and Drioli E., 2005. H_2 Purification For Pem-FC Using Polymeric Membrane Systems. *Proceeding Acts of 7th Conference on Chemical & Process Engineering* (*ICheaP 7*), Giardini Naxos (Taormina, Italy), 15-18 May.

[6.19] Scura F., Barbieri G., **Caravella A.** and Drioli E., 2005. Purification of H_2 for Fuel Cells using a Pd-based Membrane Integrated System. *Proceeding Acts of International Congress on Membranes and Membrane Processes* (*ICOM 2005*), Seoul (Korea), 21-26 August.

[6.20] Scura F., Barbieri G., **Caravella A.** and Drioli E., 2004. Purificazione di H_2 con membrane polimeriche. *S.C.I. Itinerari di Chimica in Calabria 6*, Rende (Italy), 21-22 October.

ACKNOWLEDGMENTS

Scrivere dei ringraziamenti senza risultare banale può costituire un compito arduo tanto quanto la stesura di un'intera tesi se non si fa riferimento a ciò che si sente realmente dentro. D'altro canto, non sarei neppure capace di citare sterilmente persone che per un motivo o per un altro non avessero avuto un ruolo nella mia crescita non tanto intellettuale quanto piuttosto umana. Proprio per questo, quelle citate di seguito sono le persone che hanno avuto ed hanno tuttora un posto particolare nella mia vita.

Ringrazio di tutto cuore il Prof. Francesco Paolo Di Maio e l'Ing. Alberto Di Renzo per la disponibilità, l'interesse, la pazienza e la fiducia che hanno sempre avuto nei miei confronti.

Per gli stessi motivi e con altrettanta intensità, ringrazio il Prof. Enrico Drioli e l'Ing. Giuseppe Barbieri, che hanno sempre dimostrato verso di me una considerazione che farò di tutto per continuare a meritare.

Un Ricordo speciale dal più profondo di me stesso va ad una persona che ha sempre avuto per tutti un grande affetto, che era capace di dimostrare anche solo con un sorriso, una bonaria pacca sulle spalle o un pezzo di pizza portato all'improvviso per riunirci tutti insieme ed

alleggerire, così, il fardello di una giornata più impegnativa del solito: Grazie di cuore per tutto, Signor Mazzitè.

Ringrazio i miei compagni di merende di laboratorio (nel vero senso del termine): Fernando, Vincenzino (si chiama veramente così, non sono io a sfotterlo), Ambra, Grazia, Domenico, Patrizia, Marzia, Serafino, Giovanna, Cicciopaglià (forma contratta che a breve entrerà nel linguaggio comune), Barby (con la "y") e Lucia per l'amicizia, l'affetto e la simpatia con cui hanno accompagnato ed accompagnano ancora, consapevolmente o meno, le mie giornate universitarie e non.

Ciccioscù!!!, non ti preoccupare: come potrei dimenticarmi di Te, Adele e Paola, che siete stati e rimarrete comunque un punto fisso delle mie giornate?!. Anche se non siamo più a contatto come una volta (sempre a distanza di sicurezza, è chiaro!), avrete sempre un posto speciale nella mia vita. (P.s.: ti prometto di impegnarmi al massimo per insegnare al piccolo Gennarino la parola "Ciccioscù" prima che dica "mamma" o "papà").

Infine, ultimi nell'elenco, ma primi nel mio cuore, ringrazio con tutto me stesso mia Madre e mio Fratello per l'affetto, il sostegno e la fiducia che non mi hanno mai fatto mancare in tutta la mia vita, anche se ogni tanto affiorano le fatidiche domande: "Ma che fai tutto il giorno davanti al computer???", e, soprattutto "Ma sto dottorato, che cos'è???".